



**HAL**  
open science

# Surface functionalization of zirconium based metallic glasses.

Paul Hervier

► **To cite this version:**

Paul Hervier. Surface functionalization of zirconium based metallic glasses.. Materials. Université Grenoble Alpes; Instituto superior técnico (Lisbonne), 2017. English. NNT: 2017GREAI088 . tel-01737465

**HAL Id: tel-01737465**

**<https://theses.hal.science/tel-01737465>**

Submitted on 19 Mar 2018

**HAL** is a multi-disciplinary open access archive for the deposit and dissemination of scientific research documents, whether they are published or not. The documents may come from teaching and research institutions in France or abroad, or from public or private research centers.

L'archive ouverte pluridisciplinaire **HAL**, est destinée au dépôt et à la diffusion de documents scientifiques de niveau recherche, publiés ou non, émanant des établissements d'enseignement et de recherche français ou étrangers, des laboratoires publics ou privés.



## THÈSE

Pour obtenir le grade de  
**DOCTEUR DE LA COMMUNAUTE UNIVERSITE  
GRENOBLE ALPES**

**préparée dans le cadre d'une cotutelle entre la  
Communauté Université Grenoble Alpes et l'Institut  
Supérieur Technique de Lisbonne**

Spécialité : **Matériaux, Mécanique, Génie Civil, Electrochimie**  
Arrêté ministériel : le 6 janvier 2005 - 7 août 2006

Présentée par  
**Paul HERVIER**

Thèse dirigée par **Jean-Jacques BLANDIN** et **Rui VILAR**  
co-dirigée par **Sébastien GRAVIER**

préparée au sein des **Laboratoires Science et Ingénierie des  
Matériaux et des Procédés (SIMaP)** et **Center of Physics and  
Engineering of Advanced Materials (CeFEMA)**

dans les **Écoles Doctorales Ingénierie – Matériaux Mécanique  
Énergétique Environnement Procédés Production (I-MEP2)**  
et **PhD program of Materials Engineering of IST**

## **Fonctionnalisation de surface de verres métalliques base zirconium**

Thèse soutenue publiquement le **28 Novembre 2017**,  
devant le jury composé de :

**Mme Anne TANGUY**

Professeur, INSA Lyon (Présidente)

**Mr Jean-Christophe SANGLEBOEUF**

Professeur, Université de Rennes (Rapporteur)

**Mr Victor Manuel Barbas de OLIVEIRA**

Professeur, ISE Lisbonne (Rapporteur)

**Mme Maria Amélia Martins de ALMEIDA**

Professeur, IST Lisbonne (Examinatrice)

**Mr Marc BLETRY**

Maître de Conférence, Université de Paris (Examineur)

**Mr Jean-Jacques BLANDIN**

Directeur de recherche, Université Grenoble Alpes (Directeur de Thèse)

**Mr Rui Mario Correira da Silva VILAR**

Directeur de recherche, IST Lisbonne (co-Directeur de Thèse)

**Mr Sébastien GRAVIER**

Maître de Conférence, Université Grenoble Alpes (co-encadrant)





# Acknowledgement

Before forgetting someone, I would like to extend my warmest thanks to all those who have contributed directly or indirectly to this thesis work.

I would like to thank the IDS-FUNMAT program for giving me the opportunity to realize this PhD thesis. A special thanks to the coordination team from University of Bordeaux who took care of the successful completion of this thesis. I also thank all my thesis jury for accepting to read and review my work.

I am truly grateful for the assistance and the guidance of my supervisors Pr. Rui Vilar at the Instituto Superior Tecnico of Lisbon and Jean-Jacques Blandin and Sebastien Gravier at the University of Grenoble. Thanks to them, I have acquired a great deal of technical and theoretical knowledges. Our long and fruitful discussions have been very valuable for me and gave me constant sources of motivation during these 3 years.

My grateful thanks to Vitor Oliveira who teach me how to use the laser device and also to study the laser-material interaction.

I would like to thank you Pr. Ana Paula Serro for the permission to perform wettability measurements.

I would like to thank you Pr. Ana Maria Rego, who performed the XPS analysis and her precious help for the interpretation of the results.

Many thanks to Pr. Fatima Montemor for the permission to perform the corrosion tests and her valuable advices in electro-chemistry.

My thanks to Pr. Amelia Almeida, who supports me during the period in Lisbon and gave me precious advices in microscopy and wear phenomenon.

My thanks to Isabel Nogueira for her precious help with scanning electron microscopes.

My friendly thanks to all my colleagues in the 4.1.5 room of IST: Bruno Nunes, Cristina Piotto, Tiago Ribeiro and especially to Liliana Canguero who helped me to domesticate the laser technology.

A massive thank you to the technicians of the SIMaP laboratory Franck Pelloux and Xavier Bataillon, without whom this thesis wouldn't have been so extensive. They were always good advisors by separating the attainable from the unfeasible.

A very particular thank you to Charles Josserond, the electrician master, the Labview expert, who spent hours to make the technical devices functioning and had a major contribution in my thesis results.

A cheerful thank you to all the researchers, the administration staff of the SIMaP laboratory and especially to the GPM2 group for all the good conversations and the support.

I would like to thank all the CMTC group, Stéphane Coindeau, Thierry Encinas, Frédéric Charlot and others for their help in structural analysis of materials.

A friendly thank you to all the PhD students and the interns without whom these 3 years wouldn't have been so enjoyable. A special respect to Alexis Lenain, Edouard Chauvet, Alexis Burr and Robin Gibaud from the 2014/2017 vintage!

A big thank you to the Vulkam team Nassim Mendil and Xavier Cerutti, whom were very pleasant colleagues and first order advisors and I wish all the best for the new company. I would like to also thank Rémi Daudin the new SIMaP researcher for helping me during my thesis writing.

Finally, I would like to thanks a million times my loved ones. My wonderful family, who support me since the beginning, who I owe it to be the person that I am today and of course my girlfriend, who faced my good and bad periods with a constant kindness from which I will be always grateful...

# Contents

## Introduction

### Chapter 1: Literature review

1.1. Metallic glass.....	4
1.1.1. Generalities .....	4
1.1.2. Elaboration of bulk metallic glass.....	5
1.2. Mechanical properties of metallic glass .....	9
1.2.1. Low temperature deformation.....	9
1.2.2. High temperature deformation: a BMG specificity. ....	10
1.3. Surface properties of bulk metallic glass .....	12
1.3.1. Wettability properties and generality .....	13
1.3.2. Corrosion properties.....	16
1.4. Surface texturing of materials .....	18
1.5. Femtosecond lasers in surface treatments .....	19
1.5.1. Laser operation principle .....	19
1.5.2. Femtosecond (fs) oscillators .....	21
1.5.3. Laser-material interaction in fs pulse regime.....	25
1.5.4. Effect of fs laser treatment on surface properties .....	36
1.5.5. Femtosecond laser treatments on metallic glass .....	43
1.6. Thermoforming of bulk metallic glasses.....	45
1.6.1. A specific process for amorphous metals .....	45
1.6.2. Different scales = different behaviours.....	46
1.6.3. Oxidation induced by thermoplastic forming processing .....	50
1.6.4. Surface functionalization using thermoforming capacity of bulk metallic glass...	51

1.7. Conclusion.....	54
----------------------	----

## **Chapter 2: Experimental methods**

2.1. Elaboration of Zr-based bulk metallic glasses .....	56
2.2. Rheological and thermal characterisation of $Zr_{65}Cu_{15}Al_{10}Ni_{10}$ bulk metallic glass .....	58
2.3. Femtosecond laser processing .....	60
2.3.1. Determination of the ablation threshold.....	62
2.3.2. Incubation factor of laser-irradiated materials .....	63
2.3.3. Stationary mode processing .....	63
2.3.4. Non-stationary mode processing.....	65
2.4. Thermoforming of $Zr_{65}Cu_{15}Al_{10}Ni_{10}$ bulk metallic glass .....	67
2.4.1. Thermoforming experiments in air .....	67
2.4.2. Thermoforming experiments under vacuum.....	67
2.4.3. Working problematics of thermoplastic forming under vacuum environment.....	70
2.4.4. Specifications of the moulds used for thermoplastic forming under vacuum. ....	72
2.5. Structural characterization.....	74
2.6. Surface characterisation .....	75
2.6.1. Topological characterisation .....	75
2.6.2. Chemical characterisation .....	77
2.7. Surface properties.....	78
2.7.1. Wettability measurements.....	78
2.7.2. Corrosion study.....	81

## **Chapter 3: Thermoforming of Zr-based metallic glasses**

3.1. Material's choice .....	86
3.2. Study of Zr <sub>3</sub> amorphous alloy.....	87
3.2.1. Structural characterization .....	87

3.2.2.	Thermal stability of Zr3 amorphous alloy .....	87
3.2.3.	Deformation behaviour at high temperature .....	90
3.3.	Thermoforming of Zr3 metallic glass .....	96
3.3.1.	Preliminary study in air .....	96
3.4.	Thermoforming of Zr3 BMG under vacuum .....	100
3.4.1.	Hot compression tests under vacuum environment .....	100
3.4.2.	Replication of micron-size parts using Si-moulds by TPF process. ....	102
3.4.3.	Thermoforming of nanometre size patterns .....	109
3.5.	XRD measurements of Zr3 amorphous alloys processed by TPF technique .....	116
3.6.	Conclusion.....	118

## **Chapter 4: Femtosecond laser texturing of bulk metallic glasses**

4.1.	Stationary mode experiments .....	119
4.1.1.	Determination of the ablation thresholds and incubation factors .....	119
4.1.2.	Morphological study: influence of the radiation fluence .....	124
4.1.3.	Morphological study: influence of the number of pulses. ....	126
4.1.4.	Structure formation thresholds.....	127
4.1.5.	On the formation of laser induced surface structures .....	129
4.1.6.	Structure formation below the ablation threshold.....	130
4.2.	Non-stationary experiments .....	137
4.2.1.	Effect of lateral displacement on surface structures .....	137
4.2.2.	Processing of ridges and LIPSS surface structures on metallic glasses.....	138
4.2.3.	Effect of $E_p$ and $N$ variations on structure morphology in non-stationary irradiation mode .....	141
4.3.	Surface properties of femtosecond laser textured metallic glasses .....	143
4.3.1.	Surface chemistry analysis.....	143
4.3.2.	Chemical analysis of the ablation particles.....	149

4.4. Structural characterization.....	151
4.5. Wettability measurements .....	153
4.6. Corrosion study .....	160
4.7. Conclusion.....	172

## **General Conclusion**

## **Annex**

## **Bibliography**

# List of Figures

Figure 1.1.1: Silica in crystalline (a) and amorphous (b) state, 2D analogy <sup>23</sup> . .....	4
Figure 1.1.2 : Discovery year and maximum diameters achieved in different alloy systems <sup>7</sup> . . .	5
Figure 1.1.3 : Scheme of the time-temperature-transformation (T-T-T) for a hypothetical alloy system. From the liquid state, at a too low cooling rate, as indicated by curve “1”, solidification will start at a temperature $T_1$ and a time $t_1$ . The resulted solid material will be in crystalline state. In contrary, if the liquid is cooled fast enough as presented by curve “2”, the liquid will stay in the undercooled state and when the glass transition temperature is reached, the liquid is “frozen-in” and a glassy phase is formed <sup>7</sup> . .....	6
Figure 1.1.4 : Differential thermal analysis of a Zr60Al15Ni25 amorphous alloy with both heating and cooling curves while reaching melting temperature $T_m$ <sup>27</sup> (left), zoom on a glass transition phenomena (right), adapted from <sup>34</sup> . .....	7
Figure 1.2.1: Relationship between tensile strength ( $\sigma_f$ ), Vickers hardness ( $H_v$ ) and Young’s Modulus (E) for various bulk amorphous alloys <sup>25</sup> . .....	10
Figure 1.2.2: Viscosity as a function of strain at different temperatures for a Pd <sub>40</sub> Ni <sub>40</sub> P <sub>20</sub> BMG <sup>45</sup> a), Strain modes domains for a Vit1 BMG <sup>43</sup> . .....	11
Figure 1.2.3: Master curves for normalized viscosity of Zr <sub>52.5</sub> Al <sub>10</sub> Cu <sub>22</sub> Ni <sub>13</sub> Ti <sub>2.5</sub> (D') and Zr <sub>52.5</sub> Al <sub>10</sub> Cu <sub>27</sub> Ni <sub>5</sub> Ti <sub>2.5</sub> (D'') <sup>20</sup> . .....	12
Figure 1.3.1 : Scheme of the Wenzel (right) and Cassie-Baxter (left) models. The different behaviours of a liquid droplet are represented were the liquid completely wets the surface (Wenzel) or the air is trapped within the surface structure (Cassie-Baxter) adapted from <sup>47</sup> . . .	14
Figure 1.3.2 : Scheme of the different possibilities where a droplet interact with surface with single or multi scale roughness, adapted from <sup>50</sup> . .....	15
Figure 1.3.3 : Surface free energy with dispersive and polar components for Zr <sub>55</sub> Al <sub>10</sub> Cu <sub>30</sub> Ni <sub>5</sub> (Y0), (Zr <sub>0.55</sub> Al <sub>0.10</sub> Cu <sub>0.3</sub> Ni <sub>0.05</sub> ) <sub>99</sub> Y <sub>1</sub> (Y1) and Ti6Al4V (Ti64) for rough (R) and smooth (S) surfaces <sup>13</sup> . .....	15
Figure 1.5.1: Absorption a), spontaneous emission b) and simulated emission c) mechanisms. ....	19
Figure 1.5.2: Scheme of a typical laser oscillator <sup>59</sup> . .....	20
Figure 1.5.3: Fluorescence emission spectra of some transition metal-doped broadband solid-state laser crystals, from <sup>60</sup> (a), Fourier transform of a Ti:S emission spectra (b). .....	22

Figure 1.5.4: Different field modes locked (a), and resulted total field in mode locking (b), adapted from <sup>62</sup> .....	22
Figure 1.5.5: Kerr lens mode-locking phenomenon. The refractive index of the Kerr lens increases with the laser beam intensity as $\Delta n = n_2 I(r, t)$ , where $n_2$ is the nonlinear refractive index of the amplifier medium and $I(r, t)$ the radial and time-dependent intensity of a short-pulsed laser beam <sup>63</sup> .....	23
Figure 1.5.6: Dispersion-Compensating Prism Pairs (DCPP) (a), Semiconductor Saturable Absorber Mirror (SESAM) (b).....	23
Figure 1.5.7: Simplified optical path of a femtosecond laser system, (a), (b), (c), (d) and (e) parts are described below. ....	24
Figure 1.5.8: Scheme of the chirped-pulse amplifier system, adapted from <sup>50</sup> .....	25
Figure 1.5.9: Timeline of major processes during femtosecond laser ablation of metals, adapted from Vorobyev <i>et al.</i> <sup>68</sup> and Canguero <sup>59</sup> . ....	27
Figure 1.5.10: Two Temperatures Model resolved for a 200fs laser pulse on aluminium (left) and nickel (right) targets for different fluencies, from Valette thesis <sup>74</sup> .....	29
Figure 1.5.11: Snapshots from the molecular dynamic simulation of laser irradiation of aluminium at fluence of 0.09J/cm <sup>2</sup> showing the phase of inertial confinement to liquid spallation (a) and at fluence of 0.2J/cm <sup>2</sup> illustrating conditions of thermal confinement leading to phase explosion (b) at 100 fs pulse duration, adapted from Zhigilei <i>et al.</i> <sup>78</sup> .....	31
Figure 1.5.12: Scheme of the major physical mechanisms involved in material ablation as melting, generation of sub-surface voids and material ejection from aluminium substrate. The Gaussian profile of the deposited energy in the laser beam explain the ablative phenomenon differences in between the centre (high fluence = spallation regime) and the peripheral part of the spot (low fluence = melting regime) from <sup>78</sup> .....	32
Figure 1.5.13: Ripples formed on sand (a), LIPSS (LSFLs) observed on CaF <sub>2</sub> substrate with Ti:Sapphire source of around 800nm wavelength <sup>92</sup> .....	33
Figure 1.5.14: Profiles of fine and coarse ripples obtained on BaF <sub>2</sub> substrate with s-pulse femtosecond laser at 0.9x10 <sup>13</sup> W/cm <sup>2</sup> . Fine ripples have a periodicity of $\approx 230$ nm and are perpendicular to laser polarization. Coarse ripples period is $\approx 600$ to 900 nm and are parallel to polarization, adapted from Reif <i>et al.</i> <sup>93</sup> .....	34
Figure 1.5.15: SEM images of polished and femtosecond laser treated stainless steel 304L and AISI 630 at 3 fluences, adapted from <sup>113</sup> .....	37

Figure 1.5.16: Water contact angle measurements during time for different metallic alloys at fluencies of 0.78J/cm <sup>2</sup> (left) and 2.83J/cm <sup>2</sup> , adapted from <sup>113</sup> .....	38
Figure 1.5.17: Contact angle measurements for polished and laser-treated surfaces with water (a) and HBSS solution (b). Type 1 structure corresponding to LIPSS, type 2 to nanopillars, type 3 to columnar structure and type 4 to double scale columnar structure. Adapted from <sup>114</sup> .....	39
Figure 1.5.18 : Different type of structural colours produced on Al samples and their associated reflectance spectra. Black colour is due to a micro-grooves surface pattern, iridescent colours are mainly produced by LIPSS structure <sup>6</sup> . .....	40
Figure 1.5.19: Cyclic polarization curves for treated and untreated Z30(a) and 316L(b) alloys in Ringer's solution, adapted from <sup>121</sup> .....	41
Figure 1.5.20: Fluorescence microscopy images of Staphylococcus aureus bacteria 48h after seeding (i) on polished (a-b), LIPSS (c-d) and nanopillars surfaces (e-f). SEM images and AFM images (ii) of LIPSS (a-b) and nanopillars (c-d) surface microstructure <sup>20</sup> . .....	42
Figure 1.5.21: SEM image of Zr <sub>62.5</sub> Cu <sub>22.5</sub> Fe <sub>5</sub> Al <sub>10</sub> (at. %) BMG after fs laser treatment of pulse width $\tau = 410$ fs and increasing fluence $F$ from 0.103 J/cm <sup>2</sup> (upper left) to 0.206 J/cm <sup>2</sup> (bottom right), adapted from <sup>17</sup> .....	44
Figure 1.5.22: XRD analysis of polished and treated sample with different pulse-widths of 410 fs, 12 ps and 125 ns <sup>17</sup> . .....	44
Figure 1.6.1: Required pressure for thermoforming of cylindrical features for different aspect ratios <sup>132</sup> (a), required pressure to fill a channel with a diameter $d$ and an aspect ratio $l/d = 3$ for both wetting and anti-wetting conditions with a viscous fluid <sup>133</sup> (b). .....	47
Figure 1.6.2 : Thermomoulding filling depth of metallic glass at various strain rate and temperature in a 50 $\mu$ m width and 100 $\mu$ m depth Si mould (a), flow regimes map of Zr <sub>35</sub> Ti <sub>30</sub> Be <sub>26.75</sub> Cu <sub>8.25</sub> amorphous alloy with respective filling results (b). .....	48
Figure 1.6.3 : Thermoplastically formed Pt <sub>57.5</sub> Cu <sub>14.7</sub> Ni <sub>5.3</sub> P <sub>22.5</sub> amorphous alloy at 270°C under 15MPa during 90s with pyramidal pattern (a) and nanorods pattern (b). Micro gear (c) and micro spring (d) fabricated by micro-moulding using Zr <sub>35</sub> Ti <sub>30</sub> Cu <sub>8.25</sub> Be <sub>26.75</sub> amorphous alloy. Adapted from <sup>19</sup> .....	49
Figure 1.6.4: SEM images of the pyramidal pattern thermoplastically formed on Zr <sub>48</sub> Cu <sub>36</sub> Al <sub>8</sub> Ag <sub>8</sub> BMG surface, adapted from <sup>139</sup> .....	50
Figure 1.6.5: SEM image (a) and EDX compositional distribution mapping of the SEM image for Zr (b) and Cu (c) elements, adapted from <sup>139</sup> .....	51

Figure 1.6.6 : Left: honeycomb pattern on BMG surface before chemical etching (a), associated surface condition on honeycomb peaks (b), and honeycomb pattern after chemical etching (c) and associated surface condition (c). Right: Contact angle measurements as a function of honeycomb pitch for non-etched patterned surface (micro-structure) and etched patterned surface, adapted from <sup>140</sup> .....	52
Figure 1.6.7: Corresponded cellular morphology as a function of nanorods diameter textured surface for fibroblast (B), bone derived macrophage (C) and endothelial cell (D). Actine part and nucleus part of the cells are respectively in red and blue colour <sup>141</sup> .....	53
Figure 2.1.1: Overall picture of the arc-melting device used to elaborate Zr-base metallic glass (left), zoom on the copper support where pre-alloying and liquid metal suction were made (right).....	57
Figure 2.1.2: Zr <sub>65</sub> Cu <sub>15</sub> Al <sub>10</sub> Ni <sub>10</sub> BMG casted in plate and cylindrical shape and the exceeding material removed on the left.....	58
Figure 2.2.1 : Isothermal DSC curves of a Zr <sub>52,5</sub> Cu <sub>27</sub> Al <sub>10</sub> Ni <sub>8</sub> Ti <sub>2,5</sub> for different temperatures (a). Transformed fractions from the isothermal curves (b) <sup>143</sup> .....	60
Figure 2.3.1: Schematic diagram of the femtosecond laser irradiation setup, adapted from <sup>59</sup> . .....	61
Figure 2.3.2: SEM image of a part of the experiment performed on metallic glass Zr <sub>65</sub> Al <sub>10</sub> Ni <sub>10</sub> Cu <sub>15</sub> for the determination of the Gaussian beam radius $\omega_0$ , the ablation threshold fluence $\phi_{th}$ and the incubation coefficient $S$ . Craters of different pulse energy $E_p$ and number of pulses $N$ were produced. ....	64
Figure 2.3.3 : Scheme of the XYZ table movement during non-stationary irradiation experiments, adapted from <sup>59</sup> .....	66
Figure 2.3.4 : Drawing of the Gaussian intensity profile of the laser device used in this thesis work.....	66
Figure 2.4.1: SEM images of the Si mould used for preliminary thermoforming experiment in air before cleaning (a), cross section of the Si mould to let appear the pattern profile (b). ....	67
Figure 2.4.2: Picture of the Inconel bottom clamp in the vacuum chamber. Heating resistances are supplied by armoured cables. Copper plate sample holder allow to process multiple samples without opening the chamber. ....	68
Figure 2.4.3: Picture of the thermoforming device used to pattern.....	68
Figure 2.4.4: Comprehensive scheme of the hot compression in-vacuum (HCV) device used to thermoform Zr <sub>3</sub> BMG samples. ....	69

Figure 2.4.5: Schematic view of real interaction areas of two flat solids 1 and 2 with low roughness values. ....	70
Figure 2.4.6: Optical microscope image of the Si-mould cross-section (a), tilted SEM image of the Si-mould micro-pieces imprint (b) .....	73
Figure 2.4.7: Scheme of the experimental process for LIPSS replication on Zr3 BMG by thermoforming processing.....	73
Figure 2.4.8: SEM image of tungsten mould surface textured with LIPSS by femtosecond laser treatment.....	74
Figure 2.7.1: Scheme of the experimental setup for contact angle measurement, adapted from <sup>47</sup> . .....	79
Figure 2.7.2: Picture of prepared metallic glass samples for electrochemical measurements.	82
Figure 2.7.3: Scheme of the 3-electrode set-up used in this thesis work (left), picture of the glass cell with the electrodes in 0.1 M NaCl solution (right).....	82
Figure 3.2.1: Rod sample DSC curve of Zr3 sample realized with scanning rate of 40°C/min (a). Zoom between 370°C and 430°C (b). Characteristic temperatures are indicated: crystallization onset temperature ( $T_x$ ), peak crystallization temperature ( $T_p$ ), glass transition temperature onset ( $T_{gonset}$ ) and glass transition temperature at the inflexion point ( $T_{ginflexion}$ ).....	88
Figure 3.2.2: Isothermal DSC curves of a Zr3 rod at different temperatures (a). Transformed fraction calculated from the isothermal measurements (b). ....	89
Figure 3.2.3: Plot of $\ln(t_{conset})$ as a function of $1/RT$ in order to determine the crystallization activation energy $E$ of Zr3 (a). Crystallization onset time calculated from the activation energy $E$ for every temperature in the SLR of Zr3 alloy (b).....	90
Figure 3.2.4: Curve of strain rate jump test realized at 400°C on Zr3 rods in the strain range of $2.5 \times 10^{-4} \text{ s}^{-1}$ to $2.5 \times 10^{-3} \text{ s}^{-1}$ (a), strain rate jump test curve realized at 410°C in the strain range of $5 \times 10^{-3} \text{ s}^{-1}$ to $5 \times 10^{-2} \text{ s}^{-1}$ (b). ....	91
Figure 3.2.5: Values of the viscosity $\eta$ as a function of the strain rate for different temperatures above the glass transition temperature $T_g$ . Newtonian viscosities are represented in the left part of the graph. Inspired from Gravier thesis <sup>15</sup> .....	94
Figure 3.2.6: Normalised viscosity $\eta/\eta_N$ as a function of the normalized strain rate $\eta_N \epsilon$ for the temperatures used experimentally (a). Plot of $\ln(\eta_N)$ as a function of $1/RT$ ( $R$ is the constant of ideal gases) allowing to calculate the Newtonian viscosity activation energy (b).....	95

Figure 3.3.1: Optical microscope image of the compressed Zr3 sample surface (a), zoom on the textured surface region (b). .....	97
Figure 3.3.2: Backscattered electron (a) and secondary electron (b) SEM images of the Zr3 textured area. ....	97
Figure 3.3.3: Scheme of the textured circle area upon hot compression in-air Zr3 cylinder. ..	98
Figure 3.4.1: Graph of the theoretical and measured stress plateau evolution as a function of the temperature at a strain rate of $2.5 \times 10^{-2} \text{ s}^{-1}$ with Zr3 amorphous alloy. ....	101
Figure 3.4.2: Microscope images of thermoformed BMG plates cross sections and stereoscopic imprint reconstructions of hot compression tests conducted at $420^\circ\text{C}$ under constant stress of 20 MPa during 30 s (a), 60 s (b), 120 s (c) and 300 s (d) compression time. ....	104
Figure 3.4.3: Tilted SEM images of the reproduced watch micro-piece on BMG after experiments under $420^\circ\text{C}$ and 20 MPa during 30 s (a), 60 s (b), 120 s (c) and 300 s (d) compression time.....	104
Figure 3.4.4: Plot of the experimental filling length and theoretical filling length curve as a function of the compression time for thermoforming tests at $420^\circ\text{C}$ with constant applied stress equal to the critical stress $\sigma_c = 20 \text{ MPa}$ . ....	105
Figure 3.4.5: Plot of the aspect ratio ( $l/d$ ) evolution as a function on the compression time at 20MPa for $421^\circ\text{C}$ and $430^\circ\text{C}$ with the thinner cavity part width of $d = 60\mu\text{m}$ . ....	106
Figure 3.4.6: Tilted SEM images of the micro-piece thermoformed under constant pressure of 20 MPa at $442^\circ\text{C}$ during compression time of 250s (a), zoom on the thinner part of the micro piece (b). ....	107
Figure 3.4.7 : Maximum $l/d$ ratios at $t = t_{crystonset}$ for an applied stress just below the critical stress ( $\sigma = 20 \text{ MPa}$ ) and $t_{crystonset} - t_{exp}$ as a function of the temperature for Zr3 amorphous alloy. ....	109
Figure 3.4.8: FIB cross section image of LIPSS texture realized by femtosecond laser treatment on ZrC amorphous alloy.....	110
Figure 3.4.9: Picture of a textured tungsten mould with LIPSS (a), SEM image (b), AFM image (c) and 2D roughness profile on the direction perpendicular to the structure orientation (d) of the tungsten cylinder surface textured on a $100\text{mm}^2$ area with LIPSS produced by femtosecond laser treatment .....	111
Figure 3.4.10: Theoretical filling length as a function of the time for a temperature of $400^\circ\text{C}$ and an applied pressure of 20 MPa for a $d = 500 \text{ nm}$ width cavity.....	113

Figure 3.4.11: Picture of a thermoformed Zr3 plate (a), tilted SEM image (b), AFM image of a 100 $\mu\text{m}^2$ surface (c), and 2D roughness profile on the direction perpendicular to LIPSS orientation (d) for a Zr3 BMG thermoformed at $\sigma = \sigma_c = 20$ MPa and $T = 400^\circ\text{C}$ .....	113
Figure 3.4.12 : 2D roughness profile on 3 $\mu\text{m}$ length of the mould surface (left) and the thermoformed Zr3 alloy surface at $400^\circ\text{C}$ (right) perpendicularly oriented to the structure.	115
Figure 3.4.13: Tilted SEM image and FIB cross section SEM image of LIPSS structure created on tungsten mould with femtosecond laser at a pulse energy of 800 $\mu\text{J}$ and other experimental parameters presented in Chap II.....	115
Figure 3.5.1: XRD diffractograms of Zr3 alloy after TPF processing on Si-mould at $\sigma = \sigma_c = 20$ MPa after 300 s at $410^\circ\text{C}$ and $440^\circ\text{C}$ (a), diffractograms of Zr3 alloy surface after TPF processing on laser-textured tungsten mould at $\sigma = \sigma_c = 20$ MPa after 120 s at $400^\circ\text{C}$ and $440^\circ\text{C}$ (b). .....	117
Figure 4.1.1 : Optical micrograph of a part of the sets of craters produced to determine spot diameters, laser ablation thresholds and incubation factor of $\text{Zr}_{65}\text{Cu}_{15}\text{Al}_{10}\text{Ni}_{10}$ amorphous alloy. Number of pulses are indicated on the top and laser energies on the left. Energy values displayed are not corrected (energy losses in the optical path not accounted for). .....	120
Figure 4.1.2: Semi-logarithmic plot of $D^2$ as a function of the pulse energy for 250, 100, 50 and 5 pulses for Zr3 alloy. Lines presented are linear fitting of experimental data. $R^2$ , slopes and intersection values are indicated for every fitting. ....	121
Figure 4.1.3: Semi-logarithmic plot of $D^2$ as a function of the pulse energy for 250, 100, 50 and 5 pulses for ZrC alloy. Lines presented are linear fitting of experimental data. $R^2$ , slopes and intersection values are indicated for every fitting. ....	122
Figure 4.1.4: Semi-logarithmic plot of $D^2$ as a function of the pulse energy for 250, 100, 50 and 5 pulses for Cu2 alloy. Lines presented are linear fitting of experimental data. $R^2$ , slopes and intersection values are indicated for every fitting. ....	122
Figure 4.1.5 : Accumulated fluence as a function of the number of pulses. Fitting has been done according to eq. 2.10. ....	123
Figure 4.1.6: SEM micrographs of different craters induced by femtosecond laser on a Zr3 amorphous alloy with fixed number of pulses of $N = 100$ at a repetition rate of 10 Hz, for 60, 80, 100 and 200 $\mu\text{J}$ , which correspond to average fluence of 0.07, 0.096, 0.12 and 0.24 $\text{J}/\text{cm}^2$ , respectively. The yellow arrow indicates the polarization vector of the laser beam. Zoom images has been done at the spot centre. ....	124

Figure 4.1.7 : Inferior quarters SEM micrographs of different of craters induced by femtosecond laser on a ZrC amorphous alloy with fixed average fluence of 0.18 J/cm <sup>2</sup> at a repetition rate of 10 Hz, for 50, 100, 150 and 200 pulses. The yellow arrow indicates the polarization vector of the laser beam. Zoom images were done on the centre of the spot.....	126
Figure 4.1.8: SEM micrographs of a ZrC target surface at N = 150 pulses for pulse energy of 100 μJ (a), and 200 μJ (b). Below each image the corresponding spatial profile of the laser pulse fluence is shown. The squares mark regions characterized by different surface structures at low (LIPSS structure on the left), medium (transition structure on the centre) and high fluences (ridge structure on the right). The double-headed arrows indicate the beam polarization.....	128
Figure 4.1.9: SEM image of Zr <sub>65</sub> Cu <sub>15</sub> Al <sub>10</sub> Ni <sub>10</sub> metallic glass surface irradiated with $\phi_a = 0.16$ J/cm <sup>2</sup> after 1 pulse. ....	129
Figure 4.1.10: SEM images of the overall laser spot (a), and zoom on the peripheral part of the spot (b) produced on Zr <sub>57</sub> Cu <sub>20</sub> Al <sub>10</sub> Ni <sub>8</sub> Ti <sub>5</sub> BMG at pulse energy $E_p = 50\mu\text{J}$ and after N = 200 pulses. ....	131
Figure 4.1.11: Scheme of the morphological and chemical modifications due to ultra-short pulse laser ablation of TiN in air environment, from Bonse <i>et al.</i> <sup>162</sup> . ....	133
Figure 4.1.12: SEM images of a laser spot produced on a ZrC BMG surface with pulse energy of $E_p = 100 \mu\text{J}$ and N = 150 pulses with the corresponding structures areas and the ablation threshold $\phi_{th}$ zone (a), FTT images of type-I (b) and type-II (c) with corresponded period values. ....	134
Figure 4.1.13 : LIPSS periodicity and orientation from laser polarisation as a function of SiO <sub>2</sub> layer thickness on Si (100) at a laser fluence per pulse of 2.41 J/cm <sup>2</sup> in ambient air, from Nürnberger <i>et al.</i> <sup>164</sup> . ....	135
Figure 4.1.14: SEM images of the side of laser spots and LIPSS type II periods calculated by FFT with pulse energy of 50 μJ and N = 150 (a), 200 (b), and 250 (c) pulses. ....	136
Figure 4.2.1 : SEM images of Zr <sub>3</sub> metallic glass surfaces processed with a pulse energy of 150 μJ (non-corrected) at a pulse frequency of 100 Hz, a scanning speed of 1 mm/s with lateral displacement of 100μm corresponding to a track overlapping of 20% (a) and a lateral displacement of 50μm corresponding to a track overlapping of 60% (b). The double arrow presents polarisation and scanning direction.....	137
Figure 4.2.2: Low and high magnifications SEM images of LIPSS (a,b) and Ridge (c,d) textures produced on Zr <sub>3</sub> amorphous alloy surface. LIPSS (a,b) have been processed with N = 161 and	

$\phi_a = 0.07 \text{ J/cm}^2$ and ridges (c,d) have been processed with $N = 538$ and $0.4 \text{ J/cm}^2$ . Yellow double arrows represent the laser beam polarization and the scanning orientation. ....	138
Figure 4.2.3 : SEM images of LIPSS (left) and RIDGES (right) textures on ZrC amorphous alloy at high magnification. Redeposited nanoparticles are observed on both surfaces. ....	141
Figure 4.2.4: SEM images of Zr3 alloy textured with ridges processing parameter at 200 Hz with pulse energy of 100, 200, 300, 400, 500 and 700 $\mu\text{J}$ . Scale bar represents 10 $\mu\text{m}$ in length. ....	142
Figure 4.2.5 : Evolution of ridges and LIPSS features width with pulse energy on a Zr3 amorphous alloy surface. ....	142
Figure 4.2.6 : High magnification SEM images of ridge textures processed on Zr3 surface at pulse energy of 400 $\mu\text{J}$ , lateral displacement of 0.32 mm and scanning speed of 1 mm/s at pulse frequencies of 150, 200 and 250 Hz, corresponding to $N = 24, 33$ and 41 pulses respectively. ....	143
Figure 4.3.1 : XPS survey spectra for 1 $\mu\text{m}$ polished (a), fs-laser treated with LIPSS (b) and ridges (c) textures on Zr3 amorphous alloy surfaces. ....	144
Figure 4.3.2 : XPS detailed spectra for the regions Zr 3d (a), Cu 2p (b), Ni 2p (c) and O 1s (d). ....	145
Figure 4.3.3: FIB cross-section of LSFLs on Ti/Ni multilayer substrate irradiated with s-pulse Yb:KYW femtosecond laser of 560 fs pulse duration, wavelength of 1030 nm and pulse energy of 160 $\mu\text{J}$ , scheme of the cross section depending on the energy deposition period with ablation mechanisms involved (b) <sup>75</sup> . ....	148
Figure 4.3.4: Scheme of the apparatus to collect ablation particles (a), SEM image of collected ablated particles on carbon tape prior to EDX analysis (b). ....	149
Figure 4.4.1: X-ray diffractograms of untreated Zr3, ZrC and Cu2 1 $\mu\text{m}$ polished metallic glass surfaces. ....	151
Figure 4.4.2: Bragg-Brentano (a) and grazing mode (b) X-ray diffractograms of Zr3 and ZrC amorphous alloys femtosecond laser treated with RIDGE texture ( $0.4 \text{ J/cm}^2$ ) and LIPSS texture ( $0.07 \text{ J/cm}^2$ ). ....	152
Figure 4.4.3: Grazing mode X-ray diffractograms of Cu2 amorphous alloy 1 $\mu\text{m}$ polished, treated with LIPSS texture ( $0.07 \text{ J/cm}^2$ ) and RIDGE texture ( $0.4 \text{ J/cm}^2$ ). ....	152
Figure 4.5.1: Time evolution of the apparatus contact angle for DD water (a), (b), (c) and diiodomethane (d), (e), (f) droplets on 1 $\mu\text{m}$ polished and laser textured surfaces of Zr3 (a), (d),	

ZrC (b), (e) and Cu2 (c), (f) amorphous alloys. Presented values were measured based on the droplet profiles taken in a direction perpendicular to the laser beam polarization. ....	155
Figure 4.5.2: Images of DD water droplets deposited on Zr3 surfaces after 60 seconds for 1 $\mu$ m polished surface (a), LIPSS texture surface (b) and Ridge texture surface (c). ....	156
Figure 4.5.3 : Images of diiodomethane droplets deposited on Zr3 surfaces after 60 seconds for 1 $\mu$ m polished surface (d), LIPSS texture surface (e) and Ridge texture surface (f). ....	156
Figure 4.5.4: Graph of the anisotropic wetting of Zr3 alloy with DD-water droplets on both LIPSS and RIDGE textures with observation view parallel and perpendicular from laser beam polarization. ....	159
Figure 4.6.1 : Open-circuit potential measurements during 2500 seconds (a) and anodic polarisation measurements from OCP (b) for the three amorphous alloys studied Zr3, ZrC and Cu2. ....	161
Figure 4.6.2 : Nyquist diagram of electrochemical impedance spectroscopy (EIS) measurements on the Zr3 (a), ZrC (b) and Cu2 (c) 1 $\mu$ m polished amorphous alloy surfaces. ....	162
Figure 4.6.3: Anodic polarization measurements on polished, LIPSS texture and RIDGE texture on Zr3 (a) and ZrC (b) amorphous alloy surfaces. ....	164
Figure 4.6.4: Optical microscope images of Zr3 (a) and ZrC (b) surfaces textured with LIPSS after anodic polarization measurements. ....	165
Figure 4.6.5: Nyquist diagrams of LIPSS (a) and Ridge (b) textures on Zr3 alloy and Ridge texture on ZrC alloy (c) made by EIS experiments from 2 h to 24 h of immersion in 0.1 M NaCl. ....	166
Figure 4.6.6: Bragg-Brentano XRD measurements of Zr3 Ridge texture before anodic polarization (a), grazing incidence XRD measurements of Zr3 Ridge texture after anodic polarization (b). ....	167
Figure 4.6.7 : FIB cross section SEM image of Ridge texture on ZrC alloy presenting a “mushroom-like” shape. The white material on the top was palladium deposition realized in order to prevent structural destruction by gallium ions. ....	169
Figure A-4.7.1: Nyquist diagrams of polished (a), LIPSS textured surface (b) and Ridge textured surface (c) of Cu2 alloy made by EIS experiments from 2h to 24h of immersion in 0.1 M NaCl. ....	178
Figure A-4.7.2: SEM images of corrosion pits observed on Cu2 amorphous alloy surface after 24h of immersion in 0.1 M NaCl for LIPSS textured (a) and Ridge textured (b) surfaces....	179

Figure A-4.7.3: Optical microscope image of a laser-textured Cu <sub>2</sub> alloy surface (a), SEM image of Cu <sub>2</sub> laser-textured surface on a peripheral part of a corrosion pit (b). .....	180
Figure A-4.7.4: Optical microscope image of the filling length evolution on the BMG plate border (a), scheme of the stress gradient issue (b). .....	181

## List of tables

Table 2.3-1: Specifications of the s-Pulse HP model femtosecond laser system in this work for surface treatments.....	61
Table 2.3-2 : Laser processing parameters and conditions used for laser spots processing in stationary mode. ....	64
Table 2.3-3: Laser processing parameters and conditions used for laser spots processing in non-stationary mode. ....	65
Table 3.2-1: Characteristic temperatures of Zr <sub>3</sub> , ZrC and Cu <sub>2</sub> amorphous alloys with scanning speed of 40°C/min.....	88
Table 3.2-2: Newtonian viscosity $\eta_N$ , critical strain rate $\epsilon_{limit}$ and critical applied stress $\sigma_c$ above which we pass through non-Newtonian regime for Zr <sub>3</sub> amorphous alloy. ....	94
Table 3.3-1: Photography pictures of Zr-based alloys after heat treatment in air at different time and temperature. ....	99
Table 4.1-1: Spot diameters and ablation thresholds for different number of pulses for the three amorphous alloys.....	121
Table 4.1-2 : Threshold values for LIPSS and ridges structures formation for the three metallic glasses studied. ....	127
Table 4.2-1 : Processing parameters and resulted number of pulses and fluences for LIPSS and RIDGES structures. ....	139
Table 4.2-2: Roughness parameters for the two textures (LIPSS and RIDGES) processed on the three amorphous alloys. Values are obtained from 3D reconstruction of SEM images using Alicona-Mex® software. Measurements have been took in a direction perpendicular to the laser scanning direction for ridges structure, and in a direction parallel to the scanning direction for LIPSS structure. ....	140

Table 4.3-1 : Atomic percentage of metallic elements and oxygen of the Zr3 amorphous alloy obtained by XPS analysis and atomic ratios between Zr, Ni and Cu for the three surfaces textures. ....	147
Table 4.3-2: Ratios between Zr, Cu and Ni elements measured by EDX technique on ablated particles ejected from ZrC substrate.....	149
Table 4.3-3: Boiling temperatures at vapour pressure of 100 kPa for the elements of the Zr3 alloy. ....	150
Table 4.5-1: Equilibrium contact angles of water and diiodomethane after 60 seconds for the three amorphous alloys measured experimentally. These equilibriums are average values of both perpendicular and parallel measures from laser beam polarization direction.....	157
Table 4.5-2 : Surface free energy ( $\gamma_{SV}$ ) with polar ( $\gamma_{SVp}$ ) and dispersive part ( $\gamma_{SVd}$ ) of polished and textured surfaces of the three amorphous alloys calculated by using the Owens and Wendt method combined with the geometric mean approach. Total surface free energy presented is the average of the values measured in both parallel and perpendicular directions from laser beam polarization.....	158
Table 4.6-1: Summary of the different electrochemical constants measured with OCP and anodic polarization from OCP +1V for the three amorphous alloys Zr3, ZrC and Cu2.....	161
Table 4.6-2: Summary of the corrosion behaviours of three non-textured and textured amorphous alloys surfaces. ....	171

# Introduction

Metallic glasses were first prepared in the 1960s in ribbon form, with a thickness of about 0.1 mm<sup>1</sup>. Extensive studies over the last twenty years led to develop metallic glasses in “bulk” form (> 1cm). Due to their amorphous structure, these materials have unique properties such as high mechanical strength and outstanding corrosion resistance compared to crystalline counterparts<sup>2,3</sup>. Amorphous alloys are not yet widely used in industry due to their high production costs and the complex manufacturing. However, they have been used in the biomedical, micromechanics and watchmaking sectors, where miniaturisation and high added value make possible their use as a replacement for conventional crystalline alloys<sup>4</sup>.

Today's industry is facing new challenges, forcing innovation in a context of global warming, stricter legislation and increasingly fierce competition. Surface treatments have been used for a long time to improve the resistance materials to environmental aggression. The surface treatment of materials is a growing sector, allowing cost reduction, improved performances and the addition of new surface functionalities such as controlled wettability, improved optical properties or controlled interaction with the body<sup>5,6</sup>. Today, there are large number of amorphous alloys with different compositions, such as iron, platinum, zirconium, nickel etc... and therefore different mechanical and chemical properties<sup>7</sup>. Due to their biocompatibility<sup>8</sup>, some amorphous alloys are of real interest in the biomedical field and control of their surface properties is of major importance in the case of materials interacting with the human body.

Nowadays, the metallic materials mostly used in orthopaedic implants are Ti-based alloys like Ti-6Al-4V. Their excellent biocompatibility associated with high corrosion resistance and high static and dynamic strength make them adequate for this application. However, in some cases, localized corrosion by processes like pitting corrosion can happen and initiate a release of aluminium and vanadium elements in the blood. The first of these elements may act as a cell growth inhibitor and is a possible cause of Alzheimer disease. The second one is toxic in the human body. Metallic glasses do not contain grain boundaries and others typical crystal defects (vacancies, twins and dislocations) and present high mechanical strength<sup>9</sup> and, in the case of Zr-based BMG, a high resistance passivation to pitting corrosion in different solutions<sup>10</sup> due to the formation of a stable passive oxide layer, making them promising potential alternatives for in-body biomedical devices. Zr-based and Ti-based amorphous alloys has been particularly studied for orthopaedic applications. Despite the fact that copper is a determinant alloying

element for the corrosion resistance and it increases the cytotoxicity of the metallic glass<sup>11</sup> thus decreasing the range of possible compositions, several studies shows promising results on cell/Zr-based BMG interaction. In comparison with typical Ti-6Al-4V, Zr-based bulk metallic glasses show good osteoblast response<sup>12</sup>, comparable bone-forming cell proliferation<sup>13</sup> and higher cellular differentiation with a good support to cell attachment<sup>14</sup>. The surface functionalization of these glasses is a major challenge when used in vivo, aiming at replacing conventional crystalline alloys.

The amorphous structure of a metallic glasses is in a metastable state, making it sensitive to increases in temperature above the glass transition temperature  $T_g$ , potentially leading to crystallization and thus to a loss of their unique properties<sup>15,16</sup>. Many surface treatments used for crystalline alloys such as surface melting and cladding, coating deposition by thermal spraying or heat treatment, induce an increase of the temperature at the surface and a diffusion of the heat in the volume. As a consequence, they are mostly not suitable for metallic glasses. In order to answer to this problem, this thesis focuses two innovative surface treatment techniques that allow functionalizing the surface of metallic glasses while preserving the amorphous structure of the material<sup>17</sup>. The first one is surface texturing by **thermoforming**. It uses the thermomechanical properties of bulk metallic glasses to deform them in the viscous state, corresponding to its super-cooled liquid region ( $T > T_g$ ). Good knowledge of the rheological properties of the glass, combined with controlled experimental conditions, allows the replication of micro or nanometric patterns with great precision while preserving the amorphous structure<sup>18,19</sup>. The second one involves the use of ultrashort pulse duration lasers. These lasers allow the deposition of a large quantity of energy on highly localized areas in a very short time, thus limiting the heat transfer to the bulk of the irradiated material<sup>20-22</sup>. This technique appears to be adapted to surface texturing of metallic glasses without modifying their amorphous structure.

The aim of this thesis is to study the effect of these surface treatments on the properties of Zr-based bulk metallic glasses. Femtosecond laser treatment and thermoforming allow creating different types of surface textures. Firstly, the influence of the laser processing parameters on the topography, the structural and the chemical surface modifications was studied. Then, two surface textures were chosen in order to analyse their effects on surface properties such as wettability and corrosion resistance. In parallel, due to processing issues of thermoforming under air environment, a new compression device under vacuum has been designed and tested,

and a preliminary study of thermoplastic forming of a specific Zr-based metallic glass has been performed.

The thesis is organized in four different chapters: Chapter 1 Literature review, Chapter 2 Experimental methods, Chapter 3 Thermoforming of Zr-based metallic glasses and Chapter 4 Femtosecond laser surface texturing of Zr-base metallic glasses. The Chapter 1 first presents bulk metallic glasses, their unique properties and, more specifically, the surface properties of Zr-based bulk metallic glasses. Then the techniques and principles of surface functionalization of materials by femtosecond laser treatment and, thermoforming processing, especially of metallic glasses, are discussed. Chapter 2 presents the experimental methods that have been used in this work, from the elaboration of the amorphous materials, the surface processing methods, to the surface characterization techniques used. The thermoforming experiments are presented in Chapter 3. First, the thermomechanical properties of the alloy studied were characterized. Then, the results of thermoplastic forming in air and in vacuum using different types of patterned moulds are presented. The surface treatment of three Zr-based amorphous alloys by femtosecond laser texturing is presented in Chapter 4 as well. The laser treatments were first performed with the laser beam stationary in relation to the specimens in order to create samples to determine the ablation threshold fluences and the effect of the laser pulse energy and number of pulses on the surface morphology. Then large areas were processed using a direct working method in order to prepare specimens to study the structural and chemical modification induced by the laser treatment. Finally, characterization of the textured surfaces was performed by wettability and corrosion testing. Finally, the conclusions of the study are presented and some perspectives for future developments are discussed.

# CHAPTER 1

## Literature review

### 1.1. Metallic glass

#### 1.1.1. Generalities

Metallic materials are usually characterized by two ranges of atomic order. A short range order affecting a couple of interatomic distances and a long range order affecting distances that are much longer than the interatomic distance. Commonly, the metals and alloys used in industry are crystalline. This means that they exhibit short and long range order, as seen in Figure 1.1.1.a. In this situation, it is possible to predict the positions of all the atoms that constitute the material from the repetition of the unit cell in the three directions of space. For example, in a face-centred cubic (FCC) structure, the first neighbours atoms are at a distance of  $a\sqrt{2}/2$ , where  $a$  is the lattice parameter. On the contrary, in the amorphous state only short range order is observed and only the first neighbours' positions can be evaluated (Figure 1.1.1.b). Further away the atoms are considered to be randomly positioned.

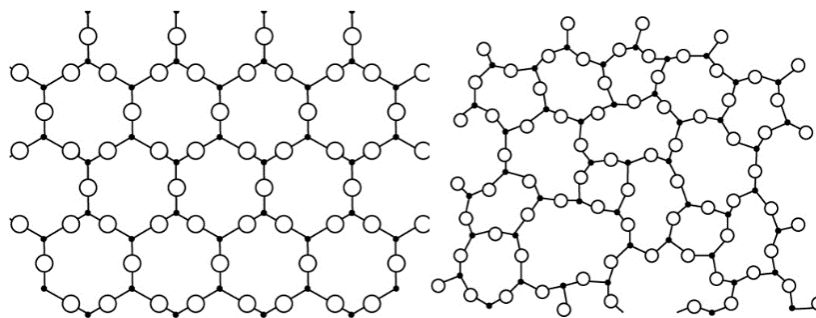


Figure 1.1.1: Silica in crystalline (a) and amorphous (b) state, 2D analogy<sup>23</sup>.

Bulk metallic glasses are in the amorphous state. Thus, they only exhibit short range order. As it will be explained later, the main condition of their preparation is the ability to prevent crystallization during solidification from the liquid phase.

#### From melt spun ribbons to bulk metallic glass

The origin of amorphous metallic alloys goes back to the 60s, when Klement *et al.*<sup>1</sup> obtained an Au-Si metallic glass by rapid solidification processing (RSP) using the wheel quenching

technique. This technique allowed to reach very high cooling rates ( $\approx 10^6$  K/s) but was limited to the preparation of ribbon with very small thickness (few tens of microns). The elaboration of Bulk Metallic Glasses (BMGs) has been first reported in 1974. Chen *et al.*<sup>24</sup> developed three-components alloys, allowing to decrease the critical cooling rate to  $10^3$  K/s and, so, to prepare specimens with larger critical diameters, such as 3 mm for the Pd-Cu-Si system. Despite this progress, the high percentage of noble metals in these alloys did not allow their commercial production. The 80s marked a turning point in bulk metallic glass development. Indeed, major advances in the development of new, easily quenchable, compositions were made, especially by A. Inoue<sup>25</sup> and co-workers. Since then, different alloys were produced, particularly Ln-Al-Mt systems (Ln = lanthanides, Mt = transition metals). Mg based alloys<sup>26</sup>, Zr based<sup>27,28</sup> as well as Fe based<sup>29</sup> or Pd based<sup>30</sup> allowed to decrease cooling rates to 0,1 K/s for critical diameters up to 72 mm for Pd<sub>40</sub>Cu<sub>30</sub>Ni<sub>10</sub>Cu<sub>20</sub> amorphous alloy.

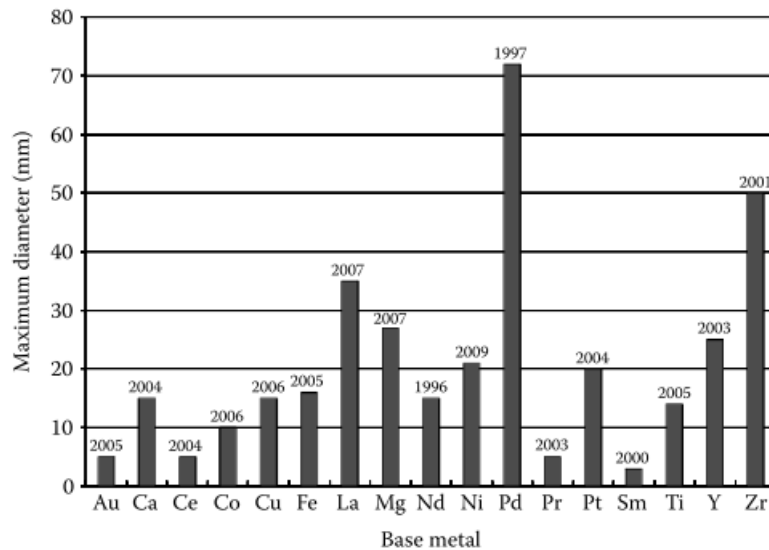


Figure 1.1.2 : Discovery year and maximum diameters achieved in different alloy systems<sup>7</sup>.

As shown in Figure 1.1.2, Zr-based bulk metallic glasses can reach a maximum critical diameter of 50 mm for a specific composition. In fact, the largest part of Zr-based amorphous alloys exhibit critical diameters between 5 and 20 mm. For example, Zr<sub>55</sub>Al<sub>10</sub>Cu<sub>35</sub>, Zr<sub>60</sub>Cu<sub>20</sub>Fe<sub>10</sub>Al<sub>10</sub> and Zr<sub>57</sub>Cu<sub>20</sub>Al<sub>10</sub>Ni<sub>8</sub>Ag<sub>5</sub> exhibit critical diameters of 10, 12 and 20mm, respectively<sup>31–33</sup>.

## 1.1.2. Elaboration of bulk metallic glass

The most usual method of preparing bulk metallic glasses is to mix the component elements in the liquid state, at a temperature higher than the melting temperature and cooling it fast enough to avoid crystallization. During cooling, the viscosity of the molten material increases, resulting

to the freezing of the liquid structure into a solid. During this last cooling step, as presented in Figure 1.1.3, a critical temperature is reached where atoms do not have enough time to reorganize themselves in a crystal lattice and the amorphous structure is frozen in. This critical temperature is called *Glass transition temperature*  $T_g$ , and is directly related to the alloy composition.

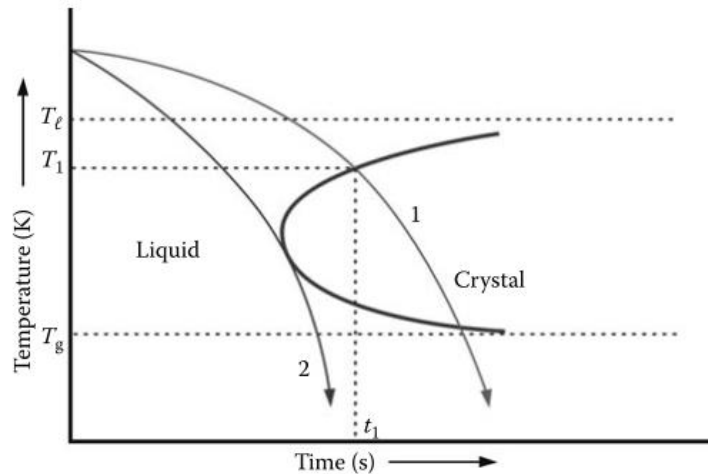


Figure 1.1.3 : Scheme of the time-temperature-transformation (T-T-T) for a hypothetical alloy system. From the liquid state, at a too low cooling rate, as indicated by curve “1”, solidification will start at a temperature  $T_1$  and a time  $t_1$ . The resulted solid material will be in crystalline state. In contrary, if the liquid is cooled fast enough as presented by curve “2”, the liquid will stay in the undercooled state and when the glass transition temperature is reached, the liquid is “frozen-in” and a glassy phase is formed<sup>7</sup>.

Different elaboration techniques are available to create amorphous metals. With the advent of alloy compositions with high critical diameters, the elaboration was greatly facilitated and new preparation methods were invented. Every alloy composition has its own critical cooling rate to maintain the amorphous structure state. To create amorphous metallic glasses from alloys with a very low Glass Forming Ability (GFA, see below), the melt spinning process is often used. It allows reaching cooling rates between  $10^5$  to  $10^6$   $\text{K}\cdot\text{s}^{-1}$ . The thickness of the resulting ribbon is in the micron scale, depending on the rotational speed of the copper wheel. To prepare amorphous alloys from materials with high GFA requires lower cooling rates, many processes are available, such as the suction-casting, arc-melting and cap-casting methods.

The complexity of bulk metallic glasses and the dependence of their thermodynamic properties on the composition require that the stoichiometry of the material is strictly respected, a difference of less than 1 % in the content of a particular element can lead to the crystallization for a given cooling rate. Systematic studies of the alloys compositions allowed to better understand how a metallic alloy becomes amorphous or not. Some empirical laws were

developed to select the good compositions in order to obtain an amorphous state. One of the better known is Inoue criterion<sup>25</sup> detailed below:

1. The alloy must contain at least three components. The facility to form an amorphous increases with increasing number of components in the alloy system.
2. Significant atomic size differences must exist between the constituent elements of the alloy. It is suggested that the atomic size differences should be more than 12 % for the main constituent elements.
3. The heat of mixing of the major constituent elements of the alloy system must be negative.

These criteria do not apply strictly to every case in metallic glass composition but gives a general orientation to guide the preparation of a metallic amorphous material. Amongst other criteria, it defines the capacity to form glasses (Glass Forming Ability) and also allows improving their thermal stability by increasing the value of  $\Delta T = T_x - T_g$ , where  $T_x$  is the crystallization temperature. This stability is crucial to allow the preparation of specimens of the alloy sufficiently large to measure the mechanical properties in the super-cooled liquid region (SLR) ( $T > T_g$ ).

### Determination of $T_g$

Different techniques are available to determine the glass transition temperature of an amorphous alloy. The most common one is Differential Scanning Calorimetry (DSC). A classical thermogram of Zr-based bulk metallic glass is shown in Figure 1.1.4.

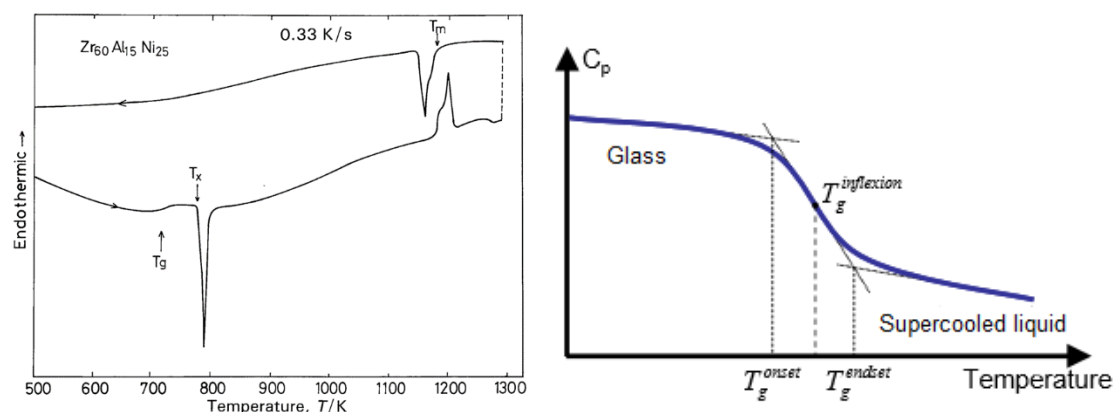


Figure 1.1.4 : Differential thermal analysis of a Zr60Al15Ni25 amorphous alloy with both heating and cooling curves while reaching melting temperature  $T_m$ <sup>27</sup> (left), zoom on a glass transition phenomena (right), adapted from<sup>34</sup>.

Above the glass transition temperature  $T_g$ , the material is in a metastable equilibrium. The glass transition temperature depends on the time required to observe the phenomena, so,  $T_g$  depends

on the cooling rate and on the heating rate used to determine it. Thus, for a cooling rate  $C_1$  higher than  $C_2$ , the glass transition temperature  $T_{g1}$  will be higher than  $T_{g2}$ . As presented in Figure 1.1.4, the glass transition is endothermic and extends from the point where the  $C_p$  curve quits the glassy state and starts to decrease ( $T_g^{onset}$ ) to the point where the curve reaches the supercooled liquid state ( $T_g^{endset}$ ). This allows to define  $T_g^{inflexion}$  as the inflexion point of the curve. As previously said, all of these temperatures are heating-rate dependent and there is no standard heating rates to determine  $T_g$  by differential scanning calorimetry. So, it is important to take into account the experimental parameters used when comparing different tests. The glass transition is time-dependent. The glass requires some time to reorganize itself and to reach a local free-energy minimum. This means that after a certain time above  $T_g$ , the alloy will naturally start to crystallise by a nucleation and growth process.

### Non-controlled crystallization during the elaboration of BMGs:

As explained above, the availability of highly stable amorphous alloys with large supercooled liquid regions allowed the development of new quenching methods adapted to large critical diameters. Most of the time, copper moulds are used because of its high thermal conductivity, which ensures fast heat extraction from the liquid and high cooling rates. However, it is often impossible to guarantee a 100 % amorphous structure at the surface and in the core of the metallic glass. Different phenomenon can occur during solidification and two crystallization processes can happen during cooling:

- homogeneous nucleation of crystals, mostly in the core of the BMG and is principally the result of a too slow cooling rate.
- heterogeneous nucleation in the entire volume of the material. It is the most unpredictable nucleation process and can be activated by many factors.

Many authors have emphasized the role of heterogeneous nucleation in Zr-based bulk metallic glasses elaborated by water-cooled copper mould casting technique. Inoue *et al.*<sup>35</sup> suggested that the scattering between the critical sample thickness and the temperature interval in the super-cooled liquid region for Zr-based BMG is due to heterogeneous nucleation, and so this close relation indicates that the large glass-forming ability is dominated by the stability of the supercooled liquid against crystallization. On the other hand, Johnson *et al.*<sup>36</sup> reported that when an alloy is cast in a mould with a mould cavity diameter larger than its critical diameter, the outer layer remain amorphous while the core is crystalline, and so they assumed that the glass

forming ability (GFA) is restricted by homogenous nucleation at the sample core rather than by heterogeneous nucleation at the copper surface. The oxygen content also affect the thermal stability of BMGs, as reported by Gebert *et al.*<sup>37</sup> In  $Zr_{65}Al_{7.5}Cu_{17.5}Ni_{10}$ , oxygen has a strong influence on the thermal stability and promotes the nucleation of the metastable  $NiZr_2$  phase, which act as an heterogeneous nucleation site for other crystalline phases. Most of the studies on the crystallization behaviour of Zr-BMGs were made in the 90s, when the identification of crystalline phases relied on classical X-ray diffraction. However, it is admitted that minor volume fractions of crystalline phases (less than 5 vol. % typically) are usually not detectable by conventional X-Ray diffraction<sup>38</sup>. Nowadays, new diffraction techniques such as grazing-incidence X-Ray diffraction allow better detection of crystalline phases near the material surface. However, only High Resolution Transmission Electron Microscopy (HR-TEM) guarantees a complete identification of very small amounts of micro crystals. This can be determinant because only small amounts of crystalline phases are required to modify significantly the properties of bulk metallic glass, in particular their corrosion resistance.

## 1.2. Mechanical properties of metallic glasses

Generally, bulk metallic glasses exhibit two distinct deformation modes, associated to different mechanical properties. As mentioned in this Section, the transition between these modes is strongly dependent on the temperature and on the strain rate. At low temperature ( $T < T_g$ ), the deformation of BMG is heterogeneous and localised in the material. The material is hard and brittle. At higher temperature, typically higher than  $T_g$ , the deformation is homogeneous and it is possible to reach very high deformation rates ( $\epsilon > 1000\%$  in tensile mode).

### 1.2.1. Low temperature deformation

The mechanical resistance of polycrystalline metallic materials depends on the activation of dislocation movement in the structure. Limitation of these movements by controlling the microstructure as explained by the Hall-Petch effect (1951 – 1952), by thermal treatment or by adding a harder phase are some ways to increase the mechanical strength. In metallic glasses, the absence of dislocations mechanism leads to high strength. Thus, due to their unique microstructure, the mechanical strength of metallic glasses is in many cases superior to their crystalline counterparts<sup>38</sup>. Conner *et al.*<sup>39</sup> measured the mechanical properties of the bulk metallic glass  $Zr_{41.2}Ti_{13.8}Cu_{12.5}Ni_{10}Be_{22.5}$  in tensile tests and found that the elastic strain of this alloy,  $\epsilon_{el}$ , is 2%, as in many other metallic glasses, while in crystalline alloys  $\epsilon_{el} \leq 1\%$ . Their

Young's modulus is comparable to crystalline metallic alloys for a same major element in the alloy, and the hardness tends to be higher than the hardness of crystalline alloys (Figure 1.2.1).

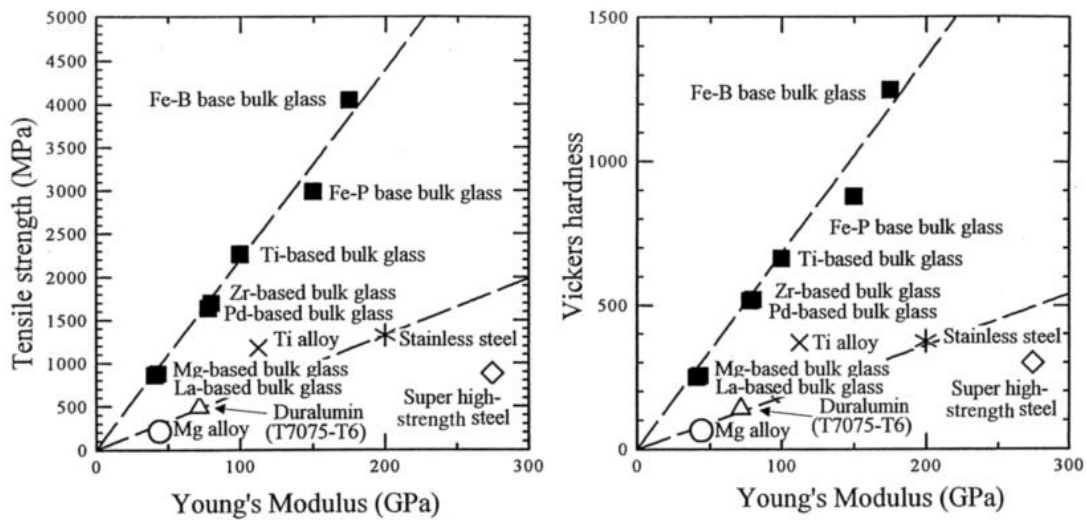


Figure 1.2.1: Relationship between tensile strength ( $\sigma_f$ ), Vickers hardness ( $H_v$ ) and Young's Modulus ( $E$ ) for various bulk amorphous alloys<sup>25</sup>.

In compression, the fracture of metallic glasses generally occurs close to  $45^\circ$  with the applied load direction. This orientation comes from the localisation of the plastic flow into shear bands leading to a catastrophic failure into one shear band.

## 1.2.2. High temperature deformation

Beyond a certain temperature close to the glass transition temperature  $T_g$ , and for a given strain rate  $\dot{\epsilon}$ , the deformation ceases to be localised and becomes homogeneous. The brittle behaviour at low temperature gives way to a ductile behaviour. The stress required to deform the material will decrease with increasing temperature. In this situation, the plastic strain can reach several thousand percent. This homogeneous strain, specific to amorphous materials, allows their thermoforming like polymeric materials. An accurate control of the strain rate according to the temperature allows achieving material deformation under Newtonian flow regime in the viscous state. Since there are no size effects and a very low shrinkage during solidification, bulk metallic glasses are promising candidates for the elaboration of small complex parts that require high mechanical strength and patterned surfaces. Different applications for thermoplastic forming (TPF) of amorphous materials exists in jewellery<sup>40</sup>, micromechanics<sup>19</sup>, MEMS<sup>41</sup> or optical components<sup>42</sup>.

The viscosity  $\eta$  of a material is a measure of the resistance to shear flow. It's the ratio between the shear stress  $\tau$  and the shear rate  $\dot{\gamma}$ ,  $\eta = \tau / \dot{\gamma}$ . Generally the viscosity of a material is

determined by uniaxial compressive tests. By measuring both the stress and strain rates in compression, the equation  $\dot{\gamma} = \sqrt{3}\dot{\epsilon}$  and  $\tau = \sigma/\sqrt{3}$  enable the calculation of the viscosity as:

$$\eta = \frac{\sigma}{3\dot{\epsilon}} \quad (1.2)$$

At a constant temperature, the viscosity can be measured depending on the stress and strain rates. It is well-known that in metallic glasses at a constant temperature, a gradual increase from low strain rates to high strain rates let appear two flow regimes<sup>43,44</sup>. At low strain rate the viscosity is independent of the strain rate. It's the Newtonian regime. When the strain rate is large enough, the viscosity decreases. It's the Non-Newtonian regime. This non-Newtonian behaviour is considered as shear-thinning behaviour.

During the compression tests of the metallic glasses, a decrease of the viscosity with increasing temperature in the non-Newtonian regime is observed. As shown in Figure 1.2.2.a for the Pd<sub>40</sub>Ni<sub>40</sub>P<sub>20</sub> metallic glass, the Newtonian regime is reached at 610 K for strain rates lower than 10<sup>-2</sup> s<sup>-1</sup>, whereas at 560 K it is not even attained below a strain rate of 10<sup>-3</sup> s<sup>-1</sup>. Thus, the transition between non-Newtonian and Newtonian regimes increases with temperature. The variation of the strain rate with the temperature can be plotted in a graph giving the shear localization and Newtonian flow regime (Figure 1.2.2.b).

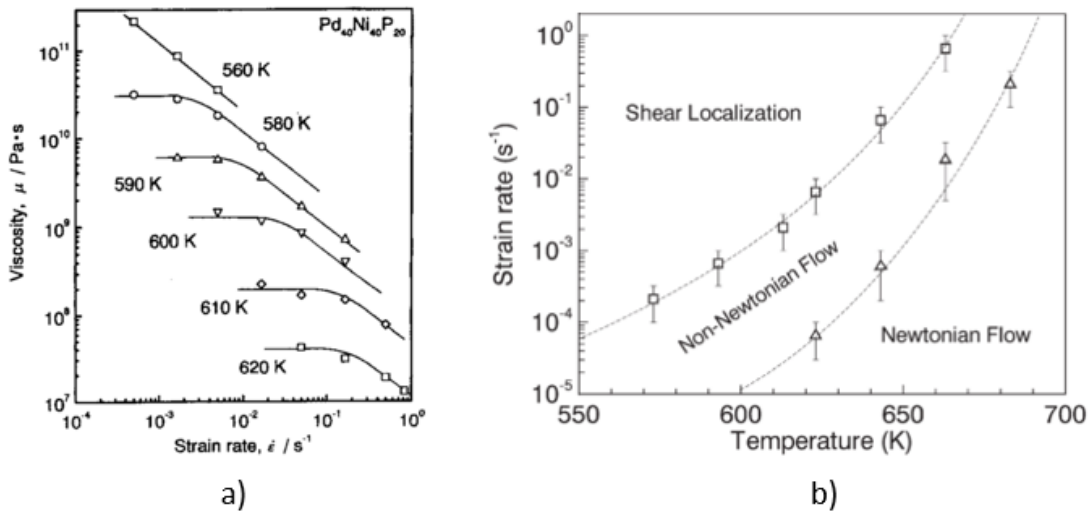


Figure 1.2.2: Viscosity as a function of strain at different temperatures for a Pd<sub>40</sub>Ni<sub>40</sub>P<sub>20</sub> BMG<sup>45</sup> a), Strain modes domains for a Vit1 BMG<sup>43</sup>.

Another representation of this temperature-viscosity dependency can be illustrated by creating the master curve proposed by Blétry<sup>16</sup> to describe the viscosity behaviour of BMGs in uniaxial tests. It consists of plotting  $\eta/\eta_N$  as a function of  $x = \tau V/2k_B T$  where  $\eta_N$  is the Newtonian

viscosity,  $V$  activation volume,  $k_B$  the Boltzmann constant and  $\tau$  the applied stress. An example of this curve for Zirconium based amorphous alloys is given in Figure 1.2.3.

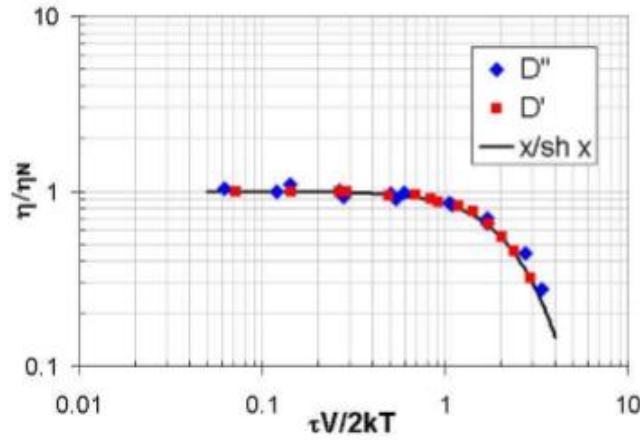


Figure 1.2.3: Master curves for normalized viscosity of  $Zr_{52.5}Al_{10}Cu_{22}Ni_{13}Ti_{2.5}$  ( $D'$ ) and  $Zr_{52.5}Al_{10}Cu_{27}Ni_5Ti_{2.5}$  ( $D''$ )<sup>20</sup>.

The evolution of the viscosity with temperature can be describe by the Vogel-Fucher-Tammann (VFT) (eq.1.3.):

$$\eta_N = \eta_0 \exp\left(\frac{D^* T_0}{T - T_0}\right) \quad (1.3)$$

where  $D^*$  is the glass fragility parameter (a.u.) and  $T_0$  an homogeneous adjustment parameter at a specific temperature  $T$  (K). Depending of  $D^*$ , two behaviours can be distinguished: strong glasses, which have a low fragility parameter and their viscosity do not vary significantly with temperature, and weak glasses which have the opposite behaviour, with a high fragility parameter and a large variation of the viscosity with temperature. At temperature close to  $T_g$ , the evolution of the viscosity with temperature can be approximated by an Arrhenius equation (eq.1.4.):

$$\eta_N = \eta_0 \exp\left(\frac{-Q}{RT}\right) \quad (1.4)$$

where  $\eta_0$  is an adjustment parameter (Pa.s),  $Q$  the activation energy ( $\text{kJ}\cdot\text{mol}^{-1}$ ),  $R$  the universal gas constant and  $T$  the absolute temperature. The activation energies for Zr-based metallic glasses are between 350 to 500  $\text{kJ}\cdot\text{mol}^{-1}$ <sup>16</sup>.

### 1.3. Surface properties of bulk metallic glass

This thesis aims at studying the surface texturing of Zr-based metallic glasses by two innovative processes, thermoforming and femtosecond laser surface texturing. The surface morphologies

resulting from these treatments and their effect on surface properties such as wettability, corrosion resistance and cellular adhesion were investigated. Prior to the study of the textured surface, it is fundamental to analyse polished surfaces (up to 1 $\mu$ m diamond) using similar experimental methods. This Section is dedicated to the wettability and corrosion resistance of these materials.

### 1.3.1. Wettability properties and generality

It is well-known that the wettability behaviour of a solid surface depends on solid-liquid interactions. Measurement of the contact angle  $\theta$  allows to define if the surface is hydrophobic ( $\theta > 90^\circ$ ) or hydrophilic ( $\theta < 90^\circ$ ) which depends on the solid-vapour interfacial tension or solid surface tension ( $\gamma_{SV}$  or  $\gamma_S$ ), solid-liquid interfacial tension  $\gamma_{SL}$  and liquid-vapour interfacial tension or liquid surface tension ( $\gamma_{LV}$  or  $\gamma_L$ ). In particular cases, wetting phenomenon are exacerbated and superhydrophobic ( $\theta > 150^\circ$ ) or superhydrophilic ( $\theta \approx 0^\circ$ ) behaviours can be observed.

Many information can be taken from contact angle measurements:

- The measurement of the contact angle with a common liquid like water gives access to the general wetting behaviour of the surface.
- By comparing several liquids with different polar and dispersive components ( $\gamma_L^p$  and  $\gamma_L^d$  respectively), it is possible to calculate the solid surface free energy (SFE) which is an intrinsic property of the solid.
- The measurement of wetting hysteresis allows to obtain accurate information on the impact of roughness on surface adhesion.

For the same liquid, the contact angle is mostly influenced by two parameters: the surface topography and the surface chemical constitution.

#### Theoretical models for textured surfaces

To evaluate the effect of the surface topography on wettability, two models were proposed: The first model was developed by Wenzel in 1936<sup>46</sup>. It assumes that the chemically homogenous surface have a roughness that is small compared to the droplet dimension and that the liquid droplet contacts completely with the surface beneath, as shown in Figure 1.3.1(left). The relation between the contact angle  $\theta_W$  on the rough surface and the equilibrium contact angle  $\theta_e$  on the flat surface for the same material is given by:  $\cos \theta_W = R_W \cos \theta_e$  where  $R_W$  is the ratio between the real surface area and the apparent surface area. The apparent surface area

do not take into account the roughness, and thus can be 10 to 100 times smaller than the real surface area.

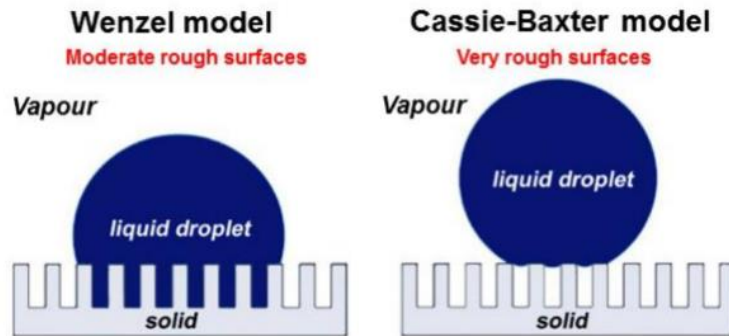


Figure 1.3.1 : Scheme of the Wenzel (left) and Cassie-Baxter (right) models. The different behaviours of a liquid droplet are represented where the liquid completely wets the surface (Wenzel) or the air is trapped within the surface structure (Cassie-Baxter) adapted from<sup>47</sup>.

Wenzel model is limited to wetting angles larger than  $0^\circ$  and lower than  $180^\circ$ , and for values of the roughness factor  $R_w \leq 2$ , where  $R_w = A_{\text{real}}/A_{\text{geom}}$ . For rougher or porous surfaces, Wenzel model cannot describe the wetting properties. Another model developed by Cassie-Baxter in 1944<sup>48</sup> is adapted for this situation. In this model, the liquid does not fill the cavities and small air pockets are trapped below the droplet, as shown in Figure 1.3.1.(right). The choice of the more appropriate model to define the wetting behaviour for a particular system is determinant in the understanding of solid/liquid interactions. The study of the contact angle variation during time allows to choose the best model. Droplets in the Wenzel state are encrusted on the surface asperities. They are not easily repelled and the contact angle does not vary significantly with time. On the contrary, in the case of droplets in agreement with Cassie-Baxter model, the solid/liquid interaction area is very low, less stable, and droplets do not adhere strongly to the surface. The contact angle will change more easily during time and repelling the droplets is easier.

### Multi-scale roughness

In nature, most of the hydrophobic or superhydrophobic surfaces such as lotus leaves and bird feathers, present multi-scale roughness, where a multiplicity of periodic surface structures at the micron and submicron scales overlap and are responsible for the wetting properties. Femtosecond laser surface treatments, as mentioned later, allows creations of multi-scale surface topographies. In this case, a combination of both models presented before can exist, which allows to modify the wetting properties (Figure 1.3.2). Different studies suggest that this leads to a multiplicity of effects, where the Wenzel state occurs for submicronic scale roughness, and the micronic scale roughness is associated with the Cassie-Baxter effect<sup>49</sup>.

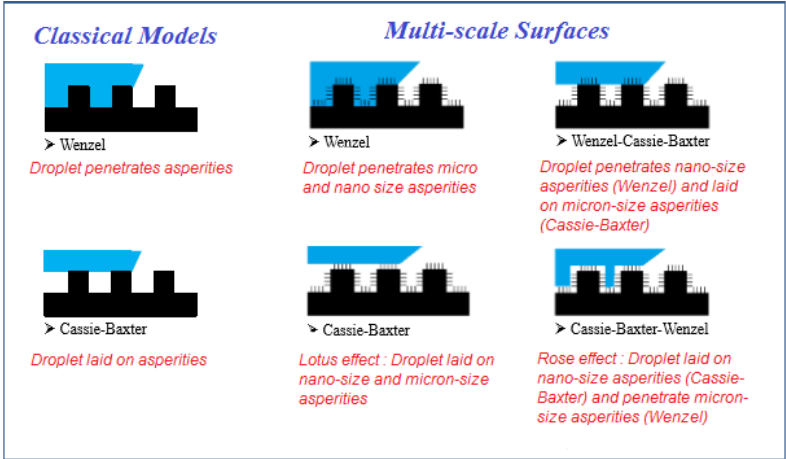


Figure 1.3.2 : Scheme of the different possibilities where a droplet interact with surface with single or multi scale roughness, adapted from<sup>50</sup>.

### Wetting properties of Zr-base bulk metallic glasses (BMGs)

To the best of our knowledge, the wetting properties of bulk metallic glasses have not been studied in detail so far. However, this information is relevant and important in particular for biomedical applications. By studying the roughness effect on cells adherence of Zr-based amorphous alloys, and by comparing these results with Ti6Al4V alloy surfaces, Huang et al<sup>13</sup> determined the surface free energy (SFE) of two metallic glasses  $Zr_{55}Al_{10}Cu_{30}Ni_{15}$  and  $(Zr_{0.55}Al_{0.10}Cu_{0.3}Ni_{0.05})_{99}Y_1$ . In order to do that, they used two liquids (Deionized Water and Diiodomethane) and measured the contact angles for  $1\mu m$  polished and ground 600 grit SiC paper surfaces for the two BMGs and the reference Ti6Al4V. The results are presented in Figure 1.3.3. The surface free energy of Zr-based metallic glasses values are between 54 and 58 mN/m<sup>2</sup> with contact angles between  $57^\circ$  to  $61^\circ$  for water, indicating an hydrophilic behaviour of the surface ( $\theta < 90^\circ$ ).

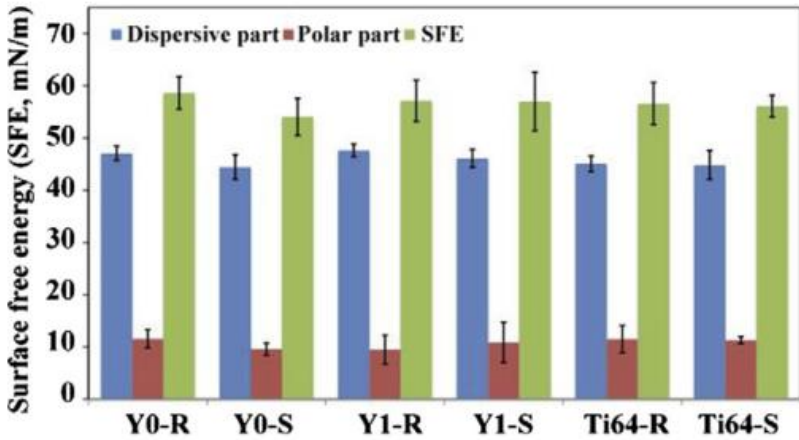


Figure 1.3.3 : Surface free energy with dispersive and polar components for  $Zr_{55}Al_{10}Cu_{30}Ni_{15}$  (Y0),  $(Zr_{0.55}Al_{0.10}Cu_{0.3}Ni_{0.05})_{99}Y_1$  (Y1) and Ti6Al4V (Ti64) for rough (R) and smooth (S) surfaces<sup>13</sup>.

For the  $Zr_{55}Al_{10}Cu_{30}Ni_5$  (Y0) alloy, the roughness seems to have a positive effect on the surface free energy and, considering what has been previously thought, the roughness maintain the water contact angle of water and the SFE values. Compared to the Ti alloy, the Zr-based surface shows similar SFE values, both for the dispersive and the polar components.

### 1.3.2. Corrosion properties

“*Good corrosion resistance under application-relevant experimental conditions is always a decisive criterion for the commercialization of new materials*”<sup>10</sup>. Zr-based bulk metallic glasses are characterized by a large elastic domain, high strength and close Young modulus compared to other metallic glasses. These mechanical properties, associated with biocompatibility for certain alloys, make them promising candidates for biomedical applications, as mentioned in the introduction. The ability to thermoform these alloys with high aspect ratios make them also valuable for other sectors, such as microelectronics or the sports industry. These applications imply a good understanding of their corrosion behaviours in general and in specific environments. Zirconium presents good corrosion resistance thanks to the creation of a  $ZrO_2$  passive oxide layer at its surface<sup>51</sup>. However, Zr-based metallic glasses reveal a wide difference in corrosion resistance between medias that do not contain and medias that contain  $Cl^-$  ions. While Zr-BMG present better corrosion resistance than its crystalline counterparts in 0.5 M  $NaClO_4$ , the corrosion resistance in 0.5 M  $NaCl$ <sup>52</sup> solution is equal or lower. This zirconia oxide exhibits higher hardness and elastic limit values compare to Zr-BMG, which can thus modify the mechanical and wear resistance properties of the bulk material<sup>53</sup>.

#### Passivation behaviour in Zr-BMGs

Contrarily to crystalline alloys, metallic glasses present an homogeneous distribution of the constituent elements at the surface. This specificity, associated with the theoretical absence of crystalline defects such as grain boundaries and dislocations, allows to understand their corrosion behaviour. Indeed, in  $Cl^-$  free solutions, their excellent passivation behaviour is related to the fact that the majority of the constituent elements such as Zr, Al and Ti passivate easily, so they spontaneously form a protective oxide layer at the amorphous alloy surface. In the case of halide-containing solutions, this passivation film do not protect the surface so effectively<sup>54</sup>, making it more susceptible to pitting corrosion. The explanation for the pitting corrosion susceptibility of Zr-BMGs in chloride solutions was presented by Gebert *et al.*<sup>55</sup> and is due to the presence of crystalline micro precipitates not detectable by classical X-Ray

diffraction, which act as nucleation points for localized chloride attack of  $\text{Cl}^-$  ions. These ions are known for their high reactivity at high energy points of metal surfaces such as grain boundaries and will preferentially react with the material near surface defects or heterogeneities<sup>3</sup>.

### Effect of surface finish and addition elements on corrosion resistance

As explained above, zirconium based metallic glasses form a native passivation film mostly composed by zirconium oxide  $\text{ZrO}_2$ , the major element in the amorphous alloy. However, different processes can modify the passivation behaviour of the surface. Gebert *et al.* studied in detail the corrosion behaviour of metallic glasses, especially Zr-based alloys. They found that in anodic polarization, the passivation of quaternary Zr-Cu-Al-Ni alloys is due to Zirconium, Aluminium and Nickel<sup>3</sup>. On the other way, copper reduces the corrosion resistance. Even in open circuit conditions, while most other elements start to passivate, copper tends to dissolve away<sup>10</sup>. Gebert *et al.*<sup>56</sup> then observed that the surface finishing method of Zr-based metallic glass can modify their surface composition and promote a surface copper enrichment which increases the susceptibility to pitting initiation. For example, SiC paper grinding and diamond suspension polishing will lead to a passive surface while polishing with  $\text{SiO}_2$ -based suspension will promote Cu-enrichment and the decrease of the corrosion resistance.

Minor additions of elements in Zr-based metallic glasses can also modify the corrosion properties and promote a better passivation behaviour. Gebert *et al.*<sup>57</sup> compared the corrosion resistance of Zr-Al-Ni-Cu quaternary amorphous alloys with Zr-based alloys containing Nb and Ti. They observed a significant decrease of pitting susceptibility in 0.01 M NaCl for the Nb or Ti containing alloys. They attributed this phenomenon to the higher glass forming ability of these alloys, which indirectly improves the corrosion resistance. Ti or Nb make these alloys less sensitive to form precipitates during casting because of pollution elements (oxygen, nitrogen, carbon...), and promote a more homogeneous single phase alloy, thus reducing localized corrosion.

## 1.4. Surface texturing of materials

### Context and issues

Since the industrial revolution in the 18th century, raw material and manufactured product consumption is in constant evolution. The transition from an agrarian to an industrial economy has maintained a dynamism in the demand for goods for two centuries, stimulating in return technical progress. Nowadays, worldwide problematics like greenhouse gases reduction and constant progress in an ultra-competitive marketplace require industries to offer even more innovative solutions. The era of over-consumption in developed countries is in decline, the time has come to optimize the efficiency and cost of manufactured materials and products. In this context, coating and surface treatment processes are essential means of improving the functional properties of materials: (a) increasing their corrosion, oxidation and wear resistance; (b) improving their fatigue resistance in all its forms (mechanically, thermomechanical and surface fatigue); (c) controlling their optical and friction properties; (d) optimizing their biocompatibility, and the body response to implant surfaces. These are some of the many problematics that surface functionalization tries to answer. In this work, the study focused on surface functionalization of three Zr-based bulk metallic glasses. As mentioned in the previous Section, the amorphous structure gives them exceptional properties and allows to consider applications that common crystalline alloys cannot fully address. However, as explained in Section 1, bulk metallic glasses, due to their metastable nature, are very sensitive to temperature. Hence, the classical surface treatments used for crystalline alloys are, in most cases, not adapted to these uncommon materials. To avoid this problem, two innovative surface texturing techniques were chosen in this work:

- The use of pulsed femtosecond lasers, which, due to the short interaction time, allows creating a large range of surface textures while hopefully maintaining the amorphous condition in the metallic glass surface.
- The thermoplastic forming process, which makes the use of the fact that amorphous alloys become viscous at relatively low temperatures and deform easily.

## 1.5. Femtosecond lasers in surface treatments

### Generalities

First described as a "trivial invention" by the prestigious scientific journal *Physical Review Letters*, lasers are in a center of a billion dollars international market. LASER is the acronym of *Light Amplification by Stimulated Emission of Radiation*. Capacity of emitting radiations from low (X-ray and Ultraviolet) to micrometric wavelengths (maser), these devices allow generating coherent radiation with intensity and pulse durations varying in extremely wide ranges. It was in 1960, while repairing electronic devices to pay the university fees that Theodore Maiman created the first ruby laser<sup>58</sup>. A strong interest arose around Maiman's discovery and in 1964, Charles Hard Townes, Nicolay Basov and Aleksandr Mikhailovich Prokhorov were awarded the Nobel Prize in Physics for their contributions to the laser development. An European program on amplification chains started in the 90's. One of the aims of this program was to develop a femtosecond laser chain. These technological advances created an intense competition between laboratories and industries, allowing a fast development in ultrafast lasers. Nowadays lasers are used in a wide range of applications and many different working modes exist.

### 1.5.1. Laser operation principle

Figure 1.5.1.a illustrates the processes that may occur when an electron pass from the fundamental state of energy  $E_1$  (1), to the excited state  $E_2$  (2) by absorbing a photon and decays later to the fundamental state. The photon disappears and so the wave is attenuated. When the electron decays by spontaneous emission, represented in Figure 1.5.1.b, the excited atom returns to the fundamental state while emitting a photon or/and a phonon, in a random direction.

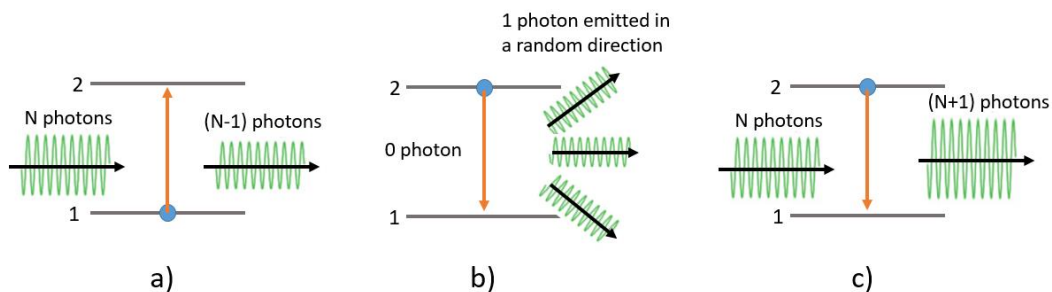


Figure 1.5.1: Absorption a), spontaneous emission b) and simulated emission c) mechanisms.

In 1917, Einstein introduced a third process of photon emission called *the stimulated emission*<sup>59</sup>.

In this case, the emitted photon is in phase with the incoming photon and presents the same direction and frequency. This phenomenon is the working principle of lasers, as indicated in the acronym of *Light Amplification by Stimulated Emission of Radiation*. In appropriate conditions, simulated emission allows amplifying the radiation intensity: for that the stimulated emission process must be predominant over the photon absorption and for this, a population inversion has to be done. Einstein showed that absorption and stimulated emission happen with probabilities given by the same expression. The only difference is that the first one is proportional to the proportion of atoms in the low energy state  $E_1$  called state 1 population ( $n_1$ ), whereas stimulated emission probability is proportional to the proportion of atoms in the excited energy state  $E_2$  ( $n_2$ ). To make stimulated emission predominant  $n_2 > n_1$ : it is called the population inversion.

To increase the number of electrons in the excited state  $E_2$  and satisfy the condition  $n_2 > n_1$ , energy has to be supplied. Part of the applied energy will be recovered as radiation in the amplification process. This is called pumping. Pumping can be made by electrical, chemical or optical processes. Similarly, there are plenty of different amplification media: from a chromium-doped sapphire crystal for the first operational laser made by Maiman<sup>58</sup> to gas phase CO<sub>2</sub> active medium used for example as laser-soft tissues surgery and laser materials cutting. Lasers are classified in 5 groups depending on the amplification medium integrated in the resonant cavity: solid, liquid, semi-conductor, gas and free electrons states. The amplification medium is placed in a resonant cavity that creates the monochromatic radiation by stimulated emission, as presented in Figure 1.5.2.

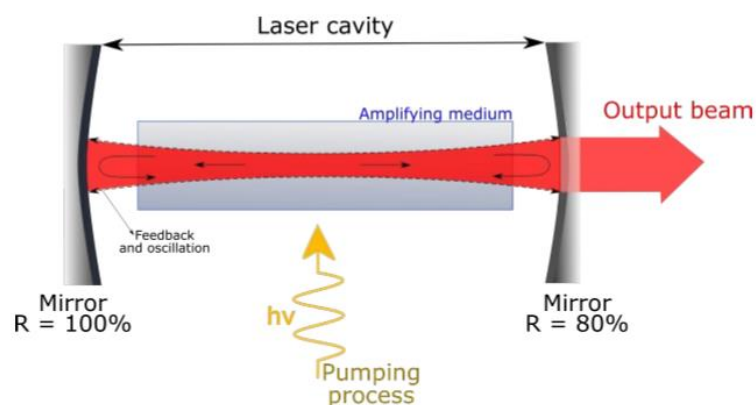


Figure 1.5.2: Scheme of a typical laser oscillator<sup>60</sup>.

Nowadays, laser applications are varied and widespread, many major advances are being made in many different technological fields. Lasers are mainly used in industry to cut, melt or ablate materials. Lasers can machine very hard materials like diamond, accurately weld complex

shapes, treat electronic devices or elaborate synthetic materials. Lasers are envisaged in the nuclear field to confine high density nuclear fusion plasmas. In France the “Mega joule” project will provide one of the most powerful laser worldwide and allow recreating nuclear explosion conditions at small scale and increase the material knowledge for physical purposes. In medicine, lasers are used in many domains from ophthalmology, dermatology, for cutting and ablation of tissues, for cancers tumours treatment in therapy, etc...

## 1.5.2. Femtosecond (fs) oscillators

The theory of operation of a femtosecond oscillator involves very complex non-linear optical phenomena and its deep understanding is not the objective of this thesis. However, in order to make understandable the main principles of this technology to the readers, a part of this chapter is dedicated to the simplification about the generation of ultra-short duration laser pulse. The invention of these ultrashort lasers is one of the greatest scientific breakthroughs in recent decades: they allow the understanding of physical phenomena that were still unexplained until today and open the way to multiple industrial applications such as micromachining, surface texturing or surgical cutting (Laser-Assisted In-Situ Keratomileusis, LASIK) with cutting-edge accuracy.

### Amplifier media

This technology is based on Heisenberg's uncertainty principle: the shorter a wave is, the wider its frequency range, and vice versa. To create ultra-short laser waves, it will then be necessary for the laser's amplifier media to emit a wide range of radiation frequencies. Thus, the emission spectrum of the amplifier will have to cover a wide range of wavelengths. The first generation of ultra-short pulse lasers used organic dye jets dissolved in viscous solvents as amplifier medias. However, these lasers were unreliable, bulky, difficult to use and produced laser beams of only few milliwatts. A major breakthrough in femtosecond amplifier technology was created in the middle of the 80's, with the discovery of wideband emission crystals such as titanium-doped sapphire Ti:S developed by Peter Moulton. This crystal amplifies wavelengths between 600 and 1100 nm (Figure 1.5.3.a), and emits pulses that last less than ten femtoseconds (Figure 1.5.3.b).

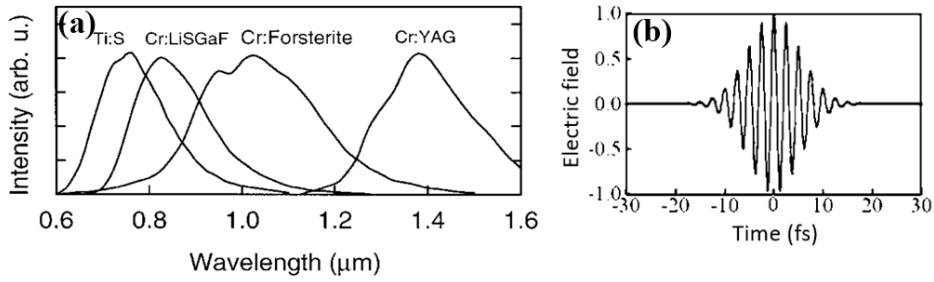


Figure 1.5.3: Fluorescence emission spectra of some transition metal-doped broadband solid-state laser crystals, from<sup>61</sup> (a), Fourier transform of a Ti:S emission spectra (b).

### Laser mode-locking

After the discovery of broadband crystals, the difficulty was to succeed in synchronizing all the vibratory modes emitted by the medium amplifier in order to create constructive interferences between every modes and thus the generation of a periodic high intensity pulse in the laser cavity (Figure 1.5.4). Hopkins and Sibbett<sup>62</sup> described this phenomenon by a clear analogy: let's imagine several bells of different sounds swinging on a bell tower. If the bells beat randomly, the result is a terrible cacophony. Conversely, if you can make the bells ring synchronously, at regular intervals, they will produce very powerful periodic harmonies.

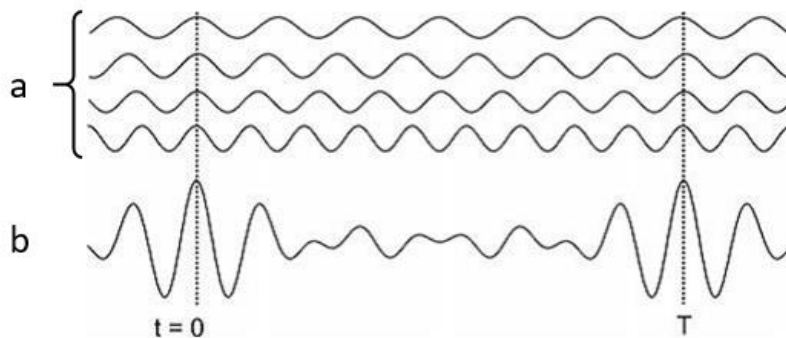


Figure 1.5.4: Different field modes locked (a), and resulted total field in mode locking (b), adapted from<sup>63</sup>.

The second major step in the production of ultrashort laser pulses was the discovery of the Kerr optic effect in 1989. Physicists at Saint Andrews University realized that it was possible to block these modes within a single cavity with a titanium doped sapphire crystal due to the birefringent nature of the amplifier medium. Indeed, by acting as a converging lens because of its non-linearity, the amplifier medium induces an autofocusing phenomenon: a slower propagation of the high intensity light waves compared to low intensity ones (Figure 1.5.5). The resonant focusing favours the pulse regime at the expense of continuous pulse regime: modes are thus added and the pulse becomes more and more important.

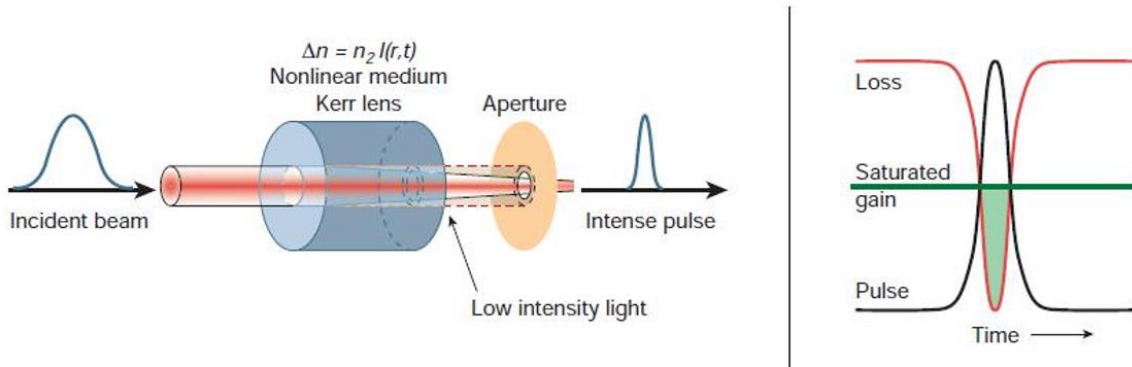


Figure 1.5.5: Kerr lens mode-locking phenomenon. The refractive index of the Kerr lens increases with the laser beam intensity as  $\Delta n = n_2 I(r, t)$ , where  $n_2$  is the nonlinear refractive index of the amplifier medium and  $I(r, t)$  the radial and time-dependent intensity of a short-pulsed laser beam<sup>64</sup>.

### Compensation of the group dispersion velocity

However, in this state, the non-linear refractive index of the amplifier medium causes a positive group velocity dispersion (GVD)  $k'' > 0$ . A round trip into the cavity induces the shift of the different frequencies (frequency drift). Thus, the impulsion is lengthened and the looping condition not satisfied. To compensate the GVD, a complementary device is incorporated where the GVD is negative ( $k'' < 0$ ), and thus enable to recombine the radiation frequencies. Two systems can be used as compensators: a Dispersion-compensating Prism Pairs (DCPP, Figure 1.5.6.a) and a Semiconductor Saturable Absorber Mirror (SESAM, Figure 1.5.6.b). Based on the refractive index dispersion in glass, the DCPP recombines the spectral components. The Semiconductor Saturable Absorber Mirror (SESAM) recombines the spectra by choosing thicknesses of the semi-conductor layer stacks leading to constructive interferences between each radiation wavelengths.

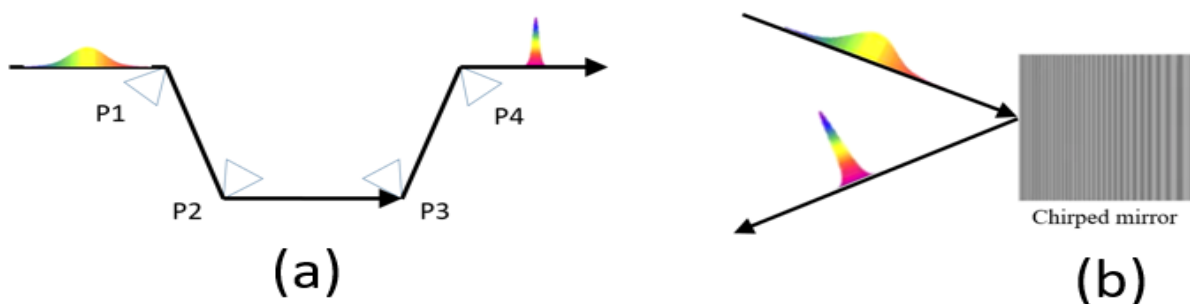


Figure 1.5.6: Dispersion-Compensating Prism Pairs (DCPP) (a), Semiconductor Saturable Absorber Mirror (SESAM) (b).

These different elements incorporated in the laser cavity are the major components required to create ultrashort pulse duration. Even so, other complex devices have to be integrated to guarantee a perfectly stable pulse regime but we decided to not present them here as long as the

most important parts of a femtosecond oscillator are presented. From that, the simplified optical path required in a laser cavity to create ultrashort pulses is presented in Figure 1.5.7.

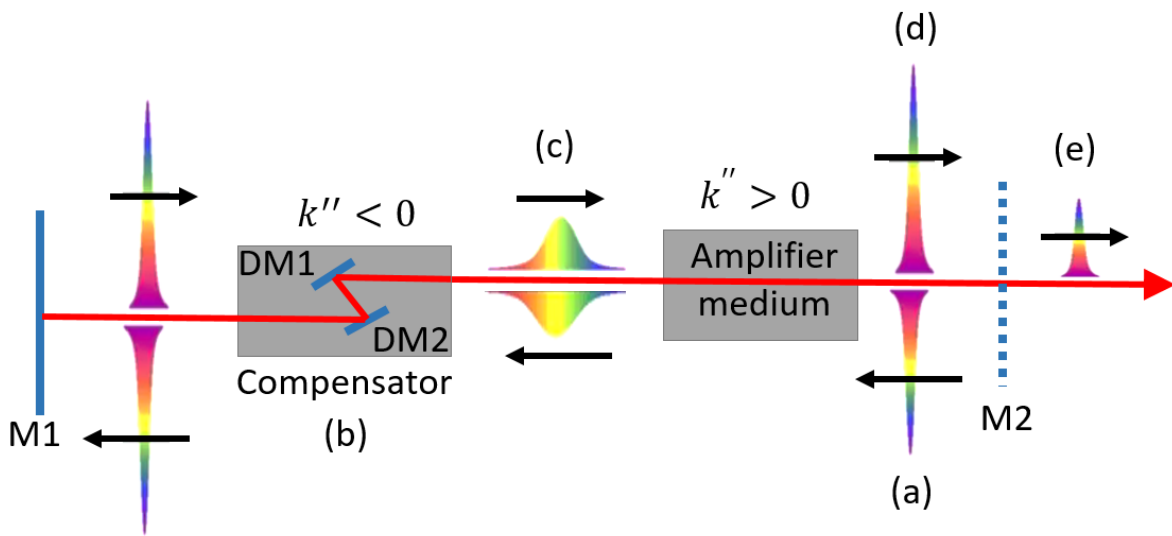


Figure 1.5.7: Simplified optical path of a femtosecond laser system. (a), (b), (c), (d) and (e) parts are described below.

Starting from a laser pulse limited by Fourier transform (a), after passing through the amplifier medium the pulse is dispersed with a frequency shift ( $k'' > 0$ ). Dispersive mirrors couple DM1/DM2 (b) recombines all spectral components and re-compress the pulse. The ultra-short pulse is then reflected by M1 (100% reflectivity) mirror cavity. The Kerr effect can be done on the mirror M1 or in the amplifier medium (here the Kerr effect is realized on the mirror). The pulse repass through the compensator system and so is re-shifted. Due to the negative dispersion factor of the compensator system, slow frequencies (blue) are now in the front part of the pulse (c). After passing through the amplifier medium, the shift is compensated and the femtosecond pulse (d) is amplified compared to the original one (a). Finally, a partially reflecting mirror M2 collect a fraction of the pulse energy (e). The other part is re-injected in the path to create a constant and stable femtosecond laser pulse wave-train.

### Chirped pulse amplification

At this stage, the pulse energy of the output beam is low ( $\sim$  nJ). However, a high energetic pulse train in the femtosecond oscillator would lead to critical damages into the cavity. To avoid this, external amplifier systems are employed, which considerably increase the pulse energy, as required for material surface processing or micromachining. The mostly used amplifier system is the chirped-pulse amplification (CPA) described in Figure 1.5.8.

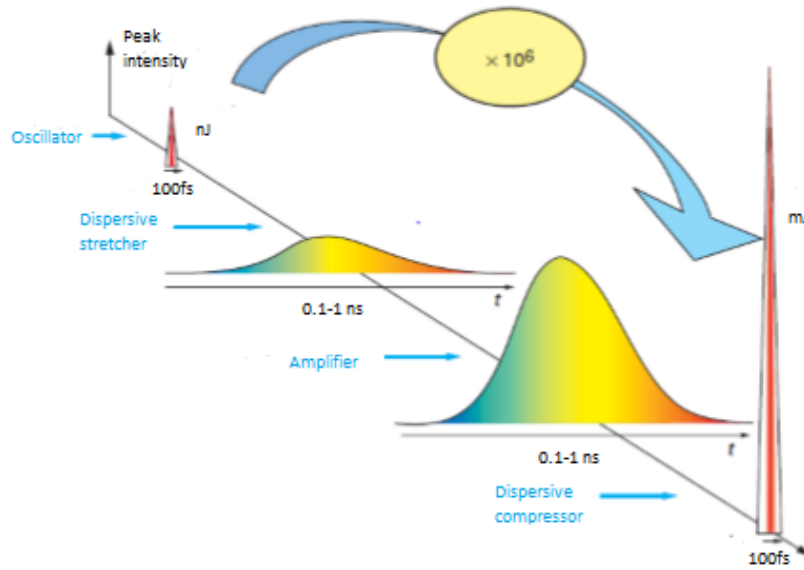


Figure 1.5.8: Scheme of the chirped-pulse amplifier system, adapted from <sup>50</sup>.

In this amplification technique, a low energy pulse from an oscillator is used to seed the amplifier line. A dispersive stretcher (optical dispersive component) widens the pulse, which is then amplified and recompressed. This system allows to increase around  $10^6$  times the seed pulse energy while keeping its ultra-short duration and so deliver a sufficient energy to activate ablation mechanisms on the material surface without altering the laser cavity.

### 1.5.3. Laser-material interaction in fs pulse regime

The study of the ablation mechanisms in femtosecond laser materials processing is a key step to understand the morphological, topological and chemical surface modifications induced by the laser treatment. The ultra-short duration of the energy deposition requires to decompose the physical and the thermal evolution in material at the beginning of the laser-material interaction, where the electronical excitation occurs from the photo-thermal and the photo-mechanical phenomena which happen at a later stage and contribute to ablation mechanism<sup>65</sup>. The first theoretical study of femtosecond laser ablation of material was reported by Shank *et al.*<sup>66</sup> in 1983 and was performed with 90 fs laser pulses on silicon substrates. Since then, many researches investigated ablation mechanisms. Crystalline metals and alloys are the most studied due to the large range of potential applications such as surface texturing and micro processing with ultrashort laser pulses, due to the low thermal effects at this time scale. The ablation mechanisms occurring during laser-metal or laser-glassy metal interaction are not the main subjects of this thesis. Their study involves complex physics, so the bibliography on this part is synthetic but gives the basic knowledge of the ablation mechanisms. The first two parts are

dedicated to the laser-material interaction and ablation process fundamentals, then the description of a particular type of surface structure called as Laser-Induced Periodic Surface Structures (LIPSS) is addressed.

### Electrons and ions behaviours

As it has been explained before, a laser pulse can be described as a group of photons with a quantum energy of  $E = h\omega$ . Elementary absorption phenomenon are the same for every type of materials. Due to the weight difference between ions and electrons, as for electricity, most of the photonic energy of the laser pulse is absorbed by the electrons. The absorption is done when photons transfer their energy to the electrons. This process induces an excitation of the electron which are transferred to higher energy levels. However, laser pulse absorption can be realized only if the excitation energy levels are allowed by the electrons.

In the case of insulant materials such as dielectric materials, absorption and ionization process is realized by complex mechanisms. Indeed, these materials exhibit a full valence band and an empty conduction band separated by a large forbidden band. Pulse energy absorption is then mostly done by valence electrons, the less attached ones to the core. Because of the presence of a forbidden band, excitation to the conduction band by linear absorption (1 photon) of a valence electron can be only done if the photon energy is higher than the forbidden band energy. Due to their large forbidden band ( $\approx 5-10$  eV) most of the dielectrics are totally transparent from the visible to the infrared spectrum, because the single photon energy is not enough to transfer the electron from the valence band to the conduction band. Thus, ionization of insulant materials is done by multiphotonic absorption process where simultaneous absorption of  $N$  photons by valence electrons is not 0 and allow electrons transfer to conduction band if the accumulated energy is higher than the forbidden band. This ionization is called avalanche ionization process where a single electron linearly absorb multiple photonic impacts (inverse Bremsstrahlung) and promote a multiplication of free-carrier electrons.

In the case of metals, photon interaction mechanisms with material is simpler. Indeed, electronic structure of conductive materials can be resumed as a partially occupied valence band overlapped with an empty conduction band or with a very small forbidden band of few meV. Thus, these bands can be assimilated as a unique band partially filled with a high amount of valence electrons ( $10^{22}$  cm<sup>-3</sup>) with a very low resistivity ( $\approx 10^{-6}$   $\Omega$ .cm). Excitation of the free electrons will be possible by single photon energy absorption and then converted to thermal energy by phonon-electron coupling.

Typically, for a wavelength of 1000 nm corresponding to a photon energy of 1.24 eV, absorption mechanism is quasi-instantaneous ( $\approx 1$  fs) and mostly due to electrons<sup>67</sup>. Indeed, the characteristic thermal equilibrium time between electrons and the lattice, that is the electron-phonon coupling time  $\tau_E$ , is in most of the cases shorter than the energy deposition time relative to the laser impulsion  $\tau$  ( $\tau < \tau_E$ ). This speed difference introduce an extreme energetic unbalance between electronic and ionic systems. The excited electrons, in a thermodynamically non-equilibrium state, will then relax by multiple impacts between them, leading to the electron cloud heating in around 100 fs<sup>68</sup>. Electrons are now in a new state characterized by electronic temperature  $T_e$ , much higher than the initial temperature. The heavy weight ions cannot absorb the optical radiation and stayed at the initial temperature. The overall system in a metallic material can be notionally explained as cold ions lattice surrounded by a hot electron cloud that can be assimilated to a thermal breaking.

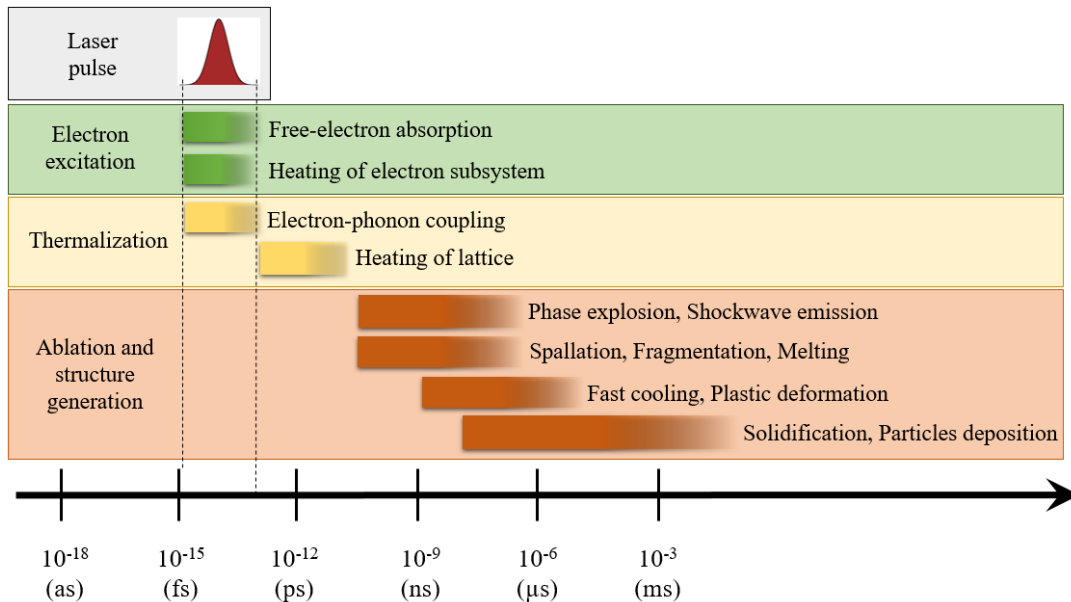


Figure 1.5.9: Timeline of major processes during femtosecond laser ablation of metals, adapted from Vorobyev *et al.*<sup>69</sup> and Canguero<sup>60</sup>.

After the electron-phonon coupling and the lattice heating (few picoseconds), the metallic material is in equilibrium state. Depending if the applied energy reach the fusion or vaporisation limit, the laser pulse can lead to a melting on the materials surface. Phase transition between 100 ps to 10 ns can happen depending the material. The laser pulse energy is then converted to kinetic energy and transferred to the material's lattice. Atoms, ions or clusters can be then ejected, conducting to material thermal ablation. The timeline of the major processes happening during femtosecond laser ablation of metal is presented in Figure 1.5.9.

The common theoretical model used to describe electronic (eq.1.5.) and ionic (eq.1.6.) sub-systems in the laser-metal interaction region with ultra-short laser pulses is the 1-dimension two-temperature model<sup>70,71</sup> (TTM). This model is valid if the laser is considered as an heating source for the electronic system. In some cases, like for insulant or semi-conductor materials with a large forbidden band, the optical energy absorption introduces non-thermal phenomenon. TTM model for conductive materials is expressed as a heat propagation equation for both sub-systems:

$$C_e \frac{\partial T_e}{\partial t} = \frac{\partial}{\partial z} K_e(T_e, T_i) \frac{\partial}{\partial z} T_e - \gamma \cdot (T_e - T_i) + S(z, t) \quad (1.5)$$

$$C_i \frac{\partial T_i}{\partial t} = \frac{\partial}{\partial z} K_i(T_i) \frac{\partial}{\partial z} T_i + \gamma \cdot (T_e - T_i) \quad (1.6)$$

where  $K_e$  and  $K_i$  are electronic and ionic thermal conductivity respectively,  $C_e$  and  $C_i$  are electronic and ionic volume heat capacities respectively,  $T_e$  and  $T_i$  electrons and ions temperatures respectively,  $\gamma$  electrons-ions coupling coefficient and  $S(z, t)$  the heat-source term representing the incident laser energy. This model is based on two hypothesis: the laser-material interaction area must be large compared to the interaction depth (1 dimension model, only depending on  $z$  direction), and the direct ionic heating has to be negligible compared to electronic heating (no source term in the second equation).

Basically, this model supposes that the hot electron cloud and the phonon bath are two distinct domains and allows amongst other to determine the temperature evolution in the couple lattice-electrons as an example presented in Figure 1.5.10. As observed, electrons temperature increases rapidly in a very short time whereas the lattice temperature increases much slowly. In this case, equilibrium is then reached in less than 2 ps for aluminium and 15 ps for nickel and after that, a classical one temperature model is enough to describe energy transport in the material. Non-thermal effect can be then observed depending the pulse energy as ultra-brief fusion<sup>66,72</sup>, super-cooling<sup>73</sup> or solid-plasma phase changing in dielectrics, leading to direct material ejection if the ablation threshold is exceeded<sup>74,69</sup>.

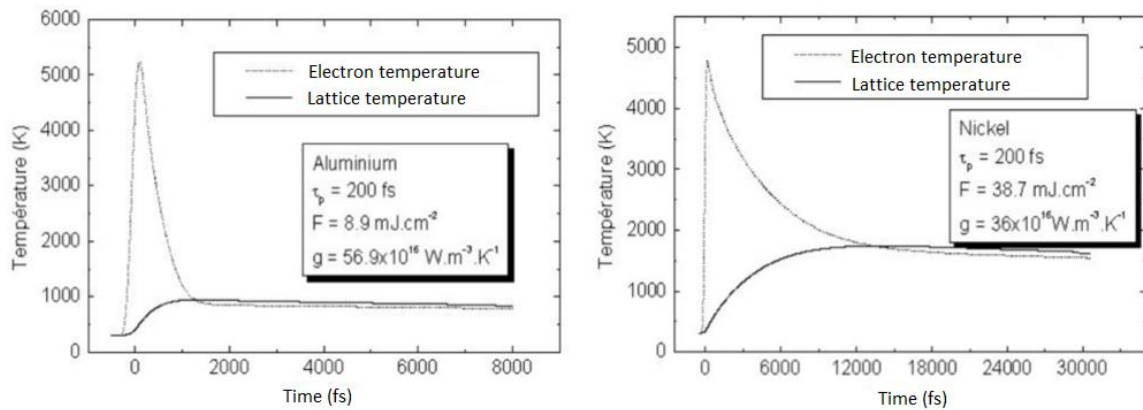


Figure 1.5.10: Two Temperatures Model resolved for a 200 fs laser pulse on aluminium (left) and nickel (right) targets for different fluencies, from Valette thesis<sup>75</sup>.

### Ablation mechanisms in metals

In conductive materials thermal ablation mechanisms are predominant. The physical processes involved can be divided in two main categories. At low fluences, close to the material ablation threshold, a **soft ablation regime** occurs. The material removal rate is low. The processes involved are classical melting and vaporization with creation of a ionized gas material plume, originating from solid state (sublimation) or liquid state (evaporation) transformation into the gas phase. In this range of fluences, nano-size ripples called *Laser-Induced Periodic Surface Structure* (LIPSS) are often generated at the surface of the material. They are attributed to a periodic variation of the absorbed laser energy due to the interference of the incident laser beam with a surface electromagnetic wave leading to a periodic variation of the pulse intensity that occur at the surface of the material. The regions with higher material removal rate being recessed (valleys of the pattern) and those with lower material removal referred to the crests of the pattern<sup>76</sup>. Above a certain critical fluence, a sharp change of the ablation rate occurs in the irradiated material due to a change of the physical processes involved: it's the **strong ablation regime**. When the ablation is due to ultra-short duration laser pulses, the energy deposition rates are extremely high and thus they promote mechanical effects. The confinement of the heated region in the very small laser-material interaction volume introduces compression stresses in the heated material and tensile stresses in the surrounding material. In this regime, the energy deposition is effective on a thickness different from the optical penetration depth, and the electron thermal diffusion must be taken into account. This mechanism is observed when the laser pulse duration  $\tau_p$  is shorter or equivalent to the time  $\tau_s$  required for the irradiated material particles (atoms or molecules) to start moving. The irradiated volume will melt without expansion and so a strong compressive stress will be formed in the melted volume. A blast

wave is then created in the material leading to the fragmentation ejection of the liquid material (liquid spallation, Figure 1.5.11.a) or even of the solid material (solid spallation). The spallation depth depends of the thermal and mechanical properties of the material and is defined the relaxation of the stresses induced by the laser energy. The tougher the material, the closer to the surface spallation will occurs. This phenomenon is called inertial confinement and occurs if:

$$\tau_p \leq \tau_s \approx d_p/C_s \quad (1.7)$$

where  $C_s$  is the sound velocity in the material and  $d_p$  the radiation penetration depth<sup>77</sup>. The other major ablation mechanism which occurs at high fluences is the phase explosion mechanism. At these fluences, the critical thermodynamic temperature is exceeded, leading to a very fast and intense vaporisation of the liquid by homogeneous nucleation. The overheated liquid layer decompose into a mixture of nano and micron-size particles, and the mixture expands leading to material ejection from the surface (Figure 1.5.11.b)<sup>78</sup>. Phase explosion has been observed for different laser pulse durations, from femto to picoseconds and for metallic and non-metallic materials. This ablation mechanism appears when the laser pulse duration is shorter than the dissipation time of the absorbed energy by thermal conduction ( $\tau_{th}$ ) as expressed by the thermal confinement condition given by the following equation:

$$\tau_p \leq \tau_{th} \approx d_p^2/\kappa \quad (1.8)$$

where  $\kappa$  is the material thermal diffusivity. For phase explosion to occur during laser processing  $t_s \leq 10^{-5}s$ , where  $t_s$  is the time for the surface temperature to reach the spinodal line in the material phase diagram.

As shown in Figure 1.5.12, in both spallation and phase explosion mechanisms, material removal is preceded by the generation of voids in the material, which depend on the radiation fluence<sup>78</sup>. The morphology and depth of the voids depends on ablation mechanism.

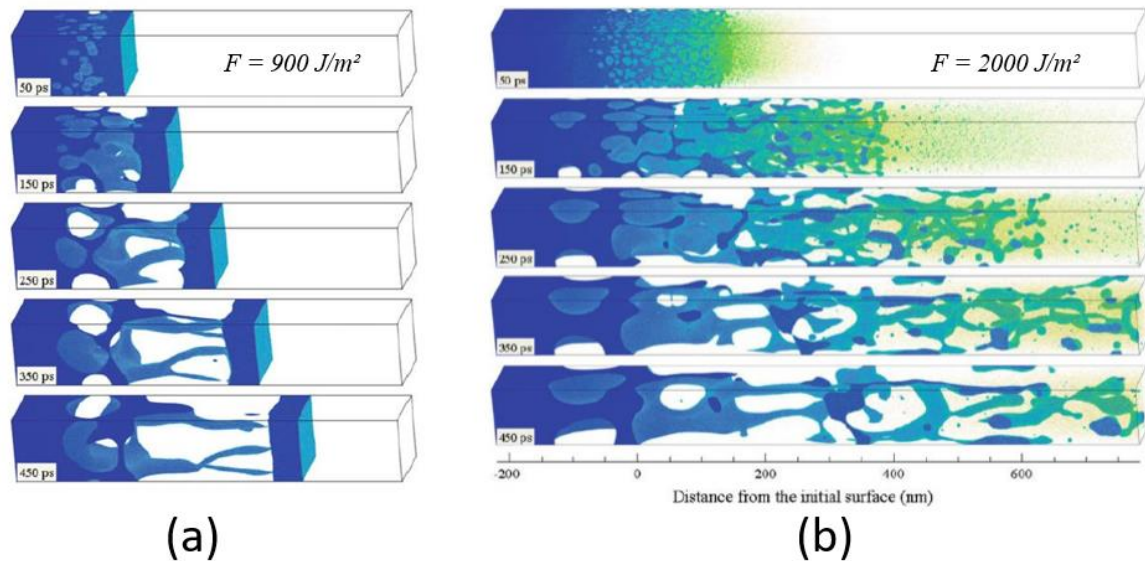


Figure 1.5.11: Snapshots from the molecular dynamic simulation of laser irradiation of aluminium at fluence of  $0.09 \text{ J/cm}^2$  showing the phase of inertial confinement to liquid spallation (a) and at fluence of  $0.2 \text{ J/cm}^2$  illustrating conditions of thermal confinement leading to phase explosion (b) at 100 fs pulse duration, adapted from Zhigilei *et al.*<sup>78</sup>.

In summary, ablation mechanisms of metallic materials in the fs pulse duration regime can be classified as follow: for low fluences, ejection of material occurs by melting and vaporization leading to the formation of a plume consisting of partially ionized particles which expands above the surface. At higher fluences, in the spallation regime, the mechanical stresses due to confinement introduce the formation of voids by stress relaxation, followed by the ejection of material particles of different sizes from nanometre to micrometre aggregates (Figure 1.5.11.b). A further increase of the pulse energy induces another ablation mechanism called phase explosion and consisting of an overheating of the liquid layer that break down into a mix of clusters and gas. This multiplicity of ablation mechanisms leads to a complex behaviour where different material states may exist simultaneously in the irradiated material during the pulse duration. (Figure 1.5.12.). In the case of metallic glass surface treatment, the ultrafast laser interaction timescale makes femtosecond pulse duration devices the most promising to affect as a minimum the metallic glass structure, and so to be able to keep its specific physical and chemical properties even at their extreme surface.

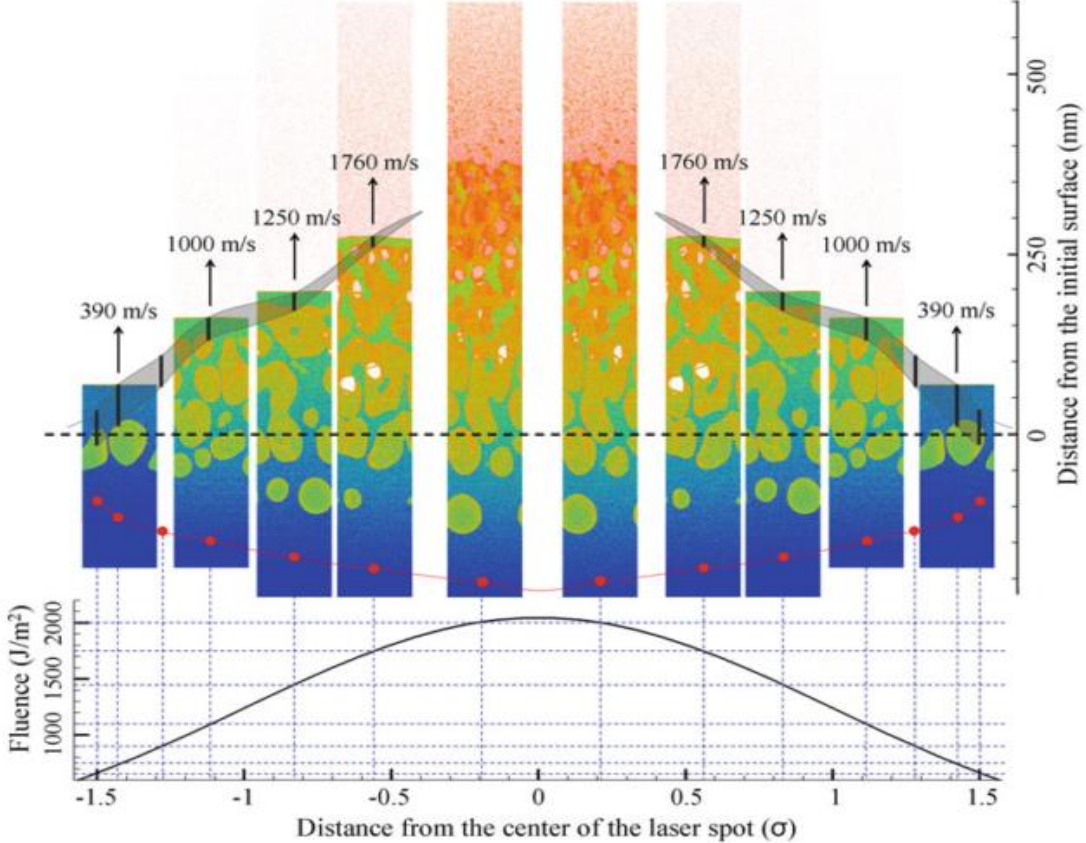


Figure 1.5.12: Scheme of the major physical mechanisms involved in material ablation as melting, generation of sub-surface voids and material ejection from aluminium substrate. The Gaussian profile of the deposited energy in the laser beam explain the ablative phenomenon differences in between the centre (high fluence = spallation regime) and the peripheral part of the spot (low fluence = melting regime) from <sup>78</sup>.

## Laser Induced Periodic Surface Structures

Laser Induced Periodic Surface Structures (LIPSS) are rectilinear periodic structures created on materials surfaces by irradiation with laser devices. These ripples, were observed for the first time in 1965 by Birnbaum<sup>79</sup> on a germanium substrate irradiated with a ruby-sourced laser with a few nanoseconds pulse duration. Since the first observation, ripples of this type were observed on a wide range of materials treated with a large variety of lasers. LIPSS were observed on metal<sup>80,81,47</sup>, dielectric<sup>60,82</sup>, polymer<sup>83,84</sup> and amorphous metal<sup>85,86,87,88,89</sup> surfaces treated with different laser sources with wavelength from the UV to the IR and pulse duration from nanosecond to femtosecond<sup>90,91,69</sup>.

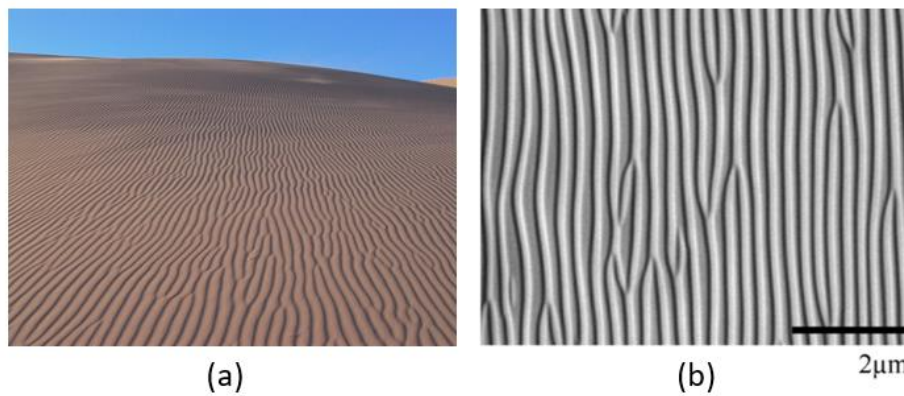


Figure 1.5.13: Ripples formed on sand (a), LIPSS (LSFLs) observed on CaF<sub>2</sub> substrate with Ti:Sapphire source of around 800 nm wavelength<sup>92</sup>.

Two types of LIPSS can be distinguished, depending on their average period:

Low Spatial Frequency LIPSS (LSFLs) are observed on different material surfaces with continuous wave, short (ns), or ultrashort pulsed lasers with linearly polarized beams. LSFLs appear generally at a fluences equal or slightly above the material damage threshold and after a few dozen of laser pulses. Their periodicity is close or somewhat lower than the radiation wavelength, and the direction is perpendicular to the beam polarization vector<sup>91</sup>. Recently, High Spatial Frequency LIPSS (HSFLs) were observed on metallic and semi-conductor surfaces. HSFLs only appear for ultra-short laser pulses (femtosecond) and the period ( $\Lambda$ ) is much smaller than the radiation wavelength ( $\Lambda \sim \frac{\lambda_{laser}}{4}$  to  $\frac{\lambda_{laser}}{10}$ ). They may be oriented parallel or perpendicular to the laser beam polarization. Both LIPSS types structures are often observed at the periphery of the laser spots, where the fluence is low, and for large number of pulses, typically between a few hundreds to a few thousand pulses<sup>93,91</sup>.

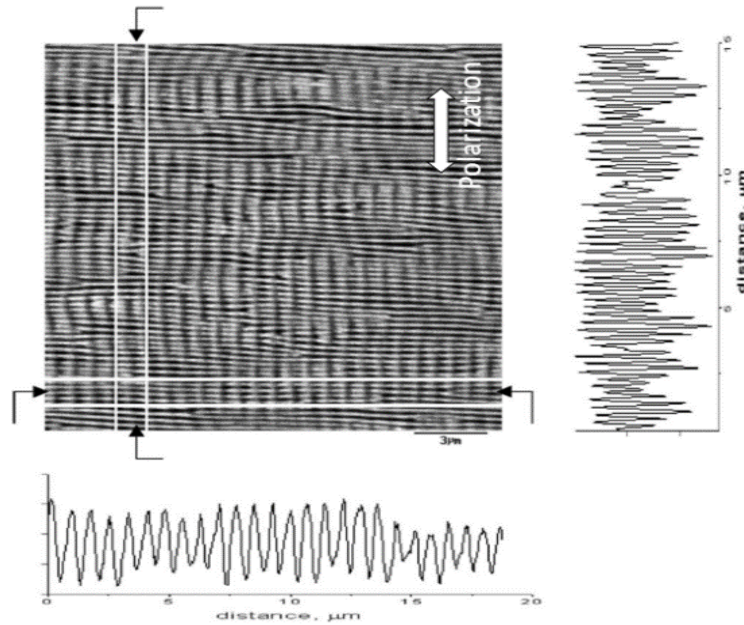


Figure 1.5.14: Profiles of fine and coarse ripples obtained on BaF<sub>2</sub> substrate with s-pulse femtosecond laser at  $0.9 \times 10^{13}$  W/cm<sup>2</sup>. Fine ripples have a periodicity of  $\approx 230$  nm and are perpendicular to laser polarization. Coarse ripples period is  $\approx 600$  to 900 nm and are parallel to polarization, adapted from Reif *et al.*<sup>93</sup>.

Many hypothesis to explain LIPSS formation has been proposed since their first observation, based on theoretical models such as Coulomb explosion model<sup>93</sup>, the Boson condensation model<sup>94</sup> and the general surface scattering (GSS) model<sup>95</sup>. The GSS model developed by Oron *et al.*<sup>95</sup> and Emmony *et al.*<sup>96</sup> was the most commonly used for a long period of time. The basic hypothesis is that LIPSS formation is due to the interference between the incident laser radiation and electromagnetic waves that propagate parallel to the surface due to scattering of the incident radiation by surface topographic irregularities. This interference creates a radiation intensity modulation and so generates periodic oscillations of the electron temperature and of the electron free-carrier density<sup>97</sup>. LIPSS formation was investigated by Sipe *et al.* and their model showed that the interferences effectively generated periodic modulation of the absorbed radiation intensity at the material surface which may generate a rippled structure with wavelength slightly inferior to the laser radiation (LSFLs)<sup>98,99</sup>.

This model was further advanced by Bonse *et al.*<sup>100</sup>, who studied LIPSS formation on semiconductor surfaces treated with femtosecond laser pulses. In their work they combined the Drude model with Sipe's theory and were able to explain the morphological specificities of LSFLs such as orientation and periodicity of the structure<sup>101,102</sup>. Based on these results, they proposed that surface plasmon-polaritons (SPPs) are excited by the incident beam which interfere with the incident radiation, generating periodic oscillation of the surface temperature and the free-carrier density. Surface defects play a predominant role in the generation and

coupling of SPPs and feedback effects referred to LIPSS formation, the phase velocity of polaritons changing on appearance of the ripples, as observed by Kielmann and co-workers<sup>103</sup>.

In synthesis, LSFLs formation can be divided in 3 steps<sup>76</sup>:

1. The incident laser radiation interacts with electromagnetic waves propagating parallel to the material surface. According to the different existing theories, this wave can be part of the incident radiation scattered by surface defects<sup>96</sup>, surface polaritons<sup>103</sup> or as it is now generally accepted, surface plasmon-polaritons<sup>22,101,102,104</sup> propagating parallel to the surface<sup>105</sup>. The interferences between the incident laser beam and these surface waves generate periodic oscillations of the electron temperature profile and free carrier density.
2. The excited electrons transfer their energy to the lattice, creating a periodic profile on electrons temperature with very high scattering, resulting on spatial modulation of the temperature on the surface<sup>97</sup>.
3. The scattered temperature profile on the material surface gives birth to different transformations as melting, vaporization, ablation, while a periodic part is not affected by hot electrons energy transfer, and so the creation of periodic surface pattern.

Despite a general acceptance of the Sipe's theory to explain LSFLs formation, some inconsistencies between experimental results and theoretical prediction remain. For example, variation of the period across the laser spot diameter, bifurcation and splitting of LIPSS<sup>93</sup> etc.. are not properly taken into account by the theory. These models do not explain the formation of HSFLs, with spatial periodicities much smaller than the radiation wavelength<sup>93,106</sup>. Despite different theories to describe HSFLs formation based on self-organization<sup>93,92</sup>, second harmonic generation<sup>107,108</sup>, or Mie scattering<sup>109</sup>, this is still an open field where further research is needed.

At higher fluencies, different structures are observed such as waves with periodicity higher than laser beam radiation wavelength, and columnar structures. These structures can be generated with continuous or pulsed lasers and are commonly explained as result of hydrodynamic convection in the melt pool, driven by the surface tension gradient generated by the inhomogeneous surface temperature profile. Due to Marangoni convection, cells appear in the liquid bath that is frozen-in during the fast solidification that follows irradiation<sup>110,111,112</sup>, leading to changes in the surface topography. Comparing to LSFLs, these surface structure were not deeply studied, in particular in metallic glasses, and their effect on surface properties is still an open field of research.

## 1.5.4. Effect of fs laser treatment on surface properties

### A way to functionalize

Surface texturing by femtosecond laser treatment is a technique presenting huge benefits in material processing when compared to continuous or short pulse duration lasers. As mentioned before, the major benefit of the ultra-short pulse regime (fs) is that the short duration of the laser pulse allows reaching extreme intensities and, consequently, very high energy deposition rates on highly localized areas. Moreover, ultra-short duration pulses limit energy diffusion in the material by heat conduction and convection. This allows material ablation without thermal diffusion in the surrounding regions.

So, femtosecond lasers treatments are particularly interesting in metallic glasses surface processing. Indeed, these metastable materials are very sensitive to temperature increasing. As explained in section 1.1.1, at temperatures higher than the glass transition temperature  $T_g$ , the structure will progressively go to lower energetically state that is the crystalline state. Thus, surface processing with ultrafast ablation mechanism, rapid cooling time of the affected area without thermal effect on the bulk is a promising way to texture while maintaining amorphous structure in the material.

### Surface functionalization by femtosecond laser treatments

This part will be dedicated to an overview of the different femtosecond surface treatments, the associated surface properties modifications and the related potential applications for common materials, such as crystalline metallic alloys, then more specifically for amorphous metallic alloys.

Modification of wetting properties is one of the most extensively studied topic in surface functionalization by femtosecond laser treatment. Indeed, the nano and micron-size patterns that can be created such as LSFLs, grooves, columns and pillars have a strong effect on wettability. The laser processing parameters can be adjusted to create different types of structures, in particular pulse frequency, number of laser pulses, fluence and laser beam lateral displacement sequence (laser track overlapping), while some intrinsic laser characteristic such as pulse duration or radiation wavelength cannot be modified.

Bizi-Bandoki *et al.*<sup>81</sup> studied the wetting properties of AISI 316L and Ti-6Al-V surfaces modified via laser treatment with varying the number of pulses per surface area between 13 and

128 and with constant fluence of  $2.04 \text{ J/cm}^2$ . A Ti:sapphire laser with pulse duration 150 fs was used to process the samples. The resulted surface texture were LSFLs for small number of pulses to micro-grooves overlapped with LIPSS for the higher numbers of pulses. They observed an increase of the contact angles  $C_a$  from  $80^\circ$  to  $125^\circ$  for the untreated sample and the specimen with the highest number of pulses respectively.  $C_a$  of the treated surfaces increased with increasing number of pulses per area. They concluded that the effect of the laser treatment on wettability was due to the Cassie-Baxter effect by increasing material roughness.

Kietzig *et al.*<sup>113</sup> studied the effect of femtosecond laser treatment on wettability of stainless steels AISI 304L, AISI 630 and the titanium alloy Ti-6Al-4V polished, with an average roughness  $R_a \approx 800\text{nm}$  and treated with a Ti:sapphire laser of 150 fs pulse duration with a number of pulses per point of the surface of 125. They studied the effect of the fluence on the structure and the surface wettability variation with time. The applied fluence varied up to  $5.16 \text{ J/cm}^2$  and the contact angle of the water droplet was measured during 50 days. A picture of two treated materials at different fluencies is presented in Figure 1.5.15.

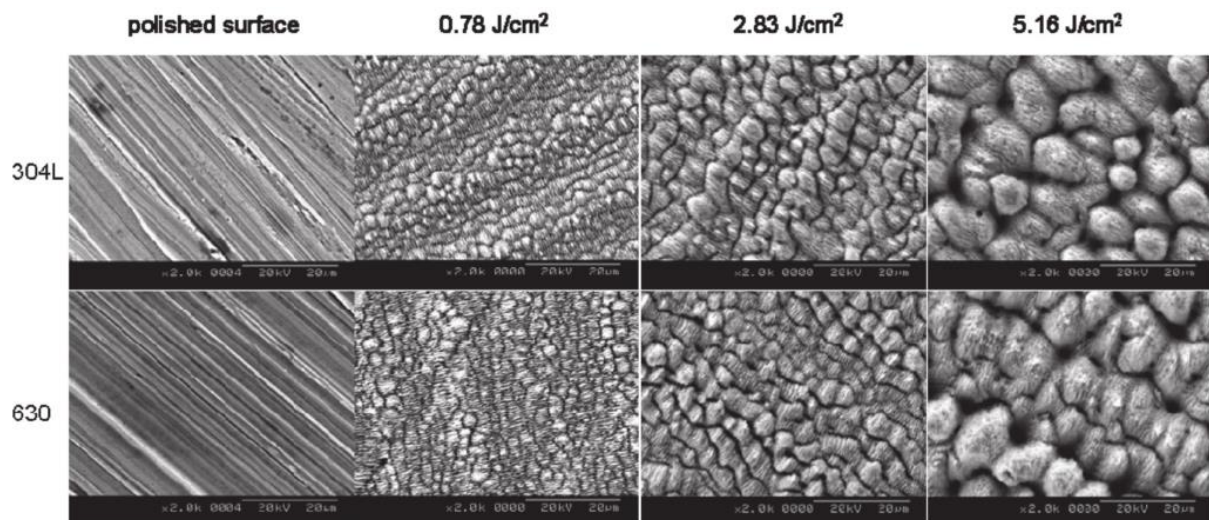


Figure 1.5.15: SEM images of polished and femtosecond laser treated stainless steel 304L and AISI 630 at 3 fluences, adapted from<sup>113</sup>.

The contact angles values are show in Figure 1.5.16. The authors observed a strong effect of the time on the wettability in the laser treated surfaces of all alloys. After the treatment, contact angles of less than  $20^\circ$  are measured, indicating a super-hydrophilic behaviour. After less than 10 days, the wettability changes to highly hydrophobic behaviour with contact angles  $130^\circ \leq C_a \leq 150^\circ$  for samples treated with  $0.78 \text{ J/cm}^2$ . The contact angle evolution was slower for high fluences, but the results do not show relevant differences on wettability behaviour between alloys. They follow the same trend of contact angle variation at low or high fluences. The results

indicate that surface topography was not the only parameter affecting wettability. XPS measurements revealed an increase of carbon content on the laser treated surfaces and the authors attributed the observed change in wettability to it. Thus, both chemical and topological effects were responsible for the surface wettability modification.

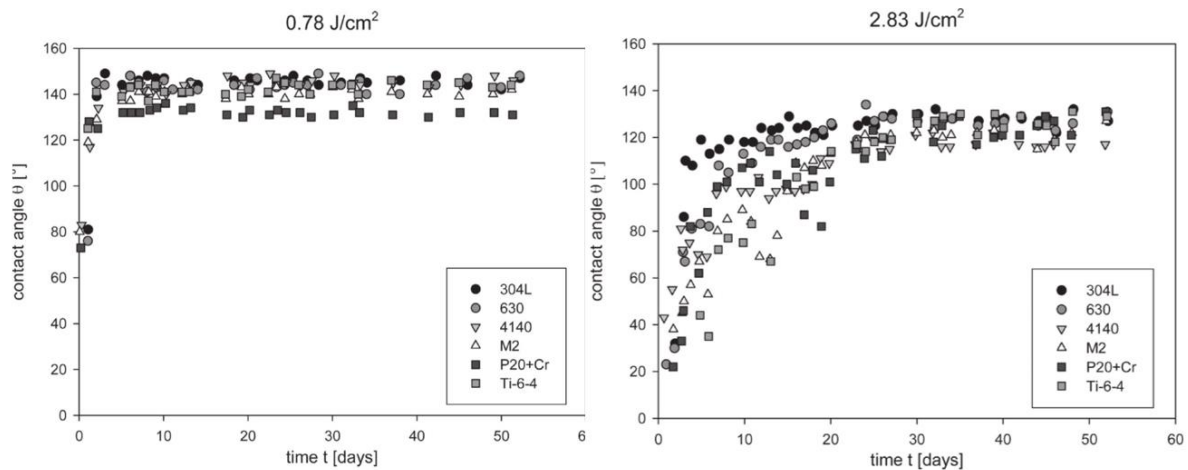


Figure 1.5.16: Water contact angle measurements during time for different metallic alloys at fluencies of  $0.78\text{J}/\text{cm}^2$  (left) and  $2.83\text{J}/\text{cm}^2$ , adapted from<sup>113</sup>.

Cunha *et al.*<sup>114</sup> studied the effect of femtosecond laser treatment on grade 2 Ti and Ti6Al4V alloys at fluences from  $0.2$  to  $0.6\text{ J}/\text{cm}^2$ . They used a Yb:KYW chirped-pulse regenerative amplification laser system with a central wavelength of  $1030\text{ nm}$  and a pulse duration of  $560\text{ fs}$ , the same device used in the present work. The ranges of fluences and the number of pulse per point of the surface varying from  $65$  to  $1880$  allowed creating different morphologies from LIPSS at low fluences to columnar structure at the highest fluences. Both distilled-deionized (DD) water and Hank's balanced salt solution (HBSS) were used to measure the wettability by the sessile drop method. For all structures and liquid combinations, a decrease of the contact angle with time was observed (Figure 1.5.17). For example  $C_a = 105^\circ$  and  $80^\circ$  for  $t = 0\text{ s}$  and  $t = 600\text{ s}$  respectively for columnar structures (type 3), i.e. surfaces become more hydrophilic with time, while for polished surfaces, the contact angle remain almost constant.

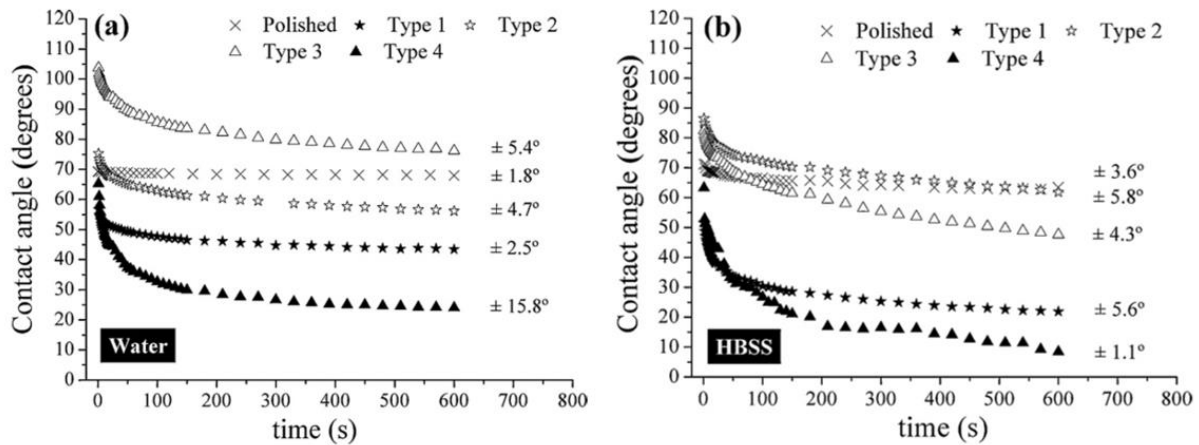


Figure 1.5.17: Contact angle measurements for polished and laser-treated surfaces with water (a) and HBSS solution (b). Type 1 structure corresponding to LIPSS, type 2 to nanopillars, type 3 to columnar structure and type 4 to double scale columnar structure. Adapted from<sup>114</sup>.

The authors also observed that the values of  $C_a$  for the LIPSS texture are anisotropic, depending of the observation direction, as a result of the rectilinear morphology of this surface texture. XPS measurements showed an increase of the oxygen content and that  $TiO_2$  and  $Al_2O_3$  formed on the laser treated surfaces due to chemical reactions between the metal and the atmosphere. Titanium oxides are known to be hydrophilic<sup>115</sup>, so the results indicates that the chemical surface modification due to the laser treatment have also an effect on the surface wettability.

The last study presented is due to Baldacchini *et al.*<sup>116</sup> and the topic is the femtosecond laser surface treatment of silicon surfaces coated with a layer of fluoroalkylsilane molecules. A Ti:sapphire laser with a pulse duration of 100 fs and a centre wavelength of 800 nm was used. The fluences varied between 0.2 to 0.9 J/cm<sup>2</sup>, the beam diameter between 30 to 250  $\mu$ m and 200 laser pulses per point of the surface. As previously shown, modifying the fluence allowed creating different types of surface structures and the contact angle  $C_a$  was also modified. The authors compared the wettability of polished silicon coated with a layer of fluoroalkylsilane molecules and femtosecond laser textured silicon coated with the same molecules. Fluoroalkylsilane are known for their hydrophobic properties<sup>117</sup>. The addition of the surface pattern and an hydrophobic coating allows reaching contact angle of about 160° with a low hysteresis, making the surface super-hydrophobic, while the polished surface with the coating only reaches  $C_a = 115^\circ$ . The authors concluded that the Cassie-Baxter model was followed for the textured surfaces and make possible an easy control of the wetting properties by changing surface topography and thus the surface roughness.

The modification of surface properties by femtosecond laser treatment open the way to many other applications as the surface treatment allows improving film adhesion on metallic alloys<sup>50</sup>, the photovoltaic properties of Si due to increased photocurrent gain by reducing the reflexion coefficient<sup>118</sup>. LIPSS with periodicities in the visible spectral range allow colorizing materials by plasmonic effect<sup>119</sup> by reflecting particular wavelengths. Figure 1.5.18 presents the range of colours and associated reflectance that can be generated on Al substrates with femtosecond lasers treatments. Each colour corresponds to an aluminium target with some specific surface created by fs laser treatment, where iridescent surface came from LIPSS that are dependent of the viewing angle, and golden colour came from micro and nano gratings, independent of the viewing angle. For every structure/colour couple, authors observed a strong decrease of the reflectance from 1  $\mu\text{m}$  to 800 nm with a small plateau, then a drop to near zero reflectivity in the UV spectral range. Authors believe that this drop is due by both inter-band transitions around 800 nm in Al<sup>120</sup> and an enhanced radiation coupling due to the LIPSS morphology.

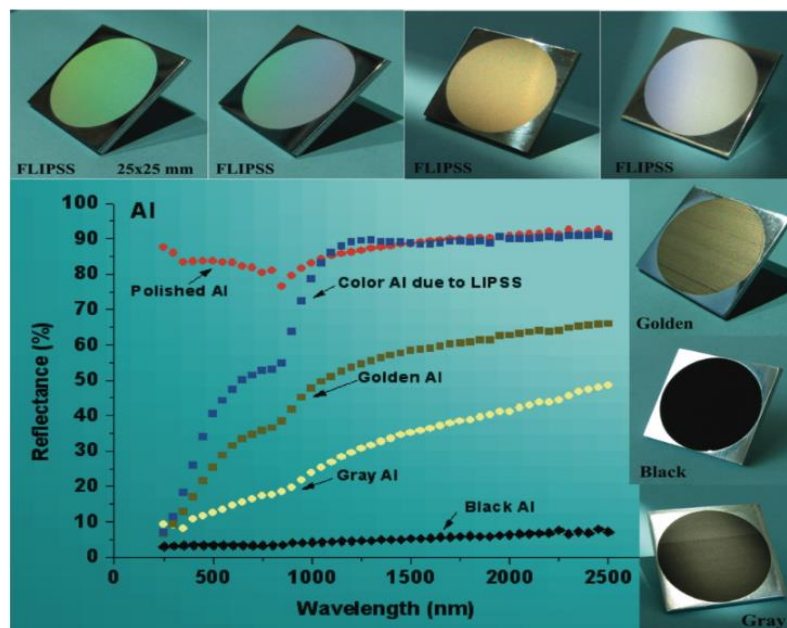


Figure 1.5.18 : Different type of structural colours produced on Al samples and their associated reflectance spectra. Black colour is due to a micro-grooves surface pattern, iridescent colours are mainly produced by LIPSS structure<sup>6</sup>.

Researches have also been conducted on the effect of the laser treatment on the corrosion resistance of crystalline metallic alloys. Valette *et al.*<sup>121</sup> studied the influence of femtosecond laser marking on the corrosion resistance of stainless steels. Marking has been realized with a Ti:Sapphire fs laser with a pulse duration of 150 fs. Polarization measurements in Ringer's solution for the textured surfaces show a shifting to positive values of the corrosion and pitting potentials with same current density values, indicating an ennoblement of the surfaces

compared to the untreated surfaces (Figure 1.5.19). The pitting corrosion potential was also increased by 50 mV for both martensitic Z30C13 and austenitic 316L alloys.

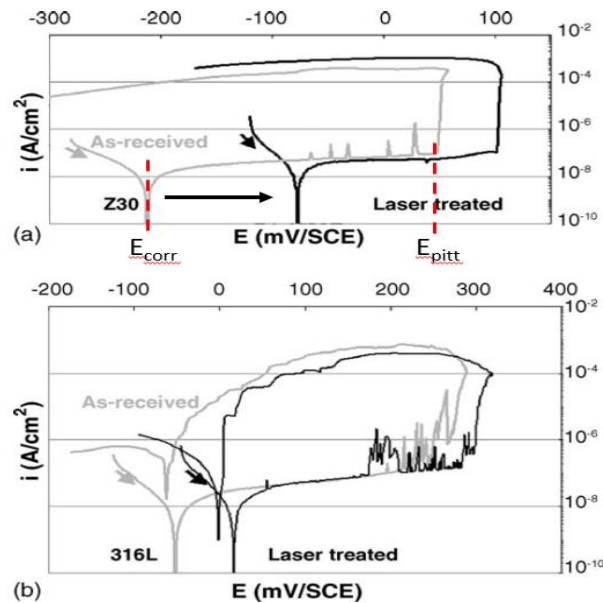


Figure 1.5.19: Cyclic polarization curves for treated and untreated Z30(a) and 316L(b) alloys in Ringer's solution, adapted from<sup>121</sup>.

The unique properties of fs laser treated surfaces found also applications in the biomedical sector. The possibility to tune the surface roughness and topology by varying the pulse energy, pulse frequency and beam polarisation without a large heat-affected zone makes ultra-short pulse laser treatments potential candidates to improve the biocompatibility of materials. Indeed, it has been largely observed that surface roughness has a positive effect on bone regrowth on implants<sup>14</sup>. So periodic structures like LIPSS might allow controlling cellular behaviour on the surface. Dumas *et al.*<sup>122</sup> studied the effect of textures created by the fs laser on the stem cell morphology, adhesion and matrix organisation. They produced 6 topographies from random nanostructures to double scale 60  $\mu\text{m}$  wide lines width with perpendicular 600 nm periodic rectilinear nanostructures. It has been found that these structures do not influence cell proliferation and cell growth was effective on all substrates. However, this nanostructures had a clear effect on the cell morphology and orientation and so could influence the regenerative efficiency. Indeed preferential cell orientation parallel to the nanostructure direction has been observed, with an increase of the cell's Feret diameter in some cases. Dumas *et al.* also did not observe a direct relation between wettability and cellular adhesion and hydrophobic surfaces do not have necessarily a positive effect on cell proliferation as it is commonly thought. Indeed, studies reported that high surface wettability (hydrophilic), generally promotes greater cell adhesion than hydrophobic surfaces<sup>123</sup>.

Cunha *et al.* studied the mesenchymal stem cell behaviour on femtosecond laser textured Ti-6Al-4V surface<sup>5</sup>. Depending the laser processing parameters, 3 different types of textured surfaces consisting of LIPSS, nanopillars (NPs) and microcolumns (MCs). They observed that both LIPSS and nanopillars textured surfaces allowed a better matrix mineralization and bone-like nodule formation compared to polished surfaces and so promoted a better stem cell differentiation. In contrary, femtosecond laser treatments can have a negative effect on cellular adhesion and act as an antibacterial coating. Cunha *et al.*<sup>20</sup> also studied the behaviour of *Staphylococcus aureus* bacteria surfaces of Ti textured with LIPSS ( $\lambda \approx 700$  nm,  $R_a \approx 0.3\mu\text{m}$ ) and nanopillars (Bottom diameter  $\approx 750$  nm,  $R_a \approx 0.3\mu\text{m}$ ) and analysed the bacteria proliferation with polished titanium surface as reference. Bacteria seems to adhere to the surface for a specific ranges of roughness<sup>124</sup>.

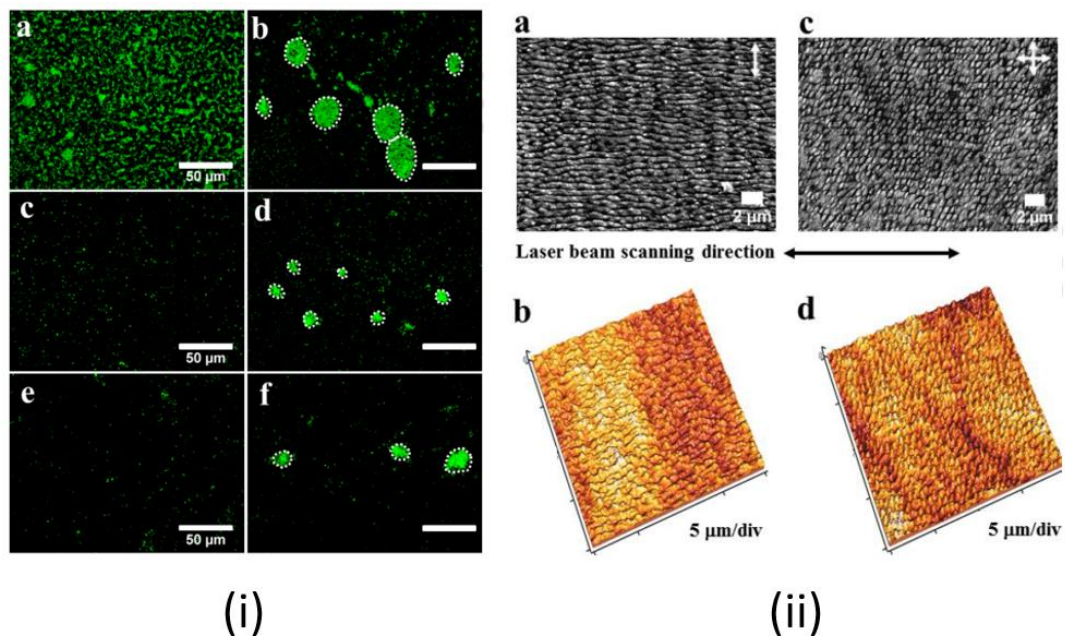


Figure 1.5.20: Fluorescence microscopy images of *Staphylococcus aureus* bacteria 48h after seeding (i) on polished (a-b), LIPSS (c-d) and nanopillars surfaces (e-f). SEM images and AFM images (ii) of LIPSS (a-b) and nanopillars (c-d) surface microstructure<sup>20</sup>.

As observed in Figure 1.5.20, bacteria adhesion and proliferation is much less effective on produced laser treated surfaces consisting of LIPSS (i, c-d) and nanopillars (i, e-f), with an average surface covering of about 25% for the polished surface and around 7% for the laser textured surfaces. The roughness value of the laser textured surface ( $R_a \approx 0.3 \mu\text{m}$ ) is smaller than the preferential roughness proliferation range of the bacteria (bacteria size typically 1-2  $\mu\text{m}$ ) and thus they cannot attach the textured surface. The regular nano structures with controlled roughness, produced by femtosecond laser treatment, allows creating antibacterial surfaces, which is very promising in the biomedical and surgery fields.

### 1.5.5. Femtosecond laser treatments on metallic glass

As previously mentioned, ultra-short pulse duration laser treatments are very promising to texture amorphous metals because of the limited thermal effects and crystallization growing with a very small laser-material interaction volume. However, to our knowledge, the effect of femtosecond laser processing on BMGs surface properties has not been deeply studied. Laser-BMGs interaction studies were made on several alloy compositions and the ablation thresholds compared with the thresholds for equivalent crystalline metallic alloys<sup>125, 85</sup>. The majority of the studies were focused on the morphologies and their evolution with fluence and number of pulses<sup>88,17,89</sup>.

By studying femtosecond laser ablation on CuZr<sub>2</sub> metallic glass, Marinier *et al.*<sup>125</sup> observed that the weaker electron-phonon coupling due to amorphous state have the effect of increasing the material ablation threshold compared to crystalline CuZr<sub>2</sub> from  $0.47 \pm 0.10$  J/cm<sup>2</sup> to  $0.51 \pm 0.10$  J/cm<sup>2</sup>. Moreover the melting depth in metallic glass ( $\approx 70$  nm for  $F = 1000$  J/cm<sup>2</sup>) was found to be higher than its crystalline counterpart ( $\approx 60$  nm for  $F = 1000$  J/cm<sup>2</sup>) partially because of the lower melting temperature. LIPSS formation on Zr-based BMG has been studied by Li *et al.*<sup>126</sup> and they indicate that the initial roughness of the surface play a significant role in LSFLs appearance. Indeed, as observed in crystalline metallic alloys, laser/surface interferences promoting LIPSS formation are enhanced by the excitation of localized surface plasmons (LSPs) around surface defects on the metallic glass.

Dold *et al.* realized a deep study on surface structuring of Zr-based metallic glass using femtosecond laser pulses<sup>17</sup>. They used a Yb:Glass femtosecond laser with a pulse duration of 410 fs and a radiation wavelength of 1030 nm. By varying the fluence from 0.103 to 0.206 J/cm<sup>2</sup>, different surface morphologies were created and presented in Figure 1.5.21. The average roughness  $R_a$  of these morphologies were between 0.1  $\mu\text{m}$  to 0.25  $\mu\text{m}$  for 0.103 to 0.206 J/cm<sup>2</sup> treatments respectively.

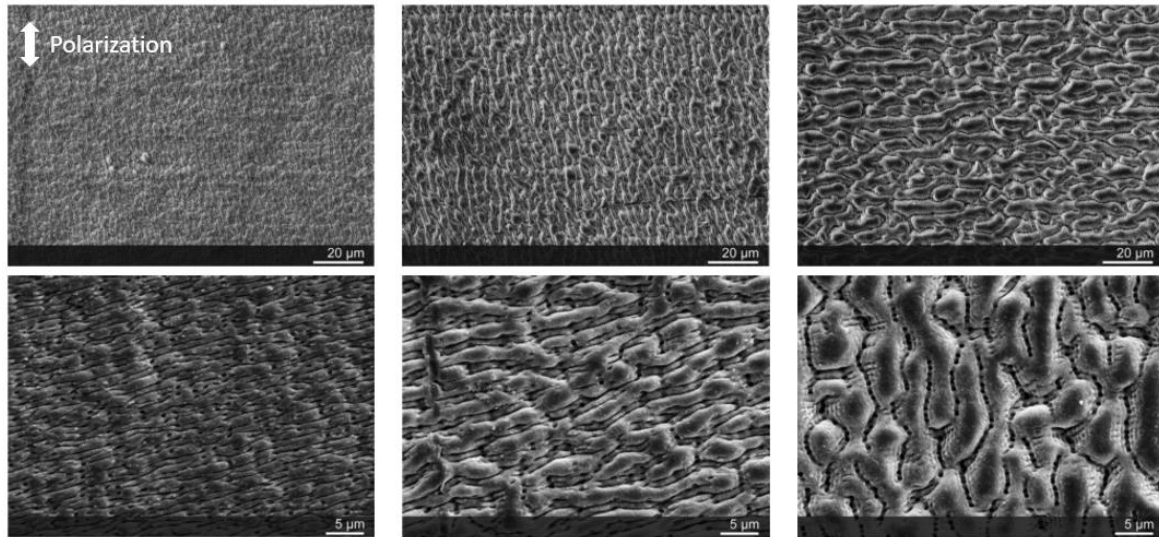


Figure 1.5.21: SEM image of  $Zr_{62.5}Cu_{22.5}Fe_5Al_{10}$  (at. %) BMG after fs laser treatment of pulse width  $\tau = 410$  fs and increasing fluence  $F$  from  $0.103 \text{ J/cm}^2$  (upper left) to  $0.206 \text{ J/cm}^2$  (bottom right), adapted from<sup>17</sup>.

To compare the surface modifications obtained with femtosecond lasers with other pulse duration lasers, they textured the same amorphous alloy with nanosecond and picosecond pulse duration lasers. As presented in Figure 1.5.22, the as-cast and the specimens treated with 410 fs pulses shows diffractograms typical of the amorphous material, while the diffractograms of the specimen tested with 12 ps and 125 ns pulse duration lasers exhibit narrow pics resulting from crystalline phases that formed during laser processing.

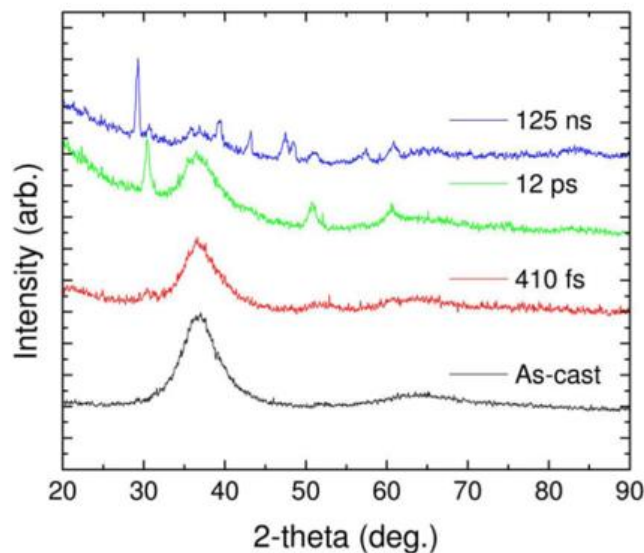


Figure 1.5.22: XRD analysis of polished and treated sample with different pulse-widths of 410 fs, 12 ps and 125 ns<sup>17</sup>.

The authors concluded that femtosecond laser treatments allow creating multiple morphologies on BMG surfaces with a wide range of surface roughness. Contrary to longer pulse duration lasers in picosecond or nanosecond ranges, despite some pics of very low intensity compared

to pico and nanosecond diffractograms, the amorphous structure is mainly preserved. The effect of surface texturing by femtosecond lasers on the mechanical properties of BMGs has been mostly studied on Zr-based alloys. Several researches showed that laser surface treatment on BMG allows increasing the plastic domain in compression. An example of the effect of laser treatment on Zr-BMG is presented in Figure 1.5.23. The effect of the processing is to increase multiple shear band activation during compression which is positive for plastic deformation of metallic glasses<sup>127,128</sup>.

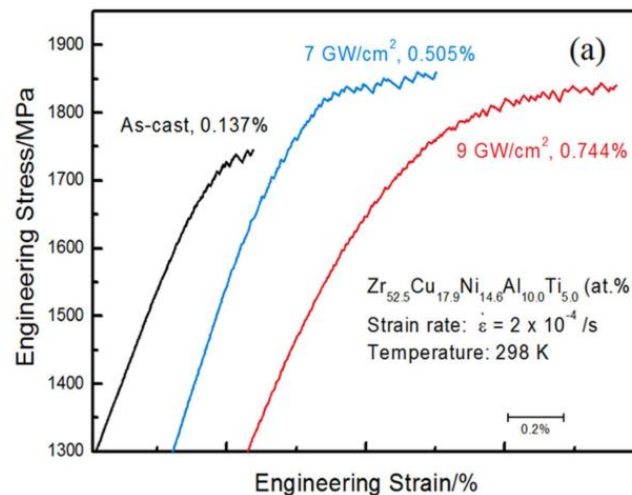


Figure 1.5.23: Compression testing results for as-cast and laser-treated BMG samples, from Cao *et al.*<sup>129</sup>

## 1.6. Thermoforming of bulk metallic glasses

### 1.6.1. A specific process for amorphous metals

Metallic glasses are metastable materials. Their amorphous structure gives them unique physical properties as explained before. Despite their high elastic strength at ambient temperature, they conserve thermal<sup>130</sup>, optical<sup>131</sup> and electrical<sup>132</sup> properties of crystalline metallic alloys due to metallic bonding. As it has been developed in the section 1.2, one of the major specificity of amorphous metallic alloys is that they exhibit a viscous domain at much lower temperature than their melting temperature  $T_m$ . Glass transition temperature  $T_g$ , similar to polymers, allows their utilization in thermoplastic deformation processes. Surface texturing by thermoforming allows the replication of accurate and complex structures at micro or nano scale, opening the gate to the biomimetism of naturally observed surface behaviours as lotus effect or gecko foot plant for example. Thanks to metallic glasses, this field has been now opened to metallic materials.

This part of the literature review will be first focused on the rheological properties and flow mechanisms associated with viscous amorphous alloys for thermoforming. Then a non-exhaustive description of the different thermoforming techniques available will be developed to finally describe surface properties modifications that can be induced with thermoformed surface structures. A small part will be also dedicated to the thermomoulding of metallic glass parts with different size-scale and the direct link with industrial application that this field created.

## 1.6.2. Different scales = different behaviours

If theoretical deformation procedures at viscous state are the same between polymers and metallic glass, their thermomechanical properties at  $T > T_g$  are very different. Indeed, at viscous state, metallic glasses compared to polymers exhibit high viscosity ( $\approx 10^8$  Pa.s vs  $\approx 10^5$  Pa.s) and high surface tension ( $\approx 1$  N.m<sup>-1</sup> vs 0.03 N.m<sup>-1</sup>). Consequently, thermoforming of amorphous metals requires high pressures and is very dependent to mould pattern dimensions<sup>133</sup>. Schroers *et al.*<sup>19</sup> developed a law for thermoplastic forming that can be quantified using creeping flow conditions and also capillary contributions. The expression for a cylindrical feature is given by:

$$P = \frac{32\eta}{t} \left(\frac{l}{d}\right)^2 - \frac{4\gamma\cos\theta}{d} \quad (1.9)$$

where  $P$  is the applied pressure,  $\eta$  is the metallic glass viscosity,  $t$  the moulding time required,  $l$  the length,  $d$  the diameter of the cylindrical feature,  $\gamma$  the surface tension and  $\theta$  the dynamic contact angle between the viscous metallic glass and the mould. Depending on this equation, Hasan *et al.*<sup>133</sup> created a plot of the required pressure to emboss different type of  $l/d$  ratios from nanometre to millimetre size of features considering a viscosity of  $10^7$  Pa.s, a surface tension of  $1$  N.m<sup>-1</sup>, a wetting angle of  $180^\circ$  and a moulding time of  $100$  s. This plot is presented in Figure 1.6.1.a).

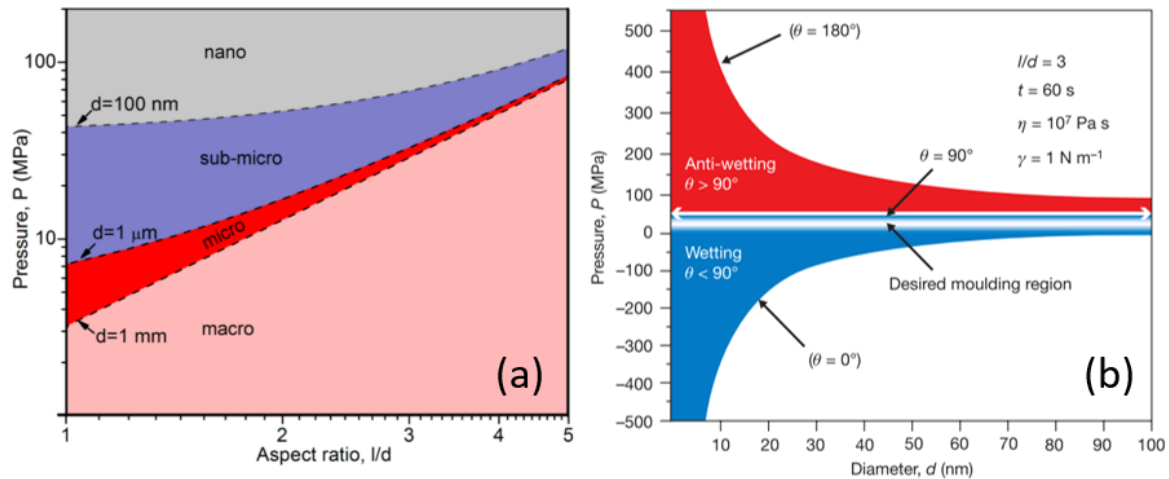


Figure 1.6.1: Required pressure for thermoforming of cylindrical features for different aspect ratios<sup>133</sup>(a), required pressure to fill a channel with a diameter  $d$  and an aspect ratio  $l/d = 3$  for both wetting and anti-wetting conditions with a viscous fluid<sup>134</sup>(b).

This thesis work is focused on thermoforming of both micronic and submicronic structures, and Kumar *et al.*<sup>134</sup> found that different moulding regimes are involved depending on the size and the aspect ratio of the features. In fact, while for low-aspect  $l/d$  ratios ( $\sim 1-3$ ) and large dimensions, the moulding regime is mostly controlled by the amorphous metal viscosity in the supercooled liquid region and follows the Hagen-Poiseuille's law. When the lateral dimension reaches values smaller than  $1\mu\text{m}$ , the moulding regime is then controlled by capillary forces and creeping flow contributions<sup>134</sup>.

Authors then calculated the required pressure to fill a nanometric channel feature with a diameter less than  $100\text{ nm}$  with a  $l/d$  ratio of  $3$  in wetting ( $\theta > 90^\circ$ ) and anti-wetting ( $\theta < 90^\circ$ ) conditions (Figure 1.6.1.b). Despite the fact that in complete wetting condition ( $\theta = 0^\circ$ ) the viscous metallic glass will fill the mould spontaneously, a partial wetting allows a better control of the thermoforming process where the optimal range found by Kumar *et al.* is indicated as the “desired moulding region” in Figure 1.6.1.b.

Since the discovery of metallic glass alloys with low viscosities in a large supercooled liquid region (SLR), thermoforming of BMG's has been deeply studied by many research groups. Because of the huge range of possible compositions in amorphous alloys elaboration, viscosity of BMGs in SLR can vary from  $10^{13}\text{ Pa/s}$  to  $10^6\text{ Pa/s}$  with a large range of glass transition temperatures from  $128^\circ\text{C}$  for  $\text{Au}_{49}\text{Ag}_{5.5}\text{Pd}_{2.3}\text{Cu}_{26.9}\text{Si}_{16.3}$ <sup>135</sup> to more than  $630^\circ\text{C}$  for  $\text{Co}_{43}\text{Fe}_{20}\text{Ta}_{5.5}\text{B}_{31.5}$ .

More recently, Li *et al.*<sup>136,137</sup> studied hot deformation of Zr-based metallic glass ( $\text{Zr}_{35}\text{Ti}_{30}\text{Be}_{26.75}\text{Cu}_{8.25}$ ) and created a map of the filling capacity of microchannel features as a

function of the strain rates and the processing temperatures in the SLR. They found that inhomogeneous, non-Newtonian and Newtonian flow regimes quantitatively correspond to non-filled, partially filled and fully filled Si-mould, respectively. By adapting Schroers formula for a cylindrical feature described above<sup>138</sup> (equation 1.9), considering the laminar behaviour of the flow during the thermoforming experiment that obeys the Hagen-Poiseuille Law, the maximum filling length  $L_{max}$  in a micrometric channel can be calculated as:

$$L_{max} = d \sqrt{\frac{P_{BMG}}{6\eta}} t \quad (1.10)$$

where  $d$  is the wide of the channel,  $P_{BMG}$  is the pressure required to move the liquid amorphous alloy of a viscosity  $\eta$  and  $t$  the compression time.

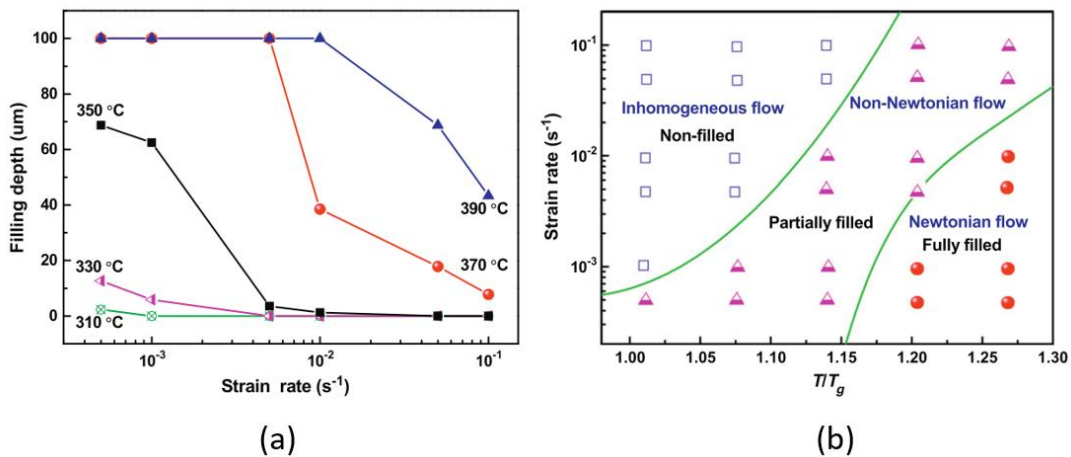


Figure 1.6.2 : Thermomoulding filling depth of metallic glass at various strain rate and temperature in a 50µm width and 100µm depth Si mould (a), flow regimes map of  $Zr_{35}Ti_{30}Be_{26.75}Cu_{8.25}$  amorphous alloy with respective filling results (b).

Consequently, by selecting adapted temperature and strain rate parameters for a selected composition and maintaining Newtonian flow regime for micron size features, multiples micro-pieces and surface structures have been realized with metallic glass using thermomoulding technique. The most extensive study about hot deformation of BMGs and replication capabilities has been realized by the team of Pr. Schroers from Yale University. Their work allowed to develop processes to mould a large range of structures at different scales: from pyramidal patterns of around 250 µm size (Figure 1.6.3.a) to nanorods of 100 nm in diameter by considering capillary flows (Figure 1.6.3.b).

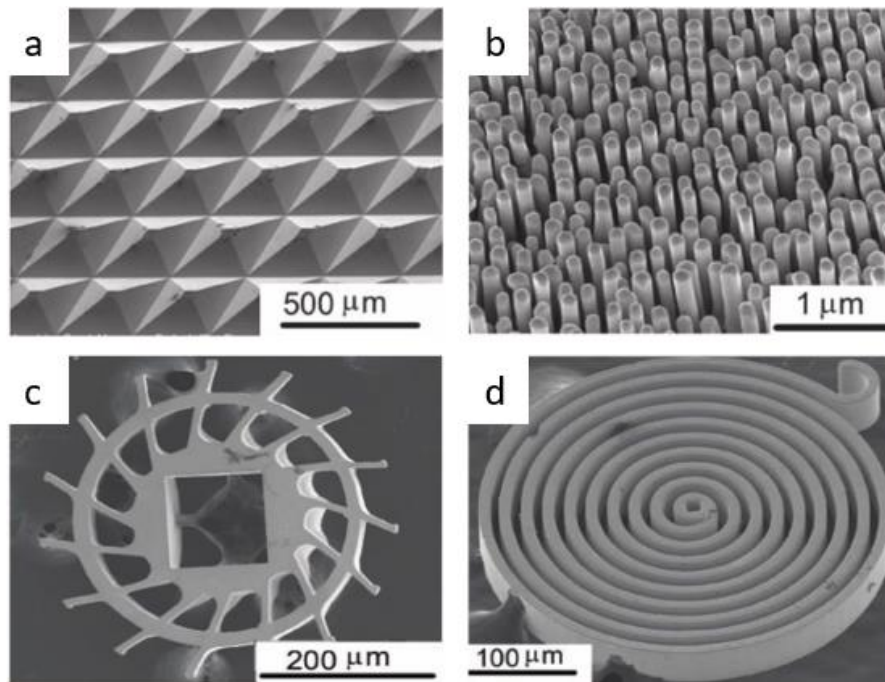


Figure 1.6.3 : Thermoplastically formed  $Pt_{57.5}Cu_{14.7}Ni_{5.3}P_{22.5}$  amorphous alloy at  $270^{\circ}C$  under 15MPa during 90s with pyramidal pattern (a) and nanorods pattern (b). Micro gear (c) and micro spring (d) fabricated by micro-moulding using  $Zr_{35}Ti_{30}Cu_{8.25}Be_{26.75}$  amorphous alloy. Adapted from<sup>19</sup>.

Using thermomoulding technique also allows to create 3D micro components with complex shapes. By controlling processing time and flow stress to avoid crystallization occurrence, it is possible to replicate bulk pieces combining good dimensional accuracy with the high-strength of the amorphous metal. Indeed, because of viscous state in the SLR and very small shrinkage during cooling, pattern replication can be extremely accurate<sup>19</sup>. Surface quality and thermomechanical properties of moulds are then important factors in thermomoulding processing techniques. Compared to Au and Pt-based metallic glasses, Zr-based bulk metallic glasses, due to their high glass transition temperature between  $350^{\circ}C$  and  $420^{\circ}C$  requires mould materials that withstand mechanical stresses at high temperatures. The most commonly used material for hot embossing Zr-based BMG is silicon. Indeed, generally used in microelectronic industry, silicon allows to create accurate patterns at micro and nano scale by photolithography technique with sufficient mechanical resistance and very good surface finishing.

BMGs sensitivity to oxidation in air during thermoforming processing ( $T > T_g$ ) typically in the SLR region, can strongly vary as a function of the amorphous alloy composition. Indeed, major elements usually rule the oxidation resistance of the metallic glass. For example, adding oxidation resistance to a low glass transition temperature make Pt-based alloys good candidates to thermoplastic forming (TPF) in air (TPF <  $300^{\circ}C$  for  $Pt_{57.3}Cu_{14.6}Ni_{5.3}P_{22.8}$  without oxidation in air environment). In comparison, Zr-based metallic glasses, with higher glass transition

temperatures, are less resistant to oxidation during TPF processing and so may need a protective atmosphere to be thermoformed without the appearance of an oxide layer on their surface.

### 1.6.3. Oxidation induced by thermoplastic forming processing

As previously said, most of thermoplastic forming experimentations on bulk metallic glasses have been realized with alloys presenting very good oxidation resistance and low glass transition temperatures such as Pt-based, Au-based or Pd-based amorphous alloys. However, utilization of noble metal-based composition induces very high production costs and so limited commercialising possibilities. In this context, using lower cost Zr-based bulk metallic glasses presenting high mechanical resistance and for some biocompatibility (Ni-free and Be-free) open a wider range of applications in industry. However, Zr-based BMG exhibit poor oxidation resistance in the SLR region at  $T > T_g$  and they rapidly form  $ZrO_2$  layer and copper precipitation on their surfaces during air-processing<sup>139</sup>. In this way, TPF processing of this alloys type requires protective atmosphere or high vacuum environment to prevent oxidation. Very recently, Eckert *et al.* realized surface thermoforming of Ni-free Zr-based BMG ( $Zr_{48}Cu_{36}Al_8Ag_8$ ) in view of biomedical applications<sup>140</sup>. Deep analysis of thermomechanical, structural and thermophysical properties allow to define crystallization incubation times as well as best processing parameters (temperature, pressure, time etc...) to reproduce micron-size pyramidal pattern on its surface by TPF technique (Figure 1.6.4).

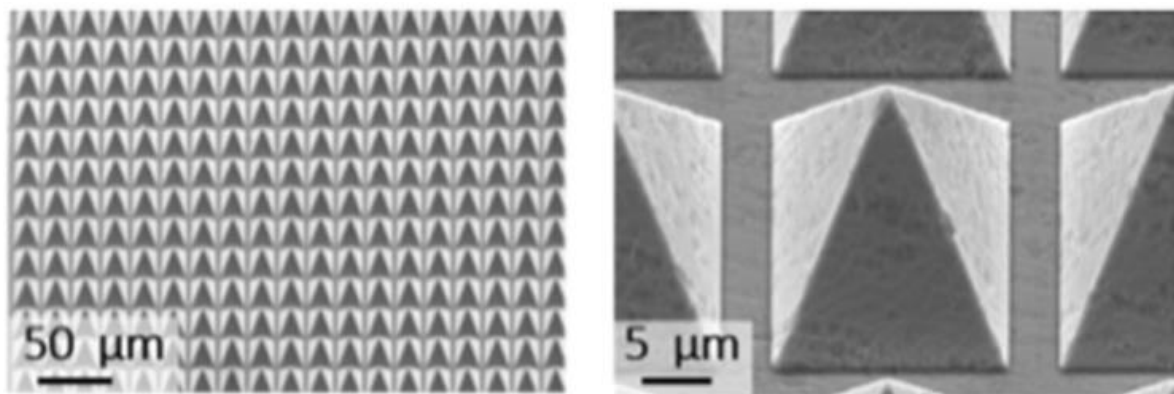


Figure 1.6.4: SEM images of the pyramidal pattern thermoplastically formed on  $Zr_{48}Cu_{36}Al_8Ag_8$  BMG surface, adapted from<sup>140</sup>.

Despite TPF realization under high vacuum ( $4 \times 10^{-4}$  mbar), a strong presence of tetragonal and monoclinic  $ZrO_2$  on irregular patches on thermoformed pyramids has been observed by EDS and XRD measurements. Zirconium oxidation also introduced a copper enrichment in the

glassy phase surface of the pyramidal pattern (Figure 1.6.5). This results indicated that even in protective conditions from oxygen contamination, TPF processing of  $Zr_{48}Cu_{36}Al_8Ag_8$  promoted surface oxidation. However, as said by the authors, zirconia can enhanced tissue interaction and cell adhesion and so it is not necessary to eliminate this oxide layer, but it might also have a significant effect on corrosion resistance of the alloy due composition heterogeneity on textured sample surface which is known to be negative for the passive layer stability of Zr-based BMGs.

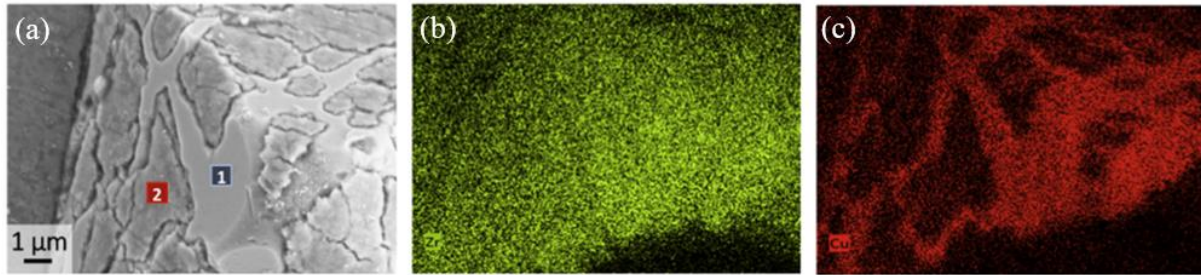


Figure 1.6.5: SEM image (a) and EDX compositional distribution mapping of the SEM image for Zr (b) and Cu (c) elements, adapted from<sup>140</sup>.

#### 1.6.4. Surface functionalization using thermoforming capacity of bulk metallic glass

We have seen in the last section that the existence of the supercooled liquid region (SLR) above the glass transition temperature  $T_g$ , where the amorphous alloy is at viscous state, allows to use them in thermoforming processes to produce multiple pattern size and shape on their surfaces. Obviously, controlling pattern shape, size and period allows to modify surface properties and so is a way to functionalize their surfaces. As for femtosecond laser treatments, wettability control and cellular adhesion of thermoplastically formed BMGs surfaces has been mostly studied. In addition to the creation of TPF ability map of Zr-base metallic glass, Li *et al.*<sup>141</sup> used thermoforming processing to pattern hierarchical structures on  $Zr_{35}Ti_{30}Be_{26.75}Cu_{8.25}$  metallic glass surface using silicon moulds. They used a honeycomb Si mould to pattern BMG surface (Figure 1.6.6(left)) with different pitch ranging from 35.5 μm to 600 μm with a thickness of 8 μm and studied the size effect on wettability properties. Li *et al.* also added a chemical etching step (5s in 10% HF solution) on the patterned BMG to see the effect of dual-scale roughness on wettability properties. The average contact angle  $C_a$  was calculated to be around 83° for non-patterned BMG surface.

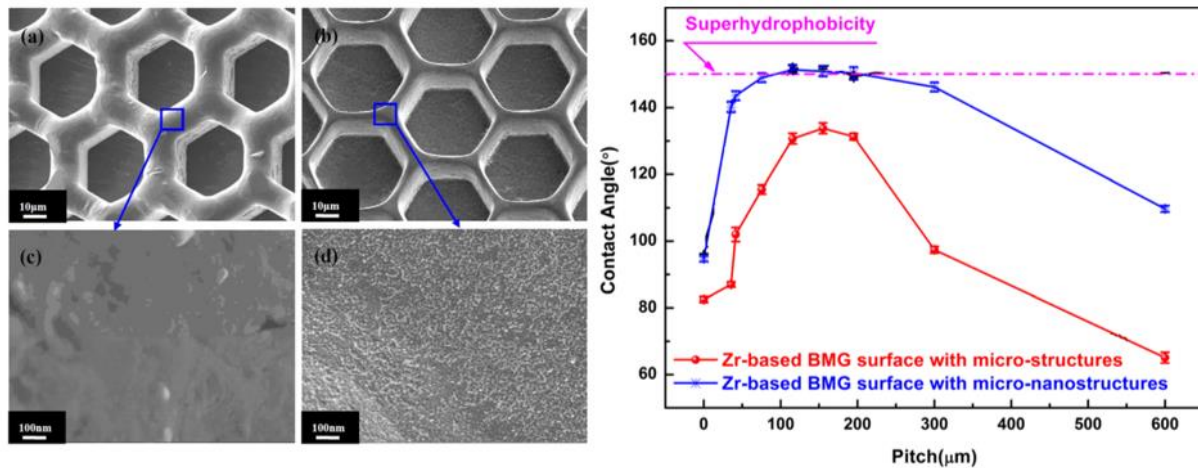


Figure 1.6.6 : Left: honeycomb pattern on BMG surface before chemical etching (a), associated surface condition on honeycomb peaks (b), and honeycomb pattern after chemical etching (c) and associated surface condition (c). Right: Contact angle measurements as a function of honeycomb pitch for non-etched patterned surface (micro-structure) and etched patterned surface, adapted from<sup>141</sup>.

As seen in Figure 1.6.6 (right), for chemically etched and honeycomb patterned alloys (from 75 μm to 200 μm pitch), BMG surface exhibited super-hydrophobicity behaviour ( $C_a \approx 150^\circ$ ) with strong adhesion compared to non-etched textured surface that reached a maximum contact angle of  $132^\circ$  for 155 μm pitch. Indeed, as seen in Figure 1.6.6.d, chemical etching introduced a second scale of texture, consisting of nano-protrusions on the surface. The etched surface present also strong adhesion, due to the pillar-like nano-structure. Authors concluded that, while micron-size pattern with specific shape can create classical Cassie-Baxter effect with an hydrophobic behaviour ( $C_a \approx 132^\circ$ ), adding a second scale of texture as nano-pillars allow to increase even more the contact angle with a strong adhesion force, resulting then from a multiscale Wenzel-Cassie-Baxter effect and so a super-hydrophobic behaviour.

As previously presented, biocompatibility and cellular adherence properties of metallic surfaces can be modified with femtosecond laser treatment by controlling roughness and microstructure. This surface functionalization for biomedical application has been also studied with thermoplastic forming process in an extensive work of Padmanabhan et al<sup>142</sup>. They created surface structures on Pt-base BMG ( $Pt_{57.5}Cu_{14.7}Ni_{5.3}P_{22.5}$ ) by TPF, consisting of arrays of nanorods with diameters varying from 60 nm to 250 nm, with porous alumina as mould. Different types of cells consisting of fibroblasts, macrophages and endothelial cells were then seeded on flat and textured BMG surfaces during 24h. Results showed that the variation nanorods sizes modified cells morphologies.

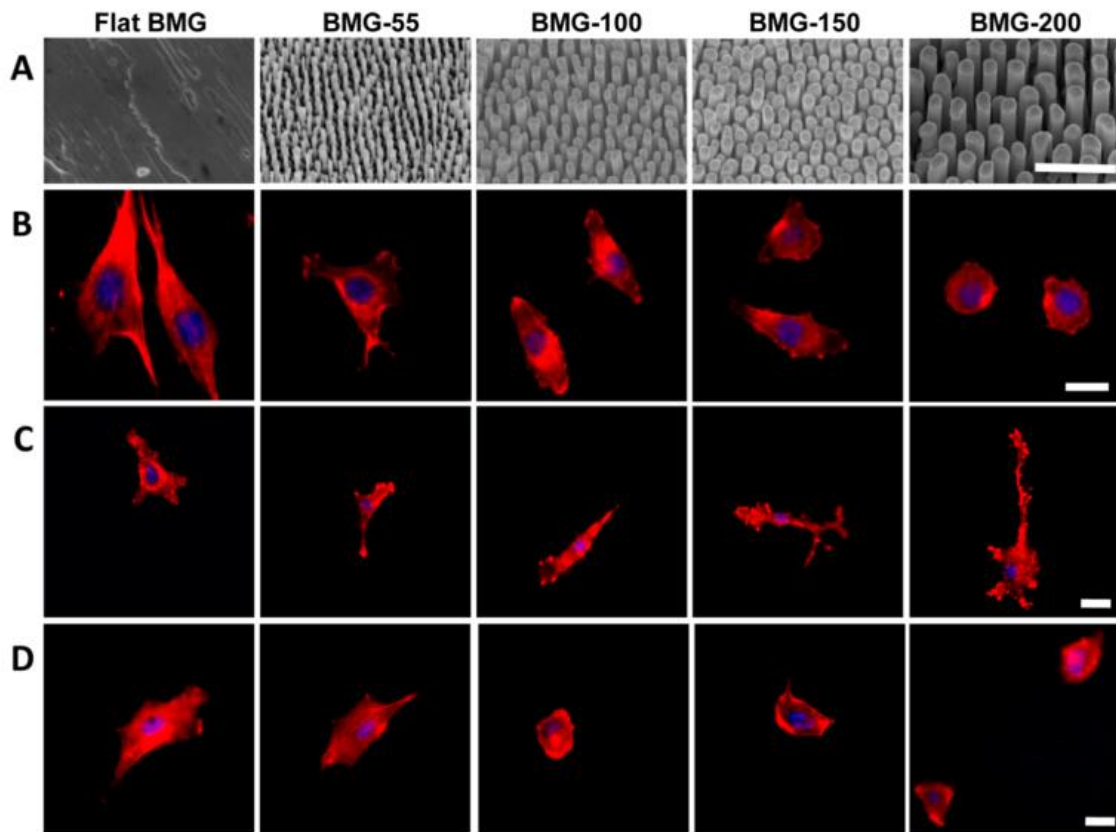


Figure 1.6.7: Corresponded cellular morphology as a function of nanorods diameter textured surface for fibroblast (B), bone derived macrophage (C) and endothelial cell (D). Actine part and nucleus part of the cells are respectively in red and blue colour. Scale bars, 1  $\mu\text{m}$  (A) and 20  $\mu\text{m}$  (B,C,D), from<sup>142</sup>.

As presented in Figure 1.6.7, increasing nanorods diameter makes fibroblast increasingly more circular, less elongated and smaller. As seen for alloys treated by femtosecond laser, TPF technique on amorphous metals make possible a selective influence on cellular morphology, opening the way towards designing cell-instructive patterns adapted from different types of morphologies promoting specific cellular proliferation. Moreover, TPF is a thermomechanical process where temperatures in the super-cooled liquid region are much lower than temperature reached during laser illumination. Thus, for this particular BMG alloy presenting very good oxidation resistance in the SLR, no chemical surface modification on patterned samples are observed and so it is possible to estimate the effect of TPF on surface properties as only topographic effect.

## 1.7. Conclusion

This bibliographic chapter has been dedicated to the main aspects that have been used in this thesis work. First, intrinsic characteristic properties of bulk metallic glasses has been presented. Then, femtosecond laser functioning, laser-material interaction and its effect on bulk metallic glass surface properties has been discussed. Finally, the last surface processing method called thermoplastic forming (TPF) has been presented and its possible effect on surface properties has been also reported. The main points coming from this chapter are the following:

1. Bulk metallic glasses possess a metastable amorphous structure conferring exceptional mechanical properties at low and high temperatures. Depending on their composition, they are characterized among others by a glass transition temperature  $T_g$  and a critical diameter  $D_c$ . At  $T > T_g$ , in the SLR, the structure will naturally tends to minimize its energy and so will start to crystallize after a given time.
2. At temperatures higher than  $T_g$ , bulk metallic glass also exhibit different deformation behaviours, passing from inhomogeneous to completely homogeneous flow regime due to its viscous state. At a given temperature, BMGs flow regime is dependent of the strain rate, making the control of processing parameters very important.
3. Zr-based BMGs naturally form a passive/protective oxide film, making them generally much more resistant to corrosion than their crystalline counterparts but also susceptible to pitting corrosion mechanism. Different parameters can modify their corrosion behaviour, such as copper content, minor element addition or surface finishing.
4. Femtosecond laser due to its complex optical architecture, allows to apply high energy pulses on ultrashort time scale with a negligible thermal effect on the non-irradiated areas. Due to this ultrafast pulse duration, femtosecond laser induces unique thermo-mechanical ablation phenomenon. While longer laser pulse duration induce crystal growth, femtosecond laser pulse allows to maintain the amorphous structure on bulk metallic glass surface.
5. Laser surface treatments on metallic surface allow to create a large range of textures with different roughness. This laser-induced morphologies can strongly affect surface properties such as wettability or cellular adhesion. Despite its valuable effect on amorphous material, chemical surface modifications has been also observed on fs-textured crystalline and glassy alloy surfaces, which can play also a significant role on the related surface properties.

6. By using its viscous flow behaviour in the supercooled liquid region, it is possible to pattern bulk metallic glass surfaces by thermoplastic forming processing (TPF). Metallic glass exhibit a very low shrinkage compared to crystalline alloys and between nanorods and micron-size pyramidal shape, there is no size limitation due to their amorphous structure. Processing time available at  $T > T_g$  is limited by the crystallization time at a given temperature, and so have to be previously determined.
7. Depending the strain rate and the temperature, Newtonian and Non-Newtonian (shear-thinning) flow regimes can be reached. To accurately control the process, the Newtonian regime has to be kept. Depending the size of the feature to mould, different forces are involved: as the flow regime is considered as laminar, nanometric cavity filling has to consider capillary forces, while micrometric and higher cavity filling are mostly related to Hagen-Poiseuille law.
8. As for femtosecond laser surface treatment, TPF processing allows to modify surface properties such as wettability or cellular interaction by mostly topological effects. Major differences between this two processing techniques is that no major chemical modification is expected on stable BMGs during thermoforming process due to its mechanical deformation principle at relatively low temperature. In contrary, fs-laser treatment will probably induce oxidation due to the really high temperature that can be reached on material surface. TPF allows a narrow control of the pattern shape to build very well organized surface texture with a high symmetry whereas laser treatment textures are inhomogeneous at small scale and governed by laser-material interaction phenomenon.

# CHAPTER 2

## Experimental methods

This chapter is dedicated to the experimental techniques that have been used in this thesis work from the elaboration of BMGs to the characterization of textured surface properties. This chapter is divided in four major parts: the elaboration of BMGs (section 2.1), the surface patterning techniques used (section 2.3 and 2.4), the topological, chemical and thermal characterization methods employed to analyse textured and non-textured samples (section 2.2, section 2.5 and 2.6) and finally the characterization of surface properties (section 2.7).

### 2.1. Elaboration of Zr-based bulk metallic glasses

In this thesis work, 3 different metallic glasses were studied. A  $Zr_{65}Cu_{15}Al_{10}Ni_{10}$  (**Zr3**) alloy, characterized by its low viscosity in the supercooled liquid region (SLR) at  $T_x > T > T_g$  making him a promising candidate for thermoplastic forming processing (TPF). A  $Zr_{57}Cu_{20}Al_{10}Ni_8Ti_5$  (**ZrC**) alloy, with the addition of 5 at.% of titanium gives higher thermal stability and better mechanical properties compared to Zr3 amorphous alloy. Finally, a third alloy  $Zr_{48}Cu_{36}Al_8Ag_8$  (**Cu2**) was chosen for its Ni-free composition and presence of 8 at.% Ag, making him potential alloy for biomedical applications. A summary of the different compositions with their respective critical diameters is presented in Table 2.1.

<b>BMG</b>	<b>Zr</b> (at. %)	<b>Cu</b> (at. %)	<b>Al</b> (at. %)	<b>Ni</b> (at. %)	<b>Ti</b> (at. %)	<b>Ag</b> (at. %)	<b>D<sub>c</sub></b> (mm) <sup>143</sup>
Zr3	65	15	10	10			6 -7
ZrC	57	20	10	8	5		10
Cu2	48	36	8			8	25

Table 2.1 : Compositions and critical diameters of the three amorphous alloys studied, compositions are given in at.%.

To elaborate these 3 amorphous alloys presenting large glass forming abilities (GFA) allowing low cooling rates, the Arc Melting casting process has been used. Zr-based metallic glasses elaboration was conducted in the GPM2 group of the SIMaP Laboratory in Grenoble and the procedure can be divided in three major steps:

## Chapter 2: Experimental methods

- **Metal preparation:** raw metallic elements Zr, Cu, Al, Ni, Ti and Ag with high purity (99.99 %) were weighed regarding the alloy stoichiometry with an error tolerance of 0.05 at.% on each elements. According to mould sizes, 15 g to 25 g of materials were needed for each elaborations.
- **Pre-alloying:** Weighed metals were put together in the Arc-Melting device (Figure 2.1.1) on a water-cooled copper support. Vacuum of about  $5 \times 10^{-5}$  mbar were done using primary and turbo-molecular pump set-up and at least one high-purity argon purge were realized. Prior to the melting of raw metals together, a Ti-gettered argon atmosphere were injected in the chamber. Pre-alloying of the overall metallic elements were then conducted with Tungsten Inert Gas (TIG) arc at relatively low intensity (90 to 110 A). Then, successive heating and cooling cycles has been done while turning over the material to ensure a good homogeneity of the overall elements in the pre-alloy.
- **Pre-alloy injection:**

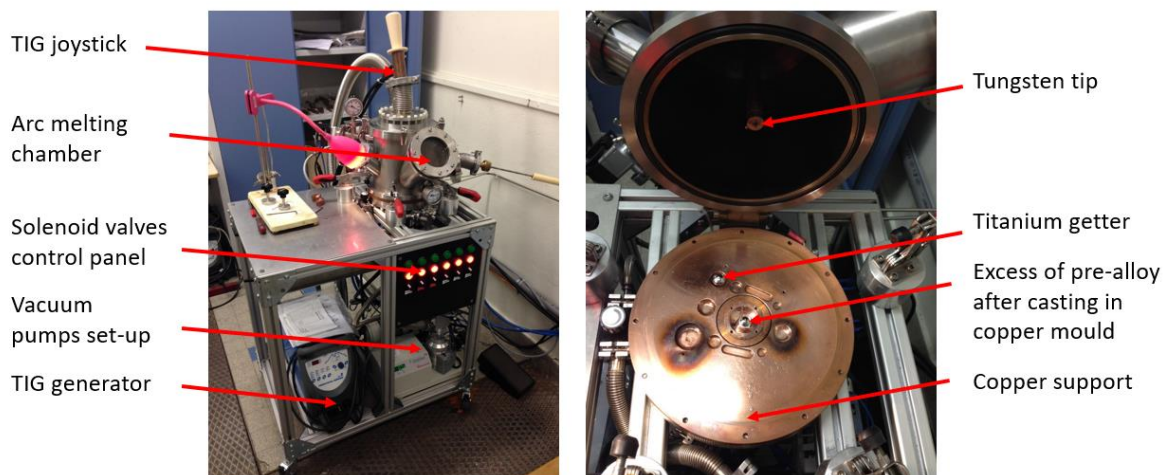


Figure 2.1.1: Overall picture of the arc-melting device used to elaborate Zr-base metallic glass (left), zoom on the copper support where pre-alloying and liquid metal suction were made (right).

After homogenisation, the pre-alloy was placed above the mould at the centre of the arc melting chamber. While heating it at the liquid state, a pressure differential between the main chamber and the tank below the mould allow to cast it in less than 1 second in the water-cooled copper mould below. At this stage, if the mould imprint is not bigger than the critical diameter of the alloy, a bulk metallic glass is elaborated.

Different types of moulds were available: from a conic shape that enable to evaluate the critical diameter of a new composition, to cylindrical or rectangular moulds to elaborate samples for characterisation or surface texturing. A picture of a  $Zr_{65}Cu_{15}Al_{10}Ni_{10}$  (Zr3) bulk metallic glass

elaborated with parallelepiped and cylindrical moulds is presented in Figure 2.1.2. For the three amorphous alloys (Zr3, ZrC and Cu2), the mould that was mostly used to a 52 x 12 x 2 mm<sup>3</sup> rectangular mould and a 3mm in diameter and 80mm in length cylindrical mould.



Figure 2.1.2: Zr<sub>65</sub>Cu<sub>15</sub>Al<sub>10</sub>Ni<sub>10</sub> BMG casted in plate and cylindrical shape and the exceeding material removed on the left.

## 2.2. Rheological and thermal characterisation of Zr<sub>65</sub>Cu<sub>15</sub>Al<sub>10</sub>Ni<sub>10</sub> bulk metallic glass

### Strain rate jump tests

As explained in the Chapter 1, rheological behaviour of bulk metallic glass at high temperature ( $T > T_g$ ) is very different compared to the behaviour at ambient temperature. Their homogeneous deformation is viscoplastic and so allow forming their surfaces with a patterned mould. Before thermoforming process, it is necessary to know their viscosity values for different range of temperatures and strain rates. In thermoplastic forming experiments, the Newtonian deformation domain at viscous state will be maintained to ensure a good control of the filling rate in the moulds. Amongst the three bulk metallic glasses studied in this work, the Zr<sub>65</sub>Cu<sub>15</sub>Al<sub>10</sub>Ni<sub>10</sub> alloy is the one that present the lowest viscosity compared to Zr<sub>57</sub>Cu<sub>20</sub>Al<sub>10</sub>Ni<sub>8</sub>Ti<sub>5</sub> and Zr<sub>48</sub>Cu<sub>36</sub>Al<sub>8</sub>Ag<sub>8</sub> for a given temperature from  $T_g$  in the SLR. It also presents good thermal stability in the SLR region as it will be developed in Chapter 3. Because of its “easier to deform” characteristic, it is the most interesting alloy for thermoplastic forming process and the one that will be used in this thesis work.

To study its rheological behaviour and to determine the different deformation behaviour domains, strain rate jump tests in compression in the viscous domain of the amorphous alloy has been done with a MTS4M compression machine. Cylinders of Zr<sub>65</sub>Cu<sub>15</sub>Al<sub>10</sub>Ni<sub>10</sub> amorphous

alloy of 3 mm in diameter and 4.5 mm in height were cut to keep an aspect ratio of 1.5. Temperatures from 390°C to 440°C has been used to cover a large range of viscosity. Strain rate jumps tests with a maximum of 5 sequences per samples has been done with strains of 0.2 between each jumps for the 5 sequences tests, which correspond to a total strain of  $\varepsilon = 1$ . The overall strain rates covered were  $2.5 \cdot 10^{-4}$ ,  $5 \cdot 10^{-4}$ ,  $1 \cdot 10^{-3}$ ,  $2.5 \cdot 10^{-3}$ ,  $5 \cdot 10^{-3}$ ,  $1 \cdot 10^{-2}$ ,  $2.5 \cdot 10^{-2}$ ,  $5 \cdot 10^{-2}$ , and  $1 \cdot 10^{-1} \text{ s}^{-1}$ . The heating clamps allowed an accurate control of the temperature with an error of  $\pm 2^\circ\text{C}$ .

### Differential Scanning Calorimetry (DSC)

Differential Scanning Calorimetry (DSC) is a thermal characterisation technique based on thermal flow comparison between an inert reference material and the material of interest. Depending the associated phenomenon, this material undergoes exothermic or endothermic phase transformations. As previously explain in the first chapter, in the case of metallic glass, this measurements allow to determine their characteristic temperatures as glass transition temperature  $T_g$  (endothermic) and crystallization temperature  $T_x$  (exothermic) for different heating rates. Isothermal test in the SLR region also provide the crystallization kinetics for a specific temperature.

Heating of a metallic glass at a temperature higher than  $T_g$  will promote a structural rearrangement where exothermic events will be visible. These events are mostly attributed to material crystallization spreading in the amorphous structure. Isothermal scanning by DSC allows to estimate the crystallization evolution at  $T_x > T > T_g$ . This technique consists of achieving isothermal treatment allowing measurement of the dissipated energy during the experiment (Figure 2.2.1). Then, integration of the curve area compared to time allow to calculate the transformed fraction in the alloy:

$$\text{Transformed fraction} = \frac{A(t)}{A_{tot}}, \quad (1.1)$$

With  $A(t)$  value of the time dependent transformed area and  $A_{tot}$  the total transformation area.

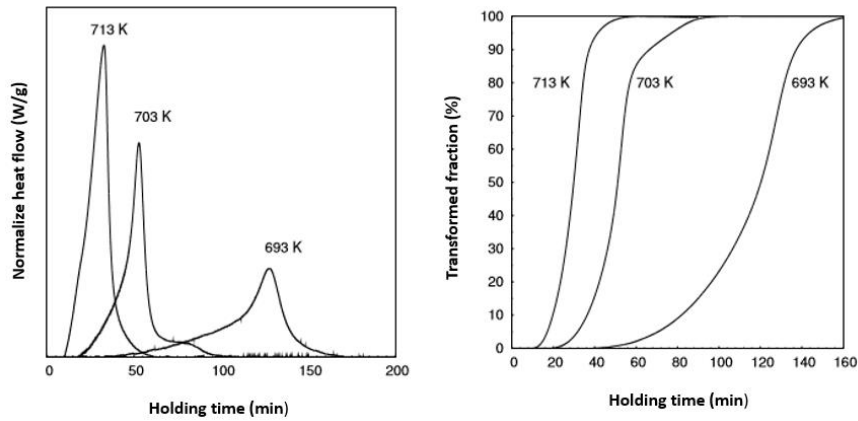


Figure 2.2.1 : Isothermal DSC curves of a  $Zr_{52.5}Cu_{27}Al_{10}Ni_8Ti_{2.5}$  for different temperatures (a). Transformed fractions from the isothermal curves (b)<sup>144</sup>.

Transformed fraction curves allow to estimate crystallization advancement process and to determine different critical times: the crystallization onset time, the percentage (10%, 20%, 95%...) to the complete transformation at 100%. It is then possible to draw a Time-Temperature-Transformation (TTT) diagram to estimate crystallization onset time and transformed fraction after a certain time at temperatures higher than  $T_g$ . These crystallization times are critical values for high temperature processing and have to be well-known in order to maintain material amorphous integrity during thermoforming process.

In this study, the DSC experiments were done with a Perkin-Elmer Diamond DSC. Thermal scans to determine  $T_g$  and  $T_x$  were performed with heating rate of  $40^\circ\text{C}/\text{min}$  up to  $550^\circ\text{C}$ . Isothermal tests to determine the crystallization kinetic were realized with a heating rate of  $200^\circ\text{C}/\text{min}$  up to the desired temperature and then temperature was maintained during 45 min. Amorphous alloy samples of every compositions were prepared from 3mm cylinders with weight of about 50 mg.

## 2.3. Femtosecond laser processing

Surface patterning of bulk metallic glasses was conducted using a femtosecond laser with a optical set-up as described in Figure 2.3.1. By varying laser parameters such as fluence or number of pulses per point of the surface, a wide range of surface structures were produced. Laser surface texturing were made in the Laser Materials Processing Laboratory of the Centre of Physics and Engineering of Advanced Materials (CeFEMA), in the Superior Technical Institute (IST) of Lisbon. The laser used in this thesis work was a s-Pulsed HP model Yb:KYW amplifying medium from Amplitude Systèmes with a chirped-pulse regenerative amplification system. Central wavelength ( $\lambda_{\text{laser}}$ ) of 1030nm and pulse duration ( $\tau_{\text{pulse}}$ ) of about 560 fs (Full

Width at Half Maximum – FWHM) were the intrinsic characteristics of the laser used for surface treatment. This laser system presents high beam quality, high repetition rate and high pulse energy and the as-specified specifications are presented in the Table 2.3-1 below:

S – PULSE HP Model	
Pulse duration	≈ 560 fs
Maximum pulse energy	≈ 1 mJ
Repetition rate	0 to 100 kHz
Central wavelength	1030 nm (NIR)
Laser beam quality	TEM <sub>00</sub>

Table 2.3-1: Specifications of the s-Pulse HP model femtosecond laser system in this work for surface treatments

From the laser beam output, a half-wave plate ( $\lambda/2$ ) was inserted to control the polarization direction of the beam. To manage the average pulse energy deposited, the  $\lambda/2$  plate was associated with a beam splitter in the optical path. Then, a series of mirrors were positioned to carry the laser beam to a 100 mm focal converging lens (L in Figure 2.3.1) with the incidence perpendicular to the specimen surface. Every experiments were conducted around 2 mm behind the focal point to ensure larger spots size and a better control of the deposited energy.

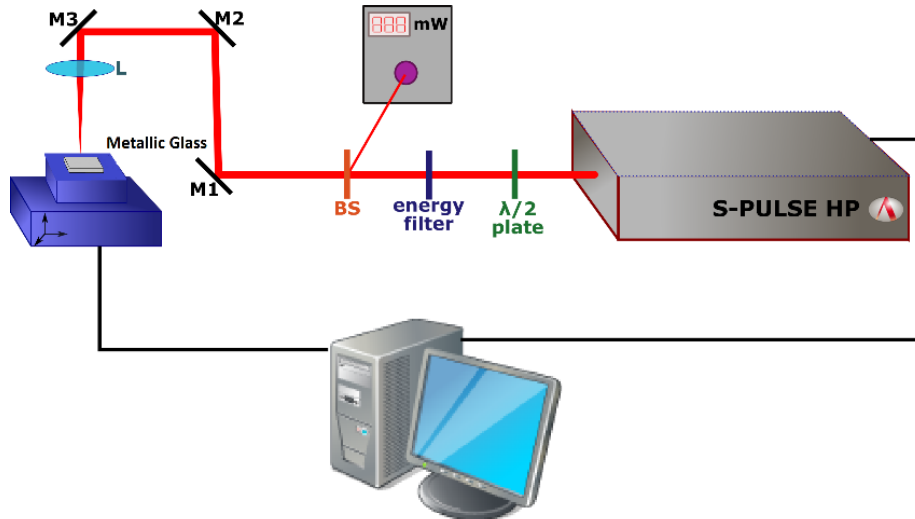


Figure 2.3.1: Schematic diagram of the femtosecond laser irradiation setup, adapted from<sup>60</sup>.

Pulse energies and pulse repetition rates used to process bulk metallic glass surfaces were between 50 to 800  $\mu\text{J}$  and 50 to 400 Hz respectively. The laser beam energy was calculated from the average beam power value using a thermal power-metre (Ophir Photonics model 10A-SH-V1.1 RoHS, Israel) positioned at the laser device output and before the converging lens to determine the energy loss of the optical path.

### 2.3.1. Determination of the ablation threshold

To determine the effect of the applied energy variation on the irradiated amorphous surfaces for each pulse durations used, the value of the pulse energy ( $E_p$ ) was calculated by dividing the beam power,  $P$  by the pulse frequency ( $f$ ):

$$E_p = \frac{P}{f}, \quad (2.1)$$

The average fluence ( $\phi_a$ ), i.e, the average energy density and the maximum fluence ( $\phi_0$ ), i.e. the maximum energy density at the spot centre were calculated using the two following equations:

$$\phi_a = \frac{E_p}{\pi\omega_0^2}, \quad (2.2)$$

$$\phi_0 = \frac{2E_p}{\pi\omega_0^2}, \quad (2.3)$$

where  $E_p$  is the average laser pulse energy and  $\omega_0$  the laser spot beam radius at  $e^{-2}$  of the maximum intensity of the Gaussian beam. The power used for sample illumination and so the values of  $E_p$  were measured with the power-metre. An energetic loss in the beam of about 14% after the optical path is observed due to the optical components (mirrors, lens etc...). A background radiation that represent  $\approx 7\%$  of the total power is measured at high voltage. This radiation is due to the low intensity signal at 50 MHz that is amplified every 1 kHz and ensure the mode-locking process. The background radiation do not contribute to ablation. For repetition rates  $\leq 1000$  Hz,  $E_p$  is independent of the pulse frequency and since irradiations were all performed at this rate, the average pulse energy was simply calculated using the following equation:

$$E_p = \frac{P_{corrected}}{1000}, \quad (2.4)$$

The Gaussian beam radius values  $\omega_0$  at the surface of each amorphous alloy compositions were estimated by using the  $D^2$  method proposed by Liu *et al.*<sup>145</sup> This method is the most accepted to determine ablation thresholds of materials. Assuming that the laser beam has a Gaussian energy distribution as presented in Figure 2.3.4, the fluence in a plane perpendicular to the laser beam is given by:

$$\phi_{(r)} = \phi_0 e^{\frac{-2r^2}{\omega_0^2}}, \quad (2.5)$$

where  $r$  is the distance to the spot centre. The ablation threshold fluence  $\phi_{th}$  were then calculated for  $r = D/2$ . It has been demonstrated that the spot diameter ( $D$ ) of a crater created by ablation phenomena with a Gaussian beam radius  $\omega_0$  is related to  $\omega_0$  by the following formula:

$$D^2 = 2\omega_0^2 \ln \frac{\phi_0}{\phi_{th}}, \quad (2.6)$$

Since  $\omega_0$  increases linearly with  $E_p$ , (eq. 2.2),  $\omega_0$  can be estimated from a plot of the square of the average crater diameter ( $D^2$ ) versus the logarithm of the pulse energy ( $\ln(E_p)$ ). At last, a linear fitting of the slope obtained allow to calculate  $\omega_0$  as follows:

$$\omega_0 = \sqrt{\frac{slope}{2}}, \quad (2.7)$$

### 2.3.2. Incubation factor of laser-irradiated materials

The incubation process was discovered in multi-pulse laser-induced damage on metals and semiconductor surfaces with a 10 ns Q-switched 1064 nm wavelength Nd:YAG laser pulse<sup>146,147</sup>. It has been observed that the ablation threshold decreased with increasing number of pulses on the same surface point. This accumulation process was described by Jee *et al.*<sup>146</sup> as an increase of the radiative energy absorption due to an accumulation of defect liked thermal strain-stress energy storage in the material. It has been found that the N-pulse fluence threshold  $F_N$  follow the equation below:

$$F_N = F_1 N^{S-1}, \quad (2.8)$$

where S is the incubation factor and N is the overlapping pulse number. This equation can be written in our case as:

$$\phi_{th}(N) = \phi_{th}(1) \cdot N^{S-1}, \quad (2.9)$$

and:

$$N \cdot \phi_{th}(N) = \phi_{th}(1) \cdot N^S. \quad (2.10)$$

### 2.3.3. Stationary mode processing

To determine ablation thresholds  $\phi_{th}$ , average spot size  $\omega_0$ , incubation factors and appearance thresholds of created structures; multiple craters were produced on the three different amorphous alloy surfaces.

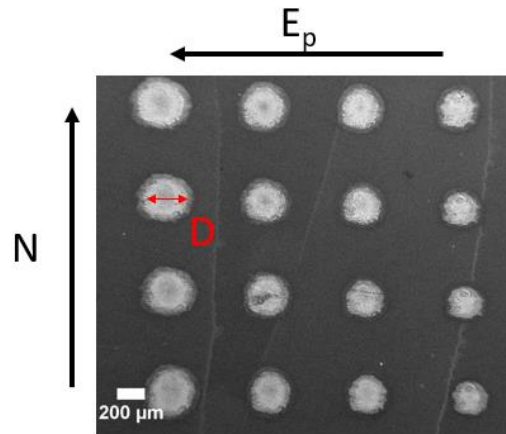


Figure 2.3.2: SEM image of a part of the experiment performed on metallic glass  $Zr_{65}Al_{10}Ni_{10}Cu_{15}$  for the determination of the Gaussian beam radius  $\omega_0$ , the ablation threshold fluence  $\phi_{th}$  and the incubation coefficient  $S$ . Craters of different pulse energy  $E_p$  and number of pulses  $N$  were produced.

STATIONARY MODE	
Average pulse energy ( $E_p$ )	43 – 301 $\mu$ J (Corrected)
Average Fluence ( $\phi_a$ )	0.06 – 0.4 J/cm <sup>2</sup>
Maximum Fluence ( $\phi_0$ )	0.12 – 0.8 J/cm <sup>2</sup>
Repetition rate ( $f$ )	10 Hz
Number of pulses ( $N$ )	2 - 250
Polarisation	Linear s
Processing atmosphere	air

Table 2.3-2 : Laser processing parameters and conditions used for laser spots processing in stationary mode.

Stationary irradiation mode was used to create single craters to study the evolution of the circular features area as a function of the pulse energy and number of pulses  $N$  as presented in Figure 2.3.2. Then, the corresponded maximum fluences  $\phi_0$  and average fluences  $\phi_a$  were determined using eq. 2.2, 2.3 and 2.5. Despite the Gaussian intensity distribution of the laser beam, in this mode every particular point on the spot surface was submitted to a constant fluence with a certain number of pulses. The number of pulses can be described as the product of the repetition rate ( $f$ ) with the exposure time ( $t$ ). Prior to create sequences with precise number of pulses the repetition rate in stationary mode was set at 10 Hz. This illumination mode was used to first study the interaction of femtosecond laser beam with amorphous metal surface and to identify surface features resulted from a particular combination of fluence and number of pulses. In order to obtain a statistical value of  $\omega_0$  using the  $D^2$  method, 72 craters were

produced on each metallic glasses compositions. The average pulse energies and laser pulses number ( $N$ ) ranging from 43 to 310  $\mu\text{J}$  and 1 to 250 respectively. A summary of the laser parameters used in stationary mode is presented in Table 2.3-2. The craters produced were observed using a JEOL JSM-7001F field emission gun scanning electron microscope, and their diameter were measured in 5 different directions for each crater, average diameters were then calculated.

### 2.3.4. Non-stationary mode processing

The non-stationary irradiation mode (scanning mode) was then used to create large surface areas on bulk metallic glasses surface in order to characterize surface properties of the resulted morphologies. The interesting features observed in stationary mode were reproduced in large scale by matching scanning mode parameters with single spot irradiation. A summary of the laser parameters used in non-stationary mode is presented in Table 2.3-3.

NON-STATIONARY MODE	
Average pulse energy ( $E_p$ )	64 – 344 $\mu\text{J}$ (corrected)
Average Fluence ( $\phi_a$ )	0.06 – 0.4 $\text{J}/\text{cm}^2$
Maximum Fluence ( $\phi_0$ )	0.12 – 0.8 $\text{J}/\text{cm}^2$
Repetition rate ( $f$ )	75 to 200 Hz
Scanning speed ( $v$ )	1 mm/s
Number of pulses per surface points	161 - 640
Lateral displacement ( $d_{lat}$ )	0.04 to 0.05 mm
Polarisation	Linear s
Processing atmosphere	air

Table 2.3-3: Laser processing parameters and conditions used for laser spots processing in non-stationary mode.

In this condition, the specimen moved on a XYZ table below the static laser beam with a positioning accuracy higher than  $0.5\mu\text{m}$ . In this mode, by the Gaussian shape of the laser beam energy distribution, the energy variation on a certain point on the surface can be described as following: an increase from 0 of the energy as the beam axis approach this point, then the energy reach the maximum value  $I_0$  when the point is in the axis of the laser beam, and finally decreases as the beam move forward (Figure 2.3.4). To be able to cover the entire surface, the laser made linear scans from  $x_{min}$  to  $x_{max}$  of the sample size with a lateral displacement  $d_{lat}$  of the beam perpendicular to the laser beam scanning direction in order to control the overlapping of the

adjacent laser tracks (Figure 2.3.3). The number of laser pulses per point of the surface is calculated using the equation 2.11 as follows:

$$N = \frac{(2\omega_0)^2 f}{v d_{lat}}, \quad (2.11)$$

where  $\omega_0$  is the laser beam radius,  $f$  the repetition rate (pulse frequency),  $v$  the scanning velocity and  $d_{lat}$  the lateral displacement between each tracks.

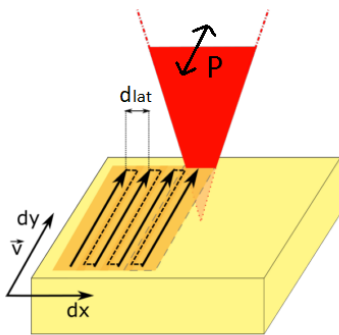


Figure 2.3.3 : Scheme of the XYZ table movement during non-stationary irradiation experiments, adapted from<sup>60</sup>.

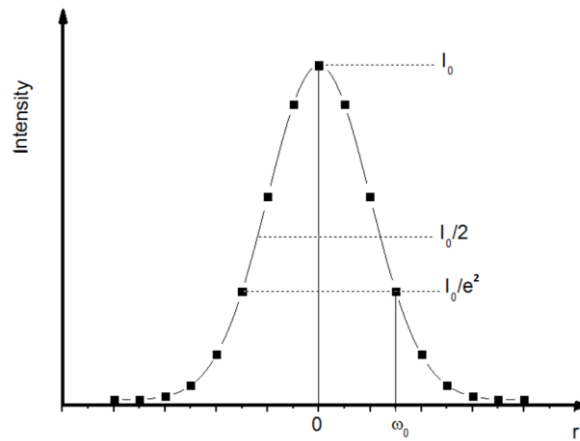


Figure 2.3.4 : Drawing of the Gaussian intensity profile of the laser device used in this thesis work.

As observed in Figure 2.3.3, the scanning direction is parallel to the polarization vector and the scan always started from the same border of the sample to guarantee a better homogeneity of the deposited energy on the sample surface. A control of the laser processing parameters such as the average fluence, the average number of pulses and the lateral displacement enabled to approach feature morphologies observed in stationary irradiation mode and so two structures were produced in large scale in order to analyse their surface properties. These structures consisted of laser-induced periodic surface structures (LIPSS) produced at low fluences, and microgrooves (ridges) produced at higher fluences.

## 2.4. Thermoforming of $Zr_{65}Cu_{15}Al_{10}Ni_{10}$ bulk metallic glass

### 2.4.1. Thermoforming experiments in air

First thermoforming experiments were conducted with the hot compression machine MTS4M previously used for strain rate jump tests to determine the rheological properties of Zr3 amorphous alloy. We used Zr3 3 mm in diameter rods of 2 mm in height preliminary polished on their circular tops to maximise surface interaction with the mould and the top clamp. The silicon mould of 1 mm thick consisted of periodic rectilinear groove of 400 nm width and with a period of 3  $\mu\text{m}$  (Figure 2.4.1.a). Grooves are 100 nm deep and exhibit right angle corners (Figure 2.4.1.b). Considering the clamp and the heating blocks geometry, the total height of the mould + BMG part was sufficiently thick to ensure that top and bottom heated parts of the device could not touch each other at the end of the experiment.

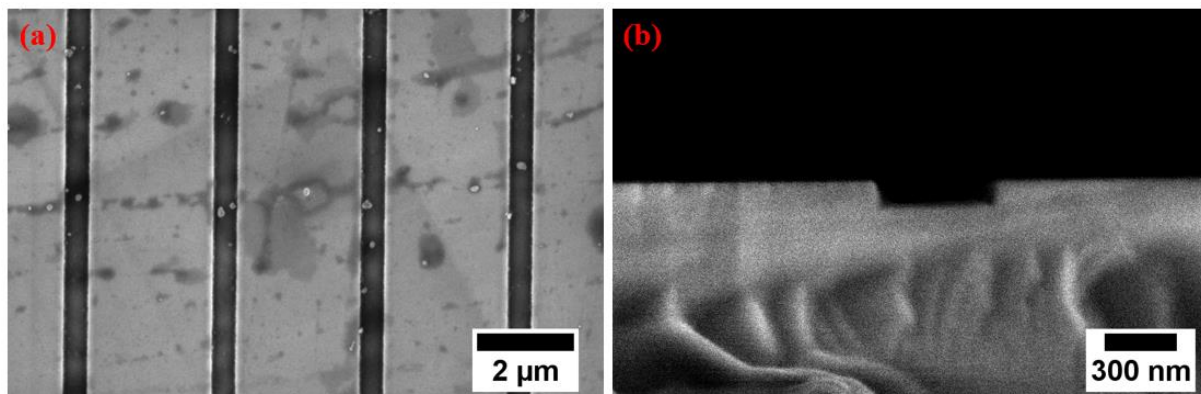


Figure 2.4.1: SEM images of the Si mould used for preliminary thermoforming experiment in air before cleaning (a), cross section of the Si mould to let appear the pattern profile (b).

### 2.4.2. Thermoforming experiments under vacuum

After determining the rheological behaviour of the amorphous alloy, thermoforming processes were conducted in a dedicated machine and an overall image is presented in Figure 2.4.3. The system is composed of a ZWICK 100 kN compression machine with a vacuum chamber allowing to work under  $10^{-5}$  mbar pressure (Figure 2.4.3). Regular punches were modified to integrate heating resistors powered by two external generators and allow to reach a maximum temperature of  $650^{\circ}\text{C}$  on the surface of the clamps. Clamp plates has been realised in Inconel 718 material to maintain mechanical resistance at elevated temperatures (Figure 2.4.2). Sample holder and storage area enable to use different moulds and metallic glass samples for each experiments. The ZWICK software allowed to work with constant force, constant strain rate or

constant pressure. Different types of moulds were used and their specifications will be described in the next section.  $Zr_{65}Cu_{15}Al_{10}Ni_{10}$  bulk metallic samples were cut in small plates of about 60 mm<sup>2</sup> to 150 mm<sup>2</sup> with thicknesses between 0.8 and 2 mm.

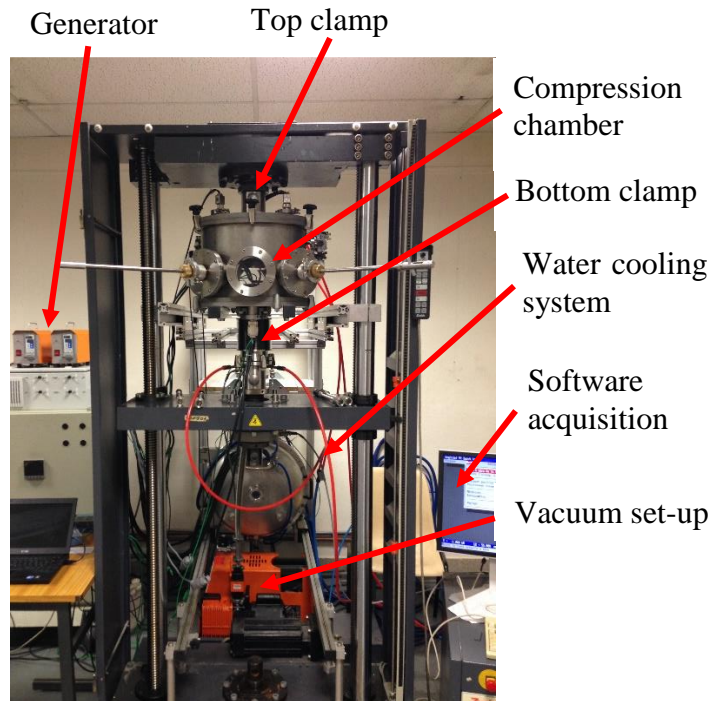


Figure 2.4.3: Picture of the thermoforming device used to pattern  $Zr_{65}Cu_{15}Al_{10}Ni_{10}$  alloy.



Figure 2.4.2: Picture of the Inconel bottom clamp in the vacuum chamber. Heating resistances are supplied by armored cables. Copper plate sample holder allow to process multiple samples without opening the chamber.

Figure 2.4.4 shows a comprehensive scheme of the major parts of the hot compression in-vacuum (HCV) system. Basically, the device is composed by 3 elements: the pumping system, the compression system and the compression clamp's heating system. Working under high temperature and high stress imply that compression plates need to keep their mechanical resistance integrity as at room temperature. In order to guarantee it in the range of 400°C to 500°C, plates have been made in Inconel 718 material which is well known for its mechanical resistance at high temperature.

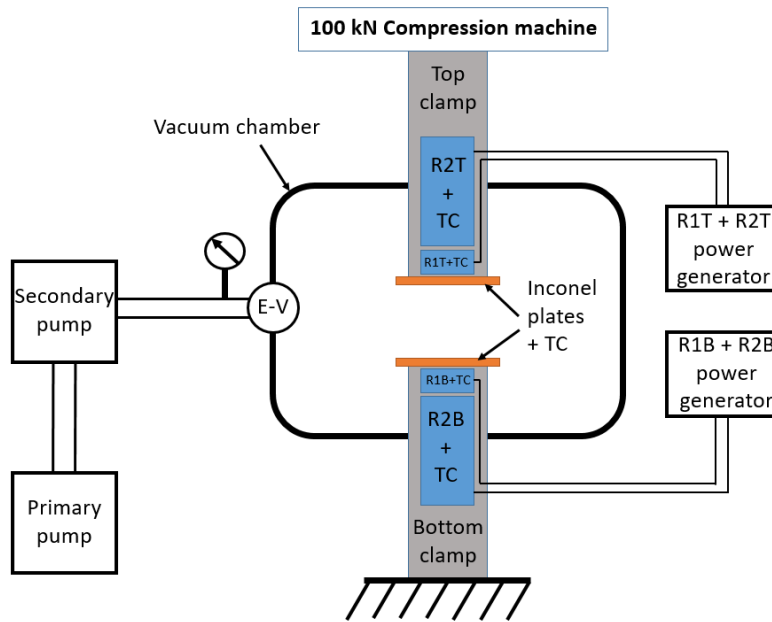


Figure 2.4.4: Comprehensive scheme of the hot compression in-vacuum (HCV) device used to thermoform Zr3 BMG samples.

The creation of the vacuum in the chamber is realized thanks to an oil pump for the primary vacuum and a turbomolecular pump for the secondary vacuum. Thus, it is possible to reach vacuum of around  $2 \times 10^{-5}$  mbar. BMG compression is done by a ZWICK compression device with a maximal applicable load of 100 kN. The lower part (bottom clamp) is fixed and attached to the machine structure whereas the higher part (top clamp) is operated by a ZWICK software allowing to work in constant force or constant speed. Clamps heating is realized by a 2 heating-resistors system (R1+R2) integrated in both top (T) and bottom (B) clamps (R1B+R2B; R1T+R2T). Big resistors R2B and R2T allow the extended heating of the two clamps and ensure temperature homogeneity and stability during compression tests. Small resistors R1B and R1T are placed just under the two Inconel compression plates in order to allow a more accurate and fast tuning of the temperature. Each clamps temperatures are adjusted independently by two generators that had two setting and display accesses. To be able to accurately control and predict the material flow behaviour during compression tests, every heating resistors are equipped with an integrated thermocouple (TC), allowing an instantaneous view of their temperature in top and bottom clamps. Complementary, each Inconel compression plates are equipped with a thermocouple centred at around 2mm beneath their surface. Thus, they allowed temperature reading at the extreme surface to more accurately control experimental conditions during hot compression and to be able to evaluate heat diffusion kinetics from resistors to the useful zone of the device. Each thermocouples data are collected in real time thanks to LabVIEW acquisition software.

### 2.4.3. Working problematics of thermoplastic forming under vacuum environment

#### Heat transfer in vacuum

As it is well-known, heat transfer between two solids in air is done by radiation, convection and conduction phenomenon. As it is presented in Figure 2.4.5 real contact areas between two flat solids are very small compare to the theoretical surface contact area. Thus, thermal conductivity of the gas  $\lambda_G$  between the two solids as to be took into account. Practically, gas layer thickness separating both solids is really small (few tens of microns) compare to the solid thickness.

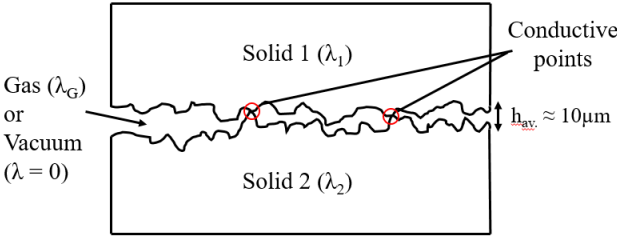


Figure 2.4.5: Schematic view of real interaction areas of two flat solids 1 and 2 with low roughness values.

Thus, in air working environment, despite the fact that air thermal conductivity is low ( $\lambda_{air} = 0.0262 \text{ W.m}^{-1}.\text{K}^{-1}$ ) the very low gas layer thickness will have a negligible effect on heat diffusion and the interfacial thermal resistance is negligible. However, by taking the same example of two solids in contact to each other, in vacuum environment the thermal conductivity is 0: space between them will prevent any thermal transfer by conduction. Thus, the total heat diffusion of the system will be done only on the real contact area by thermal conduction and so the thermal transfer will be very poor. This problem is mostly present between the mould and the plate (bottom part). On the contrary, in contact to the hot plate the metallic glass will start to become viscous and finally promoting a high contact area.

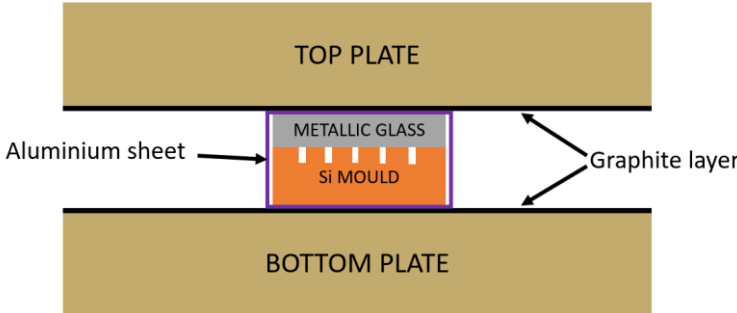


Figure 2.4.6: Scheme of the practical contact area and the apparatus to improve thermal transfer during TPF processing.

## Chapter 2: Experimental methods

As presented in Figure 2.4.6, in order to maximize contact areas and thermal transfer between Inconel plates and the mould + BMG group, a spray deposition of graphite has been realized on the compression plates. Additionally, depending the experiences, graphite sheets were added between the mould and the compression plate. Finally, micron-size parts thermoforming was conducted by embedded mould + BMG system inside aluminium sheets because of the high ductility of this metal in the range of 400°C to 500°C, allowing to even more optimize contact areas during compression tests. Other experimental problems are directly or indirectly related to the heating in vacuum effect. Increasing temperature in the clamps (more than 600°C in the internal part) inexorably inducing thermal expansion of the constituent metallic elements (Steel internal parts, Inconel plates, resistors, thermocouples...). However, each alloys do not expand in the same way and so if some elements are more constraint resulting to a better thermal conduction, spaces can also appear resulting to a much less thermal transfer efficiency under vacuum.

Experimentally, this heat-transfer issues under vacuum may have an important effect on temperature measurements. A large scattering between real and measured temperatures in the compression plate compare to temperature measurements in air can be expected. Thus, this temperature will not take into account as the real working temperatures. However, regarding to the rheological study previously done on Zr3 and by assuming that vacuum environment do not affect rheological behaviour of the alloy, it is then possible to determine the real working temperatures applied during experiments under vacuum by realizing strain rate jump tests under Newtonian regime and then comparing stress flow values with the previous ones in air. As a conclusion, the best way to accurately estimate the real working temperatures of future tests under vacuum will be to compare resulted thermomechanical properties with the one determined in the section 3.2.3 of the Chapter 3.

### Electrical resistor heating

Using an electrical heating system in a vacuum environment can induce the creation of electrical arcs and so strongly deteriorate the heating system. Indeed, as it has been demonstrated by Paschen in 1889, at a given voltage called as breakdown voltage, a discharge or an electric arc is created between two electrodes in a gas as a function of pressure and electrodes gap length. Thus, the necessary voltage to create an arc will decrease as the pressure decrease. To avoid formation of electric arc, secondary vacuum must be done before the electrical power of the heating resistor system is switched on. Additionally, a constant control of the pressure must be

done due to air leak risks because of the manipulations during the experiment. As explained above, apart from the fact that heat transfer issues can affect temperature measurements in compression plates, temperature measurement of the resistors using thermocouples can be also modified under vacuum environment. Depending heating conditions, the work under vacuum can cause the break of the resistors. Indeed, generators are equipped with PID regulators which allowing the programming of heating ramps until 500°C. Temperature regulators' measurements are done by thermocouples integrated in the resistors and so a bad contact may induces an understated temperature measurement and so a critical overheating of the resistors by the generator program. To overcome this issue, heating ramps to desired compression plates temperatures has been realized in manual mode by selecting resistors power. Consequently, a study of the optimized powers of each resistors has been realized to guarantee a constant heating rate and then a stabilized temperature in the working range of 400°C to 500°C.

### 2.4.4. Specifications of the moulds used for thermoplastic forming under vacuum.

In order to get a stabilized and homogenous temperature in the mould and the BMG sample, a contact step of 30 s at 50 N load and then a contact step of 2 min at 200 N load has been realized prior every thermoforming experiments. To optimize contact surface area between compression plates and mould + BMG plates, graphite spray deposition on Inconel plates and aluminium sheet embedded around the mould + BMG system has been used.

#### Si-mould with micron-size parts

Thermoforming experiments under vacuum were first conducted with Si-mould plates of 600  $\mu\text{m}$  thick covered by  $\text{SiO}_2$  layer of 100 nm. These moulds were provided by an industrial partner and made by photolithography followed by deep reactive-ion etching (DRIE) adapted from microelectronic technologies. Thanks to this elaboration process and as it can be observed on Figure 2.4.7.a and b, mould surface finishing is very high with very accurate corners and edges. Moulds imprints shapes are micro gears and micro parts from luxury watch mechanisms: an industrial sector requiring very high geometry accuracy under millimetre to micrometre scale. Due to industrial and commercial secrecy, overall technical listing and entire SEM images of the micro parts are not presented.

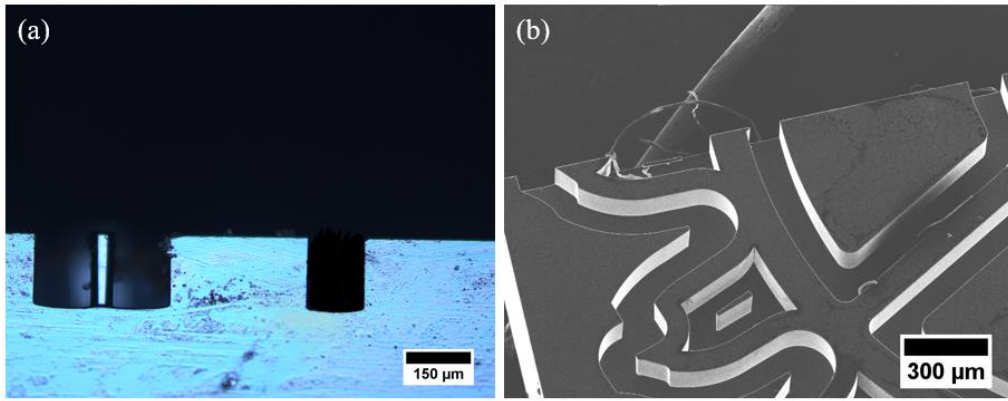


Figure 2.4.7: Optical microscope image of the Si-mould cross-section (a), tilted SEM image of the Si-mould micro-pieces imprint (b)

Figure 2.4.7.a shows microscope image of Si-mould cross section presenting the shape of the micro part imprint. Grooves have constant depth  $L$  of  $170\mu\text{m}$  and width  $d$  between  $60\mu\text{m}$  for the thinner parts to  $150\mu\text{m}$  for the thicker parts of the gear, resulting to an aspect ratio  $L/d$  varying from 1.13 to 2.8. Si-mould material has been chosen because of its good mechanical resistance under the working temperature range of Zr3 BMG (typically from  $390^\circ\text{C}$  to  $500^\circ\text{C}$ ) and no deformation or breaks of the mould have to be expected under hot compression tests.

### Tungsten moulds textured with femtosecond laser

Some 15 mm in diameter tungsten disks were cut in 4.7 to 5mm thick slices thanks to electro-erosion processing technique. Then, one of the W disks surface has been grounded to optimize the heat transfer and the other one have been  $1\mu\text{m}$  polish prior to laser texturing processing in order to optimize the surface treatment's topology. Then, Zr3 BMG plates of 1.7 mm thick with surfaces of around  $51\text{ mm}^2$  has been  $1\mu\text{m}$  polished and thermoformed on textured W disks under hot compression in vacuum device.

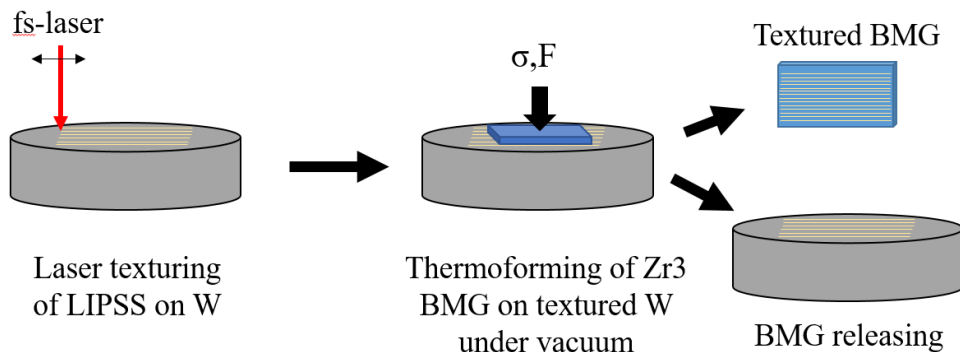


Figure 2.4.8: Scheme of the experimental process for LIPSS replication on Zr3 BMG by thermoforming processing.

Laser patterning of tungsten cylinders has been realized in CeFEMA laboratory of IST LISBON with the Yb:KYW femtosecond laser device presented in Chapter 2. Areas of about 250 mm<sup>2</sup> have been textured using a pulse energy of 400 μJ to 800 μJ at a pulse frequency of 200 Hz, lateral displacement of 0.04 mm and a scanning speed of 1 mm/s. The resulted surface texture consisted of laser-induced periodic surface structure (LIPSS) (Figure 2.4.9). The determination of the mould topology required AFM measurements and SEM images and this part of the work has been thus implemented in the Chapter 3.

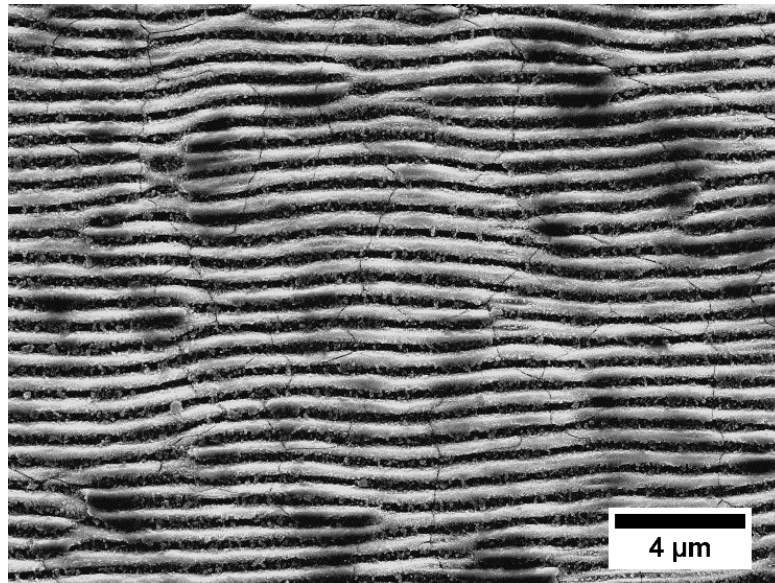


Figure 2.4.9: SEM image of tungsten mould surface textured with LIPSS by femtosecond laser treatment.

## 2.5. Structural characterization

This section presents the experimental conditions for structural analysis of the amorphous alloys. Textured, polished and as-cast surfaces were characterized using two different diffraction techniques to control their amorphous behaviour or to evaluate if any crystallization or oxidation occurred during surface treatments.

### Classical X-Ray diffraction (XRD)

XRD measurements have been done using a standard Cu K $\alpha$  radiation source ( $\lambda = 0.15418$  nm) provided by a BRUCKER D8 Advance Série II<sup>®</sup> instrument. The scanning range was from 10° to 90° with an angular speed of 1.25°/min. Every analysed sample were primarily removed from resin support to avoid any irrelevant signals. Standard X-Ray diffraction was used to generally control the amorphous structure integrity after elaboration or thermal treatments of bulk metallic glass.

## Grazing mode X-Ray diffraction (GIXD)

Grazing Incidence X-Ray diffraction allowed to determinate in-depth distribution of various crystalline phases. In the case of surface treatments of amorphous metals, GIXD allowed to reveal crystalline phases resulted from surface processing (i.e. laser treatments) on very small depth from 50 Å to 1 nm, that wouldn't be detected from standard X-Ray diffraction techniques. Because of the refractive index of solid materials in the X-Ray spectra is slightly smaller than 1 ( $10^{-5}$  to  $10^{-6}$  less), specular or quasi-totally reflexion appear for one-tenth of a degree. At this angles, the transmitted wave is evanescent and its penetration depth is very small, but strongly increases above a critical value  $\alpha_c$ . A BRUCKER D8 Advance Série II<sup>®</sup> instrument was used with a Göbel mirror. In this work, the incident angle was fixed at  $1^\circ$  with an accumulation time of 10 sec for every  $0.08^\circ$  and the acquisition range was varied from 25 to  $90^\circ$ .

## 2.6. Surface characterisation

### 2.6.1. Topological characterisation

Textured and non-textured BMG's sample surfaces were observed with optical and scanning electron (SEM) microscopes. Four different SEM and two optical microscopes were used in this thesis work. Surface morphologies were also analysed using a 3D surface reconstruction software allowing to measure average roughness  $R_a$ , linear profiles or filling depth in the case of TPF processing.

#### Optical microscopy

Surface topography and laser spots dimensions were observed using a LEICA DM 5500B<sup>®</sup> binocular optical microscope in IST-L and an Olympus BX15 M<sup>®</sup> in SIMaP laboratory.

#### Scanning electron microscopy (SEM)

Three SEM has been used to observed bulk metallic glass surfaces. In IST-L, secondary imaging mode on JEOL JSM-7001F<sup>®</sup> field emission gun microscope (FEG-SEM) or a Hitachi S2400<sup>®</sup> (SEM) operating between 20 to 25 keV and with working distances between 10 to 20 mm. In SIMaP, with the collaboration of the "Consortium des Moyens Technologiques Communs" (CMTCC) a LEO Stéréoscan 440<sup>®</sup> SEM and a FEG-GEMINI Ultra 55<sup>®</sup> with the same operating parameters as in IST-L were used.

### Stereoscopic pair analysis

Secondary electron SEM images provide information about geometrical aspects and topology of a surface. However, shadowing effect and the static position of the SE detector cannot allow a good appreciation in depth of the viewed specimen. From tilted and non-tilted images of the surface, stereoscopic pair analysis method allowed to reconstruct in three dimensions the studied area. In this work the 3D reconstruction was done with two versions of the MeX software from Alicona<sup>®</sup> company (Alicona GmbH) This technique allows, among other things, to extract quantitative results in Z-direction (Depth) such as the height of a surface structure, laser crater depth and also roughness parameters (namely  $R_a$ ,  $R_z$ ,  $R_{Sk}$  and  $R_{Ku}$ ), which give information about surface topology. This technique also enabled to get accurate measurements of the thermoformed micro-parts created in the Chapter 3. Tilted and non-tilted images were acquired with the same contrast, brightness, magnifications and working distances to ensure the best condition for the software to reconstruct 3D surfaces. In this work the three dimensional plots were done with SEM images obtained at 0 and 10° tilting angle, and surface topography was quantified according to ISO 4287 standard for roughness measurements.

### SEM-Focused Ion Beam analysis

Focused Ion-Beam (FIB) is a technique allowing to locally and accurately ablate the material at micron or even nanometre scale. Associated with a conventional SEM it allows to visualize the area of interest during the process. Ionic ablation is the result of atoms or ions ejected with elastic impacts between focused ions and the material. This technique allows to repair and modify integrated circuits, sample preparation for Transmission Electron Microscopy (TEM) or, as it was used in this work, to create cross section in a material surface. In this work the ionic source is a Gallium source ( $Ga^+$ ). This heavy ions can be accelerated between 1 kV to 30 kV. Prior to ablation, a local Platinum Chemical Vapour Deposition (CVD) was done on the desired ablated area to protect the specimen surface. The SEM GEMINI column is equipped with a Schottky-type FEG canon with a resolution of 1.1 nm at 20 kV. The FIB SIINT ZETA column equipped with a Gallium source had a 4nm resolution at 30 kV.

### Atomic Force Microscopy (AFM)

By measuring atomic interaction between a nanometric apex of a cantilever and the sample surface, the AFM enables to measure sample surface topography at the nanoscale. In this work, a Veeco Dimensions 3100<sup>®</sup> has been used in air environment. The AFM device is installed in

a controlled hygrometry chamber to improve quantitative measurements and protect experiments from environmental perturbations. AFM was used in Tapping mode, where the cantilever vibrates at its own resonance frequency with a specific amplitude. When the cantilever interacts with the surface, the resonance frequency changes and the amplitude decreases. This frequency variation enables to reconstruct the surface topography.

## 2.6.2. Chemical characterisation

### Energy-dispersive X-ray spectroscopy (EDS/EDX)

The EDS is an analytical technique that can be incorporated in electron microscopes (SEM, TEM or STEM) and allows to analyse chemical elements on sample surface. Collisions between incident electrons and atoms from the sample generate X-photons which are caught by a specific detector. Photons energy are correlated to electronic transition between band levels and then enable to determine the elements and their quantity in the analysed area. EDS measurements were done in the JEOL FEG-SEM in IST- Lisbon with an INCA 250 Premium<sup>®</sup> analytical software.

### X-Ray Photoelectron Spectroscopy (XPS)

X-Ray Photoelectron Spectroscopy is a non-destructive surface analysis technique which allows to analyse elements on a 10nm thick interaction layer. In this case, XPS measurements allowed to determine if surface treatment (laser surface treatment in particular) had an effect on the surface chemistry of metallic glass alloys. The X-Ray Photo-electron Spectroscopy is an analytical technique where charged particles (ions, electrons, photons...) passing through the material are braked by successive interactions with material atoms and then enable the emission of photons, electrons or ions. The XPS technique induces a low energy irradiation and maximises the photoelectric effect. A high-resolution electron spectrometer is then used to recover the energy spectrum of the emitted photoelectrons. The kinetic energy of these photoelectrons is given by  $E_k = h\nu - E_b - \Phi_s$ , where  $E_b$  is the electron binding energy and  $\Phi_s$  the material work function. Depending on the X-Ray source employed, a range of applied energy will be used. In this range, the corresponding binding energy of the first orbitals of the different atoms in the surface will be excited and photoelectrons peaks will appear on the spectrum. Thus, it will be possible to quantify ( $\pm 10\%$ ) the amount of each component regarding the thickness and the intensity of each photoelectrons peaks. In this work, surfaces were chemically characterized by X-ray Photoelectron Spectroscopy (XPS) using a XSAM800<sup>®</sup> dual anode spectrometer from

KRATOS<sup>®</sup>. The Al K $\alpha$  radiation ( $h\nu = 1486.6$  eV) was selected. Spectrometer operation conditions, pressure and temperature analysis were as described in the work of Ferreira *et al.*<sup>148</sup>. Spectra with a step of 0.1 eV were collected by the software Vision 2 version 2.2.9 from KRATOS. Data processing was performed using the freeware XPSPeak 4.1<sup>®</sup>. Shirley backgrounds and Gaussian-Lorentzian products were used for curve fitting. No flood gun was used for neutralizing charge accumulation. The shift due to charge accumulation was corrected using as reference the binding energy (BE) of aliphatic C 1s contamination set to 285 eV<sup>148,149</sup>. For quantification purposes, the sensitivity factors (SF) used were those furnished by the equipment library (Vision Axis Element Library): 0.278 for C 1s, 0.78 for O 1s, 2.576 for Zr 3d, 3.547 for Cu 2p<sub>3/2</sub>, and 2.696 for Ni 2p. Measurements on the surfaces were repeated three times in order to control the reproducibility of the experiments and to get statistical values.

## 2.7. Surface properties

### 2.7.1. Wettability measurements

Prior determining the surface energy of treated and untreated samples, surface wettability was evaluated by the sessile drop measurements method. Measurements were performed at room temperature using two solvents: distilled-deionized (DD) water prepared with a typical Millipore system and diiodomethane (Sigma-Aldrich, 99% purity) characterized by a very low polar component (0.358 dyne/cm) as testing medias. Prior to wettability measurements, specimens were 10min ultrasonically cleaned in three different medias as following: detergent solution diluted in DD water, an equivalent solution of ethanol and DD water and finally in DD water. After ultrasonication, the water excess was removed by blowing nitrogen over the sample surfaces followed by drying at 40°C in vacuum oven during 12 hours in order to remove carbon contamination. A scheme of the experimental setup for wettability measurements is showed in Figure 2.7.1:

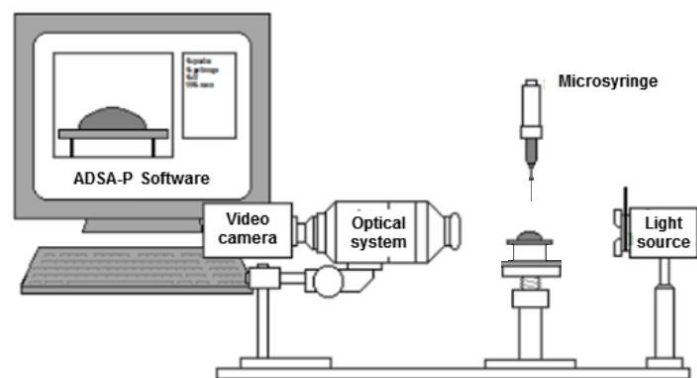


Figure 2.7.1: Scheme of the experimental setup for contact angle measurement, adapted from<sup>47</sup>.

Using a micrometric syringe, droplets of about 3 to 5  $\mu\text{l}$  of the two testing medias were deposited on the specimen surfaces. Images of the droplets were acquired using a video camera (jAI CV-A50) mounted on a microscope (Wild M3Z<sup>®</sup>, magnification x40) and connected to an image processor Video Pix Framegrabber (Sun Microsystems<sup>®</sup>, model DT3155) that produce 640 x 480 pixels digitalisation in grey levels (8-bit). Every measurements were made during 60 s starting at the droplet deposition ( $t = 0$  s) until  $t = 60$  s. Due to the short measuring timescale, it is assumed that the evaporation didn't affect the results and so no closed chamber were needed. Every measurements were made in air atmosphere.

Droplets profiles were analysed with ADSA-P<sup>®</sup> software (Applied Surface Thermodynamics Research Associates, Toronto, Canada)<sup>150</sup>. Different methods are suitable to measure droplets contact angles. In this study the software used is based on the axisymmetric drop shape analysis profile (ADSA-P) method, which was developed by Neumann et al<sup>151</sup>. Thanks to a prior calibrated grid, the software fits numerically the experimental droplet profile using a Laplace equation based mathematical model and so enable to estimate the static contact angle ( $\theta_{static}$ ). For sufficient statistics, at least 6 measurements in different areas of the alloys on each type of textures were proceed. Due to the oxidation behaviour and the photosensitivity of the diiodomethane, a special care was made to protect it from the light in a relatively inert storage conditions. In this study, the surface free energy  $\gamma_{SL}$  was determined on the polished samples by using the geometric means approach<sup>152</sup>, where the work of adhesion  $W_{SL}$  of a liquid on a solid is the necessary work to split the liquid from the solid. It is related to the surface tensions by the Dupré relation:

$$W_{SL} = \gamma_{SV} + \gamma_{LV} - \gamma_{SL}, \quad (2.12)$$

## Chapter 2: Experimental methods

where,  $\gamma_{SV}$  is the surface free energy of the solid in equilibrium with the liquid vapour,  $\gamma_{LV}$  is the surface tension of the testing liquid in equilibrium with its vapour, and  $\gamma_{SL}$  is the interfacial tension solid - liquid.

$W_{SL}$  may be expressed as the geometric mean of the work of cohesion of the solid  $W_{SS}$  and the liquid  $W_{LL}$  by :

$$W_{SL} = \sqrt{W_{SS}W_{LL}}. \quad (2.13)$$

Fowkes decomposed surfaces tensions of the solid and the liquid in two parts: the dispersive and the non-dispersive parts:

$$\gamma_S = \gamma_S^d + \gamma_S^{nd}, \quad (2.14)$$

$$\gamma_L = \gamma_L^d + \gamma_L^{nd}, \quad (2.15)$$

where  $d$  exponent correspond to the dispersive part and  $nd$  exponent to the non-dispersive part. Fowkes consider that the dispersive forces are predominant in the solid-liquid interface. By using the same decomposition into two surface tension components, Owens and Wendt<sup>153</sup> took into account in the work of adhesion of the non-dispersive part (polar part) that they attribute to hydrogen bonding. In this study we neglect the effect of Van der Walls forces comparing to the dispersive and non-dispersive forces. So, the work of adhesion being the addition of the different contributions, it is written as followed:

$$W_{SL} = 2\sqrt{\gamma_{SV}^d\gamma_{LV}^d} + 2\sqrt{\gamma_{SV}^p\gamma_{LV}^p}, \quad (2.16)$$

where the indexes  $d$  and  $p$  represent the dispersive and polar components of the  $\gamma_{SV}$  and  $\gamma_{LV}$  respectively. By combining the equation above with the Young equation we obtain that the surface free energy of a solid can be written as:

$$\gamma_{SL}(\cos \theta + 1) = 2\sqrt{\gamma_{SV}^d\gamma_{LV}^d} + 2\sqrt{\gamma_{SV}^p\gamma_{LV}^p}. \quad (2.17)$$

Then, the dispersive and polar components of the surface free energy of the solid, as well as its total surface free energy, can be calculated using equation 2.17 based on the static contact angles measurements of two different solvents whose dispersive and polar components are known.

### 2.7.2. Corrosion study

In a surface properties modification context, corrosion resistance behaviours of the alloys were studied in a specific electrolyte (solution). In this study, a 0.1 M NaCl ( $\approx 5.85$  g/L) solution was chosen to investigate corrosion properties of Zr-base metallic glass with or without surface treatments. Cl<sup>-</sup> ions are known to be the cause of a severe oxidation in crystalline metallic alloys, thus, the ion concentration is close to Hank's solution (8 g/L), a common solution used to reproduce human body fluid to analyse corrosion resistance of metallic implant devices. It is also well-known that chloride ions Cl<sup>-</sup> are highly polarisable and so can easily react with highly energetic area on solid surface as grain boundaries or other defects<sup>57</sup>. The use of NaCl solution to study bulk metallic glass corrosion resistance will also allow to see the effect of a partial crystallization or defect in the material on corrosion properties.

#### Sample preparation

Plates with minimum surface of 50 mm<sup>2</sup> have been cut for the three different Zr-based amorphous alloy compositions as Zr-based Zr3 (Zr<sub>65</sub>Cu<sub>15</sub>Al<sub>10</sub>Ni<sub>10</sub>), ZrC (Zr<sub>57</sub>Cu<sub>20</sub>Al<sub>10</sub>Ni<sub>8</sub>Ti<sub>5</sub>) and Cu2 (Zr<sub>48</sub>Cu<sub>36</sub>Al<sub>8</sub>Ag<sub>8</sub>). Bottom surfaces were connected with copper wires using silver lacquer, then glued and dried. Resistivity measurements using Ohmmeter were done between copper wire and sample surface to ensure a good electrical conductivity with an acceptable range between 0.5 and 10 Ohms. Connected samples were then embedded in epoxy resin while maintaining them horizontally without covering or corrupting the surface of interest. Then, according to the experimental requests, surface were then polished using SiC paper (P320 to P4000) and PRESI<sup>®</sup> diamond suspension to get a 1 $\mu$ m surface finishing. Then, sample surfaces were textured using femto-second laser processing with selected laser parameters. Then, samples were ultrasonicated to remove the part of ablated particles that were not attached on the surface. For every corrosion experiments (Open Circuit Potential (OCP), anodic polarization measurements and Electrochemical Impedance Spectroscopy (EIS) measurements), 1 $\mu$ m polished samples were also analysed and used as references. Picture of two samples prepared for electrochemical measurements is presented in Figure 2.7.2.

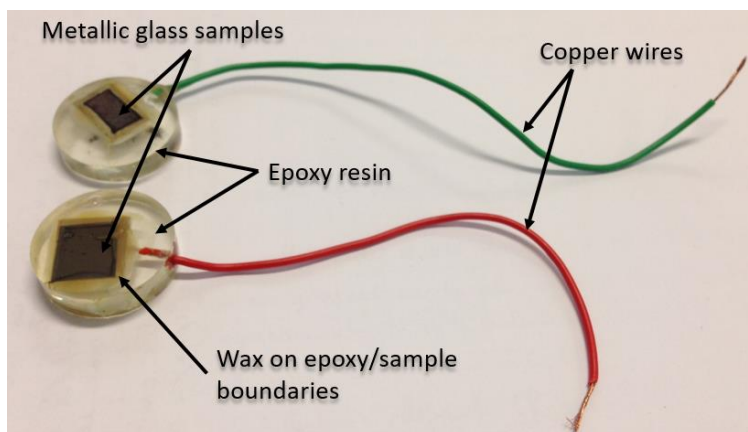


Figure 2.7.2: Picture of prepared metallic glass samples for electrochemical measurements.

To avoid localised corrosion on the edges or on the peripheral part of the samples and to ensure a controlled sample/solution interaction area, wax was putted at the sample-resin boundaries. To maintain the same amount of NaCl per surface area, a constant ratio of  $V_{solution} = 1.2 \times S_{sample}$  was respected, where V is the solution volume in ml and S is the sample surface in mm<sup>2</sup>.

### Equipment for corrosion studies

Open circuit potential, anodic polarization and also electrochemical impedance spectroscopy measurements were realized in collaboration with the “Departamento de Engenharia Química e Biológica” of the IST of Lisbon. Electrochemical investigations were performed using a typical 3 electrodes set-up (Figure 2.7.3) in a glass cell where a saturated calomel electrode (SCE) worked as the reference electrode ( $R_e$ ), a Pt net wire as the counter electrode ( $C_e$ ) and the metallic glass surface as the working electrode ( $W_e$ ).

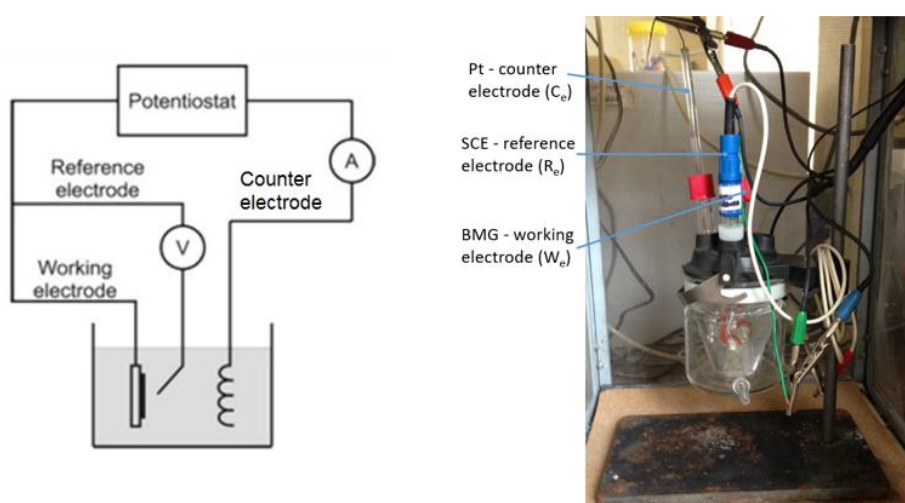


Figure 2.7.3: Scheme of the 3-electrode set-up used in this thesis work (left), picture of the glass cell with the electrodes in 0.1 M NaCl solution (right).

Electrodes were then connected to a GAMRY<sup>®</sup> potentiostat with a computational software allowing to measure and apply a large range of potentials and frequencies and also to make electrochemical impedance spectroscopy (EIS) measurements.

### Open circuit potential (OCP)

Open circuit potential (OCP) or mixed potential is the potential between the tested material and the reference electrode in a solution without any external current. A measured current equal to zero do not imply that there is no reactions in the solution: reactions can compensate themselves. OCP is the result of different contributions and do not act as an equilibrium potential, thus, it is strongly related to the environmental condition. pH variation, surface roughness or temperature evolution on the working electrode will contribute to the OCP evolution. Finally, OCP variations during time can give a general information about the sample surface behaviour in the solution and enable to determine the corrosion potential ( $E_{\text{corr}}$ ). An increase of the OCP during time imply a less reactivity of the sample surface during time and may illustrate a passivation of the specimen surface. In contrary, it's decreasing during time will imply a less noble surface which becomes more reactive in the solution and so more sensitive to corrosion. However, an increase of the potential during time do not imply necessarily an increase of the corrosion resistance of the material, and so it is important to also measure the corrosion current intensity ( $I_{\text{corr}}$ ). In this work OCP measurements were done prior to every polarization and EIS measurements during at least 40min in 0.1 M NaCl solution.

### Polarization measurements

Anodic and cathodic polarization measurements were obtained by continuously vary the applied potential in the circuit. Starting from the OCP measured previously, a variation to the negative values of the potential will promote cathodic reaction (reduction on working electrode) and in contrary, going forward in the positive values of the potential will promote anodic reaction and so oxidation (corrosion) of the sample. In this work, only anodic polarisation curves will be presented. During the experiment, current density is recorded for every corresponding potential values. Potential scanning speed must be sufficiently slow to ensure reaction reversibility. Thus, the variation of current density as a function of the potential give information about the electrochemical reactions engaged. From this polarisation curves, it is possible to determine the corrosion current intensity ( $I_{\text{corr}}$ ), the potential range of current stability and also in the case of metallic glass that are, as previously said, sensitive to pitting corrosion, the pitting potential ( $E_{\text{pitt}}$ ) and the pitting current ( $I_{\text{pitt}}$ ). In this thesis work, after 40

min of OCP, anodic and cathodic polarization measurements were carried out using GAMRY® potentiostat and applying the potentiodynamic polarization technique at a scan rate of 0.1 to 1 mV/s (anodic scan) and 1mV/s (cathodic scan). Scanned potential range were between OCP to -100 mV for cathodic direction and OCP to + 1V for anodic direction.

### Electrochemical impedance spectroscopy (EIS)

The electrochemical impedance spectroscopy is a measuring method allowing to separate contributions of different chemical and electrochemical effects going on at the sample-solution interface, and also from the electrolyte between working and reference electrode  $We$  and  $Re$  respectively. The EIS measures electrode behaviours from a low amplitude sinusoidal modulation of the potential  $\Delta E$  with frequency  $f$ :

$$\Delta E = |\Delta E| \sin \omega t , \quad (2.18)$$

where  $|\Delta E|$  is the amplitude and  $\omega = 2\pi f$  the pulsation. The potential sinusoidal disturbance inducts a sinusoidal current  $\Delta I$  over the stationary current shifted by an angle  $\theta$  from the potential:

$$\Delta I = |\Delta I| \sin \omega t - \theta , \quad (2.19)$$

The system impedance  $Z(\omega)$ , the ratio between compulsory sinusoidal voltage and the resultant current, can be defined as a complex number:

$$Z = \frac{\Delta E}{\Delta I} = \frac{|\Delta E|e^{j\omega t}}{|\Delta I|e^{j(\omega t - \theta)}} = |Z|e^{j\theta} = |Z| \cos \theta + j|Z| \sin \theta. \quad (2.20)$$

$Z(\omega)$  can be represented in polar coordinates with modulus =  $|Z|$  in Y-axis and phase =  $\theta$  in X-axis (Bode diagram) or in Cartesian coordinates with the real (X-axis) and the imaginary parts (Y-axis, Nyquist diagram). These two diagrams allow to extract different information: Nyquist plot gives direct visual comparison of the material's corrosion resistance behaviour for different immersion times, while Bode plots show impedance magnitude  $|Z|$  and phase angle  $\theta$  variations as a function of the frequency, allowing to extract characteristic time constants of the reaction.

In this thesis experiments, after sample immersion in 0.1 M NaCl solution with the 3 electrodes set-up, EIS measurements were carried out at the open circuit potential (OCP) after 5 periods of immersion: 2H, 4H, 8H, 16H, and 24H under room conditions (temperature and atmosphere). Measurements were done with a 5 mV peak to peak voltage excitation amplitude with frequency

## Chapter 2: Experimental methods

analysis over the 10 mHz to 100 kHz frequency range, that is common conditions for EIS experiments<sup>154</sup>.

## CHAPTER 3

# Thermoforming of Zr-based metallic glasses

This chapter is dedicated to the thermoforming processing technique used in this thesis to form or pattern Zr-based bulk metallic glasses. First, reasons in studied material's selection will be given. Second, the study of the thermal stability and the thermomechanical properties in the supercooled liquid region (SLR:  $T > T_g$ ) will be investigated. After determining rheological properties of the amorphous alloy, problematics of thermoplastic forming (TPF) in air followed by results of TPF processing under vacuum will be discussed. Finally, forming and texturing results at two different scales and the fitting with theoretical models will be presented.

### 3.1. Material's choice

As presented in Chapter 1, compared to crystalline metallic alloys, bulk metallic glasses exhibit a supercooled liquid region (SLR) above their glass transition temperature  $T_g$ , explaining their unique deformation behaviour. Reproducibility and controlled deformation processing of BMGs requires to work under suited experimental conditions in order to control the flow regime and to avoid crystallization occurrence. It is necessary to use an amorphous alloy composition exhibiting reasonable thermal ( $T_g$ ,  $\Delta T$ ,  $T_x...$ ) and rheological properties compared to experimental constraints (maximal working temperature and pressure of the experimental device and of the mould).

During this thesis, three zirconium-based amorphous alloys have been studied: Zr3 ( $Zr_{65}Cu_{15}Al_{10}Ni_{10}$ ) ZrC ( $Zr_{57}Cu_{20}Al_{10}Ni_8Ti_5$ ) and Cu2 ( $Zr_{48}Cu_{36}Al_8Ag_8$ ). Despite the fact that for equivalent glass transition temperature  $T_g$ , the addition of 5 %at. of titanium in ZrC alloy compared to Zr3 induces an increase of the mechanical properties and oxidation resistance<sup>57,155</sup>, rheological studies show that for equivalent temperatures and strain rates, the viscosity values of ZrC alloy are about 10 times higher than the viscosity values of Zr3 alloy. Experimentally, thermoforming of ZrC alloy will thus requires higher applied stresses than for Zr3 alloy in the supercooled liquid region (SLR) to deform the viscous material, and so might be critical for

mould and compression device integrity. Due to its Ni-free composition, Cu<sub>2</sub> alloy is of good interest for medical applications. However, its  $T_g$  is higher than Zr<sub>3</sub> and ZrC alloys ( $\approx 50^\circ\text{C}$ , see Table 3.2-1). Moreover, Cu<sub>2</sub> exhibit very poor oxidation resistance at low temperature ( $T < T_g$ ). Recent work of Eckert *et al.*<sup>140</sup> on Cu<sub>2</sub> showed that despite TPF processing under high vacuum ( $< 10^{-4}$  mbar), the formation of a ZrO<sub>2</sub> layer on the patterned surface along with a strong copper segregation is observed. Thus, we choose to focus on the Zr<sub>3</sub> amorphous alloy for which thermal properties, rheological properties and thermochemical tests are presented below. Characteristic temperatures of ZrC and Cu<sub>2</sub> alloys were also measured and they are presented for comparison with Zr<sub>3</sub> temperatures in the Table 3.2-1.

## 3.2. Study of Zr<sub>3</sub> amorphous alloy

### 3.2.1. Structural characterization

As indicated in Chap. II, the amorphous alloys were elaborated in the SIMaP Laboratory using an arc-melting device with water-cooled copper moulds. Based on needs, the molten glass was casted into rods ( $\Phi$  3 mm,  $\Phi$  5 mm) or into plates of 52 x 12 mm<sup>2</sup> and 2 mm thick. Before every high temperature experiments, it is important to verify the integrity of the structure of the elaborated amorphous alloy. Cooling rates upon casting vary as a function of the mould geometry and it is admitted that copper-mould casting can introduce heterogeneous crystallization process as well as formation of micro-crystals on the surface. Generally, small size crystals ( $< 1\mu\text{m}$ ) can form during cooling. These crystals are mostly not observable by common XRD measurements because of their small size and very small proportion in the structure. However, it has been reported that these submicron size crystals do not act as nucleation sites if crystallization phenomenon occur<sup>156</sup>. Moreover, some studies revealed that they did not affect mechanical or rheological properties<sup>156,15</sup>. Based on that, we will neglect their effect on thermomechanical properties during this work. X-ray diffraction (XRD) of the polished metallic glasses samples are referenced in Section 4.4 of Chapter 4.

### 3.2.2. Thermal stability of Zr<sub>3</sub> amorphous alloy

#### Calorimetric study

Calorimetric study of the metallic glass is used to determine the characteristic temperatures of the material. It highlights glass transition phenomenon, supercooled liquid region (SLR) and crystallization kinetics. A DSC scan in temperature gives access to the glass transition

temperature onset ( $T_g^{onset}$ ), the inflexion point ( $T_g^{inflexion}$ ) and the crystallization onset temperature ( $T_x$ ). The scan rate used for every experiment was set to 40°C/min. As explained in Chapter 1,  $T_g$  and  $T_x$  values are dependent on the scanning rate and so cannot be seen as an intrinsic temperature.

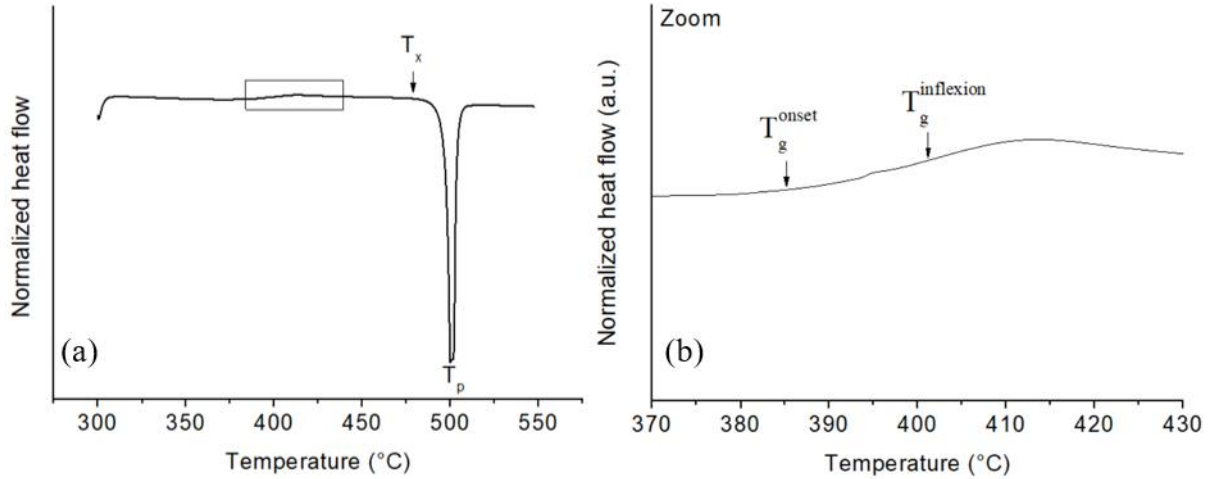


Figure 3.2.1: Rod sample DSC curve of Zr3 sample realized with scanning rate of 40°C/min (a). Zoom between 370°C and 430°C (b). Characteristic temperatures are indicated: crystallization onset temperature ( $T_x$ ), peak crystallization temperature ( $T_p$ ), glass transition temperature onset ( $T_g^{onset}$ ) and glass transition temperature at the inflexion point ( $T_g^{inflexion}$ ).

As it can be observed on the DSC scan in Figure 3.2.1.a, Zr3 amorphous alloy shows a unique crystallization peak  $T_p$ . Zoom on DSC curve between 370°C and 430°C (Figure 3.2.1.b) reveals a clear glass transition zone. The SLR zone is between the glass transition temperature onset  $T_g^{onset}$  and the crystallization temperature onset  $T_x$ . This zone can be defined as:  $\Delta T = T_x - T_g^{onset}$ . Table 3.2-1 shows the characteristic temperatures determined for Zr3 amorphous alloy and also for the two other compositions ZrC and Cu2 studied with femtosecond laser treatments in Chapter 4.

BMG	$T_g^{onset}$ (°C)	$T_g^{inflexion}$ (°C)	$T_x$ (°C)	$\Delta T$	$T_p$ (°C)
Zr3 – Φ 3mm rods	387	402	486	99	500
ZrC - Φ 3mm rods	386	403	488	102	503
Cu2 - Φ 3mm rods	433	448	524	91	534

Table 3.2-1: Characteristic temperatures of Zr3, ZrC and Cu2 amorphous alloys with scanning speed of 40°C/min.

As it can be observed, Zr3 alloy exhibits a large supercooled liquid region ( $\Delta T \approx 100^\circ\text{C}$ ) which indicates a good thermal stability against crystallization. In comparison, the Vitreloy 4 ( $\text{Zr}_{46.25}\text{Ti}_{8.25}\text{Cu}_{7.5}\text{Ni}_{10}\text{Be}_{27.5}$ ), well known for its good thermal stability and workability in the

SLR, exhibits a  $\Delta T$  of  $105^\circ\text{C}$ <sup>15</sup>. Measured  $T_g$  and  $T_x$  are in agreement with the previous studies on Zr3 despite a small shift of  $5^\circ\text{C}$  due to the use of different scanning rates<sup>157</sup>.

### Crystallization kinetics study

A common way to evaluate crystallization phenomenon is to perform isothermal treatments by DSC at different temperatures in the SLR ( $T > T_g$ ). These isothermal treatments enable the measurement of the dissipated heat flow during time and therefore the determination of the crystallization onset time as well as the crystallization kinetic at a given temperature in the SLR. To be more accurate, it is possible to calculate the crystal volume fraction in the metallic glass, but this method can be difficult to realize because of the composition variation in the matrix and the crystals<sup>15</sup>. However, isothermal DSC technique provides an idea of the transformation evolution during the crystallization phenomenon. During the isothermal experiment, an exothermic peak due to crystallization process appears (Figure 3.2.2.a). Integration of the peak surface as a function of the time allows to evaluate the transformed fraction in the material at a given time. Isothermal measurements have been performed on Zr3 rods at  $420^\circ\text{C}$ ,  $430^\circ\text{C}$  and  $450^\circ\text{C}$ . These temperatures cover a large range of the SLR and so enable the extraction of proper behaviour information on the alloy in its future thermoforming working conditions.

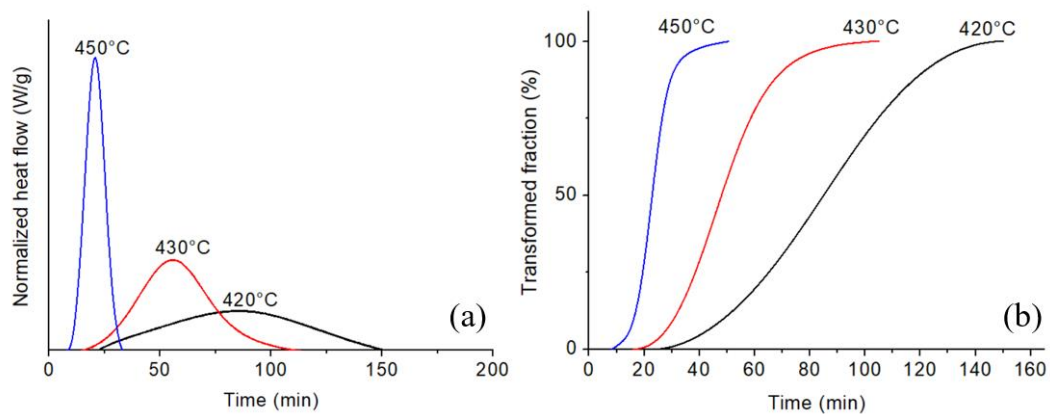


Figure 3.2.2: Isothermal DSC curves of a Zr3 rod at different temperatures (a). Transformed fraction calculated from the isothermal measurements (b).

Transformed fraction curves are presented in Figure 3.2.2.b. They give information about the crystallization kinetic in the amorphous alloy at temperatures lower than  $T_x$ . In this study, the aim is to thermoform amorphous alloy samples in the SLR before the crystallization occurrence and so before the start of the transformation. Thus, the only important parameter here is the crystallization onset time  $t_c^{onset}$  at a given temperature in the SLR. Assuming an homogeneous transformation in the volume, it is possible to calculate the crystallization activation energy  $E$ .

If  $t_x$  is the time required at a given temperature  $T$  to get a transformed fraction equal to  $x$ , the Johnson-Mehl-Avrami law (JMA) states that  $t_x$  follows an Arrhenius law as:

$$t_x = K \exp\left(-\frac{E}{RT}\right)$$

where  $K$  is a constant, and  $R$  the constant of the ideal gases. By plotting  $\ln(t_c^{onset})$  as a function of  $\frac{1}{RT}$  it is then possible to determine the crystallization activation energy  $E$ .

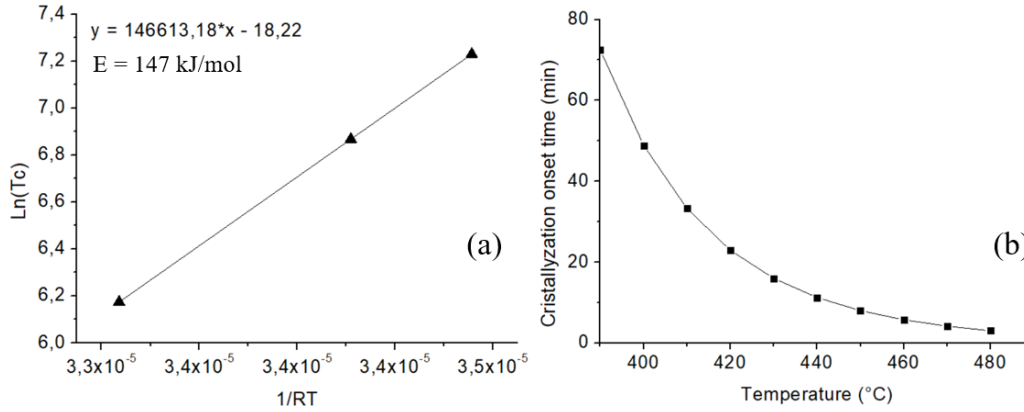


Figure 3.2.3: Plot of  $\ln(t_c^{onset})$  as a function of  $\frac{1}{RT}$  in order to determine the crystallization activation energy  $E$  of Zr3 (a). Crystallization onset time calculated from the activation energy  $E$  for every temperature in the SLR of Zr3 alloy (b).

As presented in Figure 3.2.3.a, the calculated crystallization activation energy  $E$  for the Zr3 amorphous alloy is equal to 147 kJ/mol, which corresponds to 1.5 eV. This value of  $E$  is in the range of the activation energies previously calculated for Zr-based metallic glasses<sup>157,16,15</sup>. From that, it is possible to calculate the crystallization onset time for every temperatures in the range of the SLR (Figure 3.2.3.b). Thus, it is possible to determine the critical time ( $t_{cryst}^{onset}(T)$ ) for thermomoulding experiments at a given temperature in the SLR in order to maintain the amorphous structure integrity by avoiding crystallization occurrence.

### 3.2.3. Deformation behaviour at high temperature

This part of the chapter will be dedicated to the study of the rheological behaviours of the Zr3 alloy to delimit its deformation regimes and so to be able to thermoform it in the most suited experimental conditions. For that, strain rate jumps tests experiments at different temperatures in the SLR were carried out. They allow one to evaluate the material strain rate sensitivity: the variation of the material viscosity  $\eta$  as a function of the applied strain rate  $\dot{\epsilon}$ . From that, two deformation regimes were outlined. The critical stress value  $\sigma_c$  between the two regimes was determined and the activation energy for the linear flow regime was calculated, as explained in

Chapter 1, at temperatures close to the room temperature, plastic deformation of metallic glasses is localized in a single shear band, leading to a critical failure of the material. The presence of a glass transition temperature  $T_g$  in the amorphous alloys materials makes this brittle behaviour turning into a viscoplastic and homogeneous deformation behaviour from a given temperature. This ductile behaviour allows the material to undergo very high viscoplastic strain without localization of shear bands.

### Strain rate jump experiments

Experimental parameters used in strain rate jump tests are detailed in Chapter 2. These tests enable the determination of rheological behaviours of the amorphous alloy in the SLR. Strain rates sequences varied between  $2.5 \times 10^{-4} \text{ s}^{-1}$  to  $1 \times 10^{-1} \text{ s}^{-1}$  with the last strain rate equal to the first or the second strain rate to be sure that no irreversible transformations such as crystallization occurred during the test. At the same time, crystallization onset times previously determined were used to proceed with experimental times lower than  $t_{cryst}^{onset}$  for every temperatures used in the SLR. To illustrate these experiments, two strain rate jump test curves at  $400^\circ\text{C}$  and  $410^\circ\text{C}$  are presented in Figure 3.2.4. A special care has to be made by the reader between the evolution of the different scales (strain rate and stress plateau values).

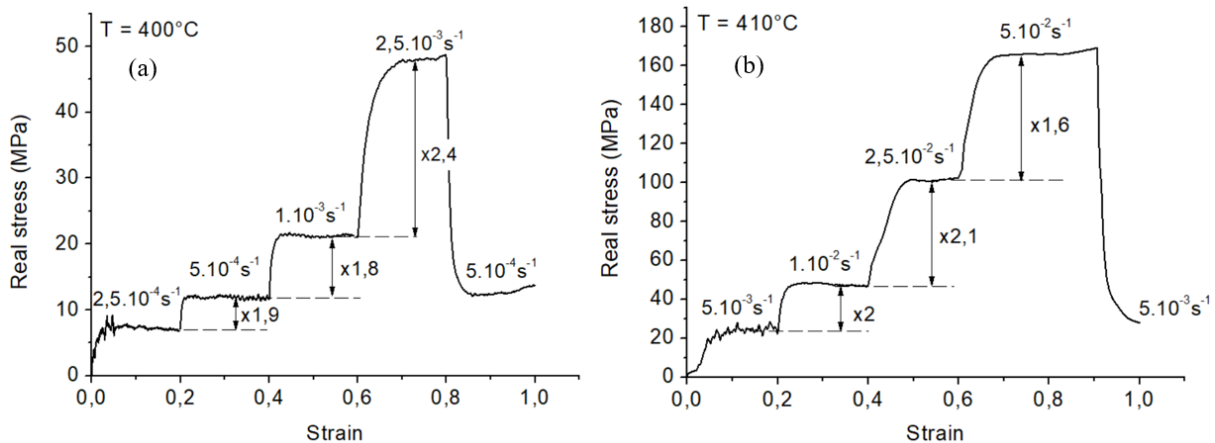


Figure 3.2.4: Curve of strain rate jump test realized at  $400^\circ\text{C}$  on Zr3 rods in the strain range of  $2.5 \times 10^{-4} \text{ s}^{-1}$  to  $2.5 \times 10^{-3} \text{ s}^{-1}$  (a), strain rate jump test curve realized at  $410^\circ\text{C}$  in the strain range of  $5 \times 10^{-3} \text{ s}^{-1}$  to  $5 \times 10^{-2} \text{ s}^{-1}$  (b).

First of all, these curves show the high deformation ability of the Zr3 amorphous alloy in the SLR, reaching a strain value of 1 at the end of the tests. Second, we observe that the resulted stress strongly depends on temperature and strain rate, as expected. Moreover, two different flow regimes can be highlighted by in these curves:

- At  $400^\circ\text{C}$  (Figure 3.2.4.a) for relatively low strain rates, we observe a linear ratio between the applied strain rate and the resulted stress. Indeed, by doubling the strain

rate from  $2.5 \times 10^{-4} \text{ s}^{-1}$  to  $5 \times 10^{-4} \text{ s}^{-1}$  (x 2), the resulted stress is also multiplied by almost 2 (1.9). At higher strain rate from  $1 \times 10^{-3} \text{ s}^{-1}$  to  $2.5 \times 10^{-3} \text{ s}^{-1}$  (x 2.5), the same tendency is observed with an almost identical ratio of 2.4 between strain rate and resulted stress plateau. This linearity between strain rates and resulted stresses means that the viscosity is independent from the strain rate: this is the Newtonian flow regime.

- At  $410^\circ\text{C}$  (Figure 3.2.4.b) at much higher strain rates (10 to 15 times higher than the test performed at  $400^\circ\text{C}$ ), we first observe the same linearity for low strain rates from  $5 \times 10^{-3} \text{ s}^{-1}$  to  $1 \times 10^{-2} \text{ s}^{-1}$  with the value of the stress plateau also multiplied by 2. However, by increasing the strain rate, we observe a decrease of the resulted stress plateau: with a strain rate multiplied by 2 (from  $2.5 \times 10^{-2} \text{ s}^{-1}$  to  $5 \times 10^{-2} \text{ s}^{-1}$ ) the resulted stress was only multiplied by 1.6. The reinforcement factor of 1.6 for a strain rate ratio of 2 means that the material's shear flow decreased with the strain rate and so have a non-Newtonian behaviour, which can also be called as a shear-thinning behaviour.

In this work, the strain rate jump tests were carried out from  $390^\circ\text{C}$  to  $430^\circ\text{C}$  and large strain rate ranges (see Chapter 2) allowed us to observe both deformation regimes (Newtonian and non-Newtonian) for each temperature. Finally, by decreasing the last strain rate of the experiment (strain from 0.8 to 1) to the first or the second strain rate previously applied ( $5 \times 10^{-4} \text{ s}^{-1}$  in Figure 3.2.4.a), we observed the same resulted stress plateau, which means that the stress plateau was independent from the thermomechanical history of the material and so that no crystallization occurred during the experiment. This result indicates the good reproducibility of the experiments with the Zr3 amorphous alloy. In contrary, strain rate jump tests experiments longer than the crystallization onset time will result to a brutal increase of the stress value due to the reinforcement induced by crystallization in the material.

### Viscosity analysis

From the strain rate jump test curves, it is possible to calculate the viscosity for every temperature/strain rate couples by the relation  $\eta = \frac{\sigma}{3\dot{\epsilon}}$  previously described in Chap. II. To determine the viscosity values, the flow stress values were taken on the plateau. These stress plateau can be described as flow stress in stationary regime. Then, it is possible to represent the viscosity values as a function of the strain rates for the different temperatures used during the corresponding strain rate jump tests. This plot is presented in Figure 3.2.5. In this plot, the two different deformation regimes can be observed: the **Newtonian regime** where the viscosity is independent from the strain rate and the **non-Newtonian** regime where the viscosity decreases when the strain rate increases. Increasing the strain rate at a constant temperature or decreasing the temperature at a constant strain rate results in the transition from the Newtonian flow regime to the non-Newtonian flow regime.

As explained in the thesis of Blétry<sup>16</sup>, it is possible to draw a master curve of the viscosity value by plotting normalized viscosity  $\eta/\eta_N$  as a function of the normalized strain rate  $\eta_N \times \dot{\epsilon}$  where  $\eta_N$  is the Newtonian viscosity (Figure 3.2.6.a) corresponding in this graph to the viscosity values that are constant with the strain rate. This master curve is presented in Figure 3.2.6.a. If the Newtonian regime cannot be reached experimentally (e.g. low strain rate at low temperature), it is possible to adjust each curve. This plot also shows the Newtonian viscosity evolution and to determine at which critical strain rate the flow regime is not Newtonian anymore. These values are presented in Table 3.2-2. The viscosity results are in agreement with previous studies of Inoue *et al.* on the rheological behaviour of this common BMG composition in the SLR<sup>157,158</sup>.

By knowing the Newtonian viscosity value  $\eta_N$  and the strain rate limit  $\dot{\epsilon}_{\text{limit}}$  at a given temperature in the SLR, it is possible to determine the critical applied stress  $\sigma_c$  from which the regime changes from Newtonian to non-Newtonian regime as  $\sigma_c = \eta_N \times 3 \dot{\epsilon}_{\text{limit}}$ . Because of the independency of the strain rate and the resulted stress plateau in the Newtonian regime,  $\sigma_c$  is constant. As observed in Table 3.2-2, from 400°C to 430°C, the average critical stress was determine to be 22.5 MPa. Because this value is an average value, and to ensure that the applied stress guarantee the Newtonian flow regime in the SLR, the critical stress value will be set at  $\sigma_c = 20$  MPa for the rest of the work.

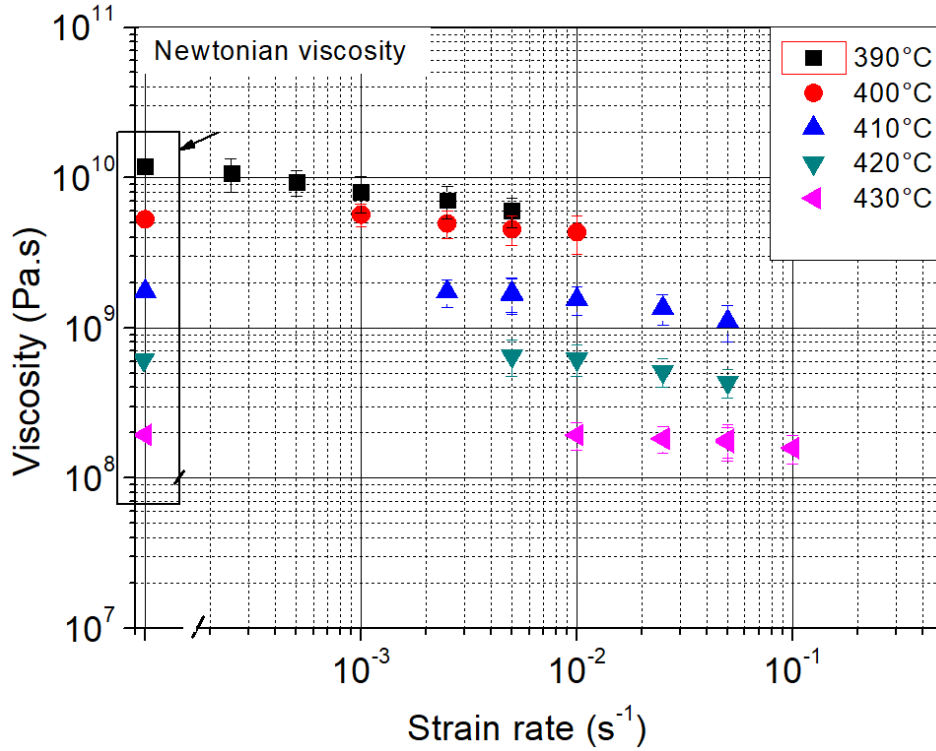


Figure 3.2.5: Values of the viscosity  $\eta$  as a function of the strain rate for different temperatures above the glass transition temperature  $T_g$ . Newtonian viscosities are represented in the left part of the graph. Inspired from Gravier thesis<sup>15</sup>.

	400°C	410°C	420°C	430°C
$\eta_N$ (Pa.s)	$5.2 \times 10^9$	$1.8 \times 10^9$	$6 \times 10^8$	$2 \times 10^8$
$\dot{\epsilon}_{limit}$ (s <sup>-1</sup> )	$1.5 \times 10^{-3}$	$4.2 \times 10^{-3}$	$1.2 \times 10^{-2}$	$4 \times 10^{-2}$
$\sigma_c$ (MPa)	24	23	21	22

Table 3.2-2: Newtonian viscosity  $\eta_N$ , critical strain rate  $\dot{\epsilon}_{limit}$  and critical applied stress  $\sigma_c$  above which we pass through non-Newtonian regime for Zr3 amorphous alloy.

### Activation energy of the Newtonian viscosity

To analyse the effect of the temperature on Newtonian viscosity  $\eta_N$ , we used an Arrhenius law relation as:

$$\eta_N = \eta_0 \exp\left(\frac{Q}{RT}\right) \quad (3.1)$$

where  $\eta_0$  is a constant,  $Q$  the activation energy and  $R$  the constant of the ideal gases. Plots of  $\ln(\eta_N)$  as a function of  $1/RT$  gives access to the activation energy of  $Q = 400$  kJ/mol with  $\eta_0 = 3.75 \times 10^{-22}$  Pa.s (Figure 3.2.6.b). The linear regression  $R^2$  is acceptable in this range of temperatures ( $R^2 = 0.998$ ). This calculated activation energy of 4.1eV is close to the activation energy obtained by Inoue *et al.* ( $Q = 3.8$  eV) and usually reported for Zr based amorphous alloys<sup>15,16</sup>.

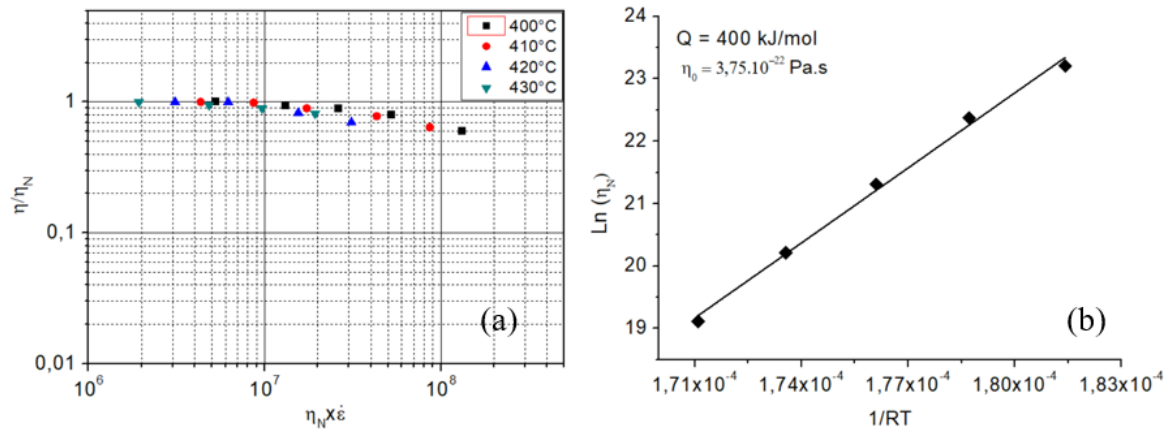


Figure 3.2.6: Normalised viscosity  $\eta/\eta_N$  as a function of the normalized strain rate  $\eta_N \dot{\epsilon}$  for the temperatures used experimentally (a). Plot of  $\ln(\eta_N)$  as a function of  $1/RT$  ( $R$  is the constant of ideal gases) allowing to calculate the Newtonian viscosity activation energy (b).

As observed in the master curve presented in Figure 3.2.6.a, in these ranges of strain rates and temperatures, the non-Newtonian flow regime is only reached at the highest strain rates. This is due to the fact that Zr3 alloy exhibits low viscosity in the SLR ( $5.2 \times 10^9$  to  $2 \times 10^8$  Pa.s in the range of  $T_g + 10^\circ\text{C}$  to  $T_g + 40^\circ\text{C}$  used in these experiments), meaning that higher strain rates have to be reached to better cover the transition zone to non-Newtonian flow regimes. Moreover, the compression device used and the sample sizes limit the possibility to reach very high strain rates. However, the aim of this work is to pattern and thermoform Zr3 BMG with micron to sub-micron sized moulds. Thus, the goal will be to keep the viscous material in the Newtonian regime to be able to control the flow. The non-linear flow regime has to be avoided and only the transition zone needs to be determined. Compared to the rheological studies in the thesis of Gravier<sup>15</sup> and Blétry<sup>16</sup>, the range of applied strain rates of this study is smaller, but the critical stress value of 20 MPa determined here is close to the critical stress values with other Zr-based amorphous alloys.

With this activation energy value of 400 kJ/mol, it is now possible to calculate the Newtonian viscosity of the Zr3 alloy for every temperature in the SLR. Experimentally, it will be possible to predict the Newtonian viscosity and also the range of acceptable strain rates to keep the deformed material in the Newtonian flow regime by knowing the maximum stress that can be applied ( $\sigma_c = 20$  MPa). Processing Zr3 samples in the linear flow regime is the best way to accurately control the filling time and the filling depth in patterned moulds<sup>136,137</sup>. Moreover, determination of the crystallization onset time in the SLR range of temperatures allows to optimize the processing condition to guarantee a good replication of the desired pattern without structural modifications in the material.

### 3.3. Thermoforming of Zr3 metallic glass

After determining the critical crystallization onset time and the rheological behaviour of Zr3 alloy for every temperature in the SLR, thermoforming experiments were conducted. In this part, the thermoplastic forming processing (TPF) investigated in air is present. The compression device for strain rate jump tests in air was used to get an idea of the feasibility of further surface patterning under oxygen environment. Processing results and limitations of thermoforming in air environment will be discussed.

#### 3.3.1. Preliminary study in air

Thermoforming tests in air were conducted using a compression device with a Si-mould as described in Chapter 2. Considering the previous study on the rheological behaviour of the Zr3 metallic glasses, and to ensure an homogeneous flow regime (Newtonian flow) of the material in the SLR, a working temperature of 420°C and a constant pressure of 15 MPa during 1 min have been chosen. Prior to compression test, a contact step of 30 sec at 50 N has been done to ensure an homogeneous heat diffusion for temperature homogenization in the sample. At 15 MPa and 420°C, regarding the Newtonian viscosity determined at  $\eta_N = 6 \times 10^8$  Pa.s (Figure 3.2.6.a), a strain rate of  $5 \times 10^{-3} \text{ s}^{-1}$  during the experiment was estimated. This value is lower than the critical strain rate value  $\dot{\epsilon}_{\text{limit}}$  of  $1.2 \times 10^{-2} \text{ s}^{-1}$  determined in the previous section because the applied stress was lower than the average critical stress  $\sigma_c = 20$  MPa. Additionally, regarding the Figure 3.2.3.b, the processing time has to be lower than 20 min ( $t_{\text{cryst}}^{\text{onset}}(420^\circ\text{C}) = 20\text{min}$ ) to avoid crystallization to occur. For this experimental conditions, a fast oxidation of the BMG surface is expected. Thus, a fast TPF experiment of 1 min was chosen to limit the oxidation phenomenon. These experimental parameters ensured suited working conditions with a Newtonian flow regime during a fast processing time.

Images of the Zr3 alloy after thermoforming in air are presented in Figure 3.3.1. First, it can be observed that the hot compressed sample have a blue dark colour with iridescent part on the periphery compared to the metallic colour of the BMG before the experiment. This aspect is the result of a massive oxidation during the hot compression process. A difference of colour has been noticed between the center of the compressed rod and the peripheral part. A purple-coloured circle in the centre is observed with a diameter of 3 mm corresponding to the rod diameter before the hot compression test. On the other way, the periphery of the compressed rod is iridescent (Figure 3.3.1a). As it can be observed in the optical microscope image, this

iridescent aspect do not come from the nanometric pattern of the Si-mould, but probably from the oxidation layer on the BMG surface. However, between these two areas, a circle of around 70  $\mu\text{m}$  in thickness presents rectilinear grooves on the surface resulting from the imprint of the Si mould (Figure 3.3.1.b.).

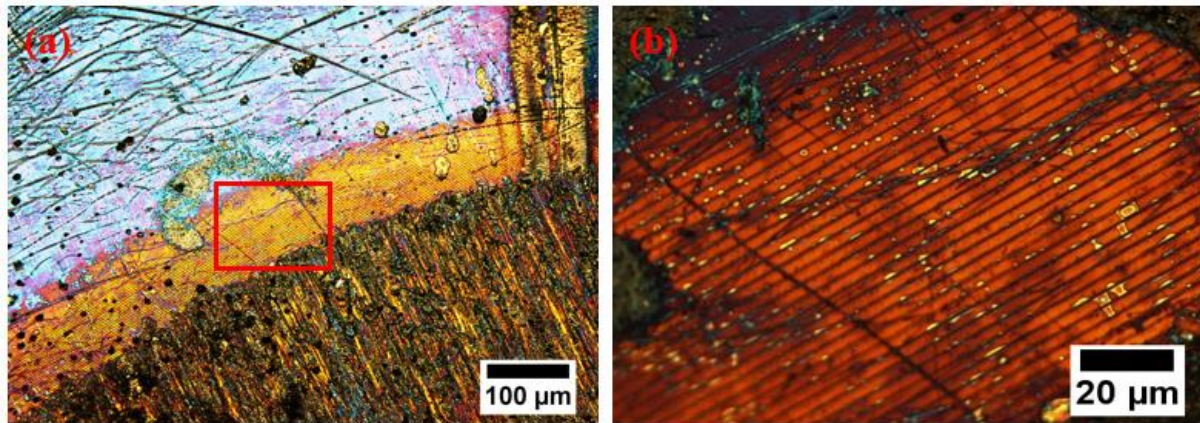


Figure 3.3.1: Optical microscope image of the compressed Zr3 sample surface (a), zoom on the textured surface region (b).

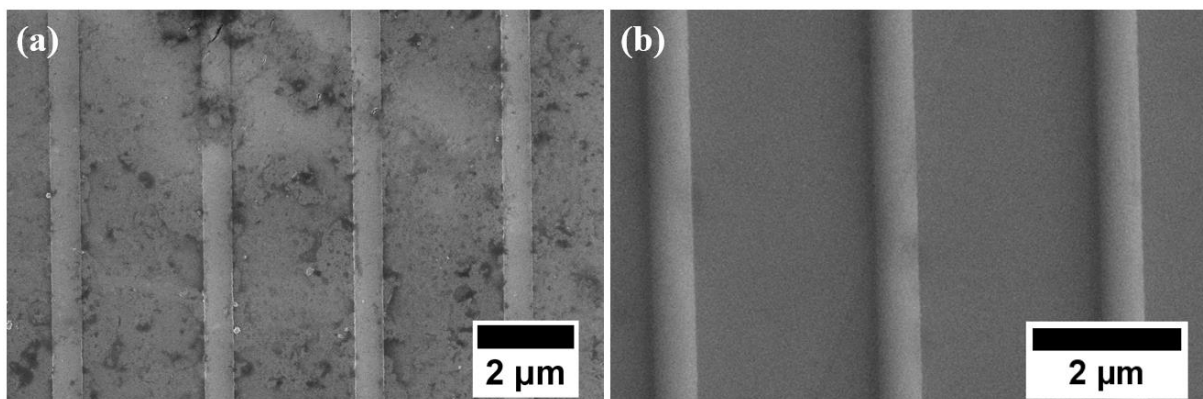


Figure 3.3.2: Backscattered electron (a) and secondary electron (b) SEM images of the Zr3 textured area.

The SEM images in Figure 3.3.2.a and Figure 3.3.2.b present two replicated areas on the BMG sample after TPF processing in air. Some oxidation traces and material debris can be observed with backscattered electron detector (Figure 3.3.2.a) which reveal the poor replication rate and the poor surface quality of the resulted textured surface. Moreover, shadow image made with the secondary electron detector indicates a round shape of the top part of the textured lines (Figure 3.3.2.b). Knowing that mould grooves have sharp edges at  $90^\circ$  (see Chap. II), the BMG sample did not fully filled the mould imprint and implying that compression time was too short. However, texturing process under air atmosphere seems to be possible at very specific locations on the surface.

The presence of these partially textured zone, surrounded by oxidised material might be the consequence of the material's flow during the compression test. The hypothesis put forward here is summarized in Figure 3.3.3. As soon as the rod sample is inserted and during the contact step of 30 s, its surface is oxidised, with a higher oxidation on the top and the bottom part in contact with the hot clamps and the hot Si mould compared to the sides (Figure 3.3.3.b). The shear flow phenomenon during the compression of the cylinder induces a fragmentation of the oxide layer created on the periphery compared to the central area. Then, during the hot compression, while conserving the same volume, the shear stress brakes the oxide layer to let appear a non-oxidised material part in the viscous state. This "clean" material area is partially protected from the oxidation due to the applied pressure and is able to fill the Si-mould (Figure 3.3.3.b). Finally, the resulted compressed BMG surface consists of a purple circle of 3mm in diameter at the centre where the oxidation is the strongest, surrounded with a partially textured area and an iridescent circle in the peripheral part (Figure 3.3.3.c).

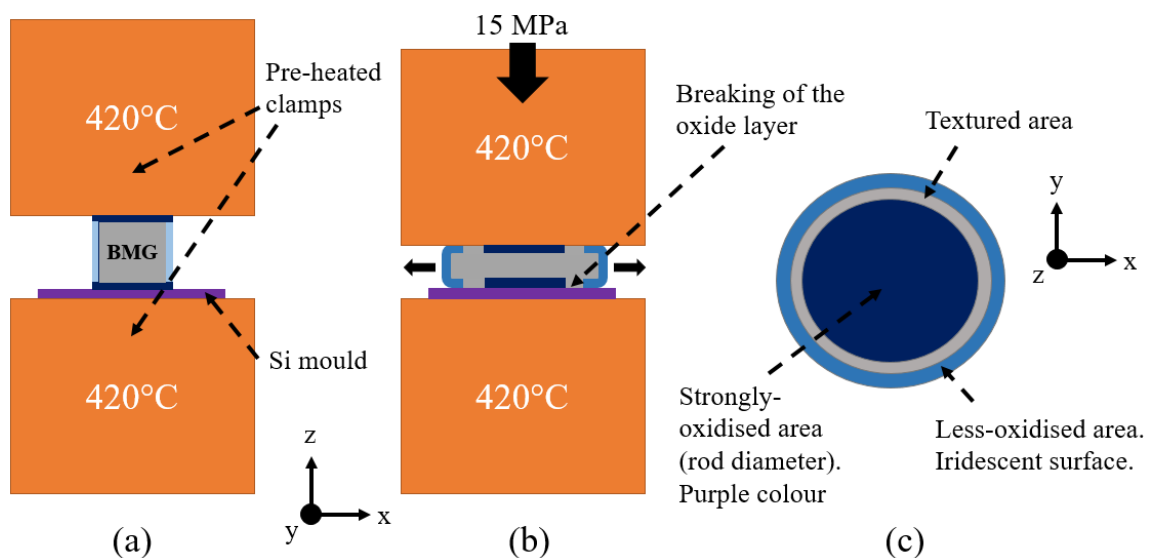


Figure 3.3.3: Scheme of the textured circle area upon hot compression in-air Zr3 cylinder.

In summary, two important information can be extracted from the results of this preliminary TPF study in air:

- The Zr3 amorphous alloy partially filled the Si mould on a circular zone. The complete filling was not reached due to the short time of the compression process (1min). However, this result indicated that the previous thermomechanical study of the Zr3 alloy properties are in agreement with the experimental thermomoulding tests. As it was developed in the Chap. I and explained by Li *et al.*<sup>136</sup>, under Non-Newtonian flow regime, the imprinting would be decrease because of the inhomogeneous flow and the

variation of the free-volume content in the material, which reduce the forming capability. Thus, the rheological behaviour knowledge of the Zr3 alloy makes possible to promote Newtonian flow regime and a better regulation of the filling conditions.

- In the SLR (viscous state), Zr3 amorphous alloy is clearly not resistant to oxidation under air atmosphere. Indeed, an oxide layer (probably a ZrO<sub>2</sub> oxide<sup>159,160</sup>) rapidly forms on the BMG surface (few seconds), making impossible the thermomoulding of the pattern on a large surface under these experimental conditions. Thus, surface texturing or moulding of this Zr-based BMG without oxidation will imply a controlled working atmosphere such as protective gas or vacuum environment.

The TPF processing tests in the SLR in air environment revealed a strong oxidation of the Zr3 alloy surfaces. In order to determine if this poor oxidation resistance is only present in the temperatures higher than T<sub>g</sub>, a simple oxidation resistance study has been conducted on a Zr-based BMG with a composition and T<sub>g</sub> close to Zr3 (T<sub>g</sub>=387°C). Heat treatments on BMG cylinders of 3 mm in diameter were done under three temperatures of 200°C, 250°C and 300°C during treatment time of 30, 60, 90 and 150 min. Photography of the cylinders after heat-treatment tests are gathered in the Table 3.3-1 below. As it is known, surface oxidation of metals and alloys changes their colours. Comparing the colour of each heat-treated specimens is an easy way to control its oxidation behaviour. However, no-colour changing after heat-treatment cannot guarantee a non-oxidised surface, as soon as Zr-based BMG naturally form a ZrO<sub>2</sub> layer in their surfaces at ambient temperature.

	30 min	60 min	90 min	150 min
200°C				
250°C				
300°C				

Table 3.3-1: Photography pictures of Zr-based alloys after heat treatment in air at different time and temperature.

No colour changing was detected between 90 to 150 min at 200°C, the BMG kept its grey metallic aspect. At 250°C, a slight colour changing was observed after 90 min of treatment and at 150 min the colour clearly changed to a less shiny brass aspect. Finally, at 300°C a colour changing is observed even after 30min, turning from gold colour aspect at 30 min to a darker copper-like colour at 90 min. Finally a slightly iridescent purple like aspect has been observed on hot compressed Zr<sub>3</sub> alloy at 300°C during 150 min. In conclusion, this test showed that Zr-base BMG are very sensitive to oxidation, even at temperatures lower than  $T_g$ . Thus, regarding both the results of TPF in air tests and oxidation tests, there is no way to accurately pattern Zr<sub>3</sub> BMG under non-protective atmosphere. From that, a new compression device under vacuum has been created to be able to thermoform Zr<sub>3</sub> samples with limited oxidation issues.

### 3.4. Thermoforming of Zr<sub>3</sub> BMG under vacuum

This section is dedicated to the overall process resulted to the thermoforming of Zr<sub>3</sub> BMG surface under protective atmosphere. As previously explained, the poor oxidation resistance of Zr<sub>3</sub> and more generally of Zr-based BMG, even at temperature lower than  $T_g$ , prevents them from accurate thermoforming in the viscous state under oxygen environment. To solve this issue, a hot compression in-vacuum device has been specially designed. However, as detailed in Chapter 2, the elaboration of a heating device under vacuum induced different technical issues to overcome such as heat transfer and electric arc generation. Results of thermomoulded micron-size parts with Si-moulds and comparison between experimental and theoretical filling time will be presented. The work on surface texturing with femtosecond laser-textured moulds will be presented.

#### 3.4.1. Hot compression tests under vacuum environment

Due to heat transfer issue under vacuum, it is necessary to determine the scatter between the working temperature (real) on the compression plate surface and the measured temperature with the thermocouples. To do so, strain rate jump tests were performed under vacuum ( $\approx 10^{-4}$  mbar) with Zr<sub>3</sub> cylinders of 5 mm in diameter and 7.5 mm in height to maintain an aspect ratio of 1.5. The imposed strain rates were  $2.5 \times 10^{-2} \text{ s}^{-1}$ ,  $5 \times 10^{-2} \text{ s}^{-1}$  and  $1 \times 10^{-1} \text{ s}^{-1}$  in the range of 430°C to 450°C by taking care of remaining in the Newtonian domain. By knowing the Newtonian activation energy of Zr<sub>3</sub> amorphous alloy, it is possible to determine theoretically the associated stress plateau for a given strain rate for each temperature in the SLR. Thus, plotting the

theoretical stress plateau values as a function of the working temperature and by comparing them with the stress plateau values measured under vacuum, is it possible to evaluate the temperature measurement errors.

Figure 3.4.1 displays theoretical stress plateau curve (square) and the experimental stress plateau curve with at a strain rate of  $2.5 \times 10^{-2} \text{ s}^{-1}$ . A difference of  $-5^\circ\text{C}$  to  $-7^\circ\text{C}$  can be observed between measured and theoretical temperatures meaning that the thermocouple have a tendency to underestimate the real temperature. The scatter might not be as constant during thermomoulding as during strain rate jump tests because of the experimental conditions (mould, graphite and aluminium sheets...). Thus, a special care will be given to adjust the real working temperature for every hot compression experiments.

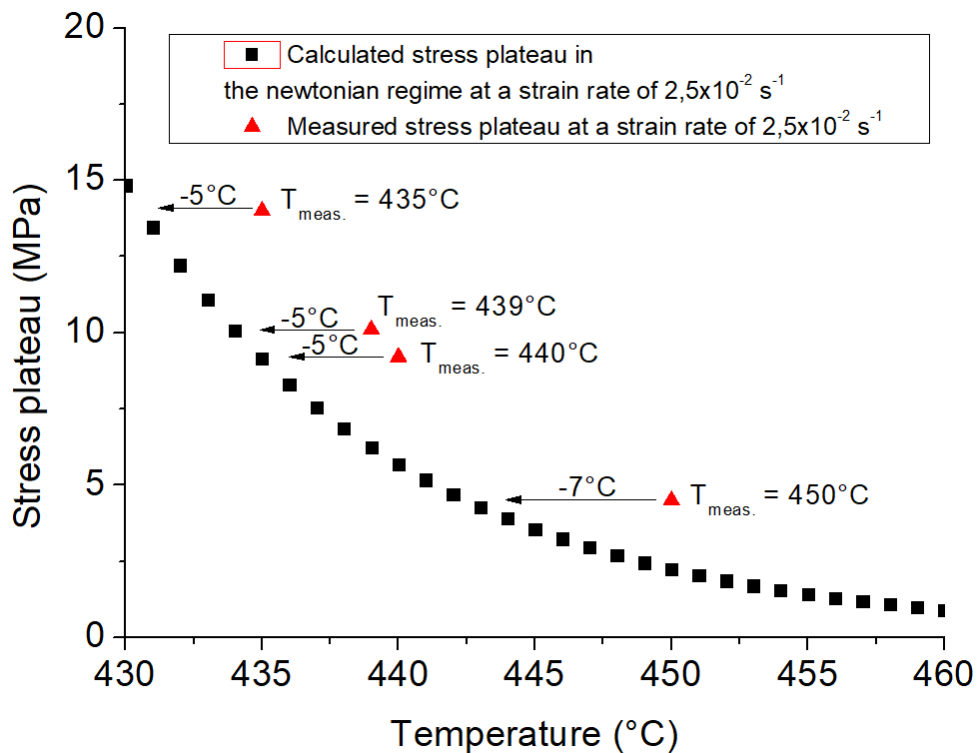


Figure 3.4.1: Graph of the theoretical and measured stress plateau evolution as a function of the temperature at a strain rate of  $2.5 \times 10^{-2} \text{ s}^{-1}$  with Zr3 amorphous alloy.

From these comparisons, every temperatures measured during thermoforming experiments under vacuum were corrected to obtain a good agreement between the rheological study and the compression tests. Temperature and viscosity values presented in this part were all corrected considering this practical test.

### 3.4.2. Replication of micron-size parts using Si-moulds by TPF process.

Under Newtonian regime and above nanometre size imprinting, viscous flow filling processes do not take into account capillary effects and can be described with an Hagen-Poiseuille flow behaviour (eq.1.10). and so the required stresses to fill the mould cavities are much lower than for patterned geometries smaller than 100 nm in the case when wetting is not accounted for. Thus, working with these moulds is a way to evaluate viscous Zr<sub>3</sub> alloy formability: its capacity to accurately reproduce mould pattern and to determine if the experimental filling rates during TPF experiments are in agreement with the theoretical filling rates by using the Hagen-Poiseuille law presented in Chapter 1.

The study of the rheological properties of Zr<sub>3</sub> BMG enables the average critical stress ( $\sigma_c = 22.5$  MPa) to be calculated, above which the regime becomes non-Newtonian. In order to optimize the filling rates during the thermoforming experiments under vacuum, the applied stress was always set to a “reasonable” stress  $\sigma = 20$  MPa. Hence, the highest strain rates during the compression tests in the Newtonian flow regime can be imposed. The experimental parameters used in TPF processing under vacuum and Si-mould specifications are presented in Chapter 2.

#### Thermoforming experiments at $T \approx 420^\circ\text{C}$

As explained above, the applied stress was set to the critical stress value of 20 MPa (constant stress during compression tests). At this stress, strain rate ( $1.5 \times 10^{-2} \text{ s}^{-1}$ ) is inside the Newtonian flow domain as expected. The calculated Newtonian viscosity of the alloy at  $420^\circ\text{C}$  was  $\eta_N = 5.3 \times 10^8 \text{ Pa}\cdot\text{s}^{-1}$  the Si-mould have a constant depth of  $l = 170 \text{ }\mu\text{m}$ . According to Hagen-Poiseuille law (eq.3.2), for a  $l/d$  ratio of 1.13 (with the largest mould cavity width being  $d = 150 \mu\text{m}$ ), the required time to reach the bottom of the mould ( $L = 170 \text{ }\mu\text{m}$ ) is 180 s. In order to verify the good agreement between theoretical filling rate  $l = f(t)$  and the TPF experiments at  $T = 420^\circ\text{C}$ , three compression tests at 30 s, 60 s and 120 s were selected before the material had reached the bottom of the mould ( $t = 180$  s). Moreover, due to side effects and stress gradient into the cavity, the complete filling of the edges of the mould is not expected at  $t = 180$  s. Thus, a last compression experiment during  $t = 300$  s was performed to let the material filling the entire mould cavity. The overall processing times in the SLR are smaller than the crystallization onset time previously determined for the Zr<sub>3</sub> alloy at  $420^\circ\text{C}$  (24 min). After each compression test,

the Si-moulds were dissolved under 25% mol. KOH solution in order to reveal the thermoformed parts on BMG compressed plates.

Figure 3.4.2 presents cross-sections and three-dimensional reconstructed images of the four experiments conducted at 30 s, 60 s, 120 s and 300 s under 420°C at the critical applied stress  $\sigma_c$  (20 MPa). Dashed lines on the three-dimensional reconstructed images show the regions where the cross sections were performed. The width difference between each cross sections is due to the difficulty to cut perpendicularly to the structure. However, every images were taken on cavities where the design exhibits a width of 150  $\mu\text{m}$ . Dashed lines on cross sections represent the mould cavity length, as explained above, the width is not respected. Filling lengths were measured by both microscopic and stereopairing techniques in order to get accurate and statistically representative data. As it can be observed, after 30 s of compression, the viscous BMG only filled about 80  $\mu\text{m}$  at the maximum height (top of the material, where the filling speed is the highest). Increasing compression time increased the filling length by reaching 103  $\mu\text{m}$  after 60 s, 163  $\mu\text{m}$  after 120 s and finally full-filled the Si-mould largest cavity after 300 s. These values were taken for the largest cavity (150  $\mu\text{m}$ ) with an aspect ratio of  $l/d = 170/150 = 1.1$ . As it can be observed on Figure 3.4.2 and Figure 3.4.3, the overall large channels were fully filled at 300 s of compression time, and the perfect edges of the silicon moulds were replicated on the BMG. In these experimental conditions, the cavities with an aspect ratio  $l/d = 1.1$  (170/150) are totally filled after 300 s with good reproduction of the edges. However, as it can be observed on the Figure 3.4.3.d in the circle zone, after 300 s, the smaller cavity part with a width of 60  $\mu\text{m}$  and thus an aspect ratio  $l/d = 2.8$  (170/60) are not totally filled and present a rounded shape. For the same experimental conditions, this part of the mould will thus require longer filling time to be fulfilled.

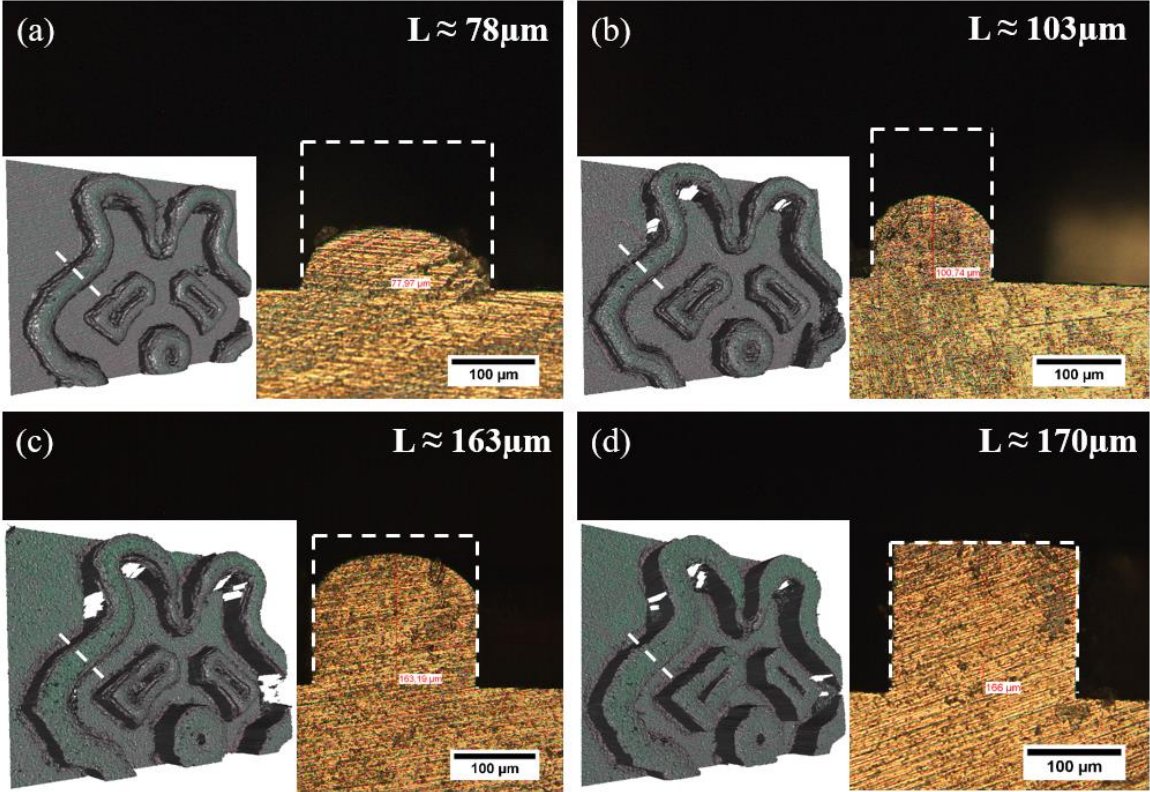


Figure 3.4.2: Microscope images of thermoformed BMG plates cross sections and stereoscopic imprint reconstructions of hot compression tests conducted at 420°C under constant stress of 20 MPa during 30 s (a), 60 s (b), 120 s (c) and 300 s (d) compression time.

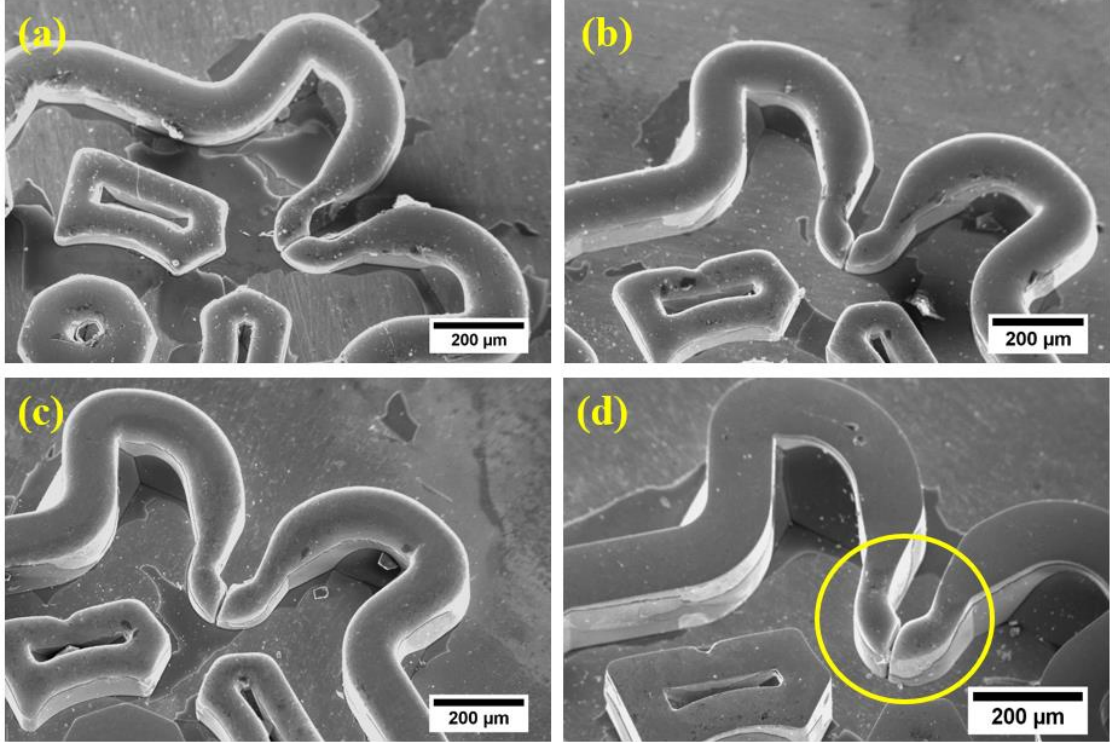


Figure 3.4.3: Tilted SEM images of the reproduced watch micro-piece on BMG after experiments under 420°C and 20 MPa during 30 s (a), 60 s (b), 120 s (c) and 300 s (d) compression time.

Experimental reproducibility evaluation of the thermomoulding tests in agreement with viscous flow theory was done by assembling measured filling depth at 420°C with the theoretical filling depth based on the Hagen-Poiseuille flow as described hereafter. In the case of a Newtonian flow regime and for micrometre size patterns, the filling length  $L$  of a cavity with a width  $d$  can be written as:

$$L = d \sqrt{\frac{P \times t}{6 \times \eta}} \quad (3.2)$$

where  $P$  is the applied pressure,  $t$  the filling time and  $\eta$  the BMG viscosity ( $= \eta_N$  in the case of a Newtonian flow regime). Figure 3.4.4 presents theoretical filling length curve from eq. 1.1 and experimental filling length measured at 420°C with the critical applied stress of 20 MPa as a function of the compression time for a 150  $\mu\text{m}$ -thick cavity. As it can be observed, experimental points fit well with the theoretical curve. The estimated Newtonian viscosities and the measured temperatures on the Inconel-316 plates are very close (1-2°C) to the real experimental temperatures of the mould and the BMG. This good agreement between experimental and theoretical values reflects the good agreement of the experimental tests under these conditions and also validates rheological properties of the amorphous alloy previously measured under air environment.

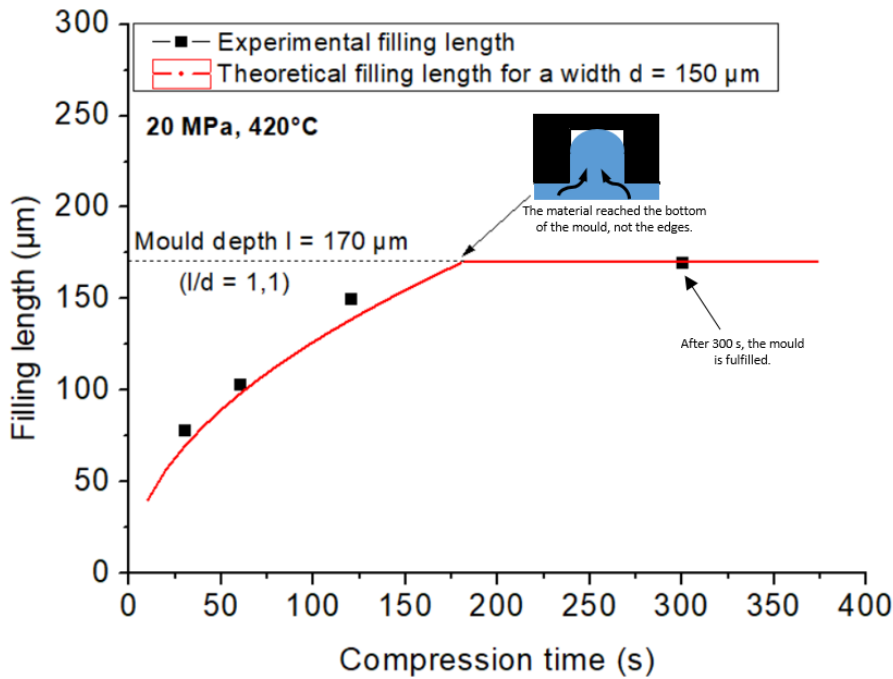


Figure 3.4.4: Plot of the experimental filling length and theoretical filling length curve as a function of the compression time for thermoforming tests at 420°C with constant applied stress equal to the critical stress  $\sigma_c = 20$  MPa.

### Optimization of the compression process for a complete filling

Values between experimental behaviour and thermoforming process has been validated in agreement with theoretical filling rates. It is then possible to predict the time required to fill the thinner groove of the micro-part at 420°C under the same constant stress of 20 MPa by knowing  $l = f(t)$ . For better clarification, aspect ratio  $l/d$  will be used to estimate the required compression time. In the case of the thinner groove,  $l/d = 170/60 = 2.8$ , Figure 3.4.5 shows the graph plotting  $l/d$  filling ratios as a function of the compression time at  $\sigma_c = 20$  MPa for temperatures of 420°C, 430°C and 440°C and the corresponding crystallization onset time  $t_{cryst}^{onset}$  for the 3 temperatures previously selected. At 20 MPa, strain rates under these temperatures are in the Newtonian flow regime.

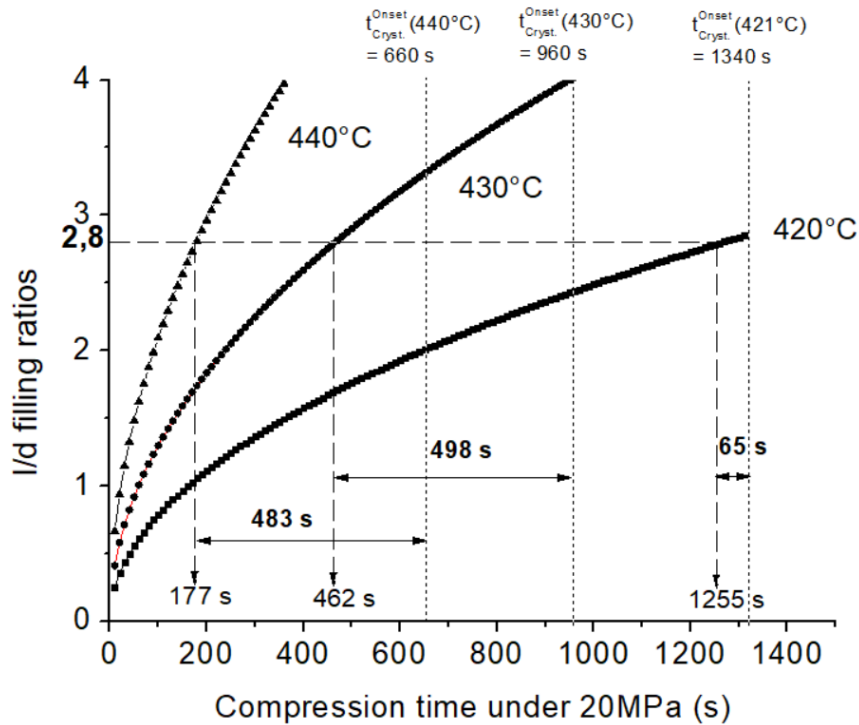


Figure 3.4.5: Plot of the aspect ratio ( $l/d$ ) evolution as a function on the compression time at 20MPa for 421°C and 430°C with the thinner cavity part width of  $d = 60\mu\text{m}$ .

At a Newtonian viscosity of  $5.3 \times 10^8 \text{ Pa}\cdot\text{s}^{-1}$  (420°C), a  $l/d$  ratio of 2.8 is reached after a compression time of 1255 s. However, it has been estimated that the crystallization onset time  $t_{cryst}^{onset}$  at this temperature is about 1340 s. So, for such conditions, only a remaining time of about 60 s is estimated. Considering the experimental time  $t_{exp}$  of 3 min before compression, and the additional time required to fill the mould edges, the filling of the entire micro-part at 420°C is not possible with the Zr3-BMG.

In contrary, by increasing the working temperature and so by decreasing the Newtonian viscosity, filling times for a  $l/d$  aspect ratio of 2.8 are passing respectively to 462 s and 177 s for 430°C and 440°C under critical applied stress of 20 MPa. Moreover, onset crystallization times are estimated respectively to 960 s and 660 s for 430°C and 440°C. In these conditions, Zr3-BMG sample will have remaining times of around 8 min before starting to crystallize. The addition of the contact time before compression with the theoretical compression time and with the additional time at the end of the compression to fill the edges, show that in these experimental conditions, it will be theoretically possible to fill the entire micro parts while maintaining the integrity of the amorphous structure.

#### Thermoforming experiment of Si-mould at higher temperature

In order to validate these filling rates estimations, thermoforming experiments have been conducted under the critical pressure of 20 MPa at a working temperature close to 440°C (442°C) during 250 s to ensure the complete filling of the mould edges. As for every experiment using the compression device in vacuum, the accurate set of the temperature was difficult and an equivalent temperature of 442°C between top and bottom compression plates was used. Comparing this slight temperature increasing (442°C) to the theoretical filling curve, it is obvious that the filling time required here will be even smaller, turning from 177 s to 148 s for 440°C to 442°C, respectively.

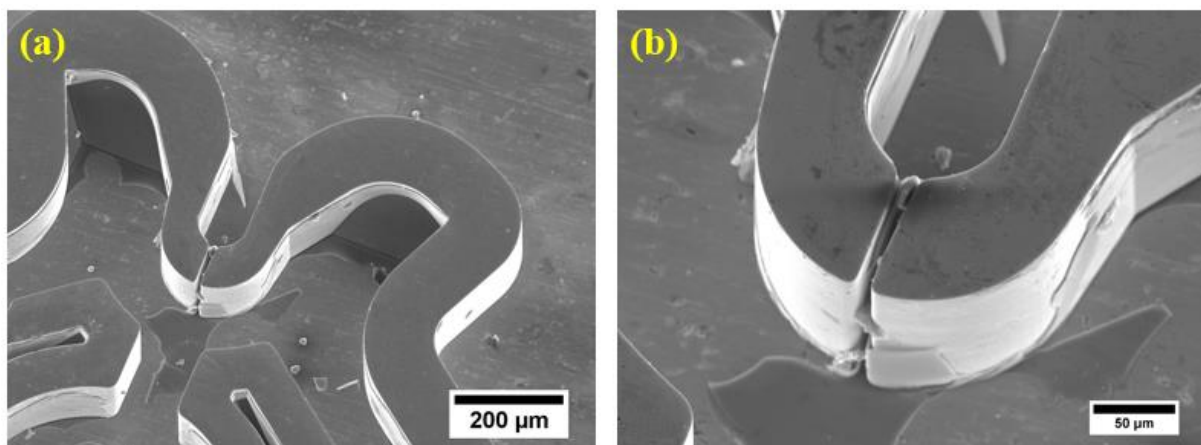


Figure 3.4.6: Tilted SEM images of the micro-piece thermoformed under constant pressure of 20 MPa at 442°C during compression time of 250s (a), zoom on the thinner part of the micro piece (b).

The resulted thermoformed micro-part under these experimental conditions is presented in Figure 3.4.6. As it can be observed, these thermoforming parameters enabled to fully and accurately replicate the entire mould geometry with sharp edges on the thicker and the thinner mould cavity parts. The thin darker layers observed in some area of the micro piece and the

BMG surface is a remaining SiO<sub>2</sub> layer from the mould surface that has not been entirely removed during KOH etching. Indeed, SiO<sub>2</sub> etching rate under KOH solution is really small compared to Si. The prediction using theoretical filling rates are then in good agreement with the experimental conditions and it will be possible to use these experimental conditions in order to produce a large amount of micro parts with high accuracy and good surface finishing.

As it has been observed in Figure 3.4.5, to improve the TPF process, higher working temperatures in the SLR has to be reached. However, the crystallization time decreases with temperature and so an optimal processing condition has to be found to obtain the largest l/d filling ratio before crystallization. By knowing the filling rates for every Newtonian viscosities in the SLR, it is possible to determine the maximum reachable l/d ratio for every temperature under optimized experimental conditions. Indeed, the maximum compression time  $t_{comp}^{max}$  at a temperature  $T$  is  $t_{comp}^{max}(T) = t_{cryst}^{onset}(T) - t_{exp}$ , where  $t_{exp}$  is the experimental time required to ensure good contacts and temperature homogeneity (= 3min in this experimental device) and  $t_{cryst}^{onset}(T)$  is the crystallization onset time at a temperature  $T$ . The critical compression stress that it is possible to apply to keep a Newtonian flow regime was estimated to be  $\sigma_c = 20$  MPa. Figure 3.4.7 shows the l/d ratios and the maximum compression time under the optimized experimental parameters. As it can be observed, the maximum l/d ratio that can be reached with Zr3 amorphous alloy is  $l/d \approx 7$  for a working temperature of 465°C and a compression time of 110 s. At higher temperature, the time remained for the compression process is too low and so the l/d ratio decrease drastically. In conclusion, this rheological study and the TPF experiments revealed a good agreement between theoretical filling rates and experimental tests and enable to determine the maximum l/d ratio of 7 at 465°C that is possible to reach with Zr3 bulk metallic glass.

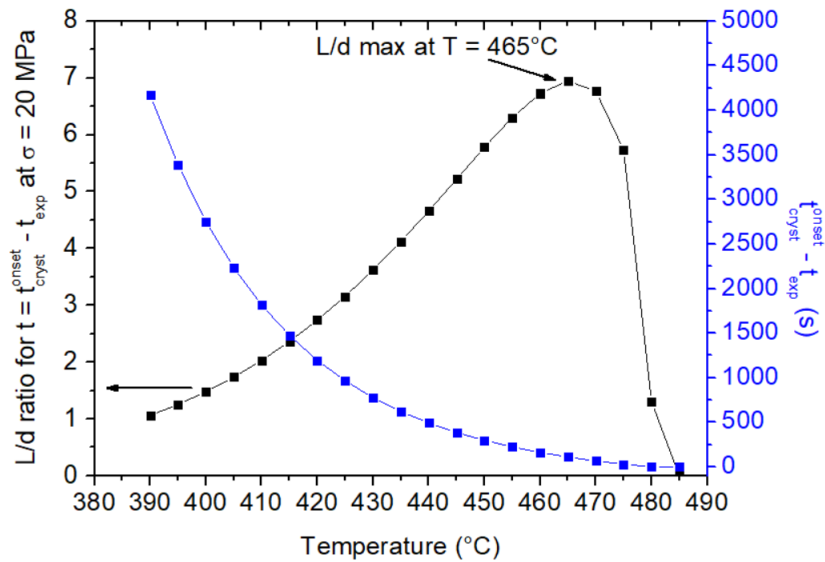


Figure 3.4.7 : Maximum l/d ratios at  $t = t_{cryst}^{onset}$  for an applied stress just below the critical stress ( $\sigma = 20$  MPa) and  $t_{cryst}^{onset} - t_{exp}$  as a function of the temperature for Zr3 amorphous alloy.

### 3.4.3. Thermoforming of nanometre size patterns

The previous part of the chapter was dedicated to the determination of the filling rate  $l = f(t)$  of viscous Zr3 amorphous alloy in moulds with different l/d aspect ratios under optimized experimental parameters ( $\sigma = \sigma_c = 20$  MPa). This study revealed the good agreement between theoretical filling predictions with experimental tests, and also validated the rheological properties of Zr3 BMG determined in the first section of this chapter. This section is now dedicated to TPF processing of sub-micron size patterned moulds. Femtosecond laser treatment can produce nanometre-size periodic ripples network at the surface of various types of materials. Thus, we decided to combine both surface treatment techniques used in this thesis. In order to do that, tungsten disks were textured with femtosecond lasers and then, laser-induced surface texture reproduction capacity of Zr3 alloy was investigated using TPF processing technique under vacuum.

#### Surface characterization of laser treated tungsten mould

Laser Induced Periodic Surface Structure (LIPSS) was chosen to be replicated because it is suitable to be used as mould pattern: valleys are not thinner on the top of the crest than on the bottom and so the filled material will be removable more easily without thermo-welding effects. A cross section image of LIPSS texture on ZrC amorphous alloy is presented in Figure 3.4.8. Because LIPSS morphology and periodicity are not related to the material but to the intrinsic

laser characteristics, it is assumed that the LIPSS texture created on tungsten will have the same topographic properties and thus might be suitable for TPF experiments as mould patterns.

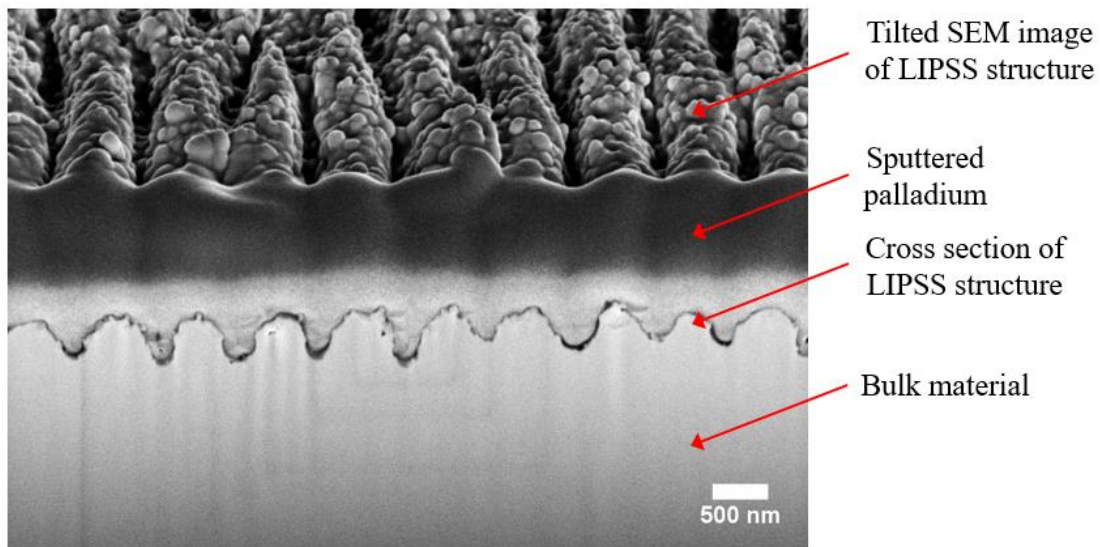


Figure 3.4.8: FIB cross section image of LIPSS texture realized by femtosecond laser treatment on ZrC amorphous alloy.

Tungsten disks dimensions and experimental laser parameters used to pattern the surfaces with Laser-Induced Periodic Surface Structures (LIPSS) are detailed in the Chapter 2. Figure 3.4.9.a shows an image of a tungsten disk textured with femtosecond laser on which LIPSS has been formed. Iridescent phenomenon observed on the textured surface (Figure 3.4.9.a) comes from the diffraction-grating network produced by the nanometre-size periodic pattern as presented on the SEM image in Figure 3.4.9.b. The circle on the SEM image shows the end of a ripple of the texture beyond which the other two closest ripples approach themselves and thus maintain the periodicity of the network. The textured structure consists in rectilinear periodic ripples with a periodicity of  $\Lambda_{\text{LIPSS}} = 740 \pm 60$  nm, perpendicularly oriented to the laser beam polarization.

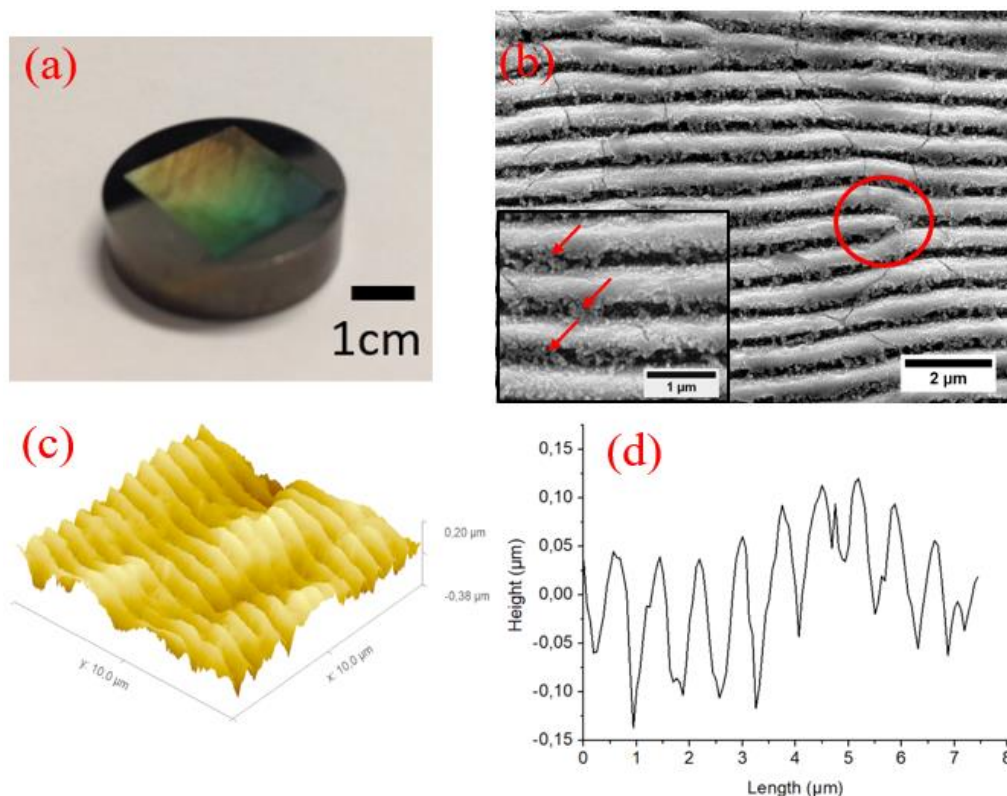


Figure 3.4.9: Picture of a textured tungsten mould with LIPSS (a), SEM image (b), AFM image (c) and 2D roughness profile on the direction perpendicular to the structure orientation (d) of the tungsten cylinder surface textured on a 100mm<sup>2</sup> area with LIPSS produced by femtosecond laser treatment

Periodicity of LIPSS textured on W moulds are close to the periodicity of LIPSS measured on textured amorphous alloys ( $750 \pm 50$  nm) because LIPSS morphology is mostly related to the laser wavelength and for a same laser, almost the same structure geometry will be observed on different types of materials. As it can be observed on the zoomed SEM image (Figure 3.4.9.a), redeposited particles from laser ablation are visible in the texture's valleys (red arrows). The AFM image in Figure 3.4.9.c shows that the tungsten surface is not perfectly flat after the laser treatment, meaning that a roughness on a larger scale than the roughness induced by the LIPSS is present. Prior to laser processing, tungsten cylinders had a mirror-like finishing aspect (1  $\mu$ m polished). Thus, this topographic change may be induced by the laser treatment, which did not ablate homogeneously the tungsten surface. Figure 3.4.9.d shows that the LIPSS structure textured on tungsten mould is not as deep as expected: where the depth of the structure is about 400 nm on metallic glass, on tungsten the average depth between ripple top and valleys is only 140 nm. This difference may be due to the presence of large amount of redeposited particles from ablation which may fill a part of the structure. Cleaning procedures with ultrasound was not successful to remove these particles, which means that they were redeposited on the LIPSS surface in the liquid or semi-liquid state and are strongly attached to the material surface.

### Thermoforming of Zr3 alloy with tungsten moulds

Multiple thermoforming experiments have been performed with Zr3 BMG plates between 1 to 1.3 mm thick and surface areas from 90 to 120 mm<sup>2</sup>. As it has been previously studied in the case of micron-size Si-moulds, experimental parameters which can vary are the working temperature  $T$ , the compression time  $t$  and the applied stress  $P$ . Effective experimental parameters were already validated with Si-mould thermoforming tests and so we choose to use same experimental conditions for LIPSS replication tests. Because of heat transfer problems under vacuum as explained in the Chap. II, an optical pyrometer was placed to target the tungsten mould before and during compression tests to get a more accurate value of the working temperature on the BMG-mould contact surface. Thus, first thermoforming experiment of Zr3 BMG with LIPSS textured tungsten surfaces has been done under the critical pressure of 20 MPa during 120 s with a mould temperature of 400°C. Working temperature of 400°C was low compared to previous work with Si-moulds: this was mainly due to a poor contact efficiency during the experiment, resulting to a very low thermal transfer between the tungsten cylinder and the Inconel compression plates. Indeed, compression plates were stabilized at 440°C during the experiments. However, under such non-optimized experimental conditions, the size of the nanometre pattern makes possible the use of the classical Hagen-Poiseuille law without considering capillary effects<sup>19,138</sup>. Thus, we considered an average width of the ripples of  $d = 500$  nm which is the medium value of the LIPSS period (740 nm) and the width on the bottom of the valley ( $\approx 240$ nm). The theoretical filling speed at 400°C presented in Figure 3.4.10 predicted a filling length of 140 nm (the average depth of the LIPSS) after almost 100 s, which is less than the compression time used in the experiment ( $t = 120$  s).

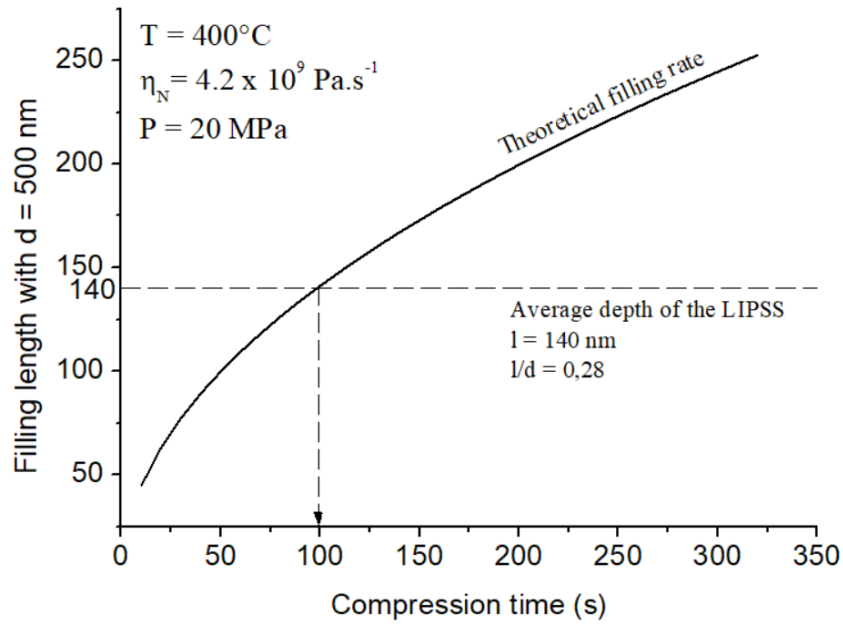


Figure 3.4.10: Theoretical filling length as a function of the time for a temperature of 400°C and an applied pressure of 20 MPa for a  $d = 500 \text{ nm}$  width cavity.

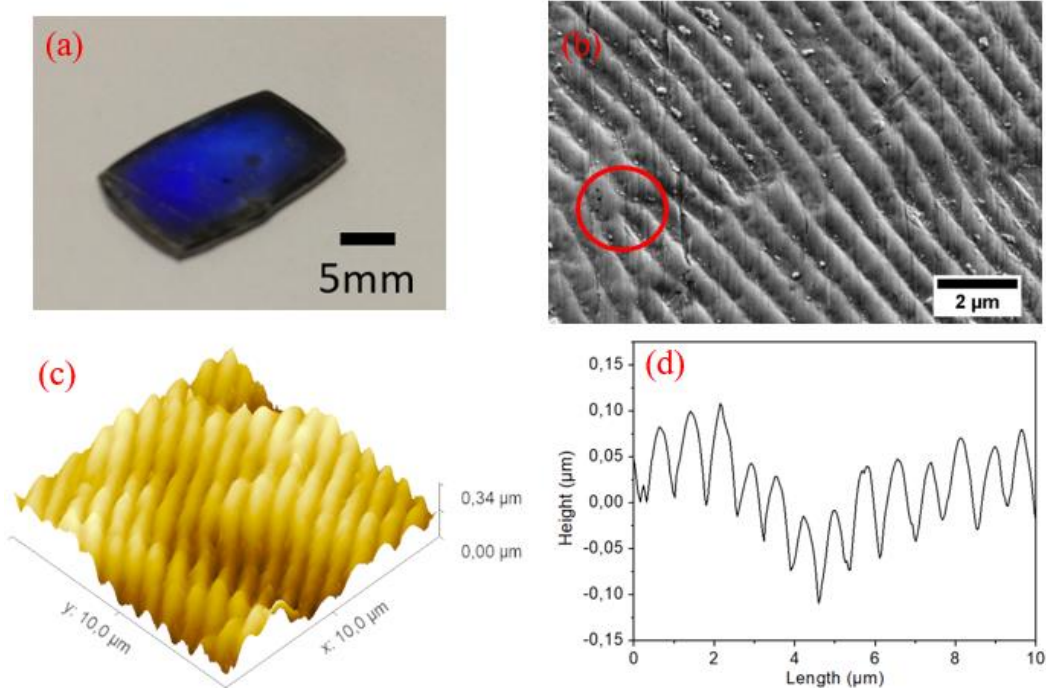


Figure 3.4.11: Picture of a thermoformed Zr3 plate (a), tilted SEM image (b), AFM image of a  $100\mu\text{m}^2$  surface (c), and 2D roughness profile on the direction perpendicular to LIPSS orientation (d) for a Zr3 BMG thermoformed at  $\sigma = \sigma_c = 20 \text{ MPa}$  and  $T = 400^{\circ}\text{C}$ .

Figure 3.4.11 shows the result of a thermoformed BMG plate image with the previously presented experimental parameters: image of the Zr3 plate after TPF processing (a), SEM image of its textured surface (b), AFM  $10 \times 10 \mu\text{m}^2$  image of the reproduced surface topology (c) and the resulted 2D topological profile in height (d). As it can be observed in Figure 3.4.11.a, like

on textured tungsten mould, BMG plate textured surface is also iridescent, but mainly reflect blue colour spectra in every viewing angle directions. This colour changing between mould and BMG plate may indicate a difference in the surface topology<sup>6,119</sup>. An intensity gradient of the iridescent phenomenon is also observed on the surface of the BMG, where the more intense zone is on the plate centre and decreases in the external direction to be not visible anymore at the extreme border of the sample. As it is explained in the Annex B, without any boundary conditions in radial direction, the material is spread and because we worked under constant force, a stress gradient was induced from the centre to the border of the sample during the thermoforming process.

Tilted SEM image in Figure 3.4.11.b shows the LIPSS texture reproduced from the tungsten mould on the centre of the BMG plate (higher stress zone during TPF). Rectilinear ripples can be observed, which correspond to the negative topology of the tungsten mould. On the valleys, some debris are present, but as demonstrated by XRD experiments in section 3.5, they do not come from tungsten mould and so they might be just uncleaned dust particles. The circle on the SEM image shows the negative replication of the ripple break observed on the SEM image of the mould in Figure 3.4.9.b. AFM image presented in Figure 3.4.11.c shows the surface topology of the thermoformed Zr<sub>3</sub> BMG. Replicated LIPSS structure from the tungsten mould is observed. Figure 3.4.11: Picture of a thermoformed Zr<sub>3</sub> plate (a), tilted SEM image (b), AFM image of a 100µm<sup>2</sup> surface (c), and 2D roughness profile on the direction perpendicular to LIPSS orientation (d) for a Zr<sub>3</sub> BMG thermoformed at  $\sigma = \sigma_c = 20$  MPa and  $T = 400^\circ\text{C}$ . presents the 2D height profile of the structure. The sharpness of the bottom of the structure may be linked to measurement artefacts. As it has been observed on mould surface, the hot compressed BMG surface with LIPSS texture exhibit a larger roughness scale. Tungsten cylinders were elaborated by powder sintering process, resulting to a rough and not fully dense structure. Some grains may be poorly sintered on the surface and are therefore easily removed during laser processing experiment. This elaboration process can thus promote an inhomogeneous material ablation which explain the poor flatness of the mould and so the replicated surface on the BMG by adding another length scale of roughness on the textured material.

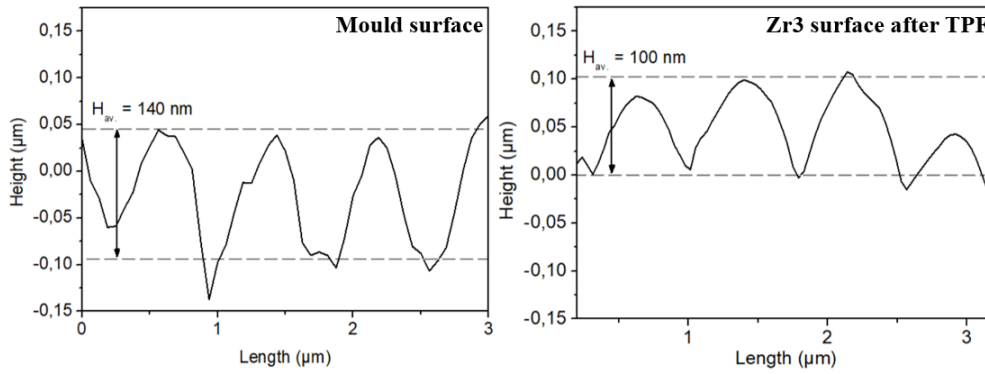


Figure 3.4.12 : 2D roughness profile on 3  $\mu\text{m}$  length of the mould surface (left) and the thermoformed Zr3 alloy surface at 400°C (right) perpendicularly oriented to the structure.

Figure 3.4.12 shows two parts of both roughness profiles of tungsten disks and BMG surface thermoformed at 400°C with the experimental conditions detailed above. The average height of the replicated structure on Zr3 alloy is  $H_{av} = 100 \text{ nm}$ , which represent around 70 % of the ripple average height of the tungsten mould. This result is different from the theoretical filling length expected at 120 s and presented in Figure 3.4.10. Other TPF experiments were carried out with the same pressure and compression time but with working temperatures increased to 430°C and 440°C. In these conditions, the theoretical filling time predicted a complete filling of the ripple structure in the first seconds after the start of the TPF process. However, AFM measurements of the thermoformed Zr3 alloys at 430°C and 440°C indicate the same filling length of around  $H = 100 \text{ nm}$ . These results indicate that this filling length value of 100 nm is a limit value from which the filling process requires much higher compression time at higher temperatures.

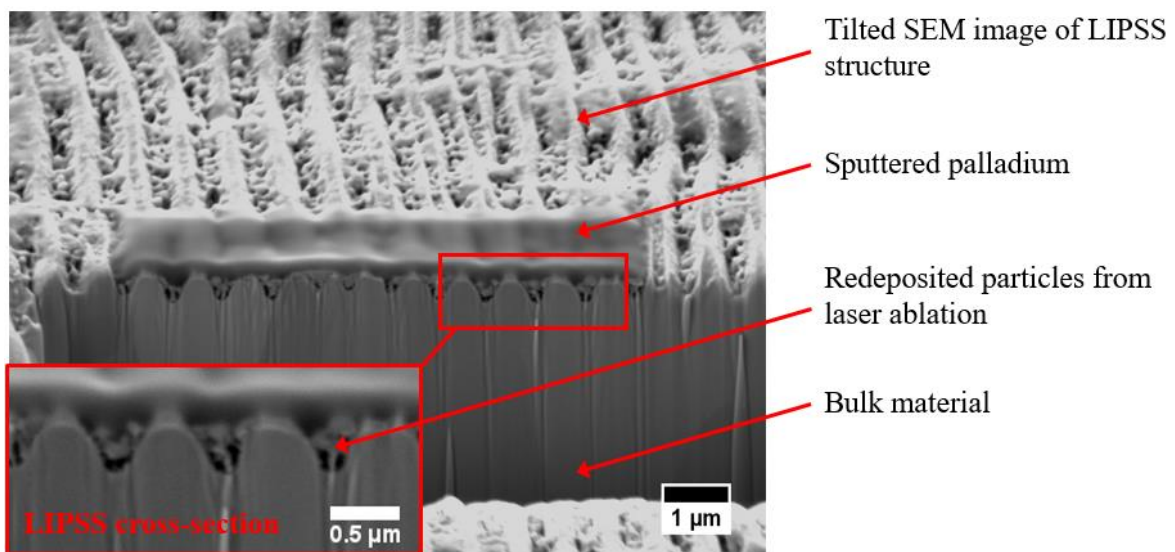


Figure 3.4.13: Tilted SEM image and FIB cross section SEM image of LIPSS structure created on tungsten mould with femtosecond laser at a pulse energy of 800  $\mu\text{J}$  and other experimental parameters presented in Chap II.

As observed in Figure 3.4.13.a and 3.4.13.b, the LIPSS texture produced on tungsten mould shows higher amount of ablation particles on its surface compared to the LIPSS texture produced on metallic glass surface presented in Figure 3.4.8. This is the extreme case where the pulse energy was the highest, but ablation particles are also present on tungsten surface treated at 400  $\mu\text{J}$  (Figure 3.4.11.b). The debris get stacked in the LIPSS valleys and thus partially fill the pattern. The incomplete filling of the LIPSS texture can thus come from different factors. First, the LIPSS texture do not have straight sides but a “U” shape as observed on SEM images. Thus, reduction of the groove width will require higher compression time to be filled. Second, ablation debris are stuck on the sides of the valleys, which might also decrease the filling rate during the experiment. Finally, the free dispersion of the viscous material due to shear flow mechanisms creates a pressure gradient during compression tests which may strongly affect the TPF capacity of the Zr<sub>3</sub> alloy. To improve the mould texture quality, a high pressure argon flow could be put on the laser spot to remove as much as possible the ablation debris before their redeposition inside the LIPSS valleys. Moreover, a specially designed sample holder must be added to horizontally constraint the material, to limit shear stress and thus stress gradient phenomenon during TPF processing.

### 3.5. XRD measurements of Zr<sub>3</sub> amorphous alloys processed by TPF technique

XRD measurements of the TPF processed samples surface were realized in order to control the amorphous structure integrity after the thermoforming processes. It indicates if any crystallization or surface oxidation appeared during the hot compression experiments. Both micrometre and nanometre thermoformed BMG specimens were characterized by X-ray diffraction technique.

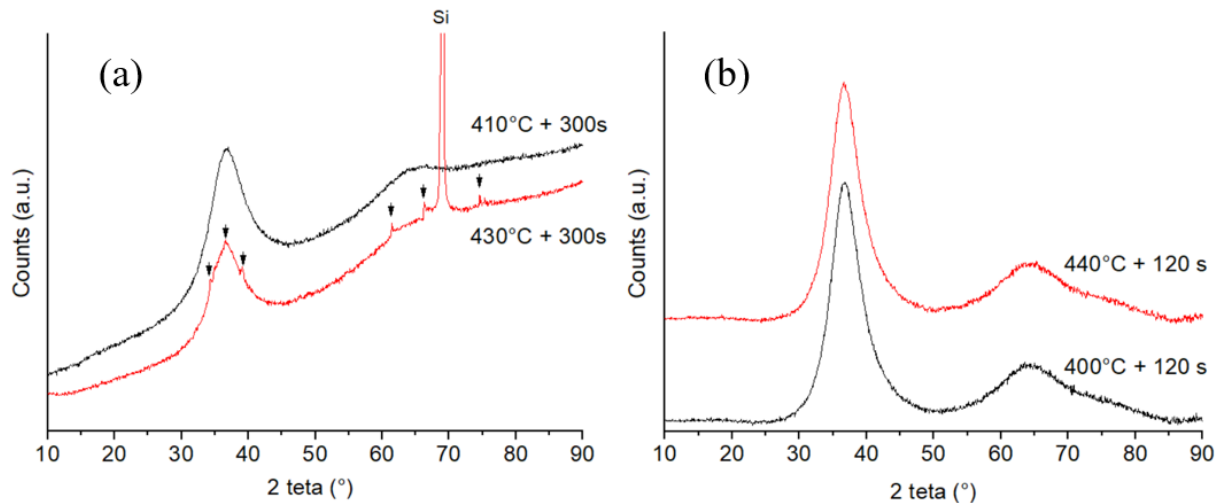


Figure 3.5.1: XRD diffractograms of Zr<sub>3</sub> alloy after TPF processing on Si-mould at  $\sigma = \sigma_c = 20$  MPa after 300 s at 410°C and 440°C (a), diffractograms of Zr<sub>3</sub> alloy surface after TPF processing on laser-textured tungsten mould at  $\sigma = \sigma_c = 20$  MPa after 120 s at 400°C and 440°C (b).

Figure 3.5.1.a shows diffractograms of Zr<sub>3</sub> sample after TPF with experimental parameters used in Section 3.4.2 and after cleaning in KOH solution. Diffractograms of the experiment conducted at 410°C shows no crystalline phases with a typical amorphous signal. At 430°C, diffractograms shows multiple low-intensity peaks between 30° and 40° and between 60° and 80° which were not possible to index with classical XRD databases. An intense peak centred at 69° is observed and correspond to Si (400) crystalline phase. Silicon peak is due to a too short cleaning procedure in KOH solution resulting in the presence of some Si or SiO<sub>2</sub> mould parts on the surface. On the other way, because of the typical amorphous signal of the diffractograms at 410°C, the multiple peaks present at 430°C may not come from a structural modification induced by TPF processing, but from the reaction of KOH solution with silicon or with the sample. The two other diffractograms presented in Figure 3.5.1.b were realized on Zr<sub>3</sub> specimen surfaces after TPF process on laser-textured tungsten moulds at 400°C and 440°C during 120 s with a pressure of  $\sigma = \sigma_c = 20$  MPa. The two diffractograms reveal no crystalline phases on their surface, which means that the sample were still completely amorphous and also that no tungsten ablation debris were bonded during the compression. This means that the debris that were deposited in the LIPSS valleys were partially fused on the surface explaining the difficulty to remove them from the moulds before TPF processing. In conclusion, these XRD measurements show that these experimental conditions under vacuum avoid surface oxidation of the thermoformed Zr<sub>3</sub> amorphous alloys. Moreover, XRD measurements indicate the good control of the compression time by avoiding crystallization occurrence, which is in agreement with Figure 3.2.3.b.

## 3.6. Conclusion

The first part of the chapter highlighted the attractive thermomechanical properties of Zr3 alloy for thermoforming processes. This alloy has a large SLR ( $\Delta T \approx 100^\circ\text{C}$ ) and the initial crystallization times are long enough to consider hot compression tests ( $t_{cryst}^{onset}(430^\circ\text{C}) \approx 16$  min). The values of the Newtonian viscosities of Zr3 alloy are particularly low in the SLR (from  $4.2 \times 10^9$  to  $2.1 \times 10^6$  Pa.s<sup>-1</sup> for  $400^\circ\text{C}$  to  $480^\circ\text{C}$  respectively) compared to other Zr-based bulk metallic glasses, which limit the required stresses for the infiltration of micrometric patterns. This low viscosity may be due to the small number of elements which have close atomic radius. These two characteristics are known to promote higher atomic mobility and thus the decrease of the viscosity but also the decrease of the thermal stability<sup>7</sup>. The identification of the transition zone between the Newtonian and non-Newtonian flow regimes made possible the determination of the critical stress value ( $\sigma_c = 20$  MPa) beyond which the flow becomes non-linear. This critical stress value, which is inherent of the rheological properties of the metallic glass, made possible the optimization of the thermoforming process in order to reduce the processing time.

First, the experiment of TPF processing under air environment highlighted the very poor oxidation resistance of the Zr3 alloy, making very difficult the surface patterning under controlled parameters in air. Thus, the development of a new hot compression device under vacuum allowed to overcome this issue. Despite the temperature control and stress distribution conditions that could be improved on the new compression device, the filling of micrometric silicon moulds under vacuum with controlled parameters validate the rheological behaviour of the alloy according to the theoretical filling curves. The analysis of the surface aspects of the thermoformed micro-parts shows the good surface finishing and the very accurate replication of the moulds. According to these experiments, the maximum l/d ratio that can be reached with the Zr3 alloy under optimized conditions ( $T=465^\circ\text{C}$ ,  $\sigma = \sigma_c = 20$  MPa and  $t = 110$  s) was estimated to be  $l/d$  (max) = 7. Preliminary tests on the reproduction by TPF of nanometric surface patterns also validated the transition to smaller scale of texture, and open the way to surface functionalization experiments. XRD analysis showed the preservation of the amorphous alloy structure without any oxidation or phase transformation during the TPF experiments. The knowledge of the thermomechanical properties of this amorphous alloy, combined with the optimization of the thermoforming parameters will help to process this alloy with different type of mould patterns with good reproducibility in order to to functionalize its surface.

# Chapter 4

## Femtosecond laser surface texturing of metallic glasses

This Chapter is dedicated to femtosecond laser texturing of Zr-based metallic glasses. This work is composed of 3 parts organized according to the research methodology applied. First of all, a study of the surface modifications created with the specimen stationary in relation to the laser beam has been conducted to determine the ablation threshold and the incubation factor for the three amorphous alloys. Having determined these parameters, a study of the effect of the laser parameters on the surface morphology and chemical composition after a laser treatment carried out by scanning the specimen surface while pulsing the laser at constant repetition rate in order to process large surface areas has been conducted. Finally, the effect of the surface textures created by the laser treatment on surface properties such as corrosion resistance and wettability has been investigated.

### 4.1. Stationary mode experiments

#### 4.1.1. Determination of the ablation thresholds and incubation factors

The ablation thresholds of the three amorphous alloys, designated by Zr3 ( $Zr_{65}Cu_{15}Al_{10}Ni_{10}$ ), ZrC ( $Zr_{57}Cu_{20}Al_{10}Ni_8Ti_5$ ), and Cu2 ( $Zr_{48}Cu_{36}Al_8Ag_8$ ) were determined using the D<sup>2</sup> method presented in Chap. II. Craters were produced for average fluences between 0.06 and 0.42 J/cm<sup>2</sup>, and different numbers of pulses (N= 5, 10, 20, 30, 50, 80, 100, 150, 200 and 250 pulses). In stationary mode experiments, the pulse repetition rate was constant and equal to 10 Hz. As explained in Chap. II, the samples were located about 2 mm below the focal plane of the lens to form a spot with a diameter of about 300  $\mu$ m, thus forming a relatively large crater with an average fluence in the correct range. Figure 4.1.1 shows a number of these spots. Prior to the calculation of the ablation threshold, the power loss in the optical path was measured leading to a value of about 14% of the output laser power. The values of the ablation threshold and

fluence were calculated after correction of the laser beam power by the equation  $P_{\text{corrected}} = 0.86 P_{\text{output}}$  to take this into account. If not, this is indicated in the thesis by (Non-corrected, NC).

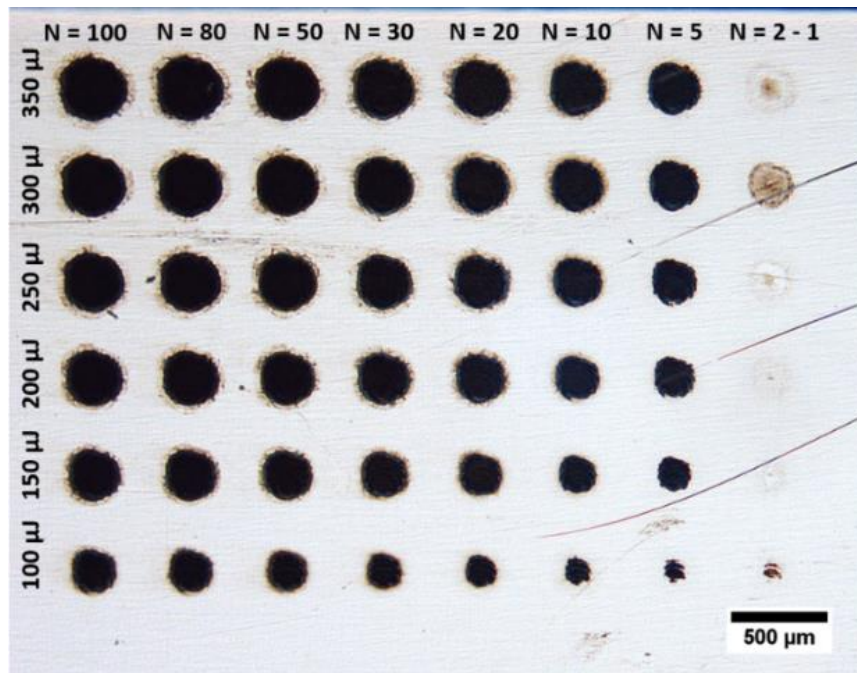


Figure 4.1.1 : Optical micrograph of a part of the sets of craters produced to determine spot diameters, laser ablation thresholds and incubation factor of  $Zr_{65}Cu_{15}Al_{10}Ni_{10}$  amorphous alloy. Number of pulses are indicated on the top and laser energies on the left. Energy values displayed are not corrected (energy losses in the optical path not accounted for).

The circular shape of the craters indicates that the deposited energy distribution at the sample surface presents the correct symmetry, reflecting the Gaussian profile of the laser beam. Five randomly oriented measurements of the craters diameter were done and the average calculated, in order to reduce the measurements error. Due to redeposited particles at the craters periphery at high fluence and for high number of pulses, the Laser-Induced Periodic Surface Structure (LIPSS) is partially obstructed so accurate measurements were not possible. This has been taken into account by interpolating the values for low and high number of pulses. The laser spot diameter at  $1/e^2$ ,  $\omega_0$ , was calculated for each sample according to equations 2.6 and 2.7 and used to calculate the fluence at the surface of the specimen. The  $\omega_0$  values obtained were  $160 \pm 6 \mu\text{m}$ ,  $162 \pm 12 \mu\text{m}$  and  $167 \pm 9 \mu\text{m}$  for Zr3, ZrC and Cu2 alloys, respectively. The values of the ablation threshold for different numbers of pulses were then determined by extrapolating a plot of  $D^2$  as a function of  $\ln(Ep)$ , the Neperian logarithm of the applied energy  $Ep$ . Figure 4.1.2, Figure 4.1.3 and Figure 4.1.4 depict these plots for 250, 100, 50 and 5 laser pulses and for the Zr3, ZrC and Cu2 alloys, respectively. Table 4.1-1 summarizes the values of  $\omega_0$  and of the ablation threshold  $\phi_{th}$  for different numbers of pulses and for the three alloys.

	Zr3	ZrC	Cu2
$\omega_0$ ( $\mu\text{m}$ )	$160 \pm 6$	$162 \pm 12$	$167 \pm 9$
Number of pulses	Ablation thresholds ( $\text{J}/\text{cm}^2$ )		
5	0.164	0.169	0.170
10	0.143	0.160	0.149
20	0.128	0.136	0.134
30	0.120	0.126	0.122
50	0.113	0.115	0.110
80	0.110	0.120	0.101
100	0.119	0.101	0.097
150	0.122	0.114	0.098
200	0.122	0.114	0.098
250	0.120	0.113	0.102

Table 4.1-1: Spot diameters and ablation thresholds for different number of pulses for the three amorphous alloys.

The single pulse ablation threshold ( $\phi_{th}(1)$ ) and the incubation coefficient ( $S$ ) of the three alloys were determined according to equation 2.10 by plotting the accumulated fluence ( $N \cdot \phi_{th}(N)$ ) as a function of the number of pulses, as shown in Figure 4.1.5. The incubation coefficients were 0.86, 0.82, 0.80 and the single pulse ablation threshold  $0.195 \pm 0.05$ ,  $0.24 \pm 0.04$  and  $0.23 \pm 0.06 \text{ J}/\text{cm}^2$  for Zr3, ZrC and Cu2 metallic glasses, respectively.

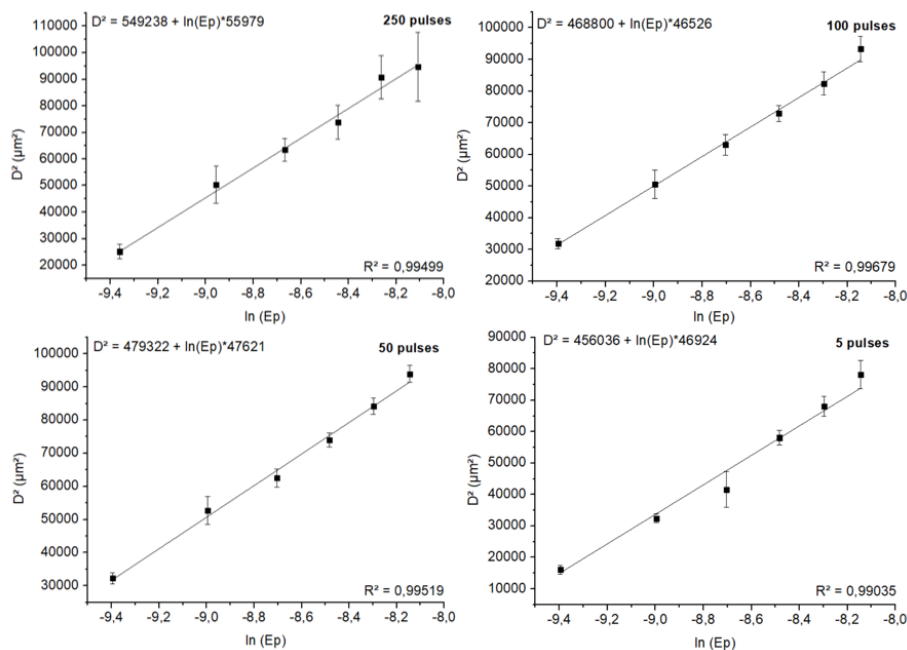


Figure 4.1.2: Plots of  $D^2$  as a function of the pulse energy for 250, 100, 50 and 5 pulses for Zr3 alloy. Lines presented are linear fitting of experimental data.  $R^2$ , slopes and intersection values are indicated for every fitting.

Chapter 4: Femtosecond laser texturing surface of metallic glasses

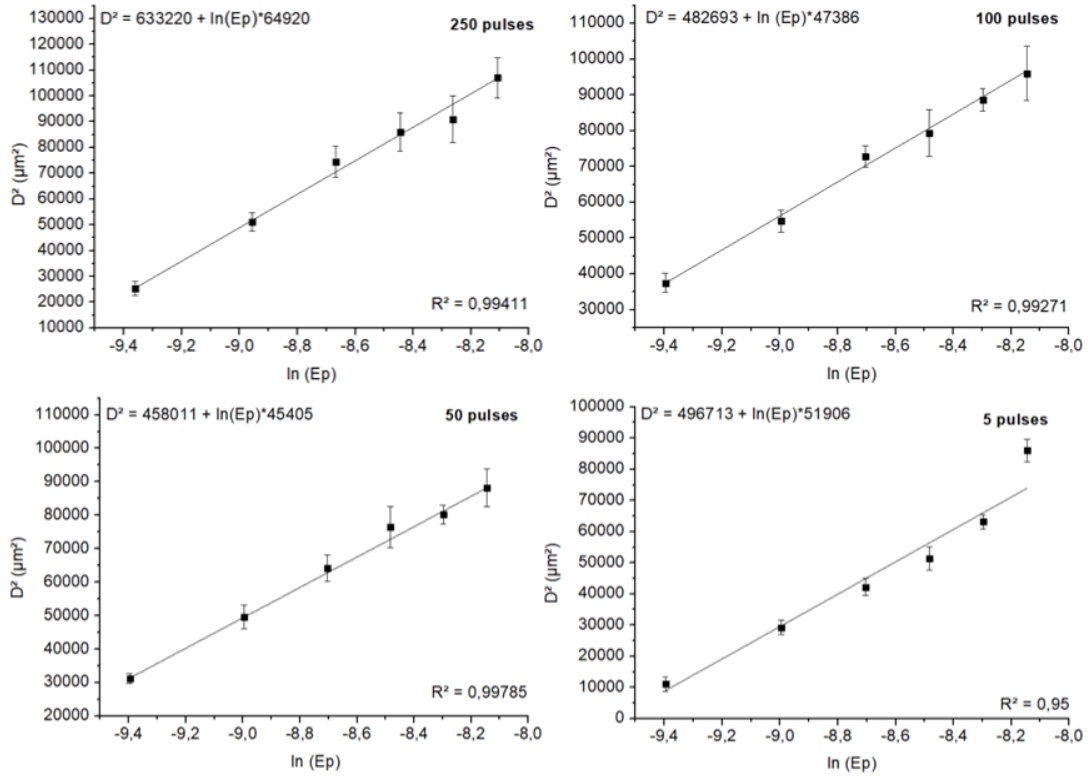


Figure 4.1.3: Plots of  $D^2$  as a function of the pulse energy for 250, 100, 50 and 5 pulses for ZrC alloy. Lines presented are linear fitting of experimental data.  $R^2$ , slopes and intersection values are indicated for every fitting.

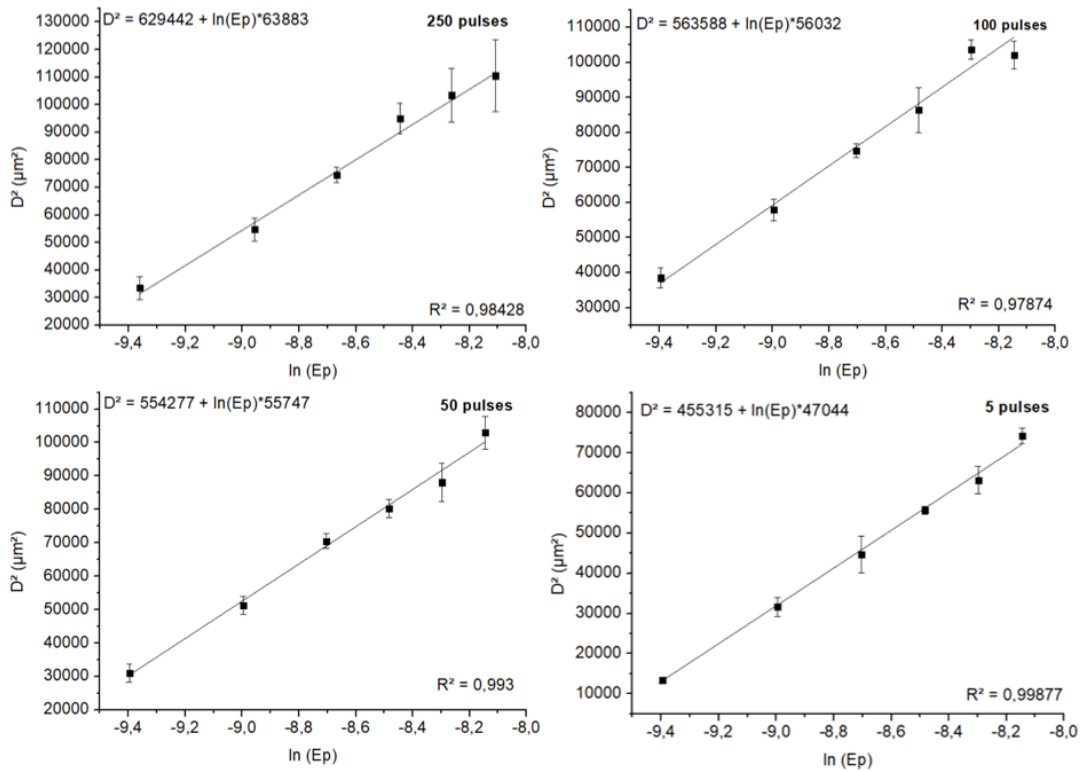


Figure 4.1.4: Plots of  $D^2$  as a function of the pulse energy for 250, 100, 50 and 5 pulses for Cu<sub>2</sub> alloy. Lines presented are linear fitting of experimental data.  $R^2$ , slopes and intersection values are indicated for every fitting.

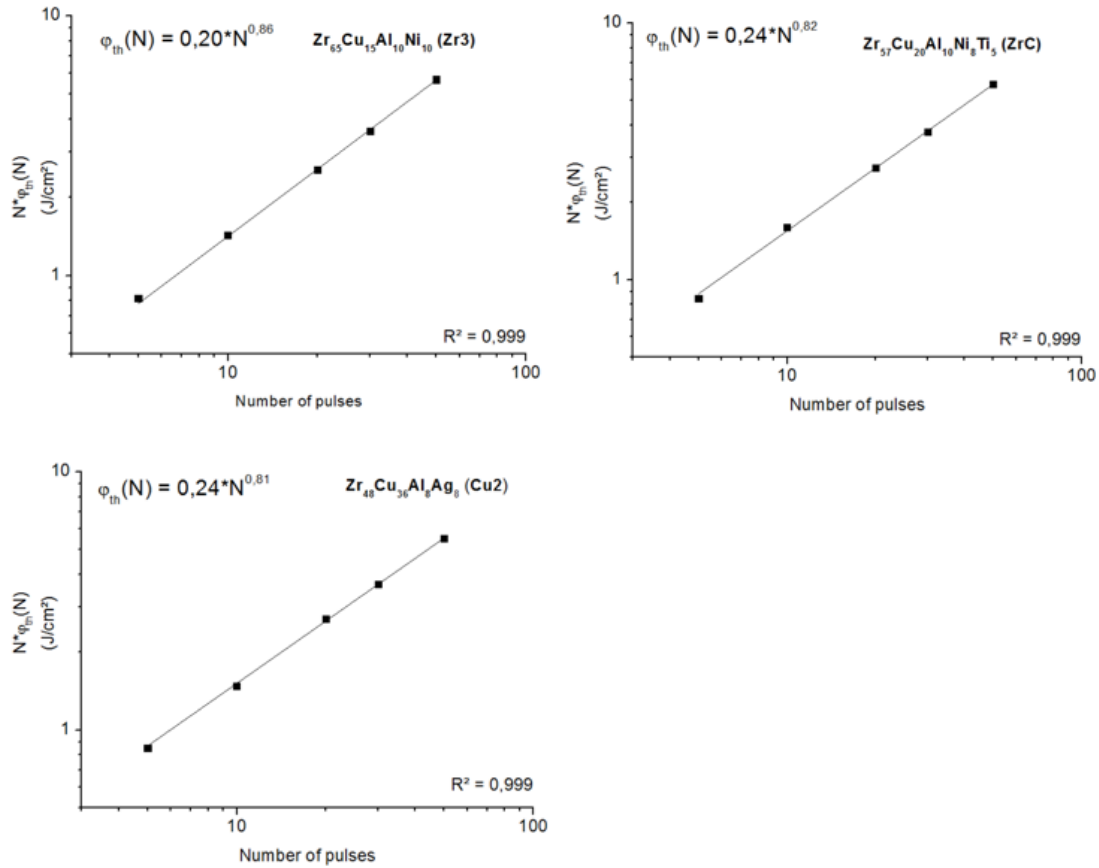


Figure 4.1.5 : Accumulated fluence as a function of the number of pulses. Fitting has been done according to eq. 2.10.

The values of the incubation factor are similar for the three alloys, (between 0.8 and 0.9), and of the same order of magnitude of the incubation factor values typically found for crystalline metallic alloys<sup>74</sup>, indicating that no major differences exist between amorphous and crystalline metallic materials under this point of view. The incubation factor reflects the accumulation of defects (surface, crystallographic, etc....) when materials are submitted to multiple pulses of radiation. This accumulation of defects leads to a decrease of the ablation threshold as compared to single pulse ablation. The above results show that the type of atomic order of the alloy (amorphous or crystalline) does not affect this behaviour. After determining the ablation threshold and the incubation factor of the alloys, the threshold for the formation of specific surface morphologies in the crater was calculated. With this aim, the influence of the pulse energy and number of pulses on the surface morphology of the craters was studied. The threshold fluence for the formation of these textures was calculated, using the D<sup>2</sup> method.

### 4.1.2. Morphological study: influence of the radiation fluence

Prior to the laser treatment, the surfaces were polished according to a conventional metallographic polishing sequence from 800 grit SiC paper to 1 $\mu$ m diamond suspension in order to minimize the influence of surface defects (scratches, roughness) on the surface texture and to obtain surfaces as flat as possible. The laser spots were produced on polished surfaces of the three alloys with pulse energies between 40 and 350  $\mu$ J, corresponding to average fluences between 0.05 and 0.42 J/cm<sup>2</sup>. Figure 4.1.6 shows SEM images of the laser spots produced with 100 pulses and pulse energies of 60, 80, 100 and 200  $\mu$ J, corresponding to average fluences  $\phi_a$  of 0.07, 0.096, 0.12 and 0.25 J/cm<sup>2</sup>, respectively. The surface topography being similar for the three alloys, only one set of results will be presented.

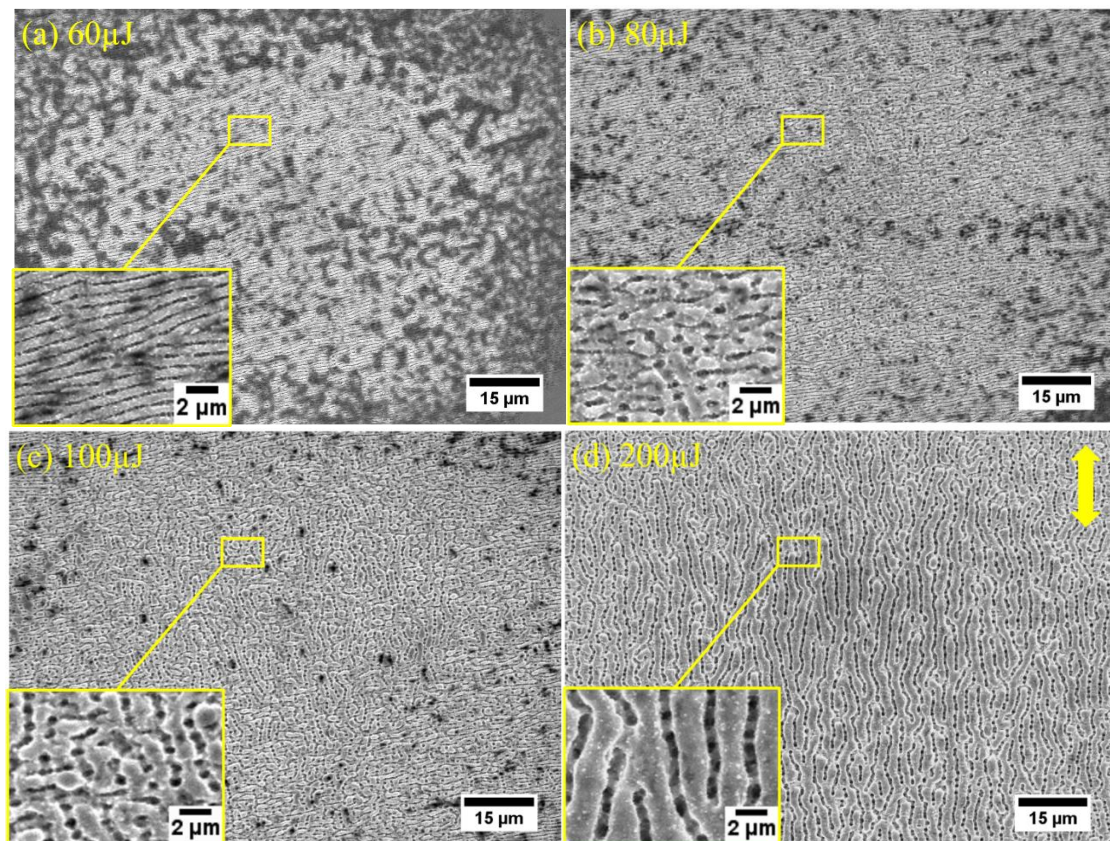


Figure 4.1.6: SEM micrographs of different craters induced by femtosecond laser on a Zr<sub>3</sub> amorphous alloy with fixed number of pulses of  $N = 100$  at a repetition rate of 10 Hz, for 60, 80, 100 and 200 $\mu$ J, which correspond to average fluence of 0.07, 0.096, 0.12 and 0.24 J/cm<sup>2</sup>, respectively. The yellow arrow indicates the polarization vector of the laser beam. Zoom images has been done at the spot centre.

The SEM images show that for an average fluence of 0.07 J/cm<sup>2</sup> ( $E_p = 60 \mu$ J), the spot present dark patches which are due to the oxide layer that initially covered the surfaces and was only partially removed by the laser treatment. The damaged region, where surface modification

occurred, is circular and about 170  $\mu\text{m}$  in diameter. In the irradiated region, we observe undulating linear ripples mostly perpendicular to the radiation polarization, indicated by the yellow arrow. These ripples have a periodicity of  $750 \pm 50$  nm. They are usually designed by as Laser Induced Periodic Surface Structures (LIPSS), mentioned in Chapter 1. When the average fluence increases to  $0.096 \text{ J/cm}^2$  (Figure 4.1.6.b), the diameter of damaged region increases to about  $185 \mu\text{m}$  and the LIPSS are only observed in a region at the periphery of the spot. At the centre, where the radiation intensity was the highest, a new structure consisting of randomly distributed features appears. These features result from the fragmentation of LIPSS at higher fluences. The ripples are fragmented due to the formation of multiple nano-sized holes along the ripples which, as a result, become discontinuous. On the other hand, the features formed coalesce in such a way that a new set of ridges oriented perpendicularly to the LIPSS forms. The amount of native surface oxide is much smaller in this specimen. At an average fluence of  $0.12 \text{ J/cm}^2$  (Figure 4.1.6.c), the damage crater increases to  $210 \mu\text{m}$  in diameter. LIPSS are observed in a narrower band at the periphery of the spot compared to the crater formed at  $0.096 \text{ J/cm}^2$ . Randomly distributed features with size and shape similar to those observed in the  $0.096 \text{ J/cm}^2$  spot in the central region are also found in a circular region at the centre of the crater. Near the centre, the density of nano-holes is much larger than before and they present a regular periodicity. As a result, well defined linear ridges perpendicular to the LIPSS (and, consequently, parallel to the laser polarization) appears. They present a period larger than the period of the LIPSS. The oxide patches are now limited to periphery of the crater, and their amount is small. For  $\phi_a = 0.24 \text{ J/cm}^2$  (Figure 4.1.6.d,  $200 \mu\text{J}$ ), the crater diameter increases to about  $270 \mu\text{m}$ . For these parameters, LIPSS are confined to a small area at the periphery of the crater. The laser processed region is covered by the ridges parallel to the radiation polarization, which originated from the hydrodynamic instabilities previously described, the latter features evolve from the LIPSS due to hydrodynamic instabilities that develop in the LIPSS at higher fluences<sup>112</sup>. No nano-holes are visible in these ridges but this nano holes are observed in the valleys between them. The periodicity of the ridges increases with the fluence. The surface at the spot centre presents some redeposited ablation particles. Their amount does not increase considerably with the pulse energy.

Considering these observations, one may conclude that two types of surface structures can be obtained by varying the laser radiation fluence, namely LIPSS oriented perpendicularly to the radiation polarization at low fluences, and ridges parallel to the radiation polarization at higher fluences.

### 4.1.3. Morphological study: influence of the number of pulses.

In order to study the influence of the number of pulses on the surface morphology, spots with a number of pulses varying from 5 to 250 were produced on specimens of the three metallic glasses. Figure 4.1.7 shows SEM images of craters made with an average fluence of  $0.18 \text{ J/cm}^2$  ( $E_p = 150 \text{ } \mu\text{J}$ ) and 50, 100, 150 and 200 laser pulses. The influence of the number of laser pulses on the surface morphology is similar for the three alloys, so only the results achieved for one composition will be presented.

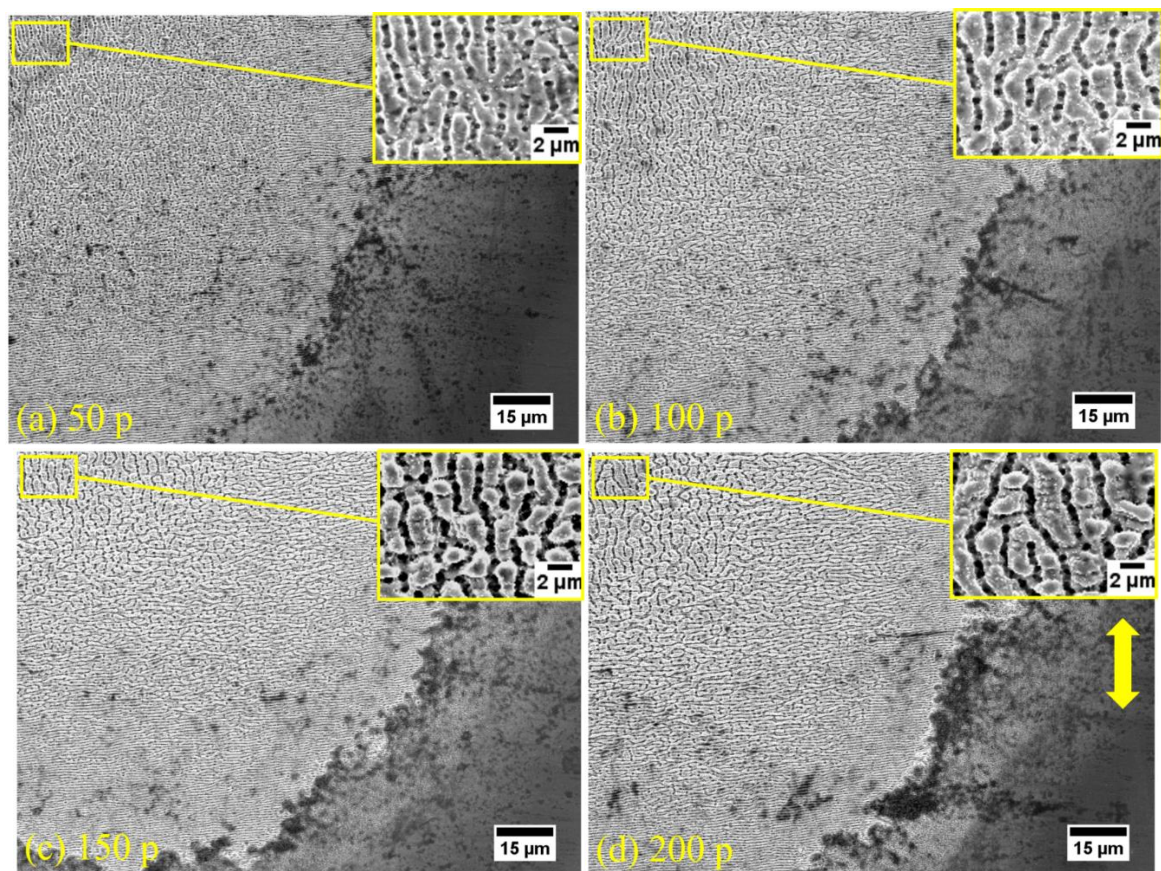


Figure 4.1.7 : Inferior quarters SEM micrographs of different of craters induced by femtosecond laser on a ZrC amorphous alloy with fixed average fluence of  $0.18 \text{ J/cm}^2$  at a repetition rate of 10 Hz, for 50, 100, 150 and 200 pulses. The yellow arrow indicates the polarization vector of the laser beam. Zoom images were done on the centre of the spot.

Each images presents lower right part of the laser spot while the larger magnification inserts show the morphology at the centre of the spot. For 50 laser pulses (Figure 4.1.7.a), the surface morphology at the centre of the spot (insert) is intermediate between the morphologies observed for  $0.12$  and  $0.24 \text{ J/cm}^2$  average fluences structures (Figure 4.1.6.c and Figure 4.1.6.d). The spot diameter is  $D \approx 220 \text{ } \mu\text{m}$ . Nano-holes joined together to create ridges parallel to the laser beam polarization. A small amount of redeposited debris are observed on the ridges. LIPSS formed in a  $\approx 15 \text{ } \mu\text{m}$  wide band at the periphery of the spot. The crater border is covered by dark oxide

films and ablation particles. For 100 pulses (Figure 4.1.7.b), the nano-holes are less visible and valleys start to form between the ridges. The ridges width is slightly larger than in the specimen prepared with 50 laser pulses. LIPSS are present at the periphery of the spot. For higher numbers of laser pulses (150 – 200 pulses, Figure 4.1.7.c and Figure 4.1.7.d), the tendency is the same, with an increase of the ridges width and with deeper valleys between the ridges. The amount of redeposited particles also increases, indicating that the volume of ablated material increased, as expectable. LIPSS are observed for any number of laser pulses, but due to the increasing amount of ablation debris at the periphery of the craters, the LIPSS are often obscured by these particles. The area covered by oxide films at the periphery of the craters increases with the number of laser pulses.

#### 4.1.4. Structure formation thresholds

To rationalize the evolution of the surface morphology as a function of the radiation fluence in a wide pulse energy range and the radius of the craters, the threshold fluence for the formation of the different structures were calculated using the D<sup>2</sup> method. The laser beam radius value used was the one calculated for the ablation threshold determination. For a Gaussian beam, the spatial fluence profile  $\phi(r)$  at the specimen surface and the maximum fluence at the centre of the beam  $\phi_0$  are given by the following equations:

$$\phi_0 = \frac{2E_p}{\pi \omega_0^2} \quad (4.1)$$

$$\phi(r) = \frac{2E_p}{\pi \omega_0^2} e^{-2\frac{r^2}{\omega_0^2}} \quad (4.2)$$

where  $r$  is the distance to the laser beam axis. The values of fluence threshold for the formation of the two structures previously described are presented in Figure 4.1.8 and in Table 4.1-2.

Fluence threshold (J/cm <sup>2</sup> )	Zr3	ZrC	Cu2
LIPSS $\phi_{\text{mini}}$	0.08 ± 0.03	0.09 ± 0.04	0.07 ± 0.02
LIPSS $\phi_{\text{max}}$	0.14 ± 0.04	0.17 ± 0.06	0.13 ± 0.05
RIDGES $\phi_{\text{mini}}$	0.22 ± 0.08	0.28 ± 0.08	0.23 ± 0.07

Table 4.1-2 : Threshold values for LIPSS and ridges structures formation for the three metallic glasses studied.

LIPSS  $\phi_{\text{mini}}$  corresponds to the minimum fluence at high number of pulses where LIPSS are present. LIPSS  $\phi_{\text{max}}$  corresponds to the maximum fluence above which the structure start to be deteriorated and transform in the transition structure observed in Figure 4.1.6.b. The values of

the thresholds are similar for the three amorphous alloys. The ridge structure threshold is about three times larger than the LIPSS formation threshold. On the other hand, the LIPSS formation threshold is slightly lower than the ablation threshold for the corresponding alloy. This can be explained by the fact that for higher fluences and larger numbers of pulses, the ablation particles obstruct partially the LIPSS formed at lower fluences at the periphery of the laser spots, so the spot diameters were underestimated and the ablation thresholds over-estimated. Similarly to what was observed for the ablation threshold and the incubation factor, the LIPSS formation threshold on the three amorphous alloys are close to the LIPSS formation threshold of crystalline metallic alloys with comparable ablation threshold. Indeed, Vorobyev *et al.*<sup>6</sup> processed iridescent LIPSS texture on aluminium samples with fluence of 0.05 J/cm<sup>2</sup>. On other metallic glass alloys, Dold *et al.*<sup>17</sup> produced LIPSS texture on Zr<sub>62.5</sub>Cu<sub>22.5</sub>Fe<sub>5</sub>Al<sub>10</sub> with laser fluence of 0.1 J/cm<sup>2</sup>.

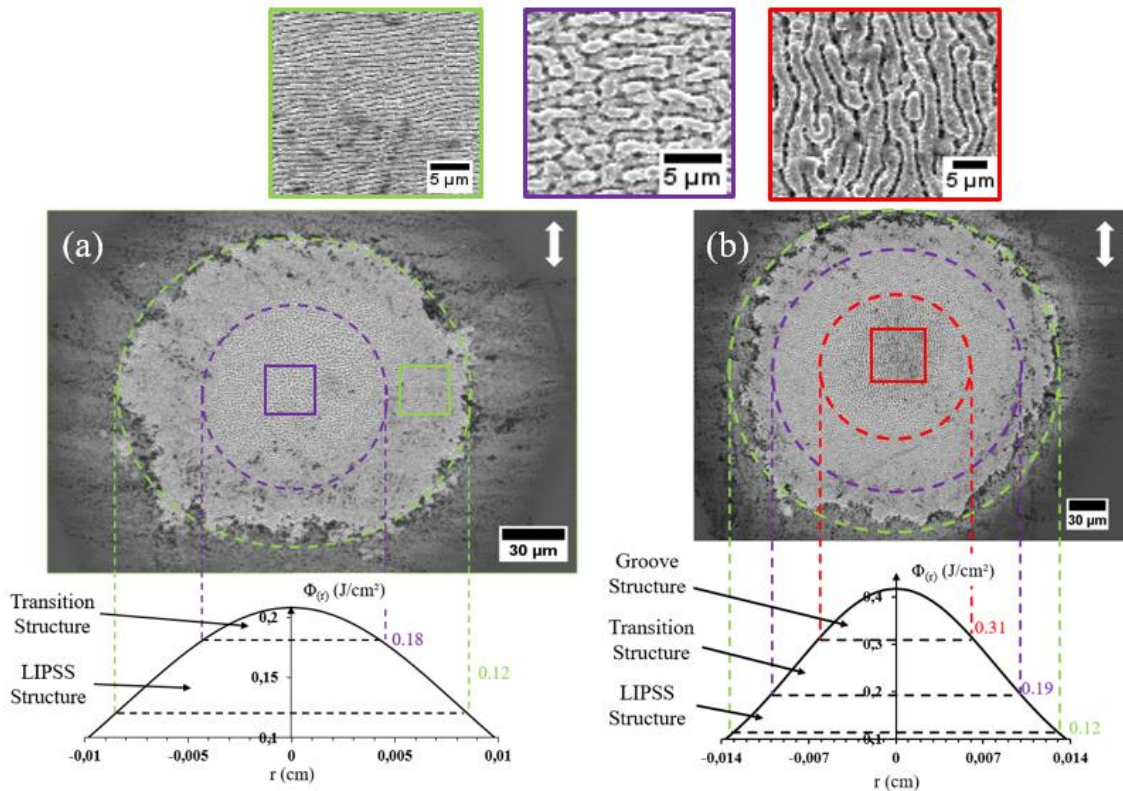


Figure 4.1.8: SEM micrographs of a ZrC target surface at  $N = 150$  pulses for pulse energy of 100  $\mu\text{J}$  (a), and 200  $\mu\text{J}$  (b).

Below each image the corresponding spatial profile of the laser pulse fluence is shown. The squares mark regions characterized by different surface structures at low (LIPSS structure on the left), medium (transition structure on the centre) and high fluences (ridge structure on the right). The double-headed arrows indicate the beam polarization.

Other studies observed Ridge-like textures on various type of materials such as silica, crystalline and amorphous metallic alloys, under comparable laser parameters<sup>17,122,150</sup>. These structures are not specific for Zr-based BMGs, and thus their amorphous structures do not have

significant effects on the ablation threshold, the incubation factor or the resulted structure morphologies compared to other materials.

#### 4.1.5. On the formation of laser induced surface structures

Figure 4.1.9 presents a SEM micrograph of a Zr3 alloy sample irradiated with a single laser pulse with an average fluence of  $\phi_a = 0.16 \text{ J/cm}^2$ . Prior to the laser irradiation, the surface was roughly polished to create fine scratches (straight black lines on the image). After the laser treatment the surface presents low amplitude periodic waves but, contrarily to the LIPSS and the ridges structure, these waves are not oriented in a single direction related to the laser beam polarization, but are parallel to the scratches, independently of their orientations. Moreover, their amplitude is larger when they are closer to the scratches and they do not form far away from them.

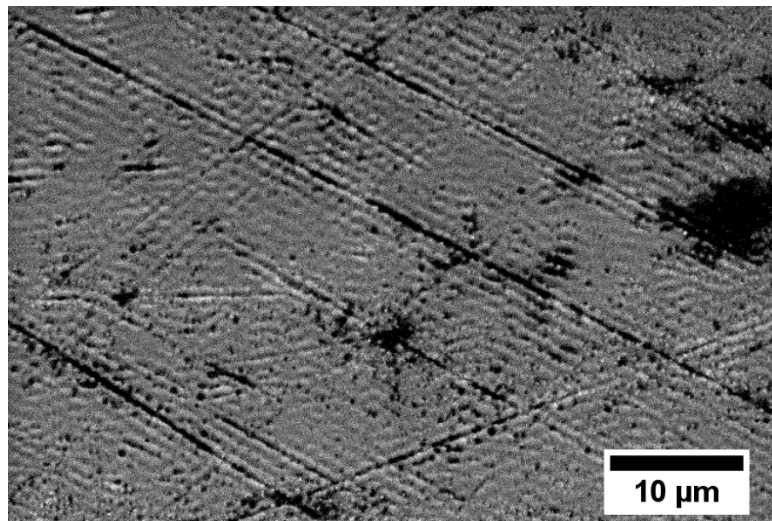


Figure 4.1.9: SEM image of  $\text{Zr}_{65}\text{Cu}_{15}\text{Al}_{10}\text{Ni}_{10}$  metallic glass surface irradiated with  $\phi_a = 0.16 \text{ J/cm}^2$  after 1 pulse.

As explained in Chapter 1, the formation of surface structures induced by fs laser treatment is linked to the material surface irregularities. LIPSS are surface structures which are formed at low fluences, typically close to the material ablation threshold. Sipe's theory of LIPSS formation, proposed in 1983 and generally accepted in the scientific community, assumes that an interference between the incident radiation wave and a wave propagating parallel to the specimen/air interface promotes inhomogeneous energy deposition<sup>98</sup>. Later authors such as Bonse<sup>91</sup> suggested that the surface waves may be surface plasmon polaritons. The Drude-Sipe's model assumes that these plasmonic waves originate from surface defects and so the formation of LIPSS is directly linked to the material roughness. The inhomogeneous energy deposition

on the irradiated material is computed through the product  $\eta(\mathbf{k}, \mathbf{k}_i) \times |b(\mathbf{k})|$  where  $\eta$  describes the efficacy with which the surface roughness at the wave vector  $\mathbf{k}$  induces inhomogeneous absorption<sup>112</sup>.  $k_i$  is the component of the wave vector of the incident beam and  $b$  represents the measures of the amplitude of the surface roughness at  $\mathbf{k}$ <sup>112</sup>. Thus, the energy absorption and subsequent phenomena are dependent on the material's surface topography but this relation is, in general, less evident than in the micrograph of Figure 4.1.9.

In this particular example, the periodicity of the waves is about 1.2 microns, which is higher than the laser wavelength so they cannot be considered as LIPSS at this stage. Their formation might be linked to diffraction phenomena by the scratches, and this testifies the important role of surface defect on laser-material interaction and on the formation of surface structures by femtosecond laser.

#### 4.1.6. Structure formation below the ablation threshold

Figure 4.1.10.a and Figure 4.1.10.b depict SEM micrographs of a fs-laser spot produced with a pulse energy of  $E_p = 50 \mu\text{J}$  and 200 laser pulses on a ZrC amorphous alloy surface. As shown in image (a), the surface material is only entirely removed in a central region of the spot, which is small compared to the spot diameter of  $140 \mu\text{m}$ . In this energy range, corresponding to an average fluence of  $0.05 \text{ J/cm}^2$ , the ablation threshold is only reached at the centre of the spot (with a radius of  $18 \mu\text{m}$ ,  $\phi_{r=18\mu\text{m}} = 0.112 \text{ J/cm}^2$ ) due to the Gaussian energy distribution in the laser beam. The partially removed surface layers reflects the fact that energy absorption is inhomogeneous. At the spot centre, in the “bright” area, low spatial frequency LIPSS (LSFLs) oriented perpendicularly to the beam polarization, are observed. In the surrounding grey area, no specific structure is observed and the surface layer of material is only partially removed. Surprisingly, while no surface structure would be expected far below the material ablation threshold, a periodic structure consisting of rectilinear ripples with orientation parallel to the laser polarization is observed at the periphery of the spot in Figure 4.1.10.b, indicated by an arrow in this Figure.

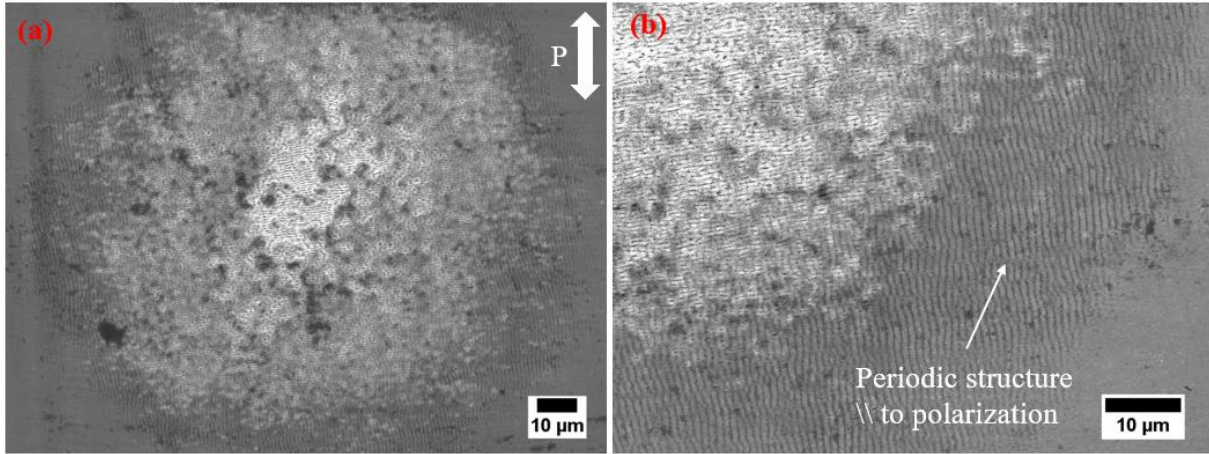


Figure 4.1.10: SEM images of the overall laser spot (a), and zoom on the peripheral part of the spot (b) produced on  $Zr_{57}Cu_{20}Al_{10}Ni_8Ti_5$  BMG at pulse energy  $E_p = 50\mu J$  and after  $N = 200$  pulses.

This type of structure, which appears at very low fluences, was already observed by previous authors<sup>161</sup>. Geometrically this structure is similar to low-frequency LIPSS<sup>22</sup> but, while LIPSS are usually perpendicular to the polarization vectors, this structure, which we will call type II, is parallel to the polarization. According to the theory of Sipe<sup>98</sup>, this structure is related to special radiations, which promote a specific electromagnetic waves close to the rough surface<sup>162</sup>, permitting to transfer energy of the incident laser beam to the material surface<sup>22</sup>. However, these structures only appear in dielectric material, when the single photon energy is smaller than the band gap energy of the material, while here it seems to be formed in a material with a metallic bond. The SEM micrographs shows that this structure is very shallow ( $<100nm$ ) and only affects a very thin surface layer of the specimen. The most probable explanation for its formation is that this alloy, being mostly composed by Zirconium, is easily oxydised to form a zirconia surface layer, which is a dielectric. At these low fluences, the  $ZrO_2$  film is not removed, allowing the formation of type II low-frequency LIPSS. In order to support this hypothesis, the period of these LSFL was measured and compared to the theoretical values calculated using eq 4.1. For a plane metal-air interface and a normal radiation incidence, the standard surface plasmon polariton (SPP) model predicts that the LSFL-I period  $\Lambda_{LSFL-I}$  is related to the bulk dielectric permittivity  $\epsilon$  by:

$$\Lambda_{LSFL-I} = \lambda \times Re\left\{\left[\frac{\epsilon + 1}{\epsilon}\right]^{1/2}\right\} \quad (4.1)$$

where  $\lambda$  is the radiation wavelength. By knowing this wavelength ( $\lambda_{laser} = 1030$  nm) and the LSFL-I periodicity calculated by FFT ( $\Lambda_{LSFL-I} \approx 750$  nm), the real part of the dielectric permittivity has been determined as  $Re(\epsilon) = 1.12$ . For type-II LSFLs parrallel to the beam

polarization, the spatial period is close to the radiation wavelength and can be calculated by the equation:

$$\Lambda_{LSFL-II} = \frac{\lambda}{n} \quad (41.2)$$

where  $n = \varepsilon^{1/2}$  is the refractive index of the dielectric material<sup>98,91</sup>. By using the previously calculated value of the dielectric permittivity  $\text{Re}(\varepsilon) = 1.12$  and the laser wavenlength of 1030nm, a theoretical spatial periodicity of type-II LSFLs  $\Lambda_{\text{type-II (theory)}} \approx 970$  nm was calculated. Using Fast-Fourier Transform image analysis performed with Image J software, a periodicity for the type-II structure at the laser spot periphery of  $940 \pm 60$  nm was determined, in good agreement with the theoretical value. This result supports the hypothesis of the structure appearing in the ZrO<sub>2</sub> dielectric surface layer. The FFT of the image and the delimitation of the areas with different structures are presented in Figure 4.1.12. Bonse *et al.*<sup>163</sup> studied the topographic and chemical modifications induced by femtosecond laser spots on the surface of a TiN alloy. They showed that the laser treatment promotes the formation of a TiO<sub>2-x</sub>/TiN<sub>x</sub>O<sub>y</sub> oxides layer at the periphery of the crater with an oxidation threshold lower than the ablation threshold. Zirconium and titanium exhibit comparable oxidation behaviour, therefore the formation of a thick ZrO<sub>2</sub> oxide layer at the crater's periphery can also be expected, and this layer may promote the formation of this particular structure, which is only observed on dielectric materials, as previously mentionned.

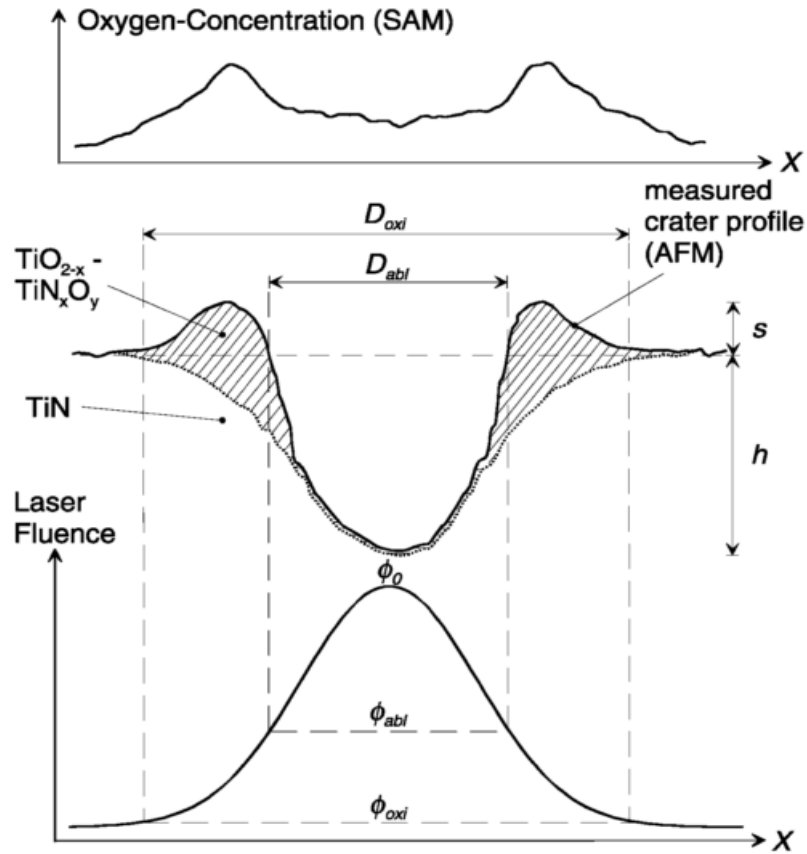


Figure 4.1.11: Scheme of the morphological and chemical modifications due to ultra-short pulse laser ablation of TiN in air environment, from Bonse *et al.*<sup>163</sup>.

The calculations based on surface plasmon polariton (SPP) model must be taken cautiously because zirconia has a dielectric permittivity value higher than 10. Moreover, the simple equation used is valid for a single pulse, and does not take into consideration the effect of the accumulation of damage induced by multiple laser pulses. It has been demonstrated that the number of laser pulses has an effect on the LIPSS periodicity, changing from a value close to the radiation wavelength for a single pulse to a smaller value for multiple pulses<sup>164</sup>. Bonse *et al.*<sup>164</sup> observed the dependence of LIPSS periodicity on the number of pulses between 1 and 80 pulses.  $\Lambda_{LIPSS}$  varying between  $0.96 \lambda_{laser}$  for 1 laser pulse to  $0.75 \lambda_{laser}$  for 80 laser pulses in silicon. For higher numbers of pulses, a decrease of this dependency is observed and the LIPSS period becomes approximately constant between 100 and 1000 pulses. In this thesis, we worked mainly with numbers of pulses larger than 100 both for stationary and non stationary irradiation modes. Thus, we can consider that in these conditions the period of the LIPSS should not depend on the number of pulses. It is also interesting to emphasize that the LIPSS period measured in the present work (750 nm) is similar to the value observed by Bonse *et al.*<sup>164</sup> for silicon for large number of pulses ( $750 \approx 0.75 \times 1030$  where 1030 nm is the laser wavelength). These results support the view that the behaviour of very different materials submitted to

femtosecond laser pulse treatment is often similar, despite the differences in properties and chemical bonds.

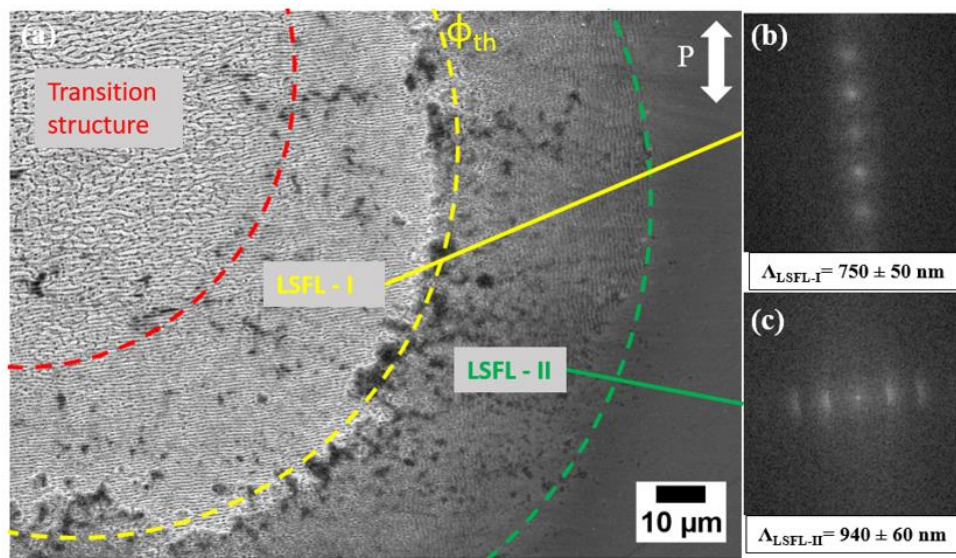


Figure 4.1.12: SEM images of a laser spot produced on a ZrC BMG surface with pulse energy of  $E_p = 100 \mu\text{J}$  and  $N = 150$  pulses with the corresponding structures areas and the ablation threshold  $\phi_{th}$  zone (a), FFT images of type-I (b) and type-II (c) with corresponded period values.

Figure 4.1.12 summarizes the different surface textures that form in laser spot created with a pulse energy of  $86 \mu\text{J}$  and 150 laser pulses. Taking into account the energy loss in the optical path, the maximum fluence at the spot centre for this energy is  $0.21 \text{ J/cm}^2$ . At this fluence a ridge structure forms at the centre of the spot, while LIPSS form at the spot periphery. In agreement with the previously calculated thresholds, the transition between these two topographies occurs for a fluence of  $0.28 \text{ J/cm}^2$ . Between  $0.17 \text{ J/cm}^2$  (first dashed curve from the left) and the edge of the spot (middle dashed curve) which corresponds to the ablation threshold of the material for 150 pulses ( $0.11 \text{ J/cm}^2$ ), type I LIPSS with a periodicity of  $750 \pm 50 \text{ nm}$  form. Outside the crater, for fluences between  $0.1$  and  $0.07 \text{ J/cm}^2$  ( $r = 112 \mu\text{m}$ ), type II LIPSS with a periodicity of  $940 \pm 60 \text{ nm}$  are observed. It is clear that exceeding the ablation threshold cannot be considered as a true condition for the formation of surface structures. Depending on the material, surface patterns can form at fluences below the ablation threshold. Fluences above the threshold lead to material ablation and the structures that may have formed will be destroyed. Working below the ablation threshold allows preserving these structures.

Nürnberg *et al.*<sup>165</sup> studied the effect of  $\text{SiO}_2$  oxide layer thickness on the orientation of LIPSS on silicon (100). As shown in Figure 4.1.13, the authors observed that for an oxide layer with a thickness of less than  $80 \text{ nm}$ , the LIPSS are oriented perpendicularly to the polarization. Between  $80$  and  $120 \text{ nm}$  they are oriented either perpendicularly or parallel to the polarization

whereas above 120 nm they are only parallel to the polarization. The authors showed that the orientation of the LIPSS is directly related to the penetration depth of the surface plasmon polaritons SPP field into the oxide layer. For a thin oxide layer ( $< 80$  nm) the penetration depth of the SPP is higher than its thickness and thus they interact with Si (which might be considered as a conductor after multiple pulse irradiation<sup>166</sup>) and LIPSS form perpendicularly to the polarization, as described in the surface plasmon polaritons model<sup>167</sup>. For a thick oxide layer ( $> 120$  nm) the penetration depth of the plasmon polaritons is smaller than the oxide layer depth and thus the plasmonic waves, called by the authors bulk plasmon polaritons (BPP), form within the SiO<sub>2</sub> layer resulting in LIPSS parallel to the polarisation, as theoretically predicted for dielectric materials<sup>98</sup>.

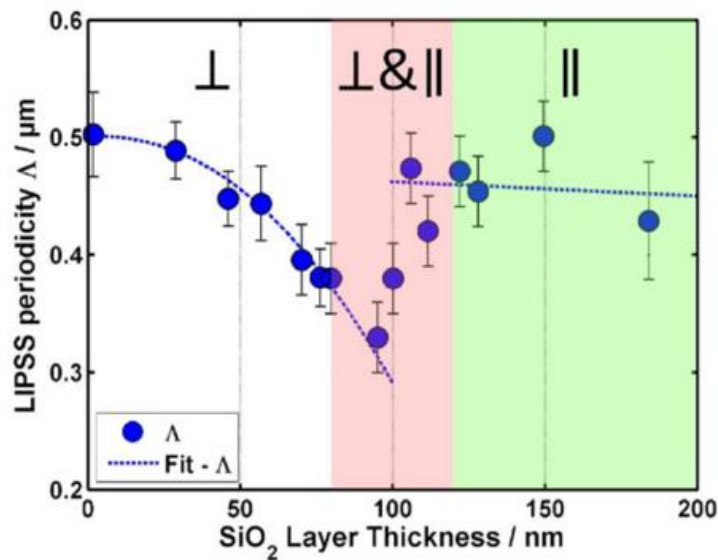


Figure 4.1.13 : LIPSS periodicity and orientation from laser polarisation as a function of SiO<sub>2</sub> layer thickness on Si (100) at a laser fluence per pulse of 2.41 J/cm<sup>2</sup> in ambient air, from Nürnberger *et al.*<sup>165</sup>.

In our case, as shown in Figure 4.1.14, type II LIPSS structure only appear from 150 laser pulses and fluences below the ablation threshold and, therefore, outside the crater. For the same fluence the area where this structure forms increases with increasing number of pulses. On the basis of our results and taking into consideration the conclusions of Bonse *et al.*<sup>164</sup> and Nürnberger *et al.*<sup>165</sup>, we suggest that in Zr-based metallic glasses the consecutive laser pulses promote the growth of an oxide layer probably composed mainly of ZrO<sub>2</sub>, which becomes thick enough for LIPSS parallel to the laser polarisation to form and that the region where they form increases with increasing number of pulses due to the resulting increase of the oxide layer thickness.

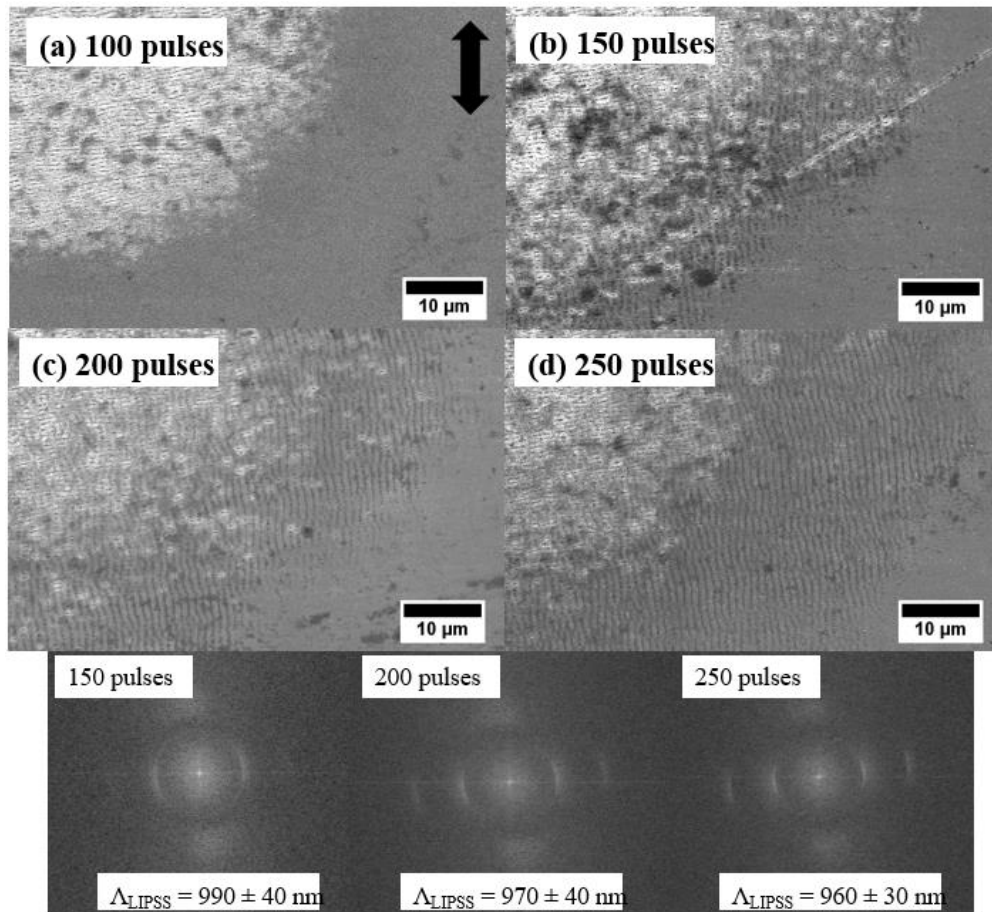


Figure 4.1.14: SEM images of the side of laser spots and LIPSS type II periods calculated by FFT with pulse energy of 50 μJ and N = 150 (a), 200 (b), and 250 (c) pulses.

This conclusion opens the way to a new type of surface treatment below the ablation threshold. This laser treatment would allow the growth of surface oxide layers on the metallic glass, provided with a shallow texture consisting of type II LIPSS. This laser treatment is expected to improve the corrosion resistance as well as modifying the wetting and biocompatibility behaviour of the surface, while preventing surface damage, because the laser treatment is performed below the ablation threshold.

## 4.2. Non-stationary experiments

This Section is devoted to the laser texturing of large areas of the three alloys with LIPSS or Ridge structures. In order to produce these structures in large areas and create the specimens required to characterize the surface properties, a parametric study was performed on the Zr3 alloy. It consisted in determining the best laser scanning parameters to ensure an homogeneous surface morphology taking into consideration the thresholds for the formation of each type of surface structure determined previously in the stationary conditions experiments. In order to process surfaces, the average number of pulses per point of the surface was determined by using equation 2.11 presented in Chapter 2.

### 4.2.1. Effect of lateral displacement on surface structures

The lateral displacement of the beam is an essential parameter that must be controlled to produce homogeneously textured surfaces. By varying this parameter, it is possible to create different types of textures with the pulse energy. As shown in Figure 4.2.1, for a pulse energy of 150  $\mu\text{J}$ , the surface structures in the direction perpendicular to the laser track are not homogeneous for an overlap of 20 % (Figure 4.2.1.a). A central line with ridges and a large number of nano-holes is observed, whereas at the borders of the image transition structures consisting of partially destroyed LIPSS and, a small number of nano-holes are observed.

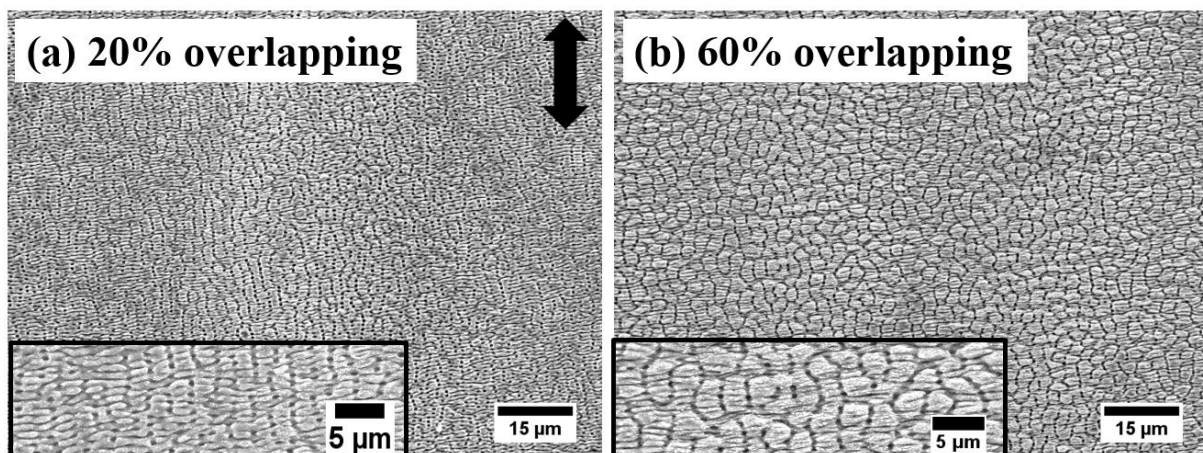


Figure 4.2.1 : SEM images of Zr3 metallic glass surfaces processed with a pulse energy of 150  $\mu\text{J}$  (non-corrected) at a pulse frequency of 100 Hz, a scanning speed of 1 mm/s with lateral displacement of 100 $\mu\text{m}$  corresponding to a track overlapping of 20% (a) and a lateral displacement of 50 $\mu\text{m}$  corresponding to a track overlapping of 60% (b). The double arrow presents polarisation and scanning direction.

On the contrary, the track produced with the same pulse energy and an overlap of 60% is much more homogeneous in the direction perpendicular to the scanning direction (Figure 4.2.1.b). An

homogeneous ridge structure covers the entire processed area. The ridge width increases slightly with increasing number of laser pulses per point of the surface. The corresponding values of the average fluence and number of pulses per point of the surface for both were 0.17 J/cm<sup>2</sup> and 52 and 105 pulses for 20 and 60% track overlapping, respectively.

#### 4.2.2. Processing of ridges and LIPSS surface structures on metallic glasses.

As previously mentioned, this thesis focused on two different surfaces structures, produced at low fluence (LIPSS) and high fluence (Ridges), respectively. After a parametric study two optimum sets of processing parameters were found to produce these two structures in large surface areas. The characterization of the surface composition and morphology and the effect of these textures on surface properties is the subject of this Section.

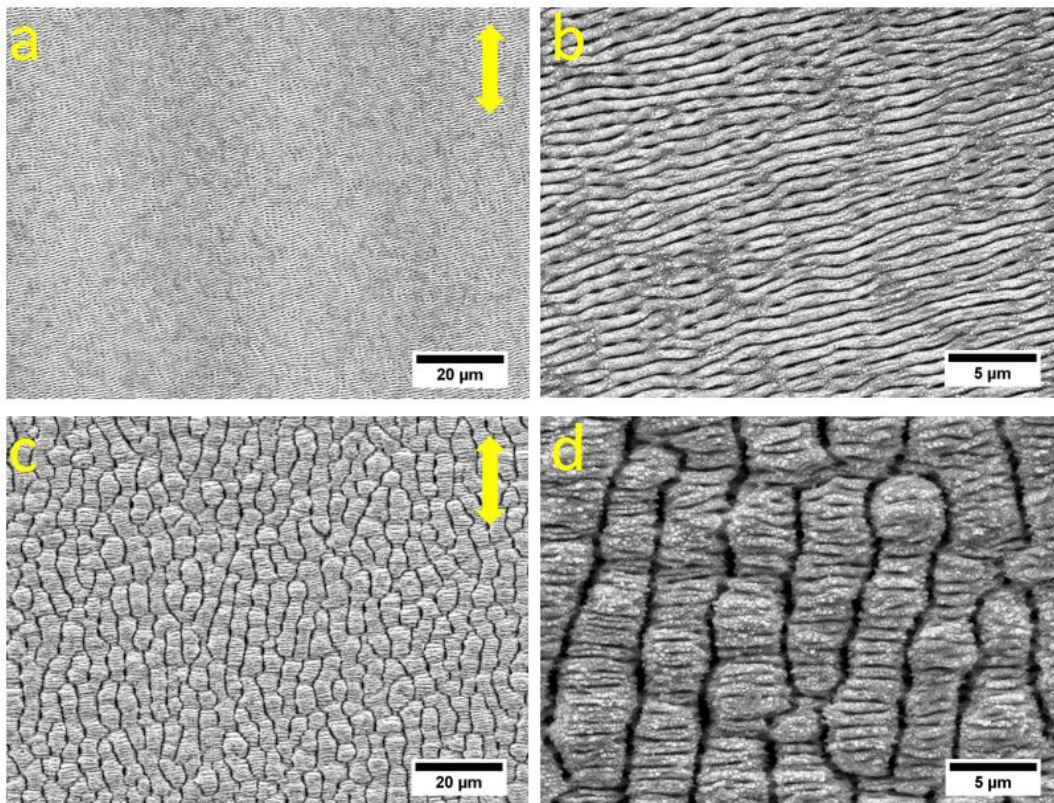


Figure 4.2.2: Low and high magnifications SEM images of LIPSS (a,b) and Ridge (c,d) textures produced on Zr<sub>3</sub> amorphous alloy surface. LIPSS (a,b) have been processed with  $N = 161$  and  $\phi_a = 0.07$  J/cm<sup>2</sup> and ridges (c,d) have been processed with  $N = 538$  and 0.4 J/cm<sup>2</sup>. Yellow double arrows represent the laser beam polarization and the scanning orientation.

As explained in Section 4.1, the three alloys present similar values of the ablation and structure formation thresholds and form similar surface structures in stationary conditions. Thus, the same processing parameters were used for all the alloys. They are summarized in Table 4.2-1.

<b>Parameters</b>	<b>LIPSS</b>	<b>RIDGES</b>
Distance to focal point (mm)	2mm below	2mm below
Laser energy ( $\mu\text{J}$ )	75	400
Pulse frequency (Hz)	50	200
Scanning velocity (mm/s)	1	1
Lateral displacement (mm)	0.05	0.04
Environment	In air	In air
Resulted number of pulses per point of the surface	161	538
Resulted fluences ( $\text{J}/\text{cm}^2$ )	0.07	0.4

Table 4.2-1 : Processing parameters and resulted number of pulses and fluences for LIPSS and RIDGES structures.

The first structure, presented in Figure 4.2.2.a and Figure 4.2.2.b, consists of LIPSS oriented perpendicularly to the beam polarisation. They were produced with fluences close to the ablation threshold ( $\approx 0.1 \text{ J}/\text{cm}^2$ ). Their periodicity is  $750 \pm 50 \text{ nm}$ , calculated by Fast Fourier Transform (FFT) analysis of the SEM micrographs. The LIPSS width is  $600 \pm 40 \text{ nm}$ . As for the ridges, the valleys are much narrower than the LIPSS width. Small amounts of ablation particles redeposited on the LIPSS. This is explained by the fact that the predominant ablation mechanism for metal at fluences just above the ablation thresholds is liquid spallation<sup>77</sup>, which leads to the projection of droplets. As shown in Figure 4.2.2.c, and Figure 4.2.2.d, homogeneously textured surfaces were successfully produced in the alloys. The surface features are parallel to the polarization. The average ridge width is  $3.8 \pm 1 \mu\text{m}$  its period is  $3.5 \pm 0.5 \mu\text{m}$ . The similarity of the period and width values is due to the fact that the valleys are much thinner than the ridge width. The SEM micrographs of Figure 4.2.2.c and Figure 4.2.2.d show that the ridges are covered by LIPSS formed on tops. This is due to the Gaussian shape of the beam energy distribution: during the scan, every point of the surface is exposed to the low intensity regions of the beam after being irradiated with peak intensity, promoting the formation of LIPSS on top of the structures formed at higher intensities. Since the fluence used in this treatment is much higher than the ablation threshold, a layer of redeposited ablation debris is observed, forming a trimodal surface structure.

The roughness parameters of the two structures, calculated by stereoscopic pairs of SEM images, are presented in Table 4.2-2. The surface profiles were taken perpendicularly to the direction of the structure.  $R_a$  is the arithmetic mean height of the structures,  $R_z$  their maximum height (distance between the lowest valley and the highest peak),  $R_{Sk}$  is a measure of the profile

asymmetry and  $R_{ku}$  is a measure of the sharpness of the features. A  $R_{ku} = 3$  means normal distribution,  $> 3$  means that the height distribution is sharp and  $< 3$  means the height distribution is blunt. The  $R_{sk}$  parameter is a measure of the asymmetry of a distribution probability, and when it is used to describe surface topography, a positive skewness ( $R_{sk} > 0$ ) represents peaks emerging from a relatively flat surface, whereas a negative skewness ( $R_{sk} < 0$ ) corresponds to wide plateaus with deep valleys<sup>47</sup>.  $R_{sk}$  and  $R_{ku}$  values are normally used to differentiate surface structures with similar values of average roughness.

<b>Zr3 (Zr<sub>65</sub>Cu<sub>15</sub>Al<sub>10</sub>Ni<sub>10</sub>)</b>				
Textures	$R_a$ ( $\mu\text{m}$ )	$R_z$ ( $\mu\text{m}$ )	* $R_{sk}$	* $R_{ku}$
LIPSS	$0.072 \pm 0.006$	$0.30 \pm 0.1$	$-0.7 \pm 0.2$	$2.8 \pm 0.4$
RIDGES	$0.36 \pm 0.06$	$1.9 \pm 0.3$	$1.5 \pm 0.2$	$2.6 \pm 0.6$
<b>ZrC (Zr<sub>57</sub>Cu<sub>20</sub>Al<sub>10</sub>Ni<sub>8</sub>Ti<sub>5</sub>)</b>				
Textures	$R_a$ ( $\mu\text{m}$ )	$R_z$ ( $\mu\text{m}$ )	* $R_{sk}$	* $R_{ku}$
LIPSS	$0.075 \pm 0.005$	$0.33 \pm 0.08$	$-0.4 \pm 0.2$	$2.7 \pm 0.2$
RIDGES	$0.39 \pm 0.1$	$1.8 \pm 0.6$	$1.5 \pm 0.1$	$2.6 \pm 0.4$
<b>Cu2 (Zr<sub>48</sub>Cu<sub>36</sub>Al<sub>8</sub>Ag<sub>8</sub>)</b>				
Textures	$R_a$ ( $\mu\text{m}$ )	$R_z$ ( $\mu\text{m}$ )	* $R_{sk}$	* $R_{ku}$
LIPSS	$0.068 \pm 0.005$	$0.34 \pm 0.07$	$-0.9 \pm 0.1$	$3.4 \pm 0.5$
RIDGES	$0.374 \pm 0.08$	$1.8 \pm 0.4$	$1.46 \pm 0.1$	$2.4 \pm 0.4$

Table 4.2-2: Roughness parameters for the two textures (LIPSS and RIDGES) processed on the three amorphous alloys. Values are obtained from 3D reconstruction of SEM images using Alicona-Mex® software. Measurements have been took in a direction perpendicular to the laser scanning direction for ridges structure, and in a direction parallel to the scanning direction for LIPSS structure.

As shown in Table 4.2-2, and as expected,  $R_a$  and  $R_z$  are larger for the Ridge texture ( $R_a = 0.39$  and  $0.37$  and  $R_z = 0.33 - 1.8 \mu\text{m}$  for ZrC and Cu2 alloys, respectively) than for the LIPSS texture ( $R_a = 0.075 - 0.068$  and  $R_z = 0.33 - 0.34 \mu\text{m}$  for ZrC and Cu2 alloys, respectively). The differences between the parameters for the same type of textures formed in the three alloys are not statistically significant.  $R_{sk}$  values around 1.5 for the ridge texture means that the surface is oriented to the protrusions, while the values for LIPSS texture are negative (-0.9 and -0.4 for ZrC and Cu2 alloys respectively) meaning that the texture consists of surface plateaux with deep valleys in between. The LIPSS texture presents  $R_{ku}$  values of 3.4 and 2.7 while ridges  $R_{ku}$  values are 2.6 and 2.4, meaning that the LIPSS texture has sharper protrusions than the Ridge texture. The high value of  $R_{ku}$  for the LIPSS texture is also due to the redeposited ablation debris which may have a strong effect on this roughness parameter. As observed in Figure 4.2.3,

both LIPSS (left) and Ridge (right) textures are covered with redeposited debris from ablation, with a much higher amount on the high energy laser treatment. These debris may thus play a significant role on surface properties and have to be considered as another scale of roughness on the textured surfaces.

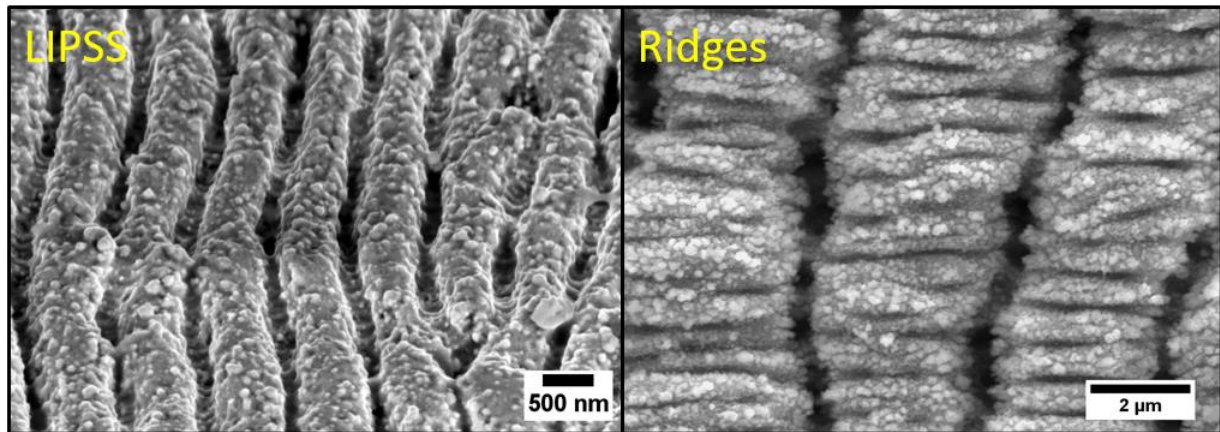


Figure 4.2.3 : SEM images of LIPSS (left) and RIDGES (right) textures on ZrC amorphous alloy at high magnification. Redeposited nanoparticles are observed on both surfaces.

For comparable range of fluences, the roughness values measured on both LIPSS and Ridge textures are similar to the values reported in the literature for common crystalline alloys and other amorphous alloys<sup>17,113</sup>. This agreement was expected because of the comparable structures created with femtosecond laser treatment under fluences between 0.05 and 0.5 J/cm<sup>2</sup>.

### 4.2.3. Effect of $E_p$ and $N$ variations on structure morphology in non-stationary irradiation mode

The influence of the pulse energy and of the number of pulses per point of the surface on the surface structure morphology has been investigated. For the influence of the pulse energy, the number of pulses per point of the surface were fixed at 525 pulses for every treatments. The pulse energy were varied between 100 μJ and 800 μJ, which corresponds to average fluences between 0.12 and 1 J/cm<sup>2</sup>. As observed in Figure 4.2.4 and Figure 4.2.5, the ridge width increases with increasing pulse energy, from  $2.17 \pm 0.5 \mu\text{m}$  to  $4.45 \pm 0.9 \mu\text{m}$  for 200 μJ and 700 μJ pulse energies, respectively. The SEM images also show that the ridge length reaches a maximum for about 600 μJ pulse energy and then decreases because holes appear in the valleys between the crests, leading to the progressive breaking down of the ridges and evolution of the structure towards shorter linear features. For higher pulse energy ( $\approx 1 \text{ mJ}$ ) a columnar morphology is expected to appear, as observed in previous studies<sup>168,116,169</sup>. In this range of

fluences, only ridge-like structures were produced. As expected, the LIPSS period and width do not vary with the pulse energy.

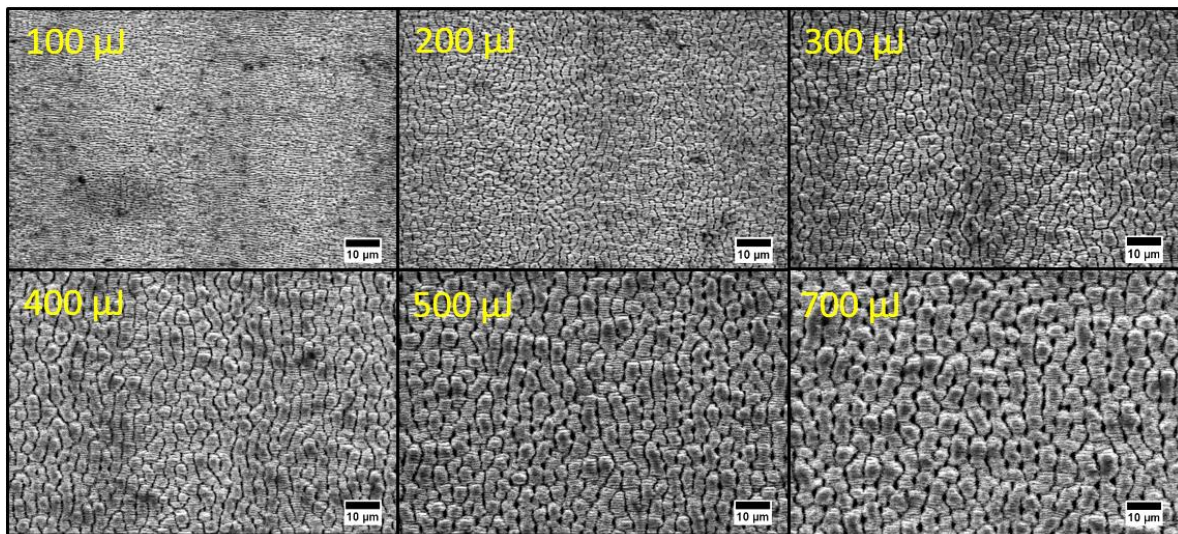


Figure 4.2.4: SEM images of Zr3 alloy textured with ridges processing parameter at 200 Hz with pulse energy of 100, 200, 300, 400, 500 and 700  $\mu\text{J}$ . Scale bar represents 10  $\mu\text{m}$  in length.

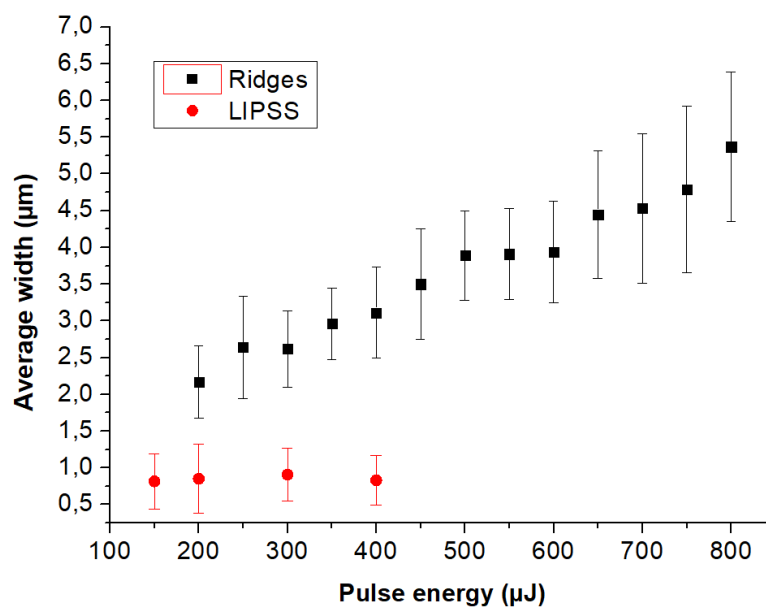


Figure 4.2.5 : Evolution of ridges and LIPSS features width with pulse energy on a Zr3 amorphous alloy surface.

Increasing the pulse frequency in the scanning mode has the same effect as increasing the number of pulses in the stationary mode. As shown in Figure 4.2.6, at a pulse frequency of 150 Hz, the valleys between the ridges are shallow and the surface presents LIPSS that overlap the ridges and create bridges between them. At higher frequencies, the valleys are deeper and for 250 Hz the Ridge structure is perfectly defined. No significant variations of the ridge width were observed.

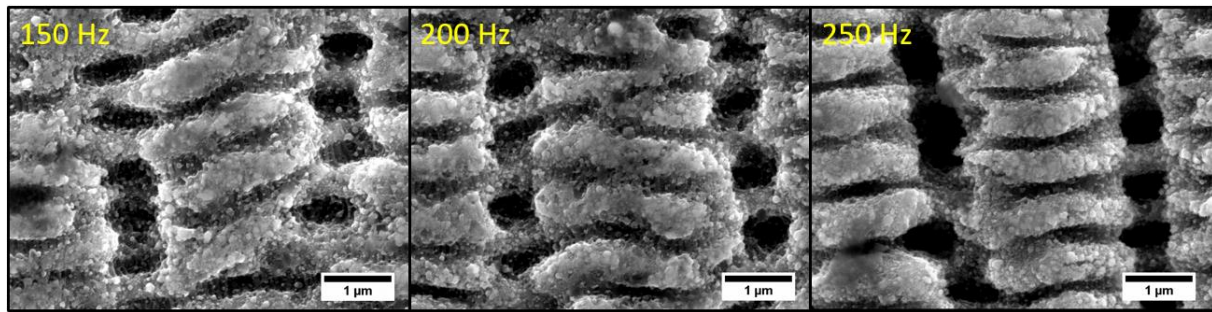


Figure 4.2.6 : High magnification SEM images of ridge textures processed on Zr3 surface at pulse energy of  $400 \mu\text{J}$ , lateral displacement of  $0.32 \text{ mm}$  and scanning speed of  $1 \text{ mm/s}$  at pulse frequencies of 150, 200 and 250 Hz, corresponding to  $N = 24, 33$  and  $41$  pulses respectively.

## 4.3. Surface properties of femtosecond laser textured metallic glasses

### 4.3.1. Surface chemistry analysis

The surface chemical composition was analysed by XPS, as explained in Chapter 2. Samples of the Zr3 ( $\text{Zr}_{65}\text{Cu}_{15}\text{Al}_{10}\text{Ni}_{10}$ ) metallic glass before and after the laser treatments were analysed. Figure 4.3.1 shows low resolution spectra of polished surface and surface with LIPSS and Ridge textures. The XPS spectra present peaks corresponding of zirconium, copper, nickel, oxygen and carbon. The aluminium peaks are not distinct because the aluminium Al 2p and Al 2s peaks overlap the copper Cu 3p and Cu 3s peaks. This overlap does not allow the quantification of aluminium. Presence of Cu 2p peak allow the quantification of copper amount and moreover, it make possible to estimate the area of copper Cu 3p peak. The effect of the surface roughness on the XPS signal intensity is important and these analysis were performed with different surface morphologies so quantification results may be affected of additional errors. Moreover, the presence of an high intensity carbon peak reveals that the surface was contaminated by carbon before the XPS analysis. All these advises to consider the XPS results only semi quantitatively.

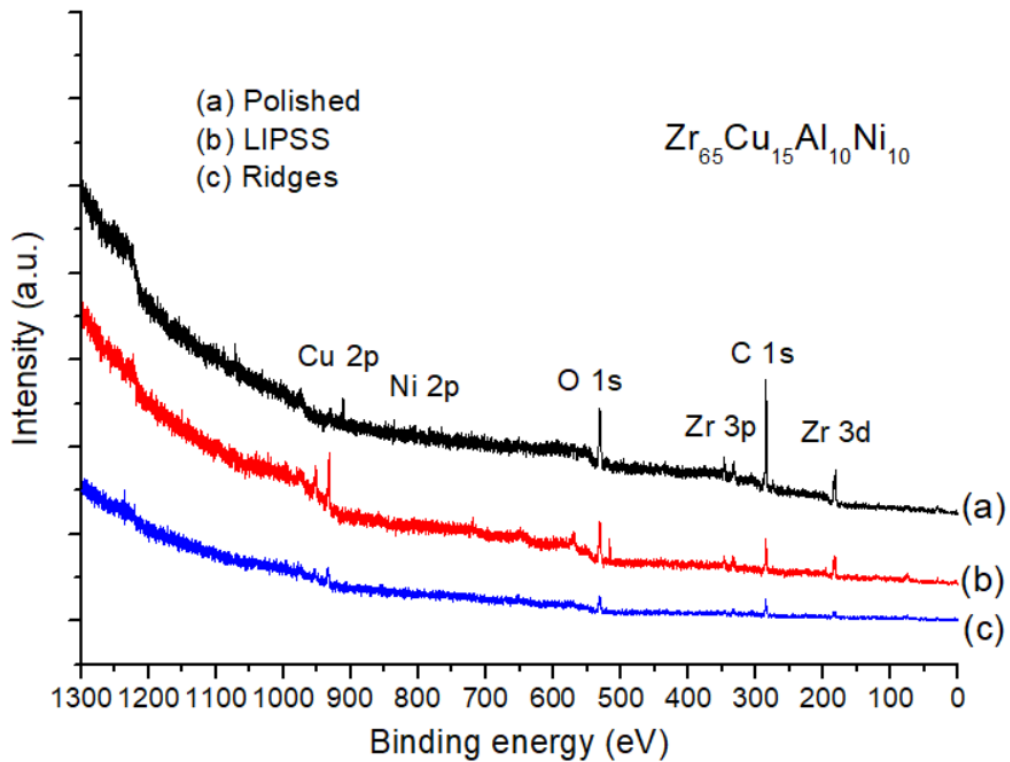


Figure 4.3.1 : XPS survey spectra for 1  $\mu\text{m}$  polished (a), fs-laser treated with LIPSS (b) and ridges (c) textures on Zr<sub>65</sub>Cu<sub>15</sub>Al<sub>10</sub>Ni<sub>10</sub> amorphous alloy surfaces.

XPS spectra exhibit several peaks at different binding energies (BE). From low to high binding energies, the peak between 182 and 185 eV can be assigned to zirconium Zr 3d triplets. The highly intense peak at 285 to 288.6 eV can be assigned to carbon C 1s triplets. Between 530 and 532 eV, an intense peak that can be assigned to oxygen O 1s doublets appears. Nickel Ni 2p peaks were detected in both laser treated samples between 855 and 863 eV but not in the polished specimen. A last peak was detected between 932.4 and 943.9 eV and can be assigned to copper Cu 2p triplets.

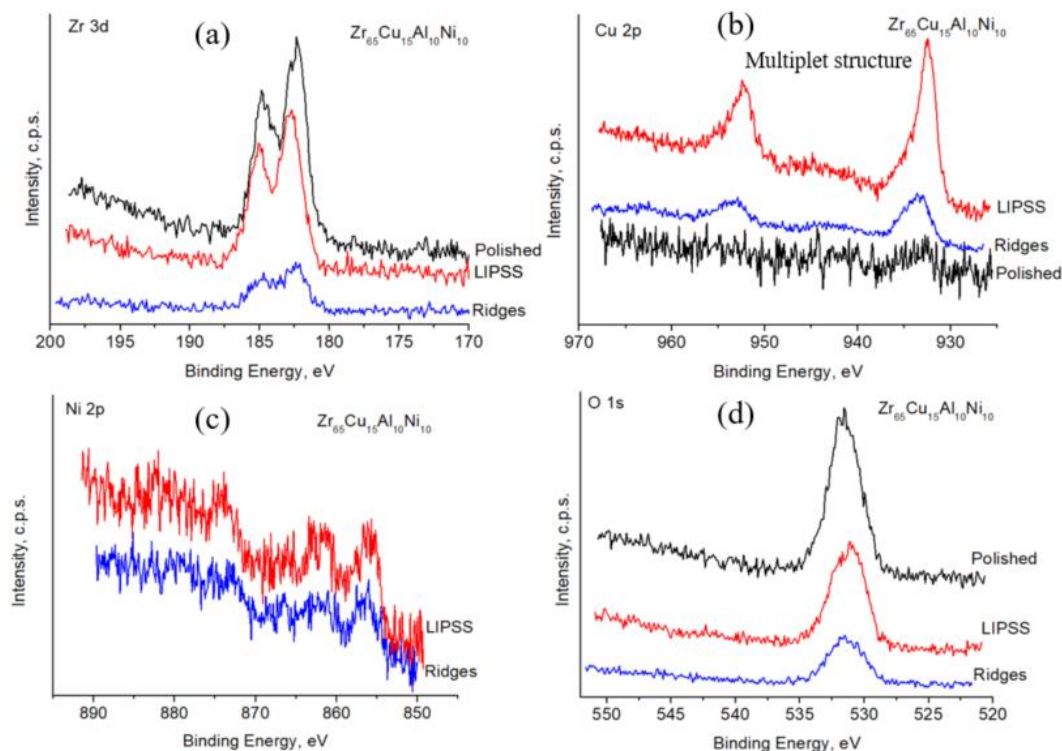


Figure 4.3.2 : XPS detailed spectra for the regions Zr 3d (a), Cu 2p (b), Ni 2p (c) and O 1s (d).

Higher resolution spectra of the main peaks are presented in Figure 4.3.2. The peaks were not decomposed in their components because the surface is covered by an oxide/hydroxide film and the evolution of oxide ratios is not relevant here as long as no metallic bonding was observed. The Zr 3d region was fitted with two doublets presenting spin-orbit splits  $\sim 2.4$  eV and with the most intense component (Zr 3d<sub>5/2</sub>) centred at 182.1 and 182.8 eV except for the LIPSS sample where the doublet at lower energies could not be fit. The two components were tentatively assigned, to Zr<sup>4+</sup> in ZrO<sub>2</sub> and in hydrous zirconia<sup>170</sup>, respectively. In the specimen with LIPSS the first component is absent, whereas for the Ridge texture zirconium peaks are very similar to the polished sample.

The Cu 2p peak presents very low signal to noise ratio in the polished making difficult the identification and the accurate quantification of all the spectra. The signal to noise ratio is significantly larger in the textured specimens. In the LIPSS texture, the dominant peak is centred at 932.5 eV and it is assignable to Cu<sup>+</sup> in Cu<sub>2</sub>O<sup>171</sup>. Two smaller peaks exist at higher binding energies, assignable to Cu 2p in CuO and Cu(OH)<sub>2</sub> or other similar copper oxide compound. In the Ridge textured sample, the XPS Cu 2p region extends towards higher binding energies, showing that copper is more oxidized than in the LIPSS-textured specimen. The intense increase in this region also suggest that surface is relatively enriched in copper. The

nickel Ni 2p peak is not detected in the polished sample, but visible in the treated surfaces and present a similar structure for both textures. The main peak (Ni 2p<sub>3/2</sub>) is centred at 855.8 eV and it may be assigned to NiO, Ni<sub>2</sub>O<sub>3</sub> or Ni(OH)<sub>2</sub><sup>172</sup>. Probably a mixture of these compounds is present.

Finally, the oxygen O 1s peak can be fit with at least two components centred respectively at 530.8 eV, and at 532.2 eV, assignable to oxygen bound to metallic ions and to carbon, respectively. The relative intensities of these peaks is similar for the treated surfaces, and the component at low binding energy is more important in this case. On the contrary, in the polished sample, the peak of oxygen bound to carbon is more intense. The peaks areas were analysed to calculate the surface atomic concentrations of the elements and the results are presented in Table 4.3-1. Carbon due to contamination was not included, so the part of the oxygen concentrations bonded to metallic elements are overestimated. The overlap of aluminium Al 2p and Al 2s peaks and copper Cu 3p and Cu 3s peaks do not allow to quantify Al.

Copper is present on the polished sample but, as expected, the results indicate a much higher content of zirconium. The Cu/Zr ratio is 0.2, in agreement with the Cu/Zr ratio in the metallic glass (Cu/Zr = 0.23). Both laser treated samples show a copper enrichment and a decrease of the zirconium content at the surfaces. The Zr content is 10 at. % for the untreated sample and 10 and 7 at. % for the LIPSS-textured and the Ridge-textured specimens, respectively. The copper concentration increases from 2 at. % for the untreated specimen to 22 at. % for the LIPSS texture and 19 at. % for the Ridge texture. Even considering the measurement errors previously described, this large increase of the copper concentration is not due to measurements artefacts, and thus reflect a copper enrichment of the laser-textured surfaces.

Similarly to copper, the surface concentration of nickel slightly increases with the laser treatment. Ni was virtually undetectable in the polished sample while after laser treatment, Ni content of 3 and 4 at. % are obtained for the LIPSS and the Ridge textures, respectively.

The XPS analysis shows that a very large concentration of oxygen is present in the polished surface (87 at. %). After the laser surface treatment, the oxygen content decreased to 65 and 70 at. % for the LIPSS and the Ridge textures, respectively. The carbon concentration on the surface is not given in the Table 4.3-1 because it was assumed that it mostly comes from surface contamination by ambient air and due to sample manipulation. The carbon content is very high for the untreated sample and decreases after laser treatment, in particular for the LIPSS textured sample. This may explain why the LIPSS specimen presents the best signal to noise ratio.

The copper/zirconium, nickel/zirconium and nickel/copper ratios were also included in Table 4.3-1. As expected the Ni/Zr and the Cu/Zr ratios increase with the laser treatment as compared to the polished surface. The Ni/Zr ratio is double for the LIPSS texture compared to the Ridge texture, (0.3 and 0.6). The Cu/Zr ratio is 0.2 and 2.2 for the polished surface and the surface with the LIPSS texture, respectively, while the Ni/Zr ratio is smaller for the Ridge than for the LIPSS texture.

Metals (at.%)	POLISHED	LIPSS	RIDGES
Zr	10.3	9.9	6.7
Cu	2.4	22.3	19.1
Ni	0.0	2.6	4.1
O	87.4	65.2	70.3
<b>Total (%)</b>	<b>100</b>	<b>100</b>	<b>100</b>
Ratios of major metallic elements			
Cu/Zr	0.2	2.2	2.9
Ni/Zr	0.0	0.3	0.6
Ni/Cu	0	0.12	0.22

Table 4.3-1 : Atomic percentage of metallic elements and oxygen of the Zr<sub>3</sub> amorphous alloy obtained by XPS analysis and atomic ratios between Zr, Ni and Cu for the three surfaces textures.

In summary, these XPS analysis revealed 3 majors information:

1. The surface is covered by metallic elements only in in the form of oxides, even for the non-textured surface.
2. A high amount of carbon is present in the surfaces which is mainly attributed to contamination. As a consequence, the amount of oxygen bound to metallic elements is difficult to quantify.
3. Despite measurement errors due to the experimental conditions, a large increase of copper and also nickel elements is observed on laser textured surfaces compared to polished surface.

Surface composition changes due to femtosecond laser treatment have already been observed. Li *et al.*<sup>126</sup> observed a variation of the chemical composition between the valleys and the top of the ripples at the LIPSS surface in a Zr-based metallic glass alloy (Zr<sub>41.2</sub>Ti<sub>13.8</sub>Cu<sub>12.5</sub>Ni<sub>10</sub>Be<sub>25.5</sub>) but taking into consideration that the electron probe is larger than the typical size of the LIPSS texture, and that the results of EDX are affected by the topography, these results must be taken with precaution. In this study, the authors did not mentioned any redeposited particles from ablation on the LIPSS surface. Chemical modifications are thus supposed to happen in the structure.

Sipe *et al.*<sup>98</sup> theory suggests that the formation of LIPSS is due to a spatial modulation of absorbed radiation energy induced by interference between the laser beam and electromagnetic waves propagating parallel to the specimen surface. In adequate conditions, this energy modulation causes a periodic variation of the material ablation mechanism, which imprints the LIPSS on the surface, as shown by Canguero *et al.*<sup>76</sup>. This study showed that the titanium/nickel multilayer structure of the material survives at the core of the LIPSS, so this formation cannot be due to hydrodynamic phenomena in the liquid state, but from preferential ablation of high deposited energy areas. Cross sectional TEM images of these ripples presented in Figure 4.3.3.a show presence of a resolidified melted area in the bottom of the valleys and on the top of the structure.

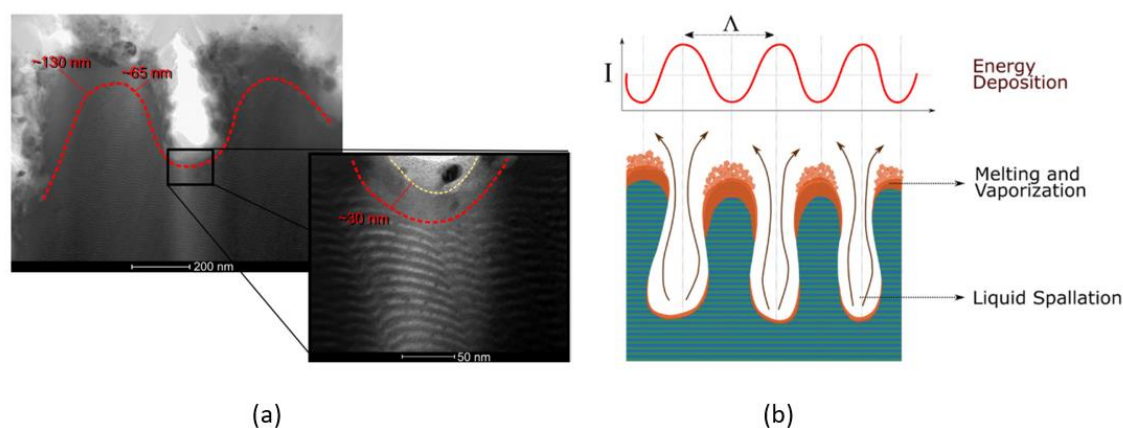


Figure 4.3.3: FIB cross-section of LSFLs on Ti/Ni multilayer substrate irradiated with s-pulse Yb:KYW femtosecond laser of 560 fs pulse duration, wavelength of 1030 nm and pulse energy of 160  $\mu$ J, scheme of the cross section depending on the energy deposition period with ablation mechanisms involved (b)<sup>76</sup>.

Li *et al.*<sup>126</sup>, suggested that their variation of the chemical composition is due to the differences of boiling temperatures of zirconium ( $T_{(Zr)} = 4405^{\circ}\text{C}$ ) and beryllium ( $T_{(Be)} = 2469^{\circ}\text{C}$ ), two elements composing the amorphous alloy. The boiling temperature of Cu and Ni ( $2561^{\circ}\text{C}$  and  $2911^{\circ}\text{C}$ , respectively) are much lower than the boiling temperature of Zr, and thus this could explain the enrichments observed in this work as well. Indeed, in our case, the LIPSS were created in the scanning mode on large surface areas, leading to a larger redeposition of ablation particles. Moreover, as shown in Figure 4.2.3.(left), the valleys are narrower than the ripples, making XPS photons interacting more with the top than with the bottom of the structure. From that, taking into account that copper and nickel have lower boiling temperatures than zirconium (see above), the suggestion that the surface segregation observed by XPS may be due to this difference can be advanced. Thus, for higher pulse energy, the amount of redeposited ablation

particles would be higher, explaining the increase of the Cu/Zr and Ni/Zr ratios for the Ridge texture.

### 4.3.2. Chemical analysis of the ablation particles

The SEM images of the ridge texture surface show that the surface is covered by redeposited ablation particles. The XPS analysis of the surface indicated an enrichment in copper oxide, which is probably related to the ablation particles. In order to verify this hypothesis, we performed a chemical analysis of these particles by collecting them on a carbon tape placed at about 1mm from the sample surface during laser processing. A schematic drawing of the setup used to collect the particles is presented in Figure 4.3.4.a.

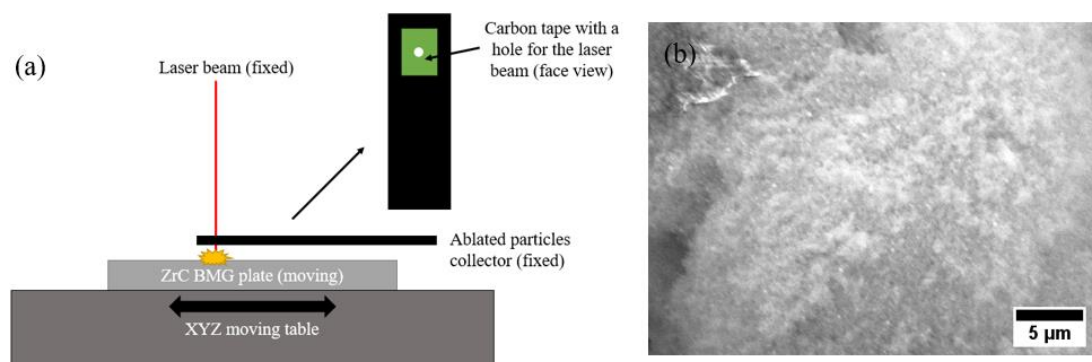


Figure 4.3.4: Scheme of the apparatus to collect ablation particles (a), SEM image of collected ablated particles on carbon tape prior to EDX analysis (b).

After collection, the chemical composition of the particles was determined by SEM-EDX. In order to reduce error, 6 EDX analysis were performed on different areas. The EDX quantification method was described in Chapter 2. In this analysis, only the Cu/Zr, Ni/Zr and Cu/Ni ratios have been taken into account. The results are presented in Table 4.3-2.

	Cu/Zr ratio	Ni/Zr ratio	Cu/Ni ratio
<b>Nominal composition</b>	<b>0.36</b>	<b>0.14</b>	<b>2.5</b>
EDX N°1	0.88	0.18	4.3
EDX N°2	1.0	0.19	5.2
EDX N°3	1.0	0.28	3.5
EDX N°4	0.91	0.29	3.1
EDX N°5	0.91	0.25	3.2
EDX N°6	0.83	0.29	3.0

Table 4.3-2: Ratios between Zr, Cu and Ni elements measured by EDX technique on ablated particles ejected from ZrC substrate.

These results show that the chemical composition of the ablation particles is different from the nominal composition of the alloy. The Cu/Zr and Ni/Zr ratios increase from 0.36 and 0.14 to  $0.92 \pm 0.07$  and  $0.24 \pm 0.05$  respectively. This means that the particles are depleted in zirconium element as compared to the nominal composition. Moreover, the Cu/Ni ratio increased from 2.5 to  $3.7 \pm 0.8$ , which means that the copper content increases more than the Ni content. These measurements show that ablation does not affect uniformly all the elements. This copper and nickel enrichment resulted from Zr depletion, also observed by XPS on the LIPSS textured surfaces (Zr3 alloy), support the hypothesis of a selective ablation of some elements, the elements that vaporize more easily (Cu and Ni) being preferentially removed (Table 4.3-3). As a consequence, they are present in the ablation plume and in the ablation particles in higher concentration. If these particles redeposit on the specimens surface, these surfaces will be enriched in these elements. Even if the vaporization is not triggered at the boiling temperature, this values in Table 4.3-3 give indications on the capability of gas-phase transformation<sup>173</sup>.

<b>Element</b>	<b>Temperature (°C)</b>
Zr	4405
Ni	2911
Cu	2561
Al	2467

Table 4.3-3: Boiling temperatures at vapour pressure of 100 kPa for the elements of the Zr3 alloy.

Researches on high temperature oxidation (773K) of Cu-based BMG ( $\text{Cu}_{60}\text{Zr}_{30}\text{Ti}_{10}$ ) by Tam *et al.*<sup>174</sup> indicated that the copper segregates due to preferential oxidation of Zr to  $\text{ZrO}_2$  leading to the formation of copper oxides on the outer layer surface. Other authors<sup>159,140</sup> suggest that oxidation of Zr-based BMGs is mostly due to the inward diffusion of oxygen, but also to copper diffusion to the surface. Indeed, the authors<sup>139</sup> reported the precipitation of crystalline Cu at the surface of the oxide scale and also a slight copper enrichment at the interface between the oxide layer (mostly  $\text{ZrO}_2$ ) and the substrate. However, these oxidation tests have been done at much lower temperatures than the femtosecond laser treatment, where thousands of degrees can be reached during very short times. Moreover, due to the very short time scale of the liquid state under femtosecond laser treatments, diffusion of copper should be very small or even negligible compared to the copper enrichment in the ablation particles from selective ablation phenomenon due to the difference of boiling temperatures between the constituent elements of the alloy.

## 4.4. Structural characterization

The structural characterization of the polished and textured samples was performed by Bragg-Brentano and grazing incidence X-ray diffraction (XRD). Figure 4.4.1 shows Bragg-Brentano diffractograms of the three alloys polished to 1  $\mu\text{m}$ . Diffractograms are typical of amorphous alloys, without crystalline phase diffraction peaks. The first wide peak centred at  $37^\circ$  is related to the first neighbours' interatomic distances and the second ones centred at  $65^\circ$ , is related to the second neighbours interatomic distances.

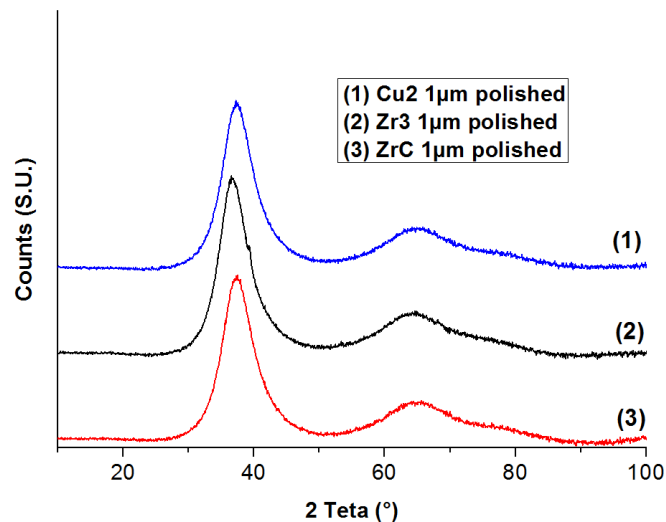


Figure 4.4.1: X-ray diffractograms of untreated Zr3, ZrC and Cu2 1  $\mu\text{m}$  polished metallic glass surfaces.

After femtosecond laser treatment, grazing X-ray diffraction was necessary because the diffraction peaks in the Bragg-Brentano diffractograms were too low in intensity to be distinguished from the background, as shown in Figure 4.4.2.a. In grazing incidence (Figure 4.4.2.b), the diffractograms of both Zr3 and ZrC revealed similar 3 peaks centred at  $30.5^\circ$ ,  $50.8^\circ$  and  $60.4^\circ$ , which were identified as tetragonal zirconium oxide  $\text{ZrO}_2$  diffraction peaks. The small peak at about  $43^\circ$  in Zr3 Ridge texture was indexed as cubic metallic copper Cu and the very low intensity one at about  $61^\circ$  may be copper II oxide, but it's hard to accurately identify it due to the very low amplitude. Copper at the surface may be the result of copper segregation from zirconium oxidation which can promote formation of nanocrystalline Cu solid solution<sup>159</sup>.

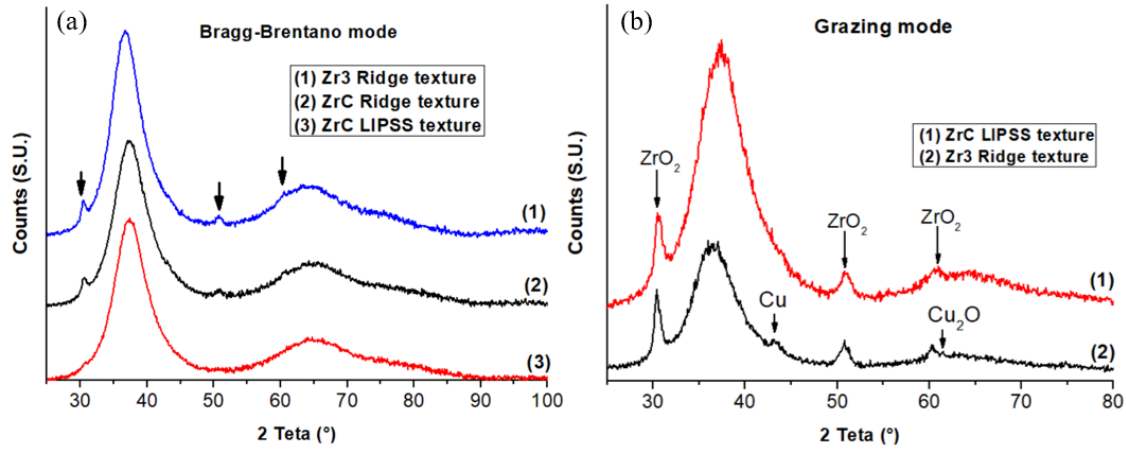


Figure 4.4.2: Bragg-Brentano (a) and grazing mode (b) X-ray diffractograms of Zr3 and ZrC amorphous alloys femtosecond laser treated with RIDGE texture (0.4 J/cm<sup>2</sup>) and LIPSS texture (0.07 J/cm<sup>2</sup>).

Grazing incidence X-ray diffractograms of the laser treated Cu<sub>2</sub> alloy with the two types of textures are presented in Figure 4.4.3. They exhibit diffractions peaks centred at 30.5°, 50.8° and 60.4° corresponding to ZrO<sub>2</sub> tetragonal zirconia, but these peaks are less intense than in the Zr3 and ZrC laser treated samples. Moreover, the specimens with the Ridge texture, also exhibit diffraction peaks centred at 41.2° and 47.8° corresponding to Cu<sub>2</sub>ZrAl intermetallic compound.

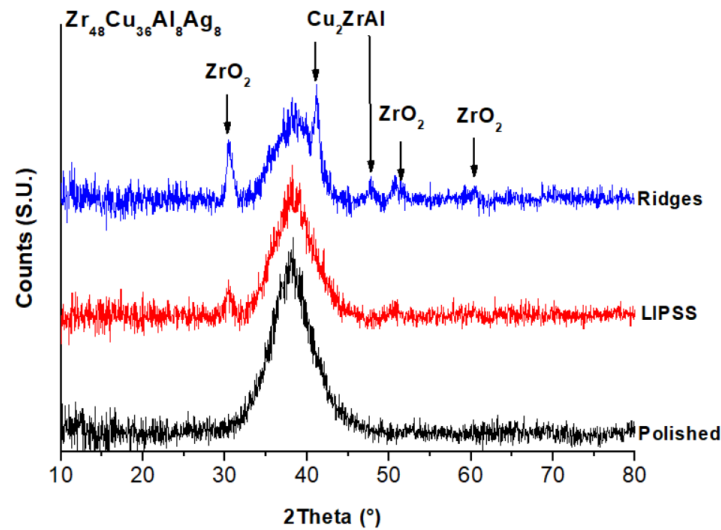


Figure 4.4.3: Grazing mode X-ray diffractograms of Cu<sub>2</sub> amorphous alloy 1µm polished, treated with LIPSS texture (0.07 J/cm<sup>2</sup>) and RIDGE texture (0.4 J/cm<sup>2</sup>).

Zirconium is the major constituent element of these alloys. Since the ablated material reaches very high temperatures during the laser treatment, and considering that Zr is very reactive with oxygen, zirconium oxide (ZrO<sub>2</sub>) formation is expectable. The tetragonal zirconia found is the most commonly formed oxide on Zr based metallic glass surfaces<sup>160,175</sup>. In the case of the Cu<sub>2</sub> alloy, the high content of copper (36 at.%) and the high temperature reached during irradiation may be the cause of the formation of other intermetallic phases such as Cu<sub>2</sub>ZrAl when the

specimens are treated with high pulse energy<sup>173</sup>. Thus, for some amorphous alloys, femtosecond laser processing can promote the formation of crystalline phases in the surface region.

## 4.5. Wettability measurements

In this Section, we analyse the effect of the femtosecond laser treatment on the wettability on the three amorphous alloys. The time-dependency of the contact angle was determined in the range of 0 s to 60 s for droplets in contact with textured and non-textured surfaces. The surface free energy (SFE) value was calculated for the polished surfaces but no SFE value were calculated for the textured surfaces because it depends on the surface chemistry, and do not take into account the surface topography. The surface free energy, was determined by the Owens-Wendt method described in Chapter 2. This method is particularly appropriate for smooth surfaces, where the topographic contribution is negligible. In the case of the textured surfaces, this method is not relevant because it is very difficult to separate the chemical and the topographic contributions.

As explained in Chapter 2, the surface free energy calculation requires the measurement of the contact angle of at least two different liquids with different polar and dispersive components (distilled-deionized (DD) water and diiodomethane). The contact angles of diiodomethane droplets was measured for the polished and the textured surfaces to evaluate the effect of the surface topography on the wetting behaviour for this liquid, characterised by the absence of the polar component, hence with a surface tension that only depends on the dispersive component ( $\gamma_L = \gamma_L^d = 50.8$  mN/m). The polar and dispersive components depend on the purity of the diiodomethane and, hence, on its age and the storage conditions. In our case the polar component  $\gamma_L^p$  was 4.08 mN/m and the dispersive component  $\gamma_L^d = 47.27$  mN/m but has been taken into account in the contact angle measurements.

The wettability was evaluated by the sessile drop method described in Chapter 2. To determine the surface free energy, DD-water and diiodomethane droplets were deposited on polished and textured surfaces of the three alloys. The evolution of the contact angles are presented in Figure 4.5.1. The polished and textured surfaces contact angle varied only slightly or not at all after 60 seconds and so the equilibrium contact angle considered to be the value for the longest measurement time (60 s). 60 s is a short time for reaching equilibrium, but as long as no strong variations were observed during the measurements, this time was considered to be sufficient to obtain repetitive results.

The largest decrease of the contact angle was observed for DD-water droplets on Zr3 polished surfaces with  $\theta_a = 63^\circ$  at 0 s and  $57^\circ$  at 20 s and then remaining constant up to 60s. However, the fact that the contact angle remains stable within this first 60 s period does not allow to predict its evolution on a longer time scale, where the surface chemistry contribution, for example surface contamination, may play a more significant role. It gives, information on the effect of surface topography on the general wetting behaviour. In the case of Ti-4Al-6V surfaces textured with fs laser in the same range of fluences, Cunha *et al.*<sup>114</sup> observed a strong time dependency of the contact angle between 0 and 200 s, with a tendency of the textured surfaces to become increasingly hydrophilic with time. On the other hand, for much longer timescales (0 to 10 days), increased hydrophobicity was reported, which was explained by an increase of carbon contamination<sup>81,113</sup>.

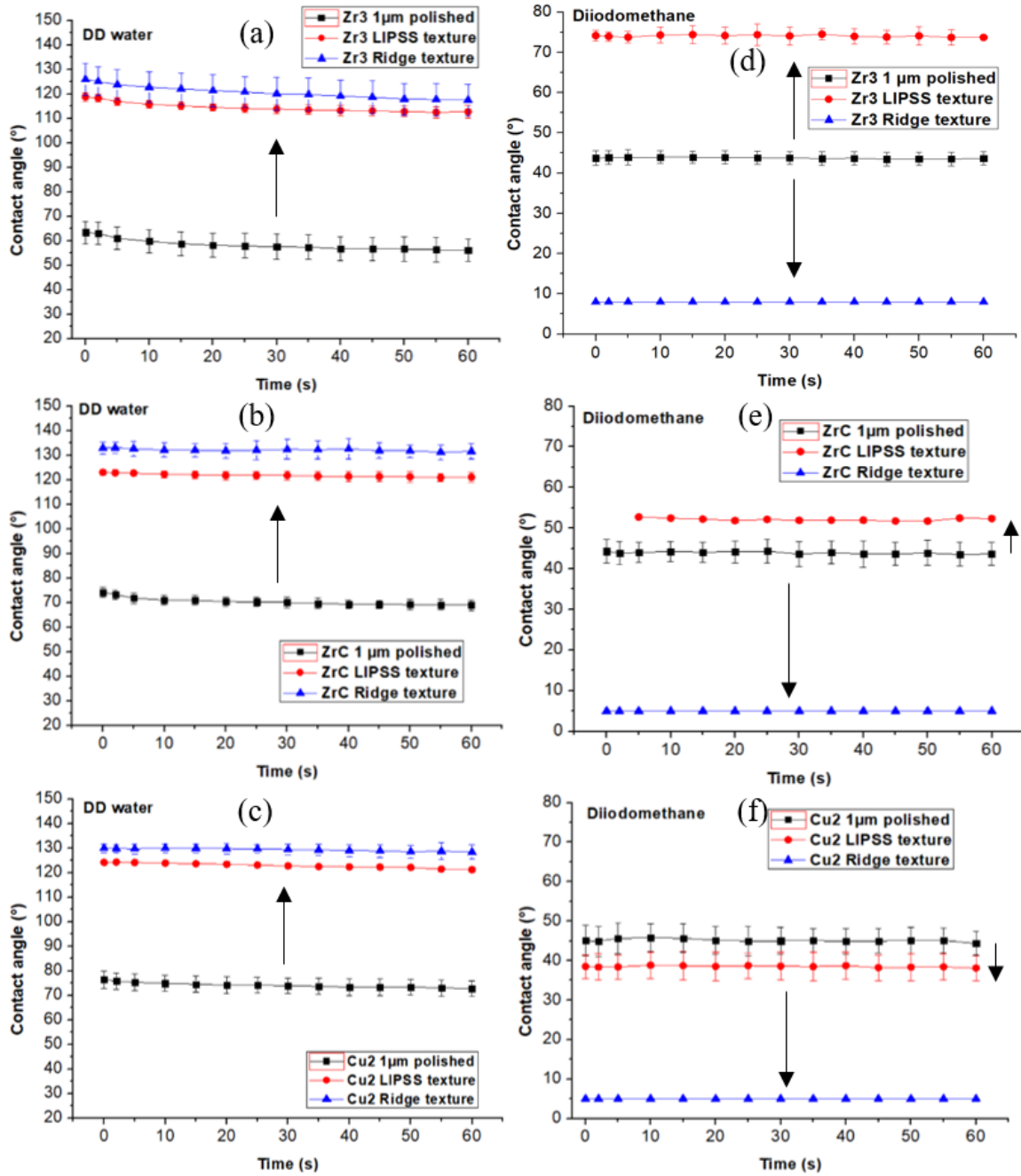


Figure 4.5.1: Time evolution of the apparatus contact angle for DD water (a), (b), (c) and diiodomethane (d), (e), (f) droplets on 1 μm polished and laser textured surfaces of Zr3 (a), (d), ZrC (b), (e) and Cu2 (c), (f) amorphous alloys. Presented values were measured based on the droplet profiles taken in a direction perpendicular to the laser beam polarization.

### Distilled-Deionized-water measurements

The values of the contact angle at 60 s for all material/texture/liquid combinations are summarized in Table 4.5-1. For DD-water, the femtosecond laser treatment increases considerably the equilibrium contact angle for the three alloys, making surfaces change from hydrophilic ( $56^{\circ} \pm 4$  for Zr3 polished surface) to highly hydrophobic ( $124^{\circ} \pm 5$  for Ridge texture on Zr3 surface). LIPSS textures contact angles with DD-water are about  $10^{\circ}$  to  $20^{\circ}$  lower than

for the Ridge texture. The values of the contact angles for the three alloys, are similar as shown in Figure 4.5.2. However, the Zr3 polished surface exhibited lower contact angles for DD water after 60 seconds ( $56^\circ \pm 4$ ) than ZrC and Cu2 surfaces ( $69^\circ \pm 2$  and  $73^\circ \pm 3$ , respectively).

### Diiodomethane measurements

The contact angles for diiodomethane present more scatter and reveal different behaviours for each type of surface texture. While polished surfaces present very similar contact angles (around  $44^\circ$ ) for all the metallic glasses, LIPSS and ridge fs-textured surfaces behave very differently. The contact angle for the LIPSS in the Zr3 is almost  $30^\circ$  larger than for the polished surface, whereas for ZrC there is no variation and for Cu2 the contact angle decreases by about  $30^\circ$  after the laser treatment (Figure 4.5.3). These differences in behaviours do not allow to understand the effect of the texture because for diiodomethane the chemical contribution is very important. For the Ridge texture, the contact angle decreases dramatically to values lower than  $10^\circ$ , indicating a super-wetting behaviour of diiodomethane for this texture. These values are approximative, due to the difficulty of measuring such low angle values with the experimental method used. A contact angle measurement method appropriate to very low angles would be more suitable in this case.

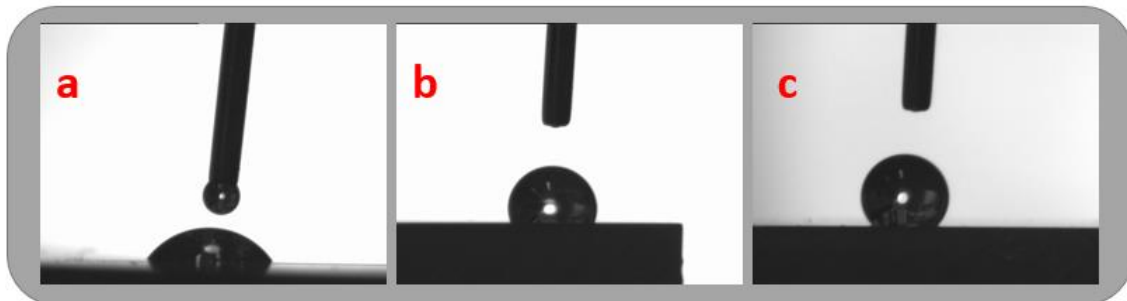


Figure 4.5.2: Images of DD water droplets deposited on Zr3 surfaces after 60 seconds for  $1\ \mu\text{m}$  polished surface (a), LIPSS texture surface (b) and Ridge texture surface (c) tip of the syringe is 0.8 mm in diameter.



Figure 4.5.3 : Images of diiodomethane droplets deposited on Zr3 surfaces after 60 seconds for  $1\ \mu\text{m}$  polished surface (d), LIPSS texture surface (e) and Ridge texture surface (f) tip of the syringe is 0.8 mm in diameter.

<b>Zr3</b>	<b>Water (°)</b>	<b>Diiodomethane (°)</b>	
1 μm polished	56 ± 3	44 ± 2	
LIPSS texture	107 ± 4	71 ± 2	
RIDGE texture	124 ± 5	8 ± 2	
<b>ZrC</b>			
1 μm polished	70 ± 2	44 ± 3	
LIPSS texture	117 ± 2	47 ± 4	
RIDGE texture	130 ± 3	8 ± 3	
<b>Cu2</b>			
1 μm polished	73 ± 3	44 ± 3	
LIPSS texture	117 ± 1	34 ± 3	
RIDGE texture	124 ± 3	9 ± 2	
<b>Surface tension (mN/m)</b>	$\gamma_L$	$\gamma_L^d$	$\gamma_L^p$
DD-water	71.96	21.34	50.61
Diiodomethane	49.35	45.27	4.08

Table 4.5-1: Equilibrium contact angles of water and diiodomethane after 60 seconds for the three amorphous alloys measured experimentally. These equilibriums are average values of both perpendicular and parallel measures from laser beam polarization direction.

An increase of the contact angles for water was reported for all kinds of laser surface textures and a wide range of alloys. This behaviour can be explained by the surface roughness created by laser texturing and also by surface chemistry contributions. Whereas the contact surface areas for smooth surfaces that exhibit an hydrophilic behaviour depends on the surface free energy of the sample, micron size patterns induce different types of interaction between the liquids and the surface. As explained in Chapter 1, both Wenzel<sup>46</sup> and Cassie-Baxter<sup>48</sup> models were proposed to explain the observed contact angles. When a Wenzel's state occurs, wetting is enhanced by roughness, meaning that a hydrophilic surface will become more hydrophilic after the surface treatment. In our case, hydrophilic flat surfaces became more hydrophobic after laser treatment, so the Wenzel model cannot be applied here<sup>81</sup>. The gas pocket effect described by Cassie-Baxter's model is more suited. The contact angle increases with the surface textures and reaches around 130° for the Ridge textured surface. This is explained by the presence of a multi-scale roughness, where micron-size ridges are covered with LIPSS and redeposited ablated particles, as seen in Figure 4.2.3.

According to the present results, the Ridge texture leads to different wetting behaviours depending on the liquid. The major difference between the two liquids is that distilled-deionized

water has a higher surface tension than diiodomethane (c.f. Table 4.5-1). Moreover water is polar in nature while for diiodomethane the dispersive component is predominant. Thus, the hypothesis advanced to explain this difference in wetting behaviour is that the high roughness of the ridge texture promotes hydrophobicity by a Cassie-Baxter mechanism when the liquid have a sufficiently large polar component in the surface tension. On the contrary, when the liquid surface tension is low and mostly dispersive, the texture promotes super wetting with very low contact angles.

### Surface free energy of polished surfaces

On the basis of the contact angles values for polished surfaces for water and diiodomethane, the surface free energy ( $\gamma_{SV}$ ) was calculated using the geometric mean approach combined with the Owens and Wendt method presented in Chapter 2. The surface free energy values calculated for the three alloys presented in Table 4.5-2. It ranges from  $50 \pm 3$  mN/m to  $41 \pm 2$  mN/m for Zr3 and Cu2 alloys, respectively. The higher surface free energy of Zr3 alloy may be due to the presence of a larger native zirconia oxide layer, explained by the higher zirconium content of this alloy. It is known that zirconia oxide, as titanium oxide, promotes hydrophilic behaviour<sup>47,150</sup>.

<b>Zr3</b>	$\gamma_{SV}$ (mN/m)	$\gamma_{SV}^p$ (mN/m)	$\gamma_{SV}^d$ (mN/m)
1 $\mu$ m polished	$50 \pm 3$	$17 \pm 3$	$33 \pm 1$
<b>ZrC</b>	$\gamma_{SV}$ (mN/m)	$\gamma_{SV}^p$ (mN/m)	$\gamma_{SV}^d$ (mN/m)
1 $\mu$ m polished	$43 \pm 2$	$10 \pm 2$	$34 \pm 2$
<b>Cu2</b>	$\gamma_{SV}$ (mN/m)	$\gamma_{SV}^p$ (mN/m)	$\gamma_{SV}^d$ (mN/m)
1 $\mu$ m polished	$41 \pm 2$	$8 \pm 2$	$34 \pm 2$

Table 4.5-2 : Surface free energy ( $\gamma_{SV}$ ) with polar ( $\gamma_{SV}^p$ ) and dispersive part ( $\gamma_{SV}^d$ ) of polished and textured surfaces of the three amorphous alloys calculated by using the Owens and Wendt method combined with the geometric mean approach. Total surface free energy presented is the average of the values measured in both parallel and perpendicular directions from laser beam polarization.

### Wetting anisotropy of the textured surfaces

The LIPSS and ridge surface textures are anisotropic due to the linear shape of the ripples. These textures lead to an anisotropic wetting behaviour as shown in Figure 4.5.4. For example, the ridge texture on Zr3 alloy leads to contact angles of  $131 \pm 3^\circ$  and  $117 \pm 5^\circ$  in directions parallel and perpendicular to the direction of the ridges, respectively.

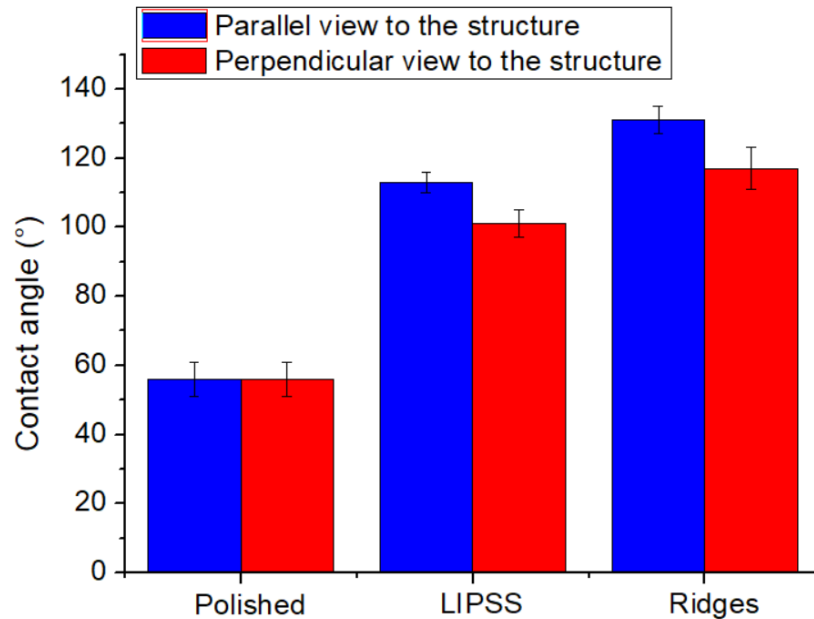


Figure 4.5.4: Graph of the anisotropic wetting of Zr3 alloy with DD-water droplets on both LIPSS and RIDGE textures with observation view parallel and perpendicular from laser beam polarization.

The influence of the chemical composition of the laser treated surfaces on wetting was not studied in detail in this thesis. XPS measurements were performed without cleaning the surface and thus a strong carbon content were measured, which is known to promote hydrophobicity<sup>53</sup>. XPS also revealed that the laser treatment reduces the amount of carbon prior to the contact angle measurements, the specimens were cleaned for 12h in a vacuum oven at 45°C, so carbon contamination was at least partially removed and the effect of carbon on wettability should be negligible. Therefore, textured samples promotes hydrophobicity despite the fact that the surface is covered by a ZrO<sub>2</sub> oxide, which promotes hydrophilicity. The removal of this oxide layer may promote even a more hydrophobic behaviour. Complementary studies may allow a better understanding of the chemical contribution to the wetting behaviour of the laser textured surfaces.

## 4.6. Corrosion study

This section is dedicated to the electrochemical study of non-textured and textured metallic glass surfaces. To evaluate the effect of initial composition and femtosecond laser surface treatments on corrosion resistance behaviour, three types of measurements were performed. As it has been developed in chap II, every corrosion measurements were realised by immersing samples in 0.1 M NaCl solution, because the NaCl content is close to the ones commonly used in physiological liquids to study corrosion behaviour in human body. It is also known that Cl<sup>-</sup> ions are highly polarisable and so very reactive with surface energy heterogeneities (defects) such as grain boundaries or dislocations<sup>57</sup> and Cl<sup>-</sup> ions are important inductors of corrosion processes under environmental conditions.

### Corrosion behaviours of non-textured amorphous alloy surfaces

First, polished surfaces of the three alloys (Zr3, ZrC, Cu2) have been studied to estimate their corrosion behaviour in NaCl solution. For that, open-circuit potential (OCP) measurements of 2400 seconds were firstly conducted in 0.1 M NaCl solution. As explained in Chap. II, electrochemical potential variations can be related to an ennoblement (increase of the potential) or higher reactivity (decrease of the potential) of the surface. Ennoblement is assumed to be related to the growth of a passive or a protective layer on the working electrode surface (sample). Then, anodic polarization measurements have been realized to understand corrosion kinetics and the corrosion rates of every samples. Finally, electrochemical impedance spectroscopy was applied with texture and non-textured specimens to get more accurate information on the interface mechanisms involved in the corrosion processes.

Figure 4.6.1.a shows OCP curves of the three 1 $\mu$ m polished metallic glasses. As observed, the three alloys behave differently in 0.1M NaCl solution. Zr3 potential started at -390 mV and increased to -280 mV after about 1000 s and then values got almost stable until 2400 s, indicating a stabilization of the surface reactivity and so an ennoblement of the surface probably due to the formation of a protective layer. ZrC surface showed a more protective behaviour, with a small increase from -255 mV to -240 mV of the OCP value in a few dozen of seconds and then a stabilization until the end, which means that the surface formed a protective film almost instantaneously. Contrarily, the Cu2 alloy potential started at almost the same value as Zr3 but then decreased to -430 mV without stabilization at 2400 s, meaning that the surface did not form a protective layer and became more reactive in the solution, and so more prone to corrosion.

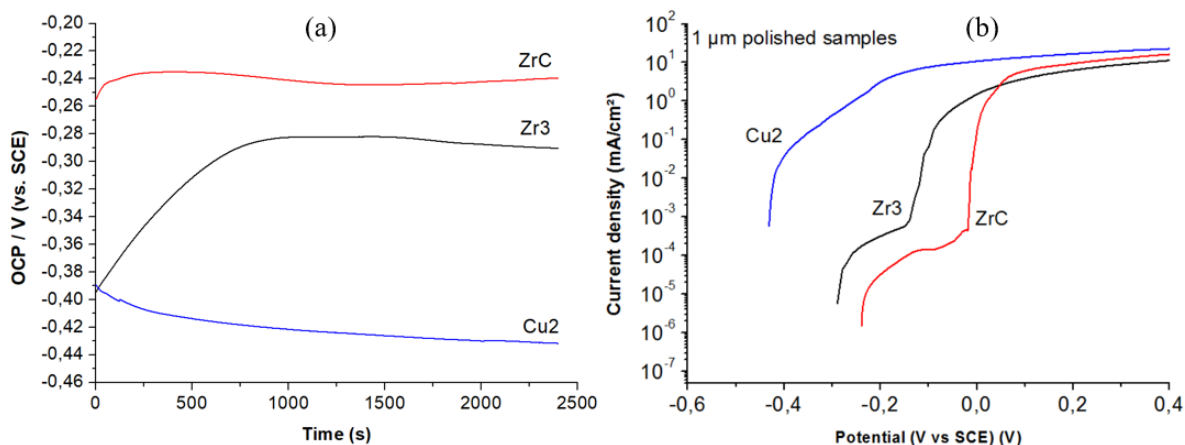


Figure 4.6.1 : Open-circuit potential measurements during 2500 seconds (a) and anodic polarisation measurements from OCP (b) for the three amorphous alloys studied Zr3, ZrC and Cu2.

Metallic glass	Corrosion potential $E_{\text{corr}}$ (from OCP) (mV)	Corrosion current density $I_{\text{corr}}$ (mA/cm <sup>2</sup> )	Pitting potential $E_{\text{pitt}}$ (mV)	Pitting current density $I_{\text{pitt}}$ (mA/cm <sup>2</sup> )	Passivation zone (mv)
Zr3	-280	9.5 E-5	-140	7.7 E-4	140
ZrC	-240	7 E-6	-17	5.1 E-4	223
Cu2	-430	3.8 E-2			

Table 4.6-1: Summary of the different electrochemical constants measured with OCP and anodic polarization from OCP +1V for the three amorphous alloys Zr3, ZrC and Cu2.

Anodic polarization curves of the three alloys were grouped in Figure 4.6.1 (b) and electrochemical constants were reported in Table 4.6-1. Every measurements started from OCP to +1V to cover a large range of potentials and to be able to observe the overall electrochemical phenomena. As for OCP measurements, different behaviours were observed in anodic polarization measurements. Both Zr3 and ZrC alloys exhibited corrosion behaviours of typical Zr-based metallic glass with low current density rates and a passivation zone at low potentials<sup>3,10,55</sup>. This passivation zone can be described as the resistance of the surface (passivation layer in the case of Zr metallic glasses) to be corroded, while the potential increased to force corrosion to be initiated. Anodic polarisation of Zr3 and ZrC alloy, depicted a sharp increase of current density at a certain potential which is the pitting potential  $E_{\text{pitting}}$ . This behaviour is related to pitting corrosion processes, where the passive layer breaks dramatically and then chloride ions start to attack the unprotected areas of the surface and the active corrosion proceeds.

However, ZrC alloy showed better resistance to pitting corrosion compare to Zr3, with corrosion current intensity  $I_{\text{corr}} \approx 9.5 \cdot 10^{-5}$  mA/cm<sup>2</sup> and  $I_{\text{corr}} \approx 7 \cdot 10^{-6}$  mA/cm<sup>2</sup> for Zr3 and ZrC,

respectively. Potential ranges of passivation were also different between these two alloys: Zr3 showed a range of 140 mV whereas ZrC exhibited a range of 215 mV from  $E_{corr}$  to  $E_{pitt}$ . After this pitting potential  $E_{pitt}$ , current density increased dramatically, meaning the break of the passive film at sample surfaces and so corrosion occurrence. Contrarily, Cu2 alloy exhibited high reactivity in 0.1 M NaCl solution. Indeed, anodic polarization curve did not show any passivation behaviour and corrosion current measured at  $3.8 \cdot 10^{-2}$  mA/cm<sup>2</sup> is 3 orders higher than for Zr3 and ZrC. These current density results indicated higher corrosion rate on Cu2 surface compared to Zr3 and ZrC.

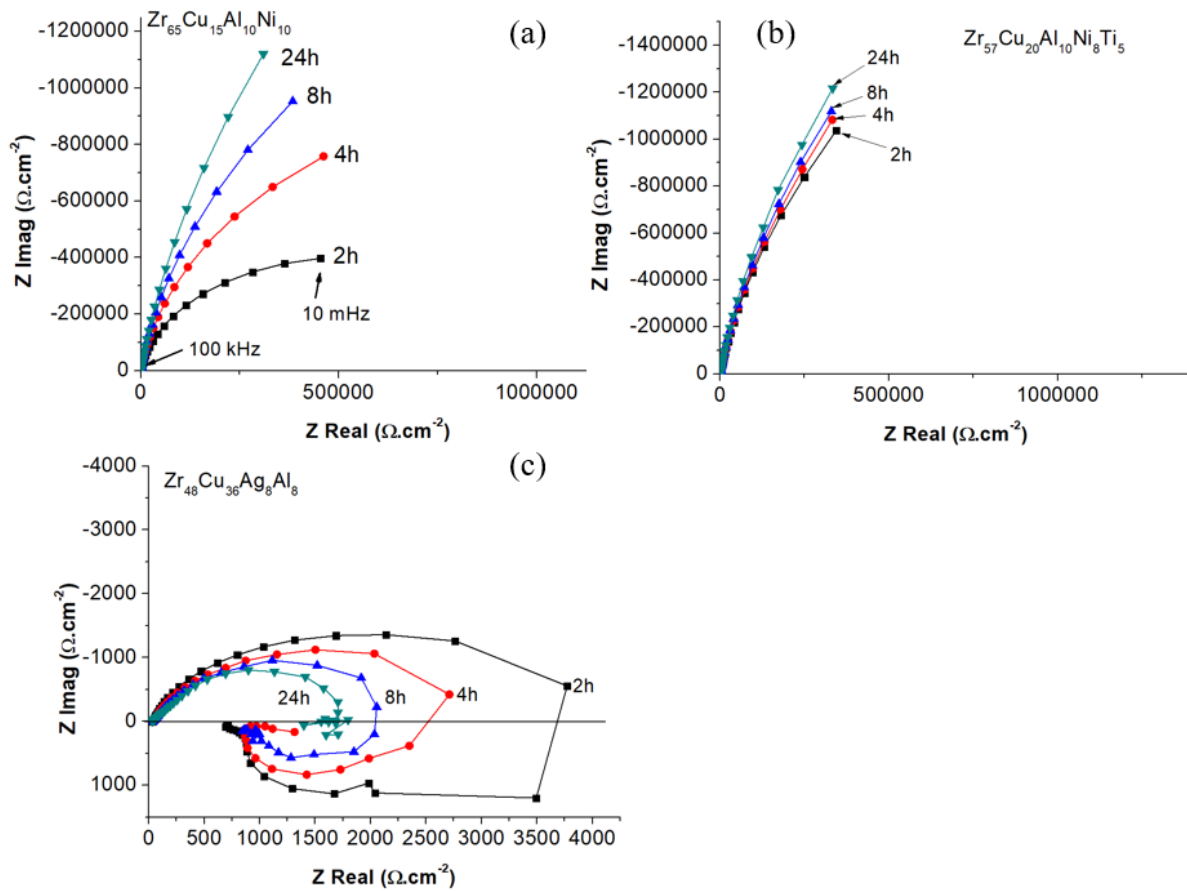


Figure 4.6.2 : Nyquist diagram of electrochemical impedance spectroscopy (EIS) measurements on the Zr3 (a), ZrC (b) and Cu2 (c) 1µm polished amorphous alloy surfaces.

Electrochemical impedance spectroscopy analysis of the three polished samples Zr3 (a), ZrC (b) and Cu2 (c) at 2, 4, 8 and 24 h of immersion in 0.1 M NaCl solution are presented in Figure 4.6.2. In these Nyquist plots, the real part of the impedance Z in X-axis represents the resistivity value of a surface between the highest and the lowest value of frequencies of a capacitive loop. This means that the larger the diameter of the loop, the more corrosion resistant is the surface. In the case of Zr3 and ZrC alloys, every diagrams showed the same trend and were composed of a capacitive loop with a large diameter (around 1 to 2 M Ω.cm<sup>2</sup>). For Zr3 alloy, the diameter

of the capacitive loop increases with immersion time, meaning that the surface became more and more resistive to corrosion attack. ZrC showed very similar curves from 2 h to 24 h, meaning that after 2 h of immersion, the surface is already highly protective, with only a small increase of the diameter to reach almost the same value as Zr3 of around  $-1200 \text{ k}\Omega\cdot\text{cm}^2$  at high frequency for 24 h of immersion. This impedance behaviour during time on the two alloy surfaces meant that protective layers were formed. For Zr3 alloy, the passive film thickness increased during time while in the case of ZrC it was already very protective after only 2 h of immersion with only a small increase of the capacitive loop diameter after 24 h.

Like for anodic polarization measurements, EIS experiments on Cu2 revealed a high susceptibility to corrosion. Indeed, EIS diagrams of Cu2 in Figure 4.6.2.c showed a strong variation of the imaginary part in function of the real part of the impedance, followed by an inductive loop in the low frequency region. The reduction in diameter of both impedance and inductive loop mean an increase of the capacity while the resistance and the impedance of the circuit decreased with frequency. This diameter variation can be related to the competition between formation and dissolution of corrosion products on the surface. Thus, presence of inductive loops in the Nyquist diagram revealed that the system is not stable after 24 h of immersion. Inductive loops are related to absorption and desorption process of metallic cations  $M^+$  which are typically formed on the metallic alloy species.

In summary, different corrosion behaviours were identified on polished samples:

1. Anodic polarization measurements indicated that the three alloys are sensitive to pitting corrosion, which is represented for Zr3 and ZrC alloy with a strong increase of current density at a certain potential that is the pitting potential  $E_{\text{pitt}}$ .
2. ZrC alloy exhibited the best corrosion resistance in 0.1 M NaCl solution, with the lowest current density at corrosion and pitting potentials. In EIS experiment, ZrC rapidly created a highly protective surface layer with a small increase of the impedance values between 2 h and 24 h of immersion.
3. Zr3 alloy exhibited lower corrosion resistance than ZrC in NaCl solution, but presented also a passivation behaviour during EIS experiments. A strong increase of the impedance between 2 h and 24 h of immersion indicated the increase of the passive layer thickness to reach almost the same value of resistivity as for ZrC after 24 h of immersion.
4. Cu2 alloy showed poor corrosion resistance in NaCl solution compared to Zr3 and ZrC alloys, without any passivation behaviour of the surface. Presence of inductive loops

and decreasing of the capacitive diameter during time in EIS measurements indicated competition between formation and dissolution of corrosion products that were obviously not stable and promoted active corrosion processes at sample surface.

### Effect of femtosecond laser treatment on corrosion properties

After non-textured metallic glass surfaces, corrosion resistance properties of textured surfaces with LIPSS and ridge textures have been investigated. For that, anodic polarization measurements has been conducted on LIPSS and Ridge textures on the three alloys. Moreover, LIPSS and Ridge textures have been also investigated using EIS analysis. These experiments were conducted with the same experimental parameters than the one used for non-textured surfaces, starting from OCP after 2400 s of immersion in 0.1 M NaCl solution. Polarization and EIS plots of Cu2 alloy has been reported on the second annex.

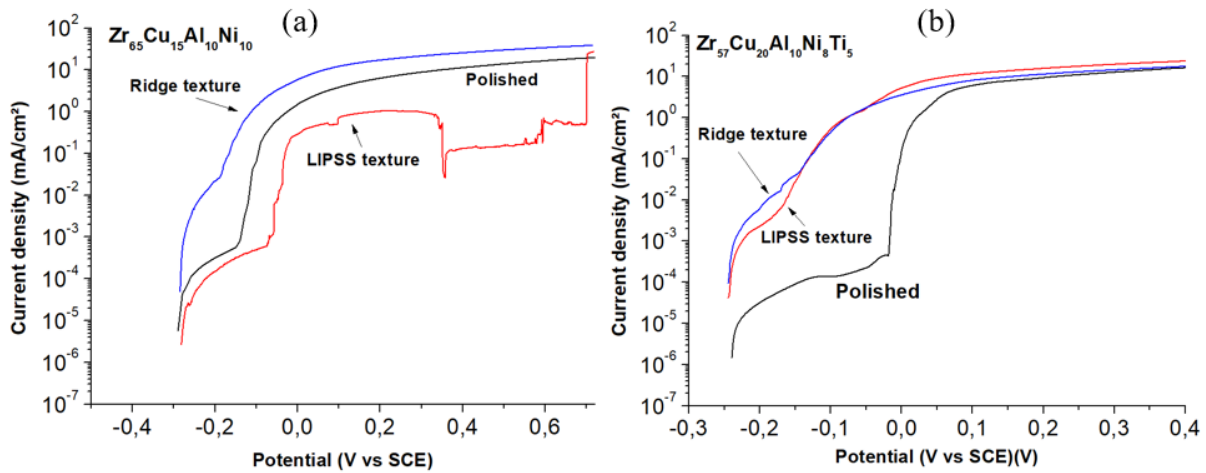


Figure 4.6.3: Anodic polarization measurements on polished, LIPSS texture and RIDGE texture on Zr3 (a) and ZrC (b) amorphous alloy surfaces.

Figure 4.6.3.a shows that both low energy (LIPSS) and high energy (Ridges) surface treatments did not have the same effect on corrosion resistance property of Zr3 alloy. Indeed, polarisation curve of the Ridge texture indicates a strong increase of current density  $I_{corr}$  at the corrosion potential  $E_{corr}$ , increasing from  $9.5 \cdot 10^{-5}$  to  $3.4 \cdot 10^{-3}$  mA/cm<sup>2</sup> for polished and ridge textured surface, respectively. Moreover, the Ridge textured surface polarisation curve do not present any passivation behaviour and the pitting potential  $E_{pitt}$  is closer to the corrosion potential  $E_{corr}$  ( $\approx 80$  mV). Contrarily, the LIPSS textured surface maintain corrosion resistance, with a slightly lower corrosion current and a larger passivation range passing from 140 mV to 210 mV for the untreated and the LIPSS texture, respectively. However, at higher potential than  $E_{pitt}$ , current variation is very unstable compared to other curves. The decrease of the current density at about

350 mV might be due to measurements artefacts. The current density limit of around 100 mA/cm<sup>2</sup> was not reached until potential of 700 mV.

In the case of ZrC (Figure 4.6.3.b), both laser treatment at low and high energy increased current density and made the passivation zone to disappear, with  $I_{\text{corr}}$  increasing from  $6.7 \cdot 10^{-6}$  to  $5.3 \cdot 10^{-4}$  and  $1.5 \cdot 10^{-3}$  mA/cm<sup>2</sup> for polished, LIPSS and ridge textured surfaces, respectively. Anodic polarisation of LIPSS textured surface showed a small passivation tendency on a tiny potential range compared to polished surface. However, it is obvious that in the case of ZrC alloy, both laser treatments strongly decreased corrosion resistance in 0.1 M NaCl solution.

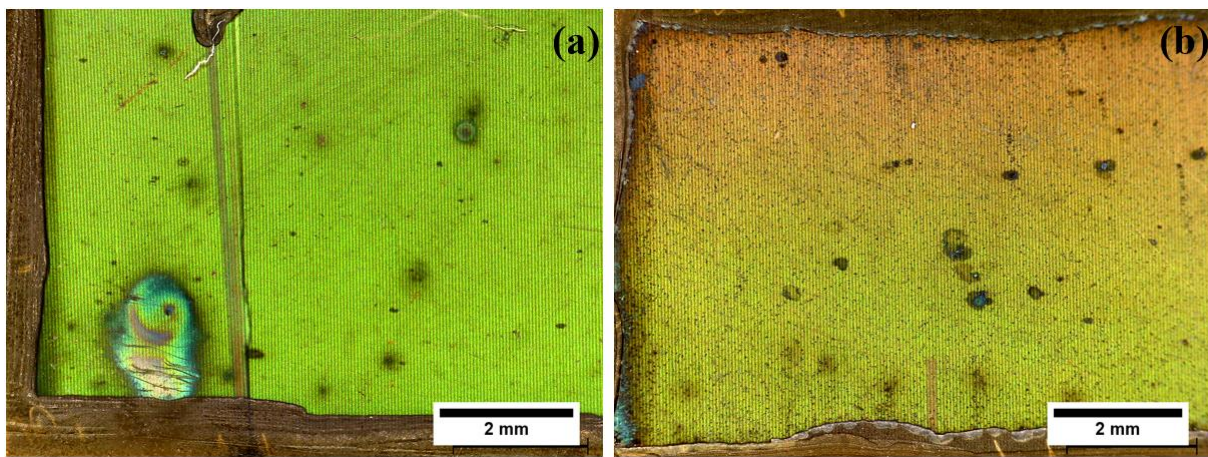


Figure 4.6.4: Optical microscope images of Zr3 (a) and ZrC (b) surfaces textured with LIPSS after anodic polarization measurements.

To illustrate this significant difference about the effect of LIPSS texture on corrosion resistance properties between Zr3 and ZrC amorphous alloys, Figure 4.6.4 presents optical microscope images of both Zr3 and ZrC LIPSS textured surfaces after anodic polarization measurements. Green colours of both surfaces come from the iridescent nature of the nanometric pattern of the LIPSS texture, which interferes with visible light. As it can be observed, after polarization, LIPSS texture on Zr3 alloy (Figure 4.6.4.a) shows several corroded points of few hundred of microns, randomly dispersed. On the other way, the LIPSS texture on ZrC alloy (Figure 4.6.4.b) after polarization exhibited also few larges and dispersed corroded points but the surface is also entirely covered with micron-size pits (black spots).

Like for untreated samples, LIPSS and ridge textured surfaces have been characterized using EIS technique. Figure 4.6.5 presents Nyquist diagrams of both ZrC and Zr3 alloys textured surfaces for 2h to 24h of immersion in 0.1 M NaCl. Figure 4.6.5.a shows Nyquist diagram of Zr3 surface with the LIPSS texture. Due to non-stability and risk of artefacts measurements after 24h curve are not presented here. For LIPSS textured surface on Zr3, Nyquist plot revealed

capacitive loops with high diameter. Diameters increased with immersion time, meaning an increase of the surface electrical resistivity. Like for untreated Zr3 surface, this trend indicates the creation of a protective layer at the sample surface. The improvement of its corrosion resistance behaviour during time is probably due to an increase of the protective layer thickness.

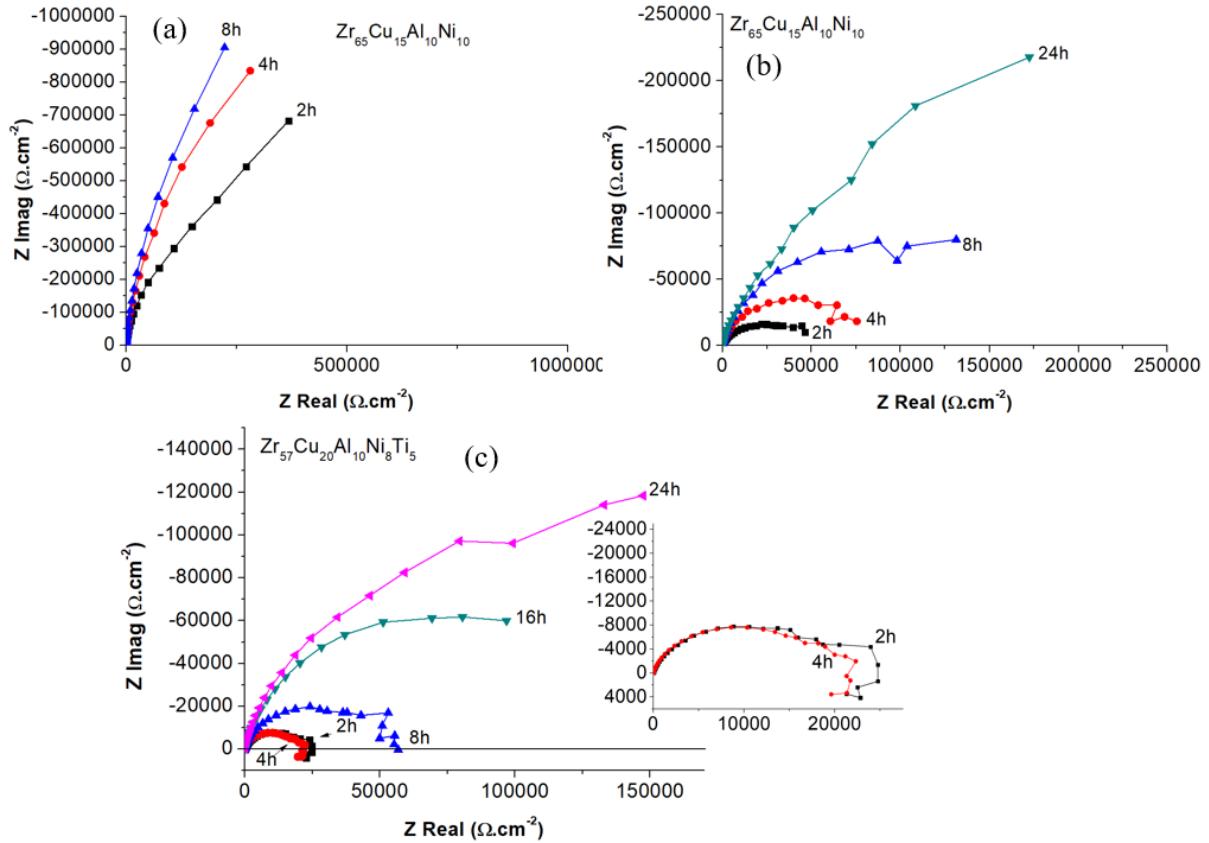


Figure 4.6.5: Nyquist diagrams of LIPSS (a) and Ridge (b) textures on Zr3 alloy and Ridge texture on ZrC alloy (c) made by EIS experiments from 2 h to 24 h of immersion in 0.1 M NaCl.

EIS plots of Zr3 alloy with the Ridge texture is presented in Figure 4.6.5.b. We observe an increase of the impedance with immersion time, but every immersion time measurements did not exhibit the same behaviour. Indeed, after 2 h and 4 h of immersion, we can observe the presence of capacitive loops where the impedance increases from the high to middle frequency rates (left part of the plot) and then decreases for the lower frequency rates (right part of the plot). Two different behaviours were so identified: the surface layer stability with a decrease of the capacity from middle to high frequencies and then an increase of the capacitance and so a decrease of the layer resistance at low frequencies. At higher immersion time, we observed an increase of the capacitive loop diameter with a stabilisation at 8h of immersion from middle to low frequencies, whereas at 24 h impedance increases significantly from high to low frequencies. Same trends have been observed for ZrC alloy with the Ridge texture (Figure

4.6.5.c), with an increase of the impedance value with immersion time but with the presence of inductive loops at 2 h and 4 h of immersion, which is an indicator of corrosion activity and more specially crevice corrosion process. As for Zr3, at higher immersion time, a strong increase of the impedance value with an increase of the capacitive loop diameter has been observed. However, impedance modulus at low frequency after 24 h of immersion is smaller for ZrC than for Zr3 alloy, indicating a better corrosion resistance for Zr3 textured alloy surface.

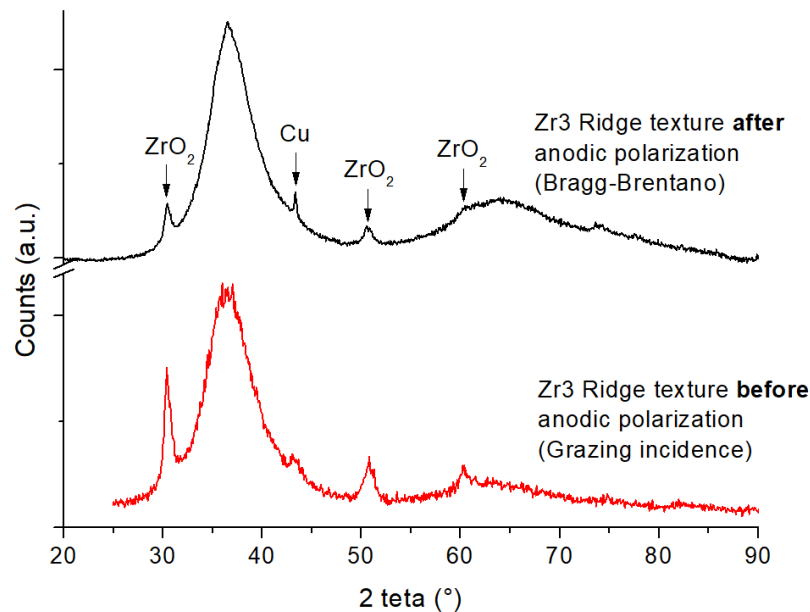


Figure 4.6.6: Bragg-Brentano XRD measurements of Zr3 Ridge texture before anodic polarization (a), grazing incidence XRD measurements of Zr3 Ridge texture after anodic polarization (b).

Presence of copper on Ridge textured surface was already reported in section 4.4. Figure 4.6.6 above presents both diffractograms of ridge texture on Zr3 surface before and after anodic polarization measurements. Because of the different XRD techniques used, it is hard to quantitatively compare both signals so we were focused on  $\text{ZrO}_2/\text{Cu}$  peaks intensity ratios. As it can be observed,  $\text{ZrO}_2/\text{Cu}$  ratio strongly decreased after corrosion measurement compared with Zr3 diffractograms before corrosion study, with almost identical intensities between  $\text{ZrO}_2$  and Cu peaks and also a sharper Cu peak at  $43^\circ$ . Presence of segregated copper due to the laser treatment is known to increase the susceptibility for corrosion<sup>10</sup>. Corrosion process seems also to enhance the copper segregation in crystalline phases, which is then transformed into  $\text{Cu}_2\text{O}$  or copper chlorides as the dominating surface reactions. In prior studies<sup>10,51</sup> it has been reported a copper enrichment after corrosion tests, localized in the pits, which may come from a selective dissolution of the other elements such as zirconium and aluminium in the weak point of the surface.

Nyquist diagrams of Cu<sub>2</sub> alloy surface with LIPSS and Ridge textures indicated a decrease of corrosion resistance with laser processing and are presented in the annex A of the thesis. Some hypothesis are put forward to explain the differences on corrosion resistance of the three textured alloy surfaces. Some contributions might be linked together and play an active role on the electrochemical surface activity. As shown in XPS measurements in section 4.3.1 and corrosion measurements of polished surfaces above, Zr<sub>3</sub> and ZrC alloys present good corrosion resistance in NaCl due to their ability to naturally form a ZrO<sub>2</sub> layer on their surfaces, allowing to protect the material to chloride ion attacks. However, as shown in polarization measurements of ZrC and Zr<sub>3</sub> and explained in Chapter 1, small surface defects or local segregation of alloy elements can make this passive layer less stable and so the alloy more susceptible to pitting corrosion. On the other way, Cu<sub>2</sub> polished alloy exhibited poor corrosion resistance. Indeed, polarization measurement of Cu<sub>2</sub> alloy indicated no passivation behaviour compared to the other alloys. Lin *et al.*<sup>11</sup> and Gebert *et al.*<sup>56</sup> demonstrated that Cu content in Zr-based metallic glasses is a determinant factor in the stability of the passive film and so in their corrosion behaviours. An excess of about 18 at.% of copper in some Zr-base metallic glasses has been estimated to enhance a fast increase of electrochemical activity and so a rapid corrosion of the alloy.

So, zirconium and copper elements are determinant elements in corrosion properties of Zr-based amorphous alloys: the first one promoting protective layer formation and the second element an active dissolution of the material in NaCl solution. From that, it is relevant to consider Zr/Cu ratios between each alloys: Zr/Cu ratio of Zr<sub>3</sub>, ZrC, and Cu<sub>2</sub> alloys are 4.33, 2.85 and 1.33 respectively. Corrosion behaviours of polished surfaces are in agreement with the different Zr/Cu ratios of each amorphous alloys. Cu<sub>2</sub> exhibited the smallest ratio: the low amount of Zr element (48 %at.) do not permit the growth of a thick and stable passive layer whereas the high amount of Cu (36 %at.) promotes a fast and sustained corrosion reaction. For Zr<sub>3</sub> and ZrC alloys, Zr/Cu ratios are much higher, and a passivation behaviour was observed.

Despite the smaller Zr/Cu ratio of ZrC metallic glass, presence of small amount of titanium element (< 10%at.) is known to improve corrosion resistance of typical quaternary Zr-Cu-Al-Ni amorphous alloys<sup>57</sup>. As explained in chap I, this phenomenon is attributed to their higher glass forming ability (GFA), making them less sensitive to impurity-induced crystallisation process, and might explain the fast growth and passive layer stability of this alloy compare to Zr<sub>3</sub> that exhibit a time relevant passivation behaviour.

Low energy laser surface treatment (LIPSS texture) did not have the same effect on Zr3 and ZrC alloys. XPS measurement on Zr3 alloy indicated that LIPSS and Ridge treatments promoted a strong increase of copper element (Cu/Zr ratio 10 times higher than polished surface) and nickel elements. Because the selective ablation phenomenon of elements is the main hypothesis of copper enrichment on textured surfaces which is related to ablation mechanisms, we estimate that same enrichment effects on the ZrC and Cu2 alloy surfaces might be expected after laser processing. The LIPSS surface texture on the Zr3 alloy appears to not decrease the corrosion resistance behaviour exhibited on polished surface. On the other way, the LIPSS texture on ZrC alloy dramatically decreased its corrosion resistance and passivation behaviour as observed in Figure 4.6.3. Both alloys have the same texture morphology, so this difference of behaviours cannot be explained by topographic effects but by might be the result of different chemical modifications induced by laser treatment between these alloys. Due to the good corrosion resistance of LIPSS texture on Zr3, we estimate that chemical segregation induced by this low energy laser treatment is not sufficiently high for altering and make disappearing its passivation behaviour, whereas for ZrC, its lower nominal Zr/Cu ratio combined with the same copper enrichment induced by laser treatment might be sufficiently critical to strongly decreases its passivation behaviour.

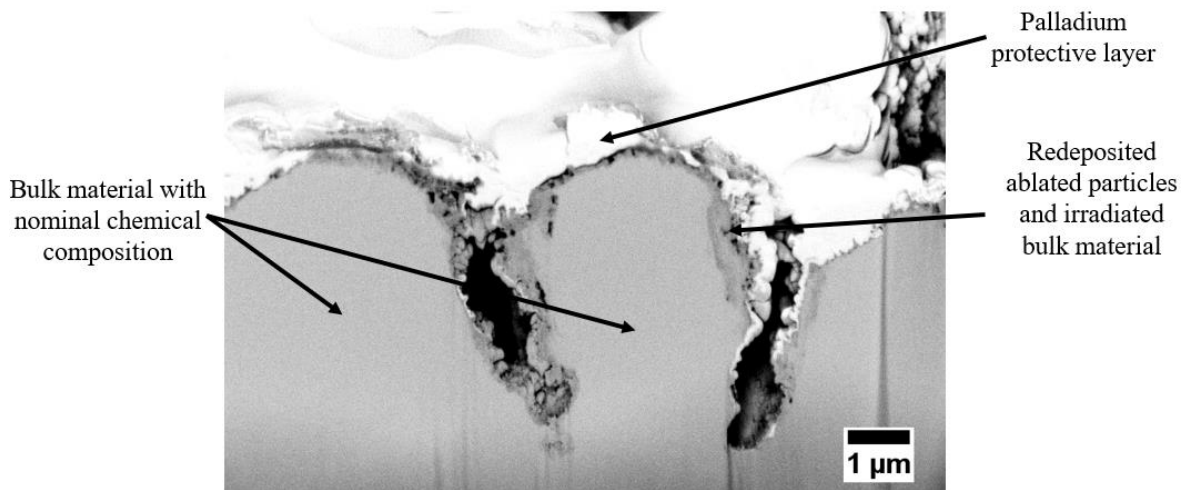


Figure 4.6.7 : FIB cross section SEM image of Ridge texture on ZrC alloy presenting a “mushroom-like” shape. The white material on the top was palladium deposition realized in order to prevent structural destruction by gallium ions.

In the case of high energetic laser treatment conducting to ridge surface texture, polarization measurements indicated that corrosion resistance dramatically decreased for the three amorphous alloy compositions. In this case, it has been estimated that both chemical and topological contribution were both relevant to understand the electrochemical behaviour. For morphological contribution, FIB cross section of ridge texture on ZrC surface (Figure 4.6.7)

showed that these ridges had a “mushroom-like” shape, with a large top part corresponding to the ridge width previously measured ( $3.8 \pm 1\mu\text{m}$ ) whereas the bottom part connected to the bulk is thinner. Moreover, compared to LIPSS texture, valleys are much thinner than hills and it get worsened due to by the high rate of redeposited ablated particles that in some point of the surface totally cover the fault, like a snow layer on a ice crevasse. This type of complex structure, possessing deep confined parts, can strongly modify the electrochemical behaviour of the material. Indeed, this type of morphologies are known to easily promote a fast deterioration and material removal by crevice corrosion process.

Crevice corrosion appears in chloride-containing environment, where confined zone promotes localized dissolution and where chemical species transfer is limited. However, as observed on EIS measurements for Zr3 and ZrC in Figure 4.6.5.b and Figure 4.6.5.c respectively, impedance curves corresponding to active corrosion (decrease of  $\text{Im}(Z)$  at low frequencies) are only observed after 2h and 4h of immersion, especially on the ZrC alloy. Then, at 16h and 24h of immersion time, impedance value increases continuously from high to low frequencies with the immersion time, showing passivation behaviour. Thus, if we consider that corrosion process such as crevice corrosion appears on the first hours of immersion time, resulted corrosion products seems to stabilize the corrosion process to act at long term as protective film on material's surface structure. The reduction of the corrosion phenomenon and the appearance of a passivation behaviour during time of both Zr3 and ZrC alloys textured with Ridges can be also the result of the formation of insoluble copper oxide products like cuprous  $\text{Cu}_2\text{O}$ , which has been observed on the corroded surface sample (red-brown powder) and can act at certain amount as a corrosion inhibitor<sup>176,177</sup>.

In summary, femtosecond laser treatment had different effects on corrosion behaviour:

1. On Zr3 alloy, the LIPSS surface texture characterized by anodic polarisation presents slightly better corrosion resistance than  $1\mu\text{m}$  polished surface (Figure 4.6.3.a)). This result is in agreement with EIS measurement of this texture presented in Figure 4.6.5.a, where an increase of the impedance and the capacitive loop diameters were reported, suggesting the formation and the growth of a protective layer on its surface.
2. On the other way, anodic polarisation of LIPSS texture on ZrC revealed a strong decrease of corrosion properties with a strong increase of current density and pitting potential and a dramatic reduction of its passivation behaviour. The hypothesis put forward is that in the case of ZrC alloy, the lower Zr/Cu ratio combined to the expected

copper enrichment due to the laser treatment tend to sufficiently modify the surface chemistry to strongly alter its corrosion resistance.

3. About corrosion properties of high energy surface treatment (ridge texture), both anodic polarisation of textured Zr3 and ZrC alloy revealed a strong decrease of corrosion resistance compare to polished surfaces, with the disappearing of any passivation behaviours. In this case, surface morphology is expected to play a more important role in the decrease of the corrosion resistance by promoting crevice corrosion phenomenon.
4. However, EIS experiments on ZrC and Zr3 ridge textures for long immersion times (16h and 24h) show a protective behaviour with an increase of the capacitive loop diameter, the increase of the impedance mean a protective behaviour of the previously corroded surface. This change of corrosion behaviour during time might be the result of the formation of stable corrosion products such as cuprous ( $\text{Cu}_2\text{O}$ ). After a given time, the amount of oxide metallic species produced may act as protective barrier.

A summary of the different corrosion behaviour of the alloys with or without laser-induced surface textures is presented below in Table 4.6-2.

	Polished surfaces	Laser-textured surfaces	
		LIPSS (Soft ablation)	Ridges (Strong ablation)
<b>Zr3</b> $\text{Zr}_{65}\text{Cu}_{15}\text{Al}_{10}\text{Ni}_{10}$ $\text{Zr}/\text{Cu} = 4.33$	PASSIVATION	PASSIVATION	NO PASSIVATION THEN PROTECTION Crevice corr. + stable products
<b>ZrC</b> $\text{Zr}_{57}\text{Cu}_{20}\text{Al}_{10}\text{Ni}_8\text{Ti}_5$ $\text{Zr}/\text{Cu} = 2.85$	PASSIVATION	LOW PASSIVATION Active corrosion	NO PASSIVATION THEN PROTECTION Crevice corr. + stable products
<b>Cu2</b> $\text{Zr}_{48}\text{Cu}_{36}\text{Al}_8\text{Ag}_8$ $\text{Zr}/\text{Cu} = 1.33$	NO PASSIVATION Active corrosion	NO PASSIVATION Active corrosion	NO PASSIVATION Active corrosion Crevice corr. + unstable products

Table 4.6-2: Summary of the corrosion behaviours of three non-textured and textured amorphous alloys surfaces.

## 4.7. Conclusion

In this Chapter 4, the surface texturing of three Zr-based metallic glasses by femtosecond laser treatment was studied. The experiments carried out with stationary samples showed that the 3 alloys react similarly to the laser treatment, with ablation thresholds for 1 laser pulse of about  $0.2 \text{ J/cm}^2$  and incubation factors between 0.8 and 0.9. These values are similar to those observed for conventional crystalline metallic alloys<sup>74</sup>. Two types of surface topography were observed for different laser fluences. At low fluence, close to the ablation threshold for high numbers of pulses ( $0.01 \text{ J/cm}^2$ ), a wavy periodic structure with the waves oriented perpendicularly to the polarization of the beam was formed. This structure is called LIPSS (laser-induced periodic surface structure) and it forms due to the interference between the incident laser beam and electromagnetic waves propagating parallel to the surface, as explained by Sipe's theory<sup>98</sup>. At higher fluences ( $0.3 \text{ J/cm}^2$ ) a near-periodic structure consisting of large parallel ridges forms, by a hydrodynamic mechanism. A parametric study in non-stationary conditions allowed reproducing of these textures on large surfaces and prepare the specimens referred to study their effect on the surface properties of the three alloys. Due to the Gaussian energy distribution in the laser beam, LIPSS overlap the Ridge structure in these specimens. Both in stationary and non-stationary conditions, the variations of fluence change the ablation mechanisms and the transformations occurring in the irradiated surfaces and thus, the type of structure formed, while an increase in the number of pulses leads to an increase of the depth of the structures and the density of ablation particles redeposited on the surface. The presence of these ablation particles on the surface may be important and must be taken into consideration. While surface structures formed by laser treatment increase the surface roughness, the ablation particles add an additional texture effect, especially for high fluences and a large number of pulses and thus increase even more the surface roughness and the surface topography complexity.

Contrarily to picosecond and nanosecond pulse duration lasers, femtosecond lasers were reported to maintain the amorphous structure of the alloys<sup>17</sup>. This was verified for Zr3 and ZrC but not for Cu2, where the DRX analysis showed that the  $\text{Cu}_2\text{ZrAl}$  intermetallic compound precipitated after high fluence treatments. The laser treatment also modified the surface chemistry. The laser treatments were performed in air and led to the formation of an oxide layer composed mainly of zirconia. Moreover, an increase of the copper and nickel content at the surface was observed. This same phenomenon was observed in the ablation particles as well, leading to the hypothesis that copper and nickel are preferentially ablated, an hypothesis,

supported by precedent studies<sup>126,17</sup>. This leads to a local modification of the surface chemical composition and a modification of the surface properties.

Due to the increase in surface roughness and surface chemistry modification, the surface textures created by the laser treatment strongly modify the wetting properties of the bulk metallic glasses, which varied from an hydrophilic behaviour for the polished surfaces ( $C_a > 90^\circ$ ) to an hydrophobic behaviour for the LIPSS texture ( $C_a = 110^\circ$ ) and to a behaviour close to superhydrophobicity for the Ridge texture ( $C_a = 125^\circ$ ). This change in the wetting properties is mainly attributed to the topological effect of the textures, promoting a Cassie-Baxter effect on the surfaces. The influence of the composition modification on the wetting behaviour was not studied in detail, but  $ZrO_2$  oxide is known to reduce the contact angle and so it may counterbalance the hydrophobic behaviour induced by the topographic effect.

Both the surface chemistry and the surface topography have a more marked effect on corrosion properties. Due to the formation of a native surface oxide layer, Zr-based metallic glasses are known to exhibit excellent corrosion resistance in non-chloride environments. However, they are sensitive to pitting corrosion in the presence of  $Cl^-$  ions. The study of polished specimens of the 3 alloys in 0.1 M NaCl showed good corrosion resistance for the Zr3 and ZrC alloys, and it is attributed to the  $ZrO_2$  passive layer which grow at their surface and protects them on a wide range of potentials. The Cu2 alloy exhibited low corrosion resistance in NaCl, attributed in the literature to its high copper content (36 at.% Cu) compared to other zirconium-based metallic glasses, which does not allow the development of a thick and stable passivation  $ZrO_2$  layer, leading to rapid corrosion of its surface<sup>10</sup>. In general, the laser treatment induced a significant decrease in the corrosion resistance. However, the LIPSS texture does not have the same effect on corrosion behaviour for Zr3 and ZrC alloys. For Zr3 alloy the LIPSS texture does not lead to a decrease of the corrosion resistance, while the LIPSS texture decreased dramatically the corrosion resistance of the ZrC alloy. This difference is attributed to the different Zr/Cu ratios of these alloys after laser treatment, which seem to increase to a critical content value of copper leading to a sharp decrease of the corrosion resistance. For the Ridge textures, both alloys exhibited the same behaviour, with a decrease of the corrosion resistance possibly induced by crevice corrosion, enhanced by texture morphology of the ridges (Figure 4.6.7). Small diameter capacitive loops at short immersion times were observed. Then, an increase of impedance after 24h of immersion in 0.1 M NaCl was observed on both specimens, which was attributed to the protective effect of the corrosion products on the surface.

# General conclusion

In this thesis, two innovative techniques were explored to modify the surface properties of several zirconium based bulk metallic glasses. These techniques are thermoplastic forming and femtosecond laser surface texturing, which potentially allow to modify the surface topography of the material while avoiding crystallization and maintaining the amorphous structure that confers to these materials their unique properties.

The most extensive work was done with femtosecond laser processing. The ablation thresholds and the incubation factors of the three amorphous alloys were determined, enabling to compare their ablation behaviour with the behaviour of crystalline metallic alloys. The incubation factor values were between 0.8 and 0.9, identical to those of crystalline metallic materials. Two interesting surface structures were identified by stationary laser treatments, and the laser processing parameters ranges allowing to achieve those topography identified. These surface textures were reproduced on large areas in order to prepare samples to characterize the surface properties. The first of these structures were laser-induced periodic surface structures (LIPSS), which appear at low fluences ( $0.1 \text{ J/cm}^2$ ), close to the ablation threshold. The second one, that was called “Ridge texture” and which consist of wave or less parallel ridges, covered with LIPSS and redeposited ablation particles is produced at higher fluences ( $0.4 \text{ J/cm}^2$ ) and forms a trimodal roughness distribution. The chemical and structural characterization of the textured surfaces revealed some modifications induced by the laser treatments. Because laser processing was performed in air, the alloy surfaces were oxidised. The predominant oxide was  $\text{ZrO}_2$ , with traces of copper oxide. For the Zr3 ( $\text{Zr}_{65}\text{Cu}_{15}\text{Al}_{10}\text{Ni}_{10}$ ) and ZrC ( $\text{Zr}_{57}\text{Cu}_{20}\text{Al}_{10}\text{Ni}_8\text{Ti}_5$ ) alloys, the XRD diffractograms revealed that no crystallization was induced by the laser treatment, while a low volume fraction of intermetallic compound  $\text{Cu}_2\text{ZrAl}$  nanocrystals formed in  $\text{Cu}_2$  ( $\text{Zr}_{48}\text{Cu}_{36}\text{Al}_8\text{Ag}_8$ ) alloy surface layer after high fluence laser treatment (ridge texture). Moreover, the EDX analysis of the ablation particles revealed that their zirconium content was lower than the Zr content of the alloy. This is probably due to a selective ablation of some of the elements constituting the alloy which is related to the vaporization temperature of each element. The XPS analysis of the textured surface reveals an increase of the copper content which is probably due to the redeposition of Zr-depleted ablation particles.

The laser surface treatment modifies the surface wettability by water and diiodomethane. While the polished surface is hydrophilic, the textured surfaces are highly hydrophobic. This

behaviour can be explained by the increase of surface roughness and the formation of a multiscale roughness induced by laser texturing. The chemical and structural changes induced by the laser treatment lead to a decrease of the corrosion resistance of Zr-based alloys. The corrosion resistance of these alloys is related to their copper content, which tends to decrease the passivation capacity. The best corrosion behaviour was found for the LIPSS textured Zr3 alloy. The hypothesis put forward to explain this fact is the difference of Zr/Cu atomic ratio between each alloy. The laser treatment induces an increase of copper content at the surface of the ZrC and Zr3 alloys. However, for the ZrC alloy, the LIPSS treatment probably creates surface chemical inhomogeneity that modified the Zr/Cu ratio, resulting to a decrease of the corrosion resistance. On the other way, the decrease of the corrosion resistance of the Cu2 alloy may be also due to the formation of intermetallic nanocrystals on the surface resulting from the laser treatment.

The measurement of the thermomechanical properties of the Zr3 alloy ( $Zr_{65}Cu_{15}Al_{10}Ni_{10}$ ) allowed determining the transition zone between Newtonian and Non-Newtonian flow regimes for this alloy in order to control the filling rate during thermoplastic forming. In parallel, onset time of crystallization was calculated in order to know the critical time at a certain temperature before crystallization starts. At a certain temperature, this value allows to determine the maximum filling length that it is possible to reach before structural transformations. The thermo-compression tests in air revealed a poor oxidation resistance of the alloy, resulting in difficulties in the replication of the mould patterns. Thanks to the development of a new hot compression device under vacuum, successful replication of micro to nanometre-size accuracy mould patterns were realized using Zr-based metallic glasses. Heating and heat transfer problems under vacuum environment were overcome and by controlling the experimental parameters, micro parts could be filled in agreement with theoretical filling time prediction, which follow a Hagen-Poiseuille law. Finally, a forming map of the Zr3 amorphous alloy was prepared, which allows estimating the optimum parameters for filling the mould for every l/d dimensional mould ratios. As expected, the XRD diffractograms revealed no trace of oxidation when processing is carried out under vacuum, which is very important to be able to accurately reproduce micron to nanometre size surface patterns.

## Suggestions for future work

**Thermoplastic forming processing:** Due to technical issues associated with design and thermoforming capability checking, the use of the TPF device has been strongly delayed. Consequently, the thermoforming experiment done during this thesis allowed to validate the operation of the device and to obtain preliminary results on TPF processing. Now that the rheological properties of the Zr<sub>3</sub> alloy are known, and that the experimental parameters can be accurately controlled, patterned surfaces of amorphous alloys with different types of morphology can be easily produced. The characteristics of each femtosecond laser texturing and TPF processing could be compared. Since metallic glasses in viscous state can accurately reproduce up to nanometre size patterns, the resolution of the surface pattern scale is only limited by the mould. Thus, the development of high resolution mould patterns has to be considered.

**Femtosecond laser surface treatment:** The surface characterization revealed a significant quantity of redeposited ablation particles, which have an impact on the surface properties. The development of methods allowing to reduce particle redeposition is relevant to quantify their effect on properties such as the corrosion resistance and wettability and to be able to avoid their negative influence on the surface properties. Another interesting work perspective is laser processing under protective atmosphere such as argon or in vacuum, to limit zirconium oxidation and minimize the redeposition of Cu and Ni-enriched ablation particles on the surface. A complementary study of the particles redeposition may allow to control the surface chemistry and to use this phenomenon as one's advantage. Processing at higher fluences may allow also to create other types of structures such as micro and nano pillars, which may have some interest in surface functionalization, but will probably enhance surface chemical heterogeneities. Finally, the effect of the laser treatments on biocompatibility and on the behaviour of cells in contact with the surface deserves to be investigated, particularly in Ni-free amorphous alloy, such as the Cu<sub>2</sub> alloy. In this case, the preferred ablation of some elements may be put to advantage in order to control the chemical composition of the surface. Thus, a surface with high zirconia enrichment could be considered by trapping the Zr-depleted particles in order to improve biocompatibility. Moreover, as presented in stationary mode experiment, the observation of a particular LIPSS structure below the ablation threshold may be the result of an increase of the oxide layer thickness on the surface. Thus, by controlling processing parameters, it may be possible to promote the growth of the ZrO<sub>2</sub> oxide layer without topologically modify

the material and so be used as an additional treatment on textured surfaces. By increasing the oxide layer, corrosion resistance, biocompatibility and also wetting properties of the surface may be strongly modified.

**Surface characterization:** Complementary wettability studies are required to differentiate the chemical and topographic contributions to the observed contact angle variations. In addition, detailed surface analysis of the textured surfaces should be performed to better understand the mechanisms of copper and nickel enrichment and Zr depletion. Electrochemical impedance spectroscopy (EIS) of LIPSS textured ZrC alloy is missing in this work better understand the difference in behaviour of Zr<sub>3</sub> and ZrC alloys in NaCl solution. Complementary studies on the wear resistance of laser textured metallic glasses may be interesting as well. Indeed, the LIPSS texture has already been recognized as improving the tribological properties of crystalline metal alloys compared to unstructured surface<sup>178,179</sup>.

## Annex A: Electrochemical Impedance spectroscopy of fs-laser textured Cu2 alloy surface.

EIS experiments on Cu2 alloy were realized in the same experimental conditions as for Zr3 and ZrC alloys presented in Chapter 4. OCP measurements and anodic polarization measurements showed the poor corrosion resistance behaviour of the 1  $\mu\text{m}$  polished Cu2 alloy compared to both 1  $\mu\text{m}$  polished Zr3 and ZrC alloys. This behaviour was reported in the literature to be the consequence of a too high amount of copper element in the material which prevent the growth of a stable and homogeneous passivation layer on its surface<sup>56,180</sup>. The study of the corrosion behaviour of these alloy textured with both LIPSS and Ridge structures by femtosecond laser was done by EIS experiments and the Nyquist plots of the three surfaces polished (a), LIPSS (b) and Ridge (c) textured are presented in Figure A-4.7.1.

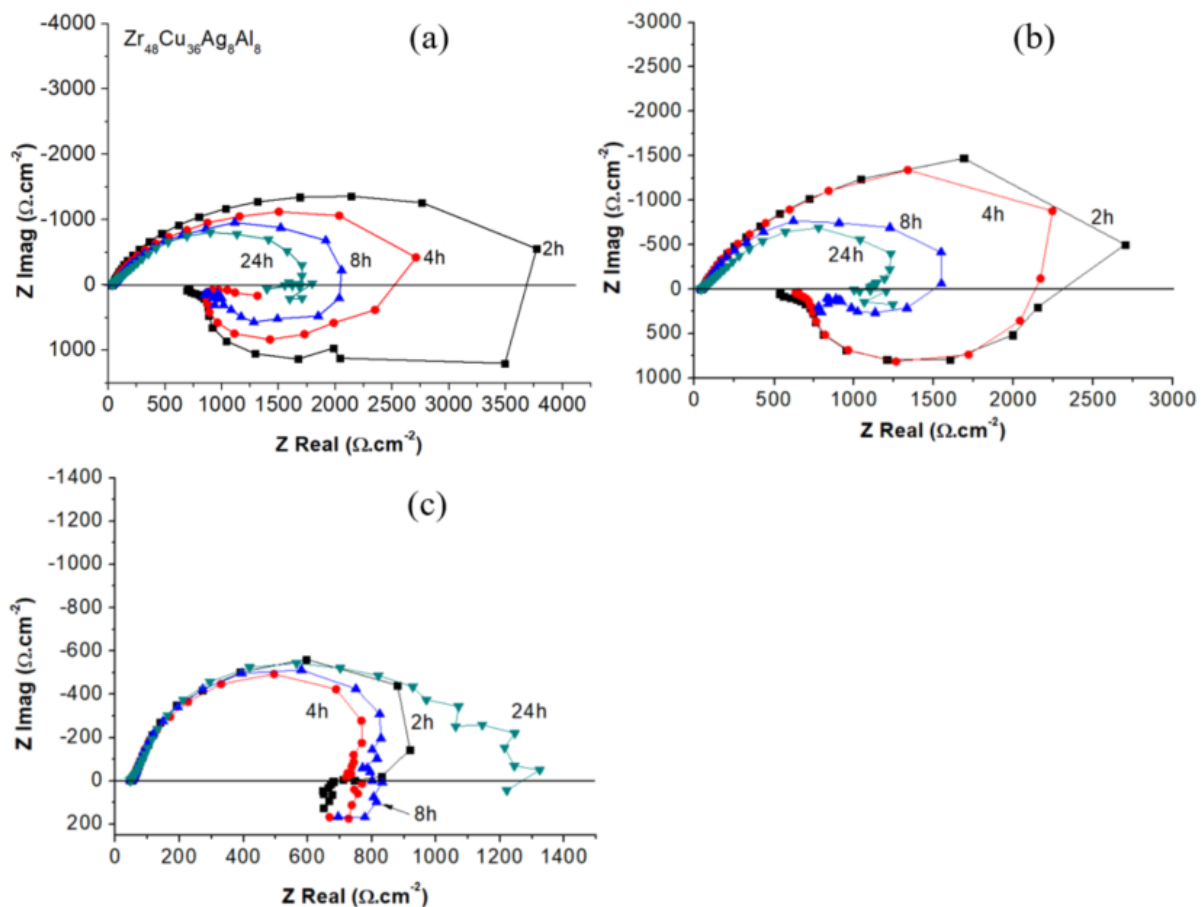


Figure A-4.7.1: Nyquist diagrams of polished (a), LIPSS textured surface (b) and Ridge textured surface (c) of Cu<sub>2</sub> alloy made by EIS experiments from 2h to 24h of immersion in 0.1 M NaCl.

As it has been already presented and discussed in the Chapter 4, the poor corrosion behaviour of the polished Cu<sub>2</sub> surface is illustrated in Nyquist plot by the presence of low impedance value capacitive circles which decrease with time and the presence of inductive loops at low frequency. These inductive loops are related to the absorption and desorption process of metallic cations M<sup>+</sup> and, with the increase of the capacity, revealed the non-stability of the system after 24 h of immersion. As observed in Figure A-4.7.1.b, LIPSS textured surface exhibits almost the same electrochemical behaviour with identical impedance value and capacitive loop diameter reduction with the immersion time. However, a small decrease of the capacitive loop diameter can be noticed compared to diameters of polished surface for the same immersion time, meaning a slight decrease of the surface resistivity. In comparison with the Nyquist plots of Zr<sub>3</sub> and ZrC alloys, Nyquist plot of Cu<sub>2</sub> surface treated with Ridge texture presents the same trend of behaviour in 0.1 M NaCl. Indeed, a general degradation of the corrosion resistance is noticed compared to LIPSS and polished surfaces with a strong decrease of the capacitive loop diameter ( $Z_{\text{Real}} \approx 800 \Omega \cdot \text{cm}^{-2}$  at 8h of immersion). However, as for ridge-textured ZrC and Zr<sub>3</sub> in a smaller scale, the impedance slightly increases after 24 h of immersion, which means a slight reduction of the corrosion activity.

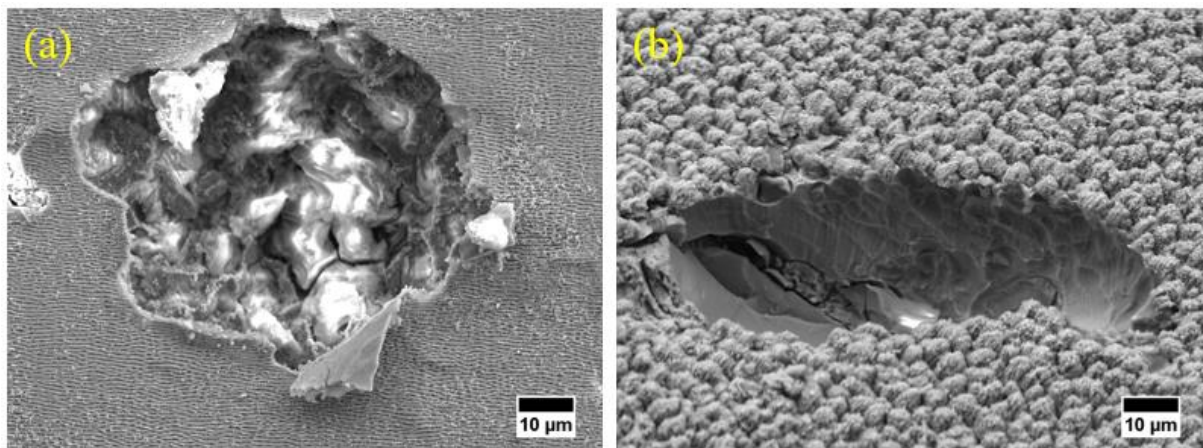


Figure A-4.7.2: SEM images of corrosion pits observed on Cu<sub>2</sub> amorphous alloy surface after 24h of immersion in 0.1 M NaCl for LIPSS textured (a) and Ridge textured (b) surfaces.

Textured surfaces with LIPSS and ridges were observed with SEM after 24h of immersion in 0.1 M NaCl. As expected with Nyquist plots values, the overall surfaces revealed corrosion pits from different form and different sizes on the two textured specimens, meaning a strong corrosion process involved during time with no sign of stabilization. As observed on Figure A-4.7.2.a and Figure A-4.7.2.b, corrosion pits which started from texture defects is digging under the laser-textured layer to then form a hollow where the corrosion reaction is entertained; this active dissolution is possibly due to an auto-catalytic reaction with the chloride ions<sup>3</sup>. Micro

cracks are also observable on both images and might be the results of a local crystallization of the alloy in the pits due to a selective dissolution of the constitutive elements in the material<sup>10</sup>.

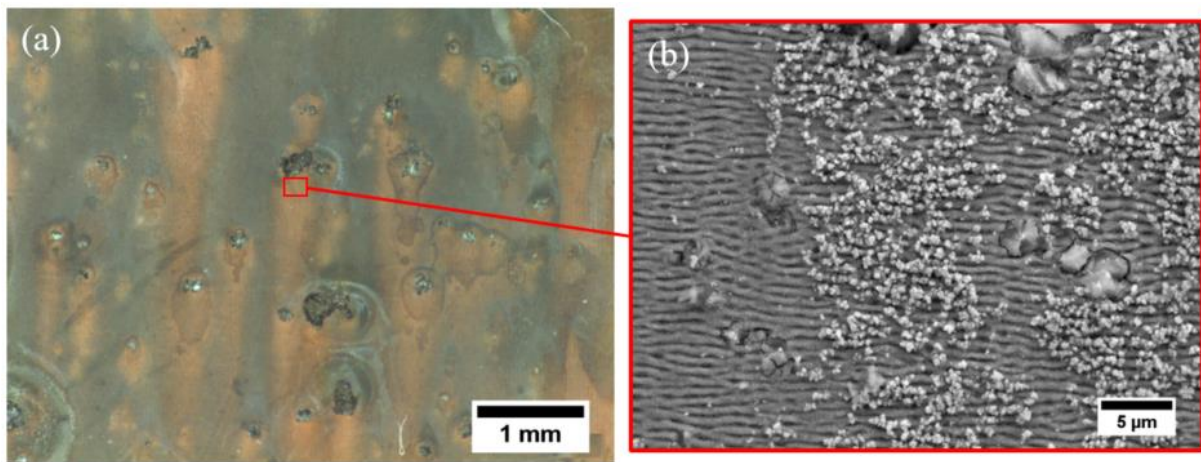


Figure A-4.7.3: Optical microscope image of a laser-textured Cu<sub>2</sub> alloy surface (a), SEM image of Cu<sub>2</sub> laser-textured surface on a peripheral part of a corrosion pit (b).

Microscope image in Figure A-4.7.3.a shows the red deposit of corrosion product on laser textured Cu<sub>2</sub> plate which have been placed vertically in the NaCl solution and so explain the vertical traces behind each pits on the surface. SEM image in Figure A-4.7.3.b shows the corrosion debris attached on the LIPSS textured Cu<sub>2</sub> surface. Starting corrosion pits are also visible on some parts of the surface, which may be initiated on defects or locally chemical heterogeneities created by the selective ablation process of the laser treatment put forward in the Chapter 4. This red powder also deposited on the bottom of the glass recipient and is mostly composed by copper oxide Cu<sub>2</sub>O which is known to have red or brown colour and comes from the selective dissolution of copper on the material surface.

In conclusion, we have seen in Chapter 4 that polished Cu<sub>2</sub> amorphous alloy exhibits much lower corrosion resistance in 0.1 M NaCl compare to Zr<sub>3</sub> and ZrC alloys due to its high copper content resulting to poor passivation capacity and so a rapid dissolution of the material in chloride-containing solution. As for Zr<sub>3</sub> and ZrC alloy in general, fs-laser surface treatments decreased corrosion resistance of the Cu<sub>2</sub> alloy to finally attain very low impedance and so low resistivity values with the ridge surface texture. This decrease of corrosion resistance properties is attributed to the chemical heterogeneity induced by the selective ablation phenomenon during laser irradiation and also structural heterogeneities in particular for Cu<sub>2</sub> alloy with the formation of Cu<sub>2</sub>ZrAl intermetallic crystalline species as observed in XRD measurements of laser-textured surface in Chapter 4. These heterogeneities on the specimen surface, combined with the structure morphology (see Chapter 4) induced by fs-laser treatment, and the original high

copper amount in this alloy all contribute to prevent the formation of a stable passive film and so promote an active dissolution of the alloy in chloride-containing solution.

## Annex B: Improvements of the thermoforming process

As it has been discussed in the Chapter 3, the development of a new hot compression device under vacuum allowed to fully replicates micron size patterns from silicon mould with high aspect ratios. These experiments validated experimental and theoretical filling kinetics in agreement with the previously determined rheological behaviours of the Zr3 amorphous alloy. However, some technical characteristics can be improve in the experimental device in order to better control TPF processing parameters.

Microscope image of the Figure A-4.7.4 shows a cross section view of the peripheral part of a thermos-compressed Zr3 plate with the micro-part Si-mould (see Chapter 2 for mould specifications) at a temperature of 432°C ( $\eta_N = 1.6 \times 10^8 \text{ Pa}\cdot\text{s}^{-1}$ ) at 20 MPa during 120s of compression time. As it can be observed, longer the groove from the plate centre is, smaller the filling length is. Indeed, in Si-mould thermoforming processing under vacuum, both BMG samples and moulds had the same surface and BMG sample were not horizontally constraint. Thus a stress gradient between the centre (maximum stress) and the peripheral part (minimum stress) was created during compression tests. However, every filling length measurements were conducted on the centre of the compressed Zr3 sample plate, where the real stress was the closest to the applied stress of 20 MPa.

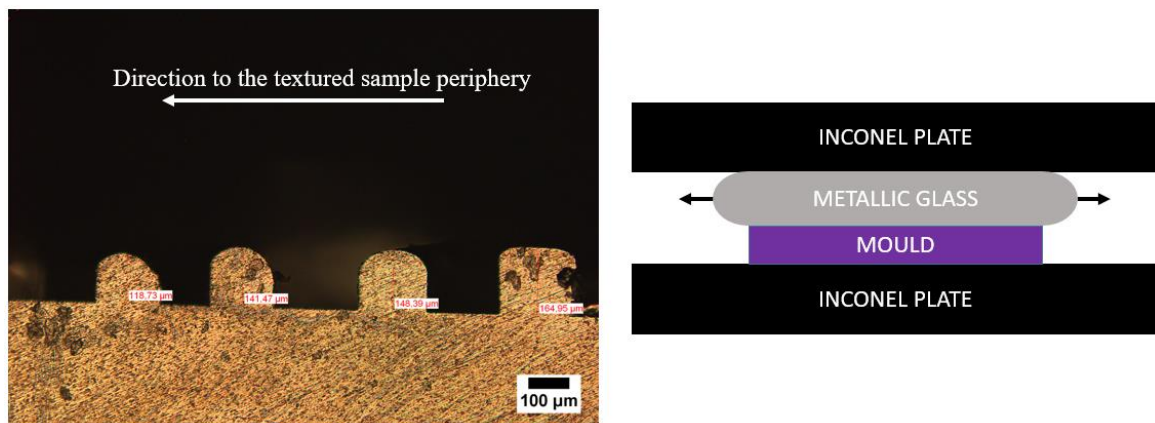


Figure A-4.7.4: Optical microscope image of the filling length evolution on the BMG plate border (a), scheme of the stress gradient issue (b).

To overcome this issue, a specific holder has been designed in copper to limit the radial expansion of the viscous material and to ensure a sufficient thermal conductivity at high temperature. However, in this temperature range, the elastic limit of the copper is very close to

the applied compression stresses. Moreover, the simple machining realized to create the holders did not allowed to get a sufficient flatness and so promoted the break of the very brittle silicon mould during compression phases. Thus, to improve the thermoforming process under vacuum, and to ensure a good stress homogeneity under the overall thermoformed area, it is necessary to radially constraint the amorphous alloy. A better designed support holder with high thermal conductivity and good mechanical resistance at high temperature need to be created.

# Bibliography

1. Klement, W., Willens, R. H. & Duwez, P. Non-crystalline Structure in Solidified Gold–Silicon Alloys. *Nature* **187**, 869–870 (1960).
2. Eckert, J., Das, J., Pauly, S. & Duhamel, C. Mechanical properties of bulk metallic glasses and composites. *J. Mater. Res.* **22**, 285–301 (2007).
3. Mudali, U. K., Baunack, S., Eckert, J., Schultz, L. & Gebert, A. Pitting corrosion of bulk glass-forming zirconium-based alloys. *J. Alloys Compd.* **377**, 290–297 (2004).
4. Schroers, J. On the formability of bulk metallic glass in its supercooled liquid state. *Acta Mater.* **56**, 471–478 (2008).
5. Cunha, A. *et al.* Human mesenchymal stem cell behavior on femtosecond laser-textured Ti-6Al-4V surfaces. *Nanomedicine (Lond).* **10**, 725–39 (2015).
6. Vorobyev, A. Y. & Guo, C. Colorizing metals with femtosecond laser pulses. *Appl. Phys. Lett.* **92**, 1–4 (2008).
7. Suryanarayana, C. Inoue, A. *Bulk Metallic Glasses.* (CRC Press, 2011).
8. He, W., Chuang, A., Cao, Z. & Liaw, P. K. Biocompatibility study of zirconium-based bulk metallic glasses for orthopedic applications. *Metall. Mater. Trans. A Phys. Metall. Mater. Sci.* **41**, 1726–1734 (2010).
9. Vishwanadh, B. *et al.* Effect of structural defects, surface irregularities, and quenched-in defects on corrosion of Zr-based metallic glasses. *Metall. Mater. Trans. A Phys. Metall. Mater. Sci.* **40**, 1131–1141 (2009).
10. Gebert, A., Gostin, F., Kühn, U. & Schultz, L. Corrosion of a Zr-based Bulk Metallic Glass with Different Surface Finishing States. *Electrochem. Soc.* **16**, 1–7 (2009).
11. Lin, C. H. *et al.* Rapid screening of potential metallic glasses for biomedical applications. *Mater. Sci. Eng. C* **33**, 4520–4526 (2013).
12. Li, H. F., Wang, Y. B., Zheng, Y. F. & Lin, J. P. Osteoblast response on Ti- and Zr-based bulk metallic glass surfaces after sand blasting modification. *J. Biomed. Mater. Res. - Part B Appl. Biomater.* **100 B**, 1721–1728 (2012).

13. Huang, L. *et al.* Responses of bone-forming cells on pre-immersed Zr-based bulk metallic glasses: Effects of composition and roughness. *Acta Biomater.* **7**, 395–405 (2011).
14. Shalabi, M. M., Gortemaker, a., Hof, M. a. V., Jansen, J. a. & Creugers, N. H. J. Implant Surface Roughness and Bone Healing: a Systematic Review. *J. Dent. Res.* **85**, 496–500 (2006).
15. Gravier, S. Mechanical behavior of bulk metallic glasses - Partial crystallization effect. (Thesis Grenoble INP, 2006).
16. Blétry, M. Déformation dans l'intervalle de transition vitreuse de verres métalliques massifs base Zirconium. (Thesis Grenoble INP, 2004).
17. Dold, C. *et al.* Surface structuring of zirconium-based bulk metallic glasses using ultrashort laser pulses. *SPIE Photonics West 2014-LASE Lasers Sources* **8967**, 89670V (2014).
18. Kumar, G., Blawdziewicz, J. & Schroers, J. Controllable nanoimprinting of metallic glasses: effect of pressure and interfacial properties. *Nanotechnology* **24**, 105301 (2013).
19. Kumar, G., Desai, A. & Schroers, J. Bulk metallic glass: The smaller the better. *Adv. Mater.* **23**, 461–476 (2011).
20. Cunha, A. *et al.* Femtosecond laser surface texturing of titanium as a method to reduce the adhesion of *Staphylococcus aureus* and biofilm formation. *Appl. Surf. Sci.* **360**, 485–493 (2016).
21. Wang, X. *et al.* Noncrystalline micromachining of amorphous alloys using femtosecond laser pulses. *Mater. Lett.* **61**, 4290–4293 (2007).
22. Bonse, J., Sandra, H., Kirner, S. V & Rosenfeld, A. Laser-Induced Periodic Surface Structures — A Scientific Evergreen. *J. Sel. Top. Quantum Electron.* **23**, (2017).
23. Zachariasen, W. H. The atomic arrangement in glass. *J. Am. Chem. Soc.* **54**, 3841–3851 (1932).
24. Chen, H. S. Thermodynamic considerations on the formation and stability of metallic glasses. *Acta Metall.* **22**, 1505–1511 (1974).
25. Inoue, A. Stabilization of metallic supercooled liquid and bulk amorphous alloys. *Acta*

- Mater.* **48**, 279–306 (2000).
26. Inoue, A., Ohtera, K., Kita, K. & Masumoto, T. New Amorphous Mg-Ce-Ni Alloys with High Strength and Good Ductility : Condensed Matter. *Jpn. J. Appl. Phys.* **27**, L2248 (1988).
  27. Inoue, A., Zhang, T. & Masumoto, T. Zr-Al-Ni Amorphous Alloys with High Glass Transition Temperature and Significant Supercooled Liquid Region. *Materials Transactions, JIM* **31**, 177–183 (1990).
  28. Peker, A. & Johnson, W. L. A highly processable metallic glass: Zr<sub>41.2</sub>Ti<sub>13.8</sub>Cu<sub>12.5</sub>Ni<sub>10.0</sub>Be<sub>22.5</sub>. *Appl. Phys. Lett.* **63**, 2342–2344 (1993).
  29. Inoue, A. Zhang, T. Itoi, T. Takeuchi, A. New Fe-Co-Ni-Zr-B Amorphous Alloys with Wide Supercooled Liquid Regions and Good Soft Magnetic Properties. *Mater. Trans. JIM* 359–362 (1997).
  30. Inoue, A. Nishiyama, N. Kimura, H. Preparation and Thermal Stability of Bulk Amorphous Pd<sub>40</sub>Cu<sub>30</sub>Ni<sub>10</sub>P<sub>20</sub> Alloy Cylinder of 72mm in Diameter. *Mater. Trans.* 179–183 (1997).
  31. Umetsu, R. Y., Tu, R. & Goto, T. Thermal and Electrical Transport Properties of Zr-Based Bulk Metallic Glassy Alloys with High Glass-Forming Ability. *Mater. Trans.* **53**, 2–6 (2012).
  32. Chen, B. *et al.* Optimization of mechanical properties of bulk metallic glasses by residual stress adjustment using laser surface melting. *Scr. Mater.* **66**, 1057–1060 (2012).
  33. Cui, X., Zu, F., Jiang, W., Wang, L. & Wang, Z. Achieving superior glass forming ability of Zr – Cu – Al – Ni – Ti / Ag bulk metallic glasses by element substitution. *J. Non. Cryst. Solids* **375**, 83–87 (2013).
  34. Puech, S. Elaboration, caractérisation structurale et mise en forme d'alliages de magnésium vitreux. (Thesis, Grenoble INP, 2008).
  35. Inoue, A., Zhang, T. & Masumoto, T. Preparation of Bulky Amorphous Zr-Al-Co-Ni-Cu Alloys by Copper Mold Casting and Their Thermal and Mechanical Properties. *Mater. Trans.* **36**, 391 to 398 (1995).
  36. Lin, X. H. & Johnson, W. L. Formation of Ti-Zr-Cu-Ni bulk metallic glasses. *J. Appl.*

- Phys.* **78**, 6514–6519 (1995).
37. Gebert, A., Eckert, J. & Schultz, L. Effect of oxygen on phase formation and thermal stability of slowly cooled Zr<sub>65</sub>Al<sub>17.5</sub>Cu<sub>17.5</sub>Ni<sub>10</sub> metallic glass. *Acta Mater.* **46**, 5475–5482 (1998).
  38. Löffler, J. F. Bulk metallic glasses. *Intermetallics* **11**, 529–540 (2003).
  39. Conner, R. D., Rosakis, A. J., Johnson, W. L. & Owen, D. M. Fracture Toughness Determination for a Beryllium-Bearing Bulk Metallic Glass. *Scr. Mater.* **37**, 1373–1378 (1997).
  40. Schroers, J. The Superplastic Forming of Bulk Metallic Glasses. *J. Miner. Met. Mater. Soc.* **57**, 35–39 (2005).
  41. Schroers, J., Pham, Q. & Desai, A. Thermoplastic Forming of Bulk Metallic Glass — A Technology for MEMS and Microstructure Fabrication. *J. Microelectromechanical Syst.* **16**, 240–247 (2007).
  42. Saotome, Y., Fukuda, Y., Yamaguchi, I. & Inoue, A. Superplastic nanoforming of optical components of Pt-based metallic glass. *J. Alloys Compd.* **434–435**, 97–101 (2007).
  43. Lu, J., Ravichandran, G. & Johnson, W. L. Deformation behavior of the Zr<sub>41.2</sub>Ti<sub>13.8</sub>Cu<sub>12.5</sub>Ni<sub>10</sub>Be<sub>22.5</sub> bulk metallic glass over a wide range of strain-rates and temperatures. *Acta Mater.* **51**, 3429–3443 (2003).
  44. Kato, H., Kawamura, Y., Inoue, A. & Chen, H. S. Newtonian to non-Newtonian master flow curves of a bulk glass alloy Pd<sub>40</sub>Ni<sub>10</sub>Cu<sub>30</sub>P<sub>20</sub>. *Appl. Phys. Lett.* **73**, 3665–3667 (1998).
  45. Kawamura, Y., Nakamura, T. & Kim, K. B. Superplasticity in Pd<sub>40</sub>Ni<sub>40</sub>P<sub>20</sub> Metallic Glass. *Mater. Sci. Forum* **304–306**, 349–354 (1999).
  46. Wenzel, R. N. Resistance of Solid Surfaces To Wetting By Water. *Ind. Eng. Chem.* **28**, 988–994 (1936).
  47. Cunha, A. Multiscale Femtosecond Laser Surface Texturing of Titanium and Titanium Alloys for Dental and Orthopaedic Implants. (Thesis, Instituto Superior Tecnico de Lisboa / Université de Bordeaux, 2009).
  48. Cassie, A. B. D. & Baxter, S. Wettability of porous surfaces. *Trans. Faraday Soc.* **40**,

- 546–551 (1944).
49. Jeong, H. E., Kwak, M. K., Park, C. I. & Suh, K. Y. Wettability of nanoengineered dual-roughness surfaces fabricated by UV-assisted capillary force lithography. *J. Colloid Interface Sci.* **339**, 202–207 (2009).
  50. Belaud, V. Structuration de surfaces au moyen d'un traitement laser femtoseconde : applications à la fonctionnalisation de surface du polypropylène en vue de sa métallisation. (Thesis, Université de Lyon, 2014).
  51. Kawashima, A., Ohmura, K., Yokoyama, Y. & Inoue, A. The corrosion behaviour of Zr-based bulk metallic glasses in 0.5 M NaCl solution. *Corros. Sci.* **53**, 2778–2784 (2011).
  52. Schroeder, V., Gilbert, C. J. & Ritchie, R. O. Comparison of the corrosion behavior of a bulk amorphous metal, Zr<sub>41.2</sub>Ti<sub>13.8</sub>Cu<sub>12.5</sub>Ni<sub>10</sub>Be<sub>22.5</sub>, with its crystallized form. *Scr. Mater.* **38**, 1481–1485 (1998).
  53. Watanabe, H., Saito, K., Kokubun, K., Sasaki, H. & Yoshinari, M. Change in surface properties of zirconia and initial attachment of osteoblastlike cells with hydrophilic treatment. *Dent. Mater. J.* **31**, 806–814 (2012).
  54. Gebert, A. *et al.* Investigations on the electrochemical behaviour of Zr-based bulk metallic glasses. *Mater. Sci. Eng. A* **267**, 294–300 (1999).
  55. Gebert, A., Mummert, K., Eckert, J., Schultz, L. & Inoue, A. Electrochemical investigations on the bulk glass forming Zr<sub>55</sub>Cu<sub>30</sub>Al<sub>10</sub>Ni<sub>5</sub> alloy. *Mater. Corros. und Korrosion* **48**, 293–297 (1997).
  56. Gebert, A., Gostin, P. F. & Schultz, L. Effect of surface finishing of a Zr-based bulk metallic glass on its corrosion behaviour. *Corros. Sci.* **52**, 1711–1720 (2010).
  57. Raju, V. R. *et al.* Corrosion behaviour of Zr-based bulk glass-forming alloys containing Nb or Ti. *Mater. Lett.* **57**, 173–177 (2002).
  58. Maiman, T. H. Stimulated Optical Radiation in Ruby. *Nature* **187**, 493–494 (1960).
  59. Einstein, A. The Quantum Theory of Radiation. *J. Phys.* **18**, 121 (1917).
  60. Canguero, L. T. Ultrafast laser tissue cutting and removal for applications in orthopaedic surgery. (Thesis, Instituto Superior Tecnico, 2016).
  61. Brabec, T. & Krausz, F. Intense few-cycle laser fields: Frontiers of nonlinear optics. *Rev.*

- Mod. Phys.* **72**, 545–591 (2000).
62. Hopkins, J. M. & Sibbett, W. Ultrashort-pulse lasers: big payoffs in a flash. *Sci. Am.* **283**, 72–79 (2000).
  63. Renk, K. F. *Basics of Laser Physics: For Students of Science and Engineering*. (2012).
  64. Keller, U. Recent developments in compact ultrafast lasers. *Nature* **424**, 831–838 (2003).
  65. Zhigilei, L. V., Kodali, P. B. S. & Garrison, B. J. Molecular Dynamics Model for Laser Ablation and Desorption of Organic Solids. *J. Phys. Chem. B* **101**, 2028–2037 (1997).
  66. Shank, C. V., Yen, R. & Hirlimann, C. Time-Resolved Reflectivity Measurements of Femtosecond-Optical-Pulse-Induced Phase Transitions in Silicon. *Phys. Rev. Lett.* **50**, 454–457 (1983).
  67. Meijer, J. Laser beam machining (LBM), state of the art and new opportunities. *J. Mater. Process. Technol.* **149**, 2–17 (2004).
  68. Breitling, D., Ruf, A. & Dausinger, F. Fundamental aspects in machining of metals with short and ultrashort laser pulses. *Phot. Process. Microelectron. Photonics III* **5339**, 49–63 (2004).
  69. Vorobyev, A. Y. & Guo, C. Direct femtosecond laser surface nano/microstructuring and its applications. *Laser Photonics Rev.* **7**, 385–407 (2013).
  70. Anisimov, S. I., Kapeliovich, B. L. & Perel-man, T. L. Electron emission from metal surfaces exposed to ultrashort laser pulses. *J. Exp. Theor. Phys.* **66**, 375–377 (1974).
  71. Chichkov, B. N., Momma, C., Nolte, S., von Alvensleben, F. & Tünnermann, A. Femtosecond, picosecond and nanosecond laser ablation of solids. *Appl. Phys. A Mater. Sci. Process.* **63**, 109–115 (1996).
  72. Sokolowski-Tinten, K., Bialkowski, J. & Von Der Linde, D. Ultrafast laser-induced order-disorder transitions in semiconductors. *Phys. Rev. B* **51**, 14186–14198 (1995).
  73. Knox, W. H. *et al.* Femtosecond excitation of nonthermal carrier populations in GaAs quantum wells. *Phys. Rev. Lett.* **56**, 1191–1193 (1986).
  74. Mannion, P. T., Magee, J., Coyne, E., O’Connor, G. M. & Glynn, T. J. The effect of damage accumulation behaviour on ablation thresholds and damage morphology in ultrafast laser micro-machining of common metals in air. *Appl. Surf. Sci.* **233**, 275–287

- (2004).
75. Valette, S. Effets thermiques dus à l'interaction laser-matère dans les métaux en régime femtoseconde. (Thesis, Ecole Nationale Supérieure des Mines de Saint-Etienne, 2003).
  76. Canguero, L. T., Cavaleiro, A. J., Morgiel, J. & Vilar, R. Mechanisms of the formation of low spatial frequency LIPSS on Ni / Ti reactive multilayers. *J. Phys. D. Appl. Phys.* **49**, (2016).
  77. Leveugle, E., Ivanov, D. S. & Zhigilei, L. V. Photomechanical spallation of molecular and metal targets: Molecular dynamics study. *Appl. Phys. A Mater. Sci. Process.* **79**, 1643–1655 (2004).
  78. Wu, C. & Zhigilei, L. V. Microscopic mechanisms of laser spallation and ablation of metal targets from large-scale molecular dynamics simulations. *Appl. Phys. A* **114**, 11–32 (2014).
  79. Birnbaum, M. Semiconductor surface damage produced by Ruby lasers. *J. Appl. Phys.* **36**, 3688–3689 (1965).
  80. Wang, J. & Guo, C. Ultrafast dynamics of femtosecond laser-induced periodic surface pattern formation on metals. *Appl. Phys. Lett.* **87**, 1–3 (2005).
  81. Bizi-Bandoki, P., Benayoun, S., Valette, S., Beaugiraud, B. & Audouard, E. Modifications of roughness and wettability properties of metals induced by femtosecond laser treatment. *Appl. Surf. Sci.* **257**, 5213–5218 (2011).
  82. Krüger, J. & Kautek, W. Femtosecond-pulse visible laser processing of transparent materials. *Appl. Surf. Sci.* **96–98**, 430–438 (1996).
  83. Baudach, S., Bonse, J. & Kautek, W. Ablation experiments on polyimide with femtosecond laser pulses. *Appl. Phys. A Mater. Sci. Process.* **69**, 395–398 (1999).
  84. Krüger, J. *et al.* Femto- and nanosecond laser treatment of doped polymethylmethacrylate. *Appl. Surf. Sci.* **247**, 406–411 (2005).
  85. X. Wang, L. Peixiang, D. Nengli, L. Yuhua, L. Changrui, C. Yanxiao, Y. Guang, Z. Q. Morphology and oxidation of Zr-based amorphous alloy ablated by femtosecond. *Appl. Phys. A Mater. Sci. Process.* **552**, 547–552 (2007).
  86. Ma, F., Yang, J., XiaonongZhu, Liang, C. & Wang, H. Femtosecond laser-induced

- concentric ring microstructures on Zr-based metallic glass. *Appl. Surf. Sci.* **256**, 3653–3660 (2010).
87. Shinonaga, T. & Tsukamoto, M. Femtosecond and nanosecond laser irradiation for microstructure formation on bulk metallic glass. *Trans. JWRI* **38**, 81–84 (2009).
  88. Zhang, W., Cheng, G., Hui, X. D. & Feng, Q. Abnormal ripple patterns with enhanced regularity and continuity in a bulk metallic glass induced by femtosecond laser irradiation. *Appl. Phys. A Mater. Sci. Process.* **115**, 1451–1455 (2014).
  89. Wang, H. *et al.* Effects of femtosecond laser ablation on the surface morphology and microstructure of a bulk TiCuPdZr glass alloy. *Rare Met.* **28**, 272–276 (2009).
  90. Siegman, A. E. & Fauchet, P. M. Stimulated Wood 's anomalies on laser-illuminated surfaces. *J. Quantum Electron.* 1384–1403 (1986).
  91. Bonse, J., Krüger, J., Höhm, S. & Rosenfeld, A. Femtosecond laser-induced periodic surface structures. *J. Laser Appl.* **24**, 42006 (2012).
  92. Varlamova, O., Costache, F., Ratzke, M. & Reif, J. Control parameters in pattern formation upon femtosecond laser ablation. *Appl. Surf. Sci.* **253**, 7932–7936 (2007).
  93. Reif, J., Costache, F., Henyk, M. & Pandelov, S. V. Ripples revisited: Non-classical morphology at the bottom of femtosecond laser ablation craters in transparent dielectrics. *Appl. Surf. Sci.* **197–198**, 891–895 (2002).
  94. Schütte, D. & Da Providencia, J. A solvable model of boson condensation. *Nucl. Physics, Sect. A* **282**, 518–532 (1977).
  95. Oron, M. & Sorensen, G. New experimental evidence of the periodic surface structure in laser annealing. *Appl. Phys. Lett.* **35**, 782–784 (1979).
  96. Emmony, D. C., Howson, R. P. & Willis, L. J. Laser mirror damage in germanium at 10.6  $\mu\text{m}$ . *Appl. Phys. Lett.* **23**, 598–600 (1973).
  97. Derrien, T. J., Sarnet, T., Sentis, M. & Itina, T. E. Application of a two-temperature model for the investigation of the periodic structure formation on Si surface in femtosecond laser interactions. *J. Optoelectron. Adv. Mater.* **12**, 610–615 (2010).
  98. Sipe, J. E., Young, J. F., Preston, J. S. & Van Driel, H. M. Laser-induced periodic surface structure. I. Theory. *Phys. Rev. B* **27**, 1141–1154 (1983).

99. Sipe, J. E. & Van Driel, H. M. Laser Induced Periodic Surface Structure: An Experimental and Theoretical Review. in *Third International Conference on Trends in Quantum Electronics* 302–318 (1988).
100. Höhm, S., Herzlieb, M., Rosenfeld, A., Krüger, J. & Bonse, J. Dynamics of the formation of laser-induced periodic surface structures (LIPSS) upon femtosecond two-color double-pulse irradiation of metals, semiconductors, and dielectrics. *Appl. Surf. Sci.* **374**, 331–338 (2016).
101. Bonse, J., Rosenfeld, A. & Krüger, J. On the role of surface plasmon polaritons in the formation of laser-induced periodic surface structures upon irradiation of silicon by femtosecond-laser pulses. *J. Appl. Phys.* **106**, 104910 (2009).
102. Derrien, T. J. Y., Itina, T. E., Torres, R., Sarnet, T. & Sentis, M. Possible surface plasmon polariton excitation under femtosecond laser irradiation of silicon. *J. Appl. Phys.* **114**, (2013).
103. Keilmann, F. & Bai, Y. H. Periodic surface structures frozen into CO<sub>2</sub> laser-melted quartz. *Appl. Phys. A Solids Surfaces* **29**, 9–18 (1982).
104. Garrelie, F. *et al.* Evidence of surface plasmon resonance in ultrafast laser-induced ripples. *Opt. Soc. Am.* **19**, 9035–9043 (2011).
105. Kerr, N. C., Omar, B. a., Clark, S. E. & Emmony, D. C. The topography of laser-induced ripple structures. *J. Phys. D. Appl. Phys.* **884**, 884–889 (1990).
106. Tomita, T., Kinoshita, K., Matsuo, S. & Hashimoto, S. Effect of surface roughening on femtosecond laser-induced ripple structures. *Appl. Phys. Lett.* **90**, 1–4 (2007).
107. Bonse, J., Munz, M. & Sturm, H. Structure formation on the surface of indium phosphide irradiated by femtosecond laser pulses. *J. Appl. Phys.* **97**, (2005).
108. Dufft, D., Rosenfeld, A., Das, S. K., Grunwald, R. & Bonse, J. Femtosecond laser-induced periodic surface structures revisited: A comparative study on ZnO. *J. Appl. Phys.* **105**, (2009).
109. Obara, G. *et al.* Growth of high spatial frequency periodic ripple structures on SiC crystal surfaces irradiated with successive femtosecond laser pulses. *Opt. Express* **21**, 26323–34 (2013).

110. Anthony, T. R. & Cline, H. E. Surface rippling induced by surface-tension gradients during laser surface melting and alloying. *J. Appl. Phys.* **3888**, (2002).
111. Chan, C. L., Mazumder, J. & Chen, M. M. Effect of surface tension gradient driven convection in a laser melt pool: Three-dimensional perturbation model. *J. Appl. Phys.* **64**, 6166–6174 (1988).
112. Tsibidis, G. D., Fotakis, C. & Stratakis, E. From ripples to spikes: A hydrodynamical mechanism to interpret femtosecond laser-induced self-assembled structures. *Phys. Rev. B - Condens. Matter Mater. Phys.* **92**, 1–6 (2015).
113. Kietzig, A. M., Hatzikiriakos, S. G. & Englezos, P. Patterned superhydrophobic metallic surfaces. *Langmuir* **25**, 4821–4827 (2009).
114. Cunha, A. *et al.* Wetting behaviour of femtosecond laser textured Ti-6Al-4V surfaces. *Appl. Surf. Sci.* **265**, 688–696 (2013).
115. Serro, A. P. & Saramago, B. Influence of sterilization on the mineralization of titanium implants induced by incubation in various biological model fluids. *Biomaterials* **24**, 4749–4760 (2003).
116. Baldacchini, T., Carey, J. E., Zhou, M. & Mazur, E. Superhydrophobic surfaces prepared by microstructuring of silicon using a femtosecond laser. *Langmuir* **22**, 4917–4919 (2006).
117. Dopierala, K., Maciejewski, H., Karasiewicz, J. & Prochaska, K. Alkyl- and fluoroalkyltrialkoxysilanes for wettability modification. *Appl. Surf. Sci.* **283**, 453–459 (2013).
118. Torres, R. *et al.* Femtosecond laser texturization for improvement of photovoltaic cells: Black silicon. *J. Optoelectron. Adv. Mater.* **12**, 621–625 (2010).
119. Guay, J.-M. *et al.* Topographical coloured plasmonic coins. *Physics.optics* (2016).
120. Bennett, H. E., Silver, M. & Ashley, E. J. Infrared Reflectance of Aluminum Evaporated in Ultra-High Vacuum. *J. Opt. Soc. Am.* **53**, 1089–1095 (1963).
121. Valette, S. *et al.* Influence of femtosecond laser marking on the corrosion resistance of stainless steels. *Appl. Surf. Sci.* **252**, 4696–4701 (2006).
122. Dumas, V. *et al.* Multiscale grooved titanium processed with femtosecond laser

- influences mesenchymal stem cell morphology, adhesion, and matrix organization. *J. Biomed. Mater. Res. - Part A* **100 A**, 3108–3116 (2012).
123. Dewez, J. L., Doren, A., Schneider, Y. J. & Rouxhet, P. G. Competitive adsorption of proteins: Key of the relationship between substratum surface properties and adhesion of epithelial cells. *Biomaterials* **20**, 547–559 (1999).
  124. Truong, V. K. *et al.* The influence of nano-scale surface roughness on bacterial adhesion to ultrafine-grained titanium. *Biomaterials* **31**, 3674–3683 (2010).
  125. Marinier, S. & Lewis, L. J. Femtosecond laser ablation of  $\text{Cu}_x\text{Zr}_{1-x}$  bulk metallic glasses: A molecular dynamics study. *Phys. Rev. B* **92**, 184108 (2015).
  126. Li, C. *et al.* Initial Cumulative Effects in Femtosecond Pulsed Laser-induced Periodic Surface Structures on Bulk Metallic Glasses. *J. Laser Micro/Nanoengineering* **11**, 357–365 (2016).
  127. Wu, G. J., Li, R., Liu, Z. Q., Chen, B. Q. & Zhang, T. Effects of the laser surface treatment on the mechanical properties of CuZr-based bulk metallic glasses. *Sci. China-Physics Mech. Astron.* **56**, 925–927 (2013).
  128. Chen, B. *et al.* Improvement in mechanical properties of a Zr-based bulk metallic glass by laser surface treatment. *J. Alloys Compd.* **504**, S45–S47 (2010).
  129. Cao, Y. *et al.* Laser shock peening on zr-based bulk metallic glass and its effect on plasticity: Experiment and modeling. *Sci. Rep.* **5**, 1–8 (2015).
  130. Choy, C. L., Tong, K. W., Wong, H. K. & Leung, W. P. Thermal conductivity of amorphous alloys above room temperature. *J. Appl. Phys.* **70**, 4919–4925 (1991).
  131. Ray, S. & Tauc, J. Optical and magneto-optical properties of metallic glass  $\text{Fe}_{80}\text{B}_{20}$ . *Solid State Commun.* **34**, 769–772 (1980).
  132. Komatsu, T., Takeuchi, M., Matusita, K. & Yokota, R. Study of structural relaxation of  $\text{Ni}_{78}\text{Si}_8\text{B}_{14}$  metallic glass by electrical resistivity and thermal expansion measurements. *J. Non. Cryst. Solids* **57**, 129–136 (1983).
  133. Hasan, M., Schroers, J. & Kumar, G. Functionalization of metallic glasses through hierarchical patterning. *Nano Lett.* **15**, 963–968 (2015).
  134. Kumar, G., Tang, H. X. & Schroers, J. Nanomoulding with amorphous metals. *Nature*

- 457**, 868–872 (2009).
135. Schroers, J., Lohwongwatana, B., Johnson, W. L. & Peker, A. Gold based bulk metallic glass. *Appl. Phys. Lett.* **87**, 2003–2006 (2005).
  136. Li, N. *et al.* A thermoplastic forming map of a Zr-based bulk metallic glass. *Acta Mater.* **61**, 1921–1931 (2013).
  137. He, J. J. *et al.* The precision replication of a microchannel mould by hot-embossing a Zr-based bulk metallic glass. *Intermetallics* **21**, 50–55 (2012).
  138. Schroers, J. Processing of Bulk Metallic Glass. *Adv. Mater.* **22**, 1566–1597 (2010).
  139. Liu, L. & Chan, K. . Oxidation of Zr 55 Cu 30 Al 10 Ni 5 bulk metallic glass in the glassy state and the supercooled liquid state. *Appl. Phys. A* **1744**, 1737–1744 (2005).
  140. Sarac, B. *et al.* Hierarchical surface patterning of Ni- and Be-free Ti- and Zr-based bulk metallic glasses by thermoplastic net-shaping. *Mater. Sci. Eng. C* **73**, 398–405 (2017).
  141. Li, N., Xia, T., Heng, L. & Liu, L. Superhydrophobic Zr-based metallic glass surface with high adhesive force. *Appl. Phys. Lett.* **102**, (2013).
  142. Padmanabhan, J. & Kinser, E. Engineering Cellular Response Using Nanopatterned Bulk Metallic Glass. *Am. Chem. Soc.* 4366–4375 (2014).
  143. Zhang, Q., Zhang, W. & Inoue, A. Preparation of Cu 36 Zr 48 Ag 8 Al 8 Bulk Metallic Glass with a Diameter of 25 mm by Copper Mold Casting. *Mater. Trans.* **48**, 629–631 (2007).
  144. Ragani, J. Élaboration par co-déformation de matériaux stratifiés alliage léger / verre métallique. (Thesis, INP Grenoble, 2011).
  145. Liu, J. M. Simple technique for measurements of pulsed Gaussian-beam spot sizes. *Opt. Lett.* **7**, 196 (1982).
  146. Jee, Y., Becker, M. F. & Walser, R. M. Laser-induced damage on single-crystal metal surfaces. *J. Opt. Soc. Am. B* **5**, 648 (1988).
  147. Sardar, D. K., Becker, M. F. & Walser, R. M. Multipulse laser damage of GaAs surfaces. *J. Appl. Phys.* **62**, 3688–3693 (1987).
  148. Ferreira, A. C. *et al.* Partial oxidation of methane over bimetallic nickel – lanthanide

- oxides. *J. Alloys Compd.* **489**, 316–323 (2010).
149. Briggs, D. & Beamson, G. High Resolution XPS of Organic Polymers, The Scienta ESCA300 Database. *Wiley* **70**, (1992).
  150. Nunes, B. *et al.* Ageing effects on the wettability behavior of laser textured silicon. *Appl. Surf. Sci.* **257**, 2604–2609 (2011).
  151. Li, D. & Neumann, A. Contact Angles On Hydrophobic Solid-surfaces And Their Interpretation. *J. Colloid Interface Sci.* **148**, 190–200 (1992).
  152. Good, R. J. & Girifalco, L. a. A theory for estimation of surface and interfacial energies. *J. Phys. Chem.* **24**, 561–565 (1960).
  153. Owens, D. K. & Wendt, R. C. Estimation of the surface free energy of polymers. *J. Appl. Polym. Sci.* **13**, 1741–1747 (1969).
  154. Lai, W. Y., Zhao, W. Z., Yin, Z. F. & Zhang, J. EIS and XPS studies on passive film of AISI 304 stainless steel in dilute sulfuric acid solution. *Surf. Interface Anal.* 418–425 (2012).
  155. Nowak, S., Perrière, L., Dembinski, L., Tusseau-Nenez, S. & Champion, Y. Approach of the spark plasma sintering mechanism in Zr<sub>57</sub>Cu<sub>20</sub>Al<sub>10</sub>Ni<sub>8</sub>Ti<sub>5</sub> metallic glass. *J. Alloys Compd.* **509**, 1011–1019 (2011).
  156. Heilmaier, M. Deformation behavior of Zr-based metallic glasses. *J. Mater. Process. Tech.* **117**, 374–380 (2001).
  157. Kawamura, Y., Shibata, T., Inoue, a. & Masumoto, T. Workability of the supercooled liquid in the Zr<sub>65</sub>Al<sub>10</sub>Ni<sub>10</sub>Cu<sub>15</sub> bulk metallic glass. *Acta Mater.* **46**, 253–263 (1998).
  158. Kawamura, Y., Shibata, T., Inoue, A. & Masum. Superplastic deformation of Zr<sub>65</sub>Al<sub>10</sub>Ni<sub>10</sub>Cu<sub>15</sub> metallic glass. *Scr. Mater.* **37**, 431–436 (1997).
  159. Jastrow, L. & Köster, U. Oxidation of Zr-based metallic glasses and nanocrystalline alloys. *Mater. Sci. Eng. A* **451**, 57–62 (2007).
  160. Triwikantoro, Toma, D., Meuris, M. & Köster, U. Oxidation of Zr-based metallic glasses in air. *J. Non. Cryst. Solids* **252**, 719–723 (1999).
  161. Soileau, M. J. Ripple Structures Associated with Ordered Surface Defects in Dielectrics. *J. Quantum Electron.* **20**, 464–467 (1984).

162. Sipe, J. E., Van Driel, H. M. & Young, J. F. Surface electrodynamics: radiation fields, surface polaritons, and radiation remnants. *Can. J. Phys* **63**, 104 (1985).
163. Bonse, J., Sturm, H., Schmidt, D. & Kautek, W. Chemical, morphological and accumulation phenomena in ultrashort-pulse laser ablation of TiN in air. *Appl Phys A-Mater* **71**, 657–665 (2000).
164. Bonse, J. & Krüger, J. Pulse number dependence of laser-induced periodic surface structures for femtosecond laser irradiation of silicon. *J. Appl. Phys.* **108**, (2010).
165. Nürnberger, P. *et al.* Orthogonally superimposed laser-induced periodic surface structures (LIPSS) upon nanosecond laser pulse irradiation of SiO<sub>2</sub>/Si layered systems. *Appl. Surf. Sci.* **425**, 682–688 (2017).
166. Yu, J. J., Zhang, J. Y., Boyd, I. W. & Lu, Y. F. Excimer-laser-induced micropatterning of silicon dioxide on silicon substrates. *Appl. Phys. A* **72**, 35–39 (2001).
167. Huang, M., Zhao, F., Cheng, Y., Xu, N. & Xu, Z. Origin of laser-induced near-subwavelength ripples: Interference between surface plasmons and incident laser. *ACS Nano* **3**, 4062–4070 (2009).
168. Wu, B. *et al.* Superhydrophobic surfaces fabricated by microstructuring of stainless steel using a femtosecond laser. *Appl. Surf. Sci.* **256**, 61–66 (2009).
169. Moradi, S., Kamal, S., Englezos, P. & Hatzikiriakos, S. G. Femtosecond laser irradiation of metallic surfaces: effects of laser parameters on superhydrophobicity. *Nanotechnology* **24**, 415302 (2013).
170. Huang, C., Tang, Z. & Zhang, Z. Differences between Zirconium Hydroxide (  $Zr(OH)_4 \cdot nH_2O$  ) and. *J. Am. Ceram. Soc.* **38**, 1637–1638 (2001).
171. Marques, M. T., Ferraria, A. M., Correia, J. B., Botelho, A. M. & Vilar, R. XRD , XPS and SEM characterisation of Cu – NbC nanocomposite produced by mechanical alloying. *Mater. Chem. Phys.* **109**, 174–180 (2008).
172. Oliveira, M. C. & Botelho, A. M. The effect of the hypophosphite ion oxidation on the Ni surface electrode — an XPS study. *J. Alloys Compd.* **425**, 64–68 (2006).
173. Zhang, Y. *et al.* Femtosecond laser-induced phase transformations in amorphous Cu<sub>77</sub>Ni<sub>6</sub>Sn<sub>10</sub>P<sub>7</sub> alloy. *J. Appl. Phys.* **117**, 23109 (2015).

174. Tam, C. Y. & Shek, C. H. Oxidation behavior of Cu 60 Zr 30 Ti 10 bulk metallic glass. *J. Mater. Res.* (2017).
175. Kiene, M., Strunskus, T., Hasse, G. & Faupel, F. Oxide formation on the bulk metallic glass Zr<sub>46.75</sub>Ti<sub>8.25</sub>Cu<sub>7.5</sub>Ni<sub>10</sub>Be<sub>27.5</sub>. *Mater. Res. Soc.* **554**, 167–172 (1999).
176. Kear, G., Barker, B. D. & Walsh, F. C. Electrochemical corrosion of unalloyed copper in chloride media--a critical review. *Corros. Sci.* **46**, 109–135 (2004).
177. Hamilton, J. C., Farmer, J. C. & Anderson, R. J. In Situ Raman Spectroscopy of Anodic Films Formed on Copper and Silver in Sodium Hydroxide Solution. *J. Electrochem. Soc.* **133**, 739 (1986).
178. Yu, J. J. & Lu, Y. F. Laser-induced ripple structures on Ni – P substrates. *Appl. Surf. Sci.* 248–252 (1999).
179. Yasumaru, N., Miyazaki, K. & Kiuchi, J. Control of tribological properties of diamond-like carbon films with femtosecond-laser-induced nanostructuring. *Appl. Surf. Sci.* **254**, 2364–2368 (2008).
180. Jayaraj, J., Gebert, A. & Schultz, L. Passivation behaviour of structurally relaxed Zr 48 Cu 36 Ag 8 Al 8 metallic glass. *J. Alloys Compd.* **i**, 257–261 (2009).